University of Trento

Enrico Cazzador (Ph.D. Student)

# SEISMIC PERFORMANCE ANALYSIS OF BRIDGES WITH ISOLATION DEVICES ENHANCED BY HYBRID DYNAMIC SUBSTRUCTURING

Prof. Oreste Salvatore Bursi (Tutor)

April, 2016

UNIVERSITY OF TRENTO

Doctorate in Engineering of Civil and Mechanical Structural Systems

Cycle: XXVIII

Head of the Doctoral School: Prof. Paolo Scardi

Final Examination: 21 / 04 / 2016

Board of examiners:

Prof. Alexander Movchan (University of Liverpool - Department of Mathematical Sciences, M&O Building)

Prof. Bozidar Stojadinovic (ETH Zurich - Department of Civil, Environmental and Geomatic Engineering)

Prof. Daniele Zonta (University of Trento - Department of Civil, Environmental and Mechanical Engineering)

# ABSTRACT

The Seismic Performance Analysis of Bridges (SPAB) constitutes one of the biggest challenges for structural and civil engineers. In fact, the handling of these design problems requires a deep knowledge of structural behavior and a huge expertise with numerical and analytical tools necessary to perform advanced Finite Element (FE) simulations including dynamic and probabilistic aspects. Within the scope of SPAB, this thesis proposes the analysis of complex bridges assisted by the profitable well-known method of Dynamic Substructuring (DS), advanced model updating strategies, fully probabilistic approaches and innovative time integration algorithms. SPAB includes the evaluation of several nonlinear behaviors inside the structural components and the quantification of benefits generated by safety systems such as isolation devices. As a result, in order to highlight the main advantages of a well designed isolation system, most of the cases analyzed include the comparison between non isolated and isolated configurations. In greater detail, four different bridges have been analyzed and will be presented in this thesis.

First, the Rio Torto highway viaduct, an existing Reinforced Concrete (RC) viaduct on the A1 Italian highway between Florence and Bologna. The structure has been investigated at the laboratory of the Joint Research Center in Ispra (VA) by means of Hybrid Simulations (HSs). The set of 1 : 2.5 scaled substructures included two RC frame piers and the isolation system. The critical issues of the structure due to the complexity of the geometry and the awfulness was the presence of poor seismic details characterized by plain steel rebars. Owing to lack in knowledge for this type of rebars, tests were needed to analyze the seismic response in the *as built* configuration and to evaluate the effectiveness of a seismic retrofitting designed with a traditional Concave Sliding Bearings (CSBs) system.

Then, a typical RC bridge with an innovative prototype of Concave Sliding Bearing (CSB) has been tested at the EUCENTRE Tress Laboratory in Pavia (PV) through HSs. The set of Physical Substructures (PSs) included a 1 : 2 scaled RC box section pier and a full-scale CSB. The prototype was characterized by an asymptotic relation between friction coefficient and load rate. All the benefits of the DS were exhibited during the test; in fact, to exploit the actual potentiality of the isolation system, even with the low speed of the test, the restoring force coming from the CSB was numerically corrected at each time step.

Furthermore, a short-medium span Steel Concrete Composite Bridge made with Hot rolled I-girders (SCCBH) has been investigated. The SCCBH is an example of structural optimization; in fact, it combines both economic and functional benefits deriving from the reduction of *in site* works, e.g. welding, and short construction time. In particular, The novelties were threefold: *i*) the testing of a novel connection between a steel I-girder and a Concrete Cross Beam (CCB); *ii*) the development of a novel mechanical model for this connections; *iii*) the application of the Performance Based Earthquake Engineering (PBEE) to SCCBH. The experimental campaign has been performed on six $1:2$ scaled substructures, representing a deck sub-assembly, tested in both longitudinal and transverse loading directions.

Finally, a simulation-based reliability assessment of a complex cable-stayed foot/-cyclic bridge located close to the sea and equipped with dynamic viscous dampers was performed. The scope was to investigate the benefits of Circular Hollow Section (CHS) structural members for this type of structure when erected in an aggressive environment. A FE model of the structure has been validated, and then used to perform a probabilistic time dependent analysis. Therefore, two corrosion models, i.e. general and localized, capable of evaluating the reduced load bearing section were implemented; and appropriate probability distribution functions were assigned to input model parameters to evaluate the response of the facility during its service life. As a result, the time dependent probabilities of failure have been evaluated and compared with the codes prescriptions.

$^*$ *A complete list of acronyms is available in Section 8.*

## ACKNOLEDGEMENTS

*I would like to express my deep gratitude to Professor Oreste Salvatore Bursi, my research supervisor, for his patient guidance, enthusiastic encouragement and useful critiques during my Ph.D.*
*This research activity would not have been possible without the interaction and cooperation with all the people of the research group. A particular thanks to Dr. Giuseppe Abbiati, Dr. Nicola Tondini, Mr. Manuel Fassin, Dr. Alessio Bonelli, Dr. Fabrizio Paolacci, Mr. Andrea Morbioli.*
*Thanks to ArcelorMittal Europe for the opportunity to spend a fruitful period in its Research and Development Department. Especially, thanks to Ms. Nicoleta Popa, Dr. Oliver Hechler, Mr. Riccardo Zanon.*
*A thanks to the partners of each research project and to each structure that allowed me for developing my research activity. In greater detail, The Laboratory of the University of Trento, the ELSA Laboratory of Joint Research Centre of Ispra, the EUCENTRE TREES Laboratory of Pavia.*
*A special thanks to all my closest friends that even though we are faraway, they are always an important part of my life.*
*Finally, the most important thanks. To my family, my mother Stefania, my brother Riccardo and Giulia that gave me and still give me support and motivation everyday in my life.*

## PUBLICATIONS

As a result of the work conducted in this thesis, the following publications have been produced:

### Journal publications

- O.S. Bursi, **E. Cazzador**, A. Ussia, 2015. Probabilistic analysis of a twin deck curved cable-stayed footbridge subjected to multiple inputs and corrosion. *Journal of Engineering Structures*. Volume 105, 15 December 2015, Pages 87-98. doi: 10.1016/j.engstruct.2015.09.034.

- O.S. Bursi , **E. Cazzador**, M. Fassin, F. Paolacci, S. Alessandri, 2016. A novel componet-based model of steel I-girder-to-concrete cross beam connections for the seismic response of composite short-medium span bridges. Journal of Earthquake Engineering and Structural Dynamics. (In preparation to be submitted).

- F. Paolacci, S. Alessandri, R. Giannini, O.S. Bursi , **E. Cazzador**, 2016. Probabilstic seismic response of steel concrete composite bridges made with hot rolled I-girders and concrete cross beam. (In preparation to be submitted).

- O.S. Bursi, G. Abbiati, **E. Cazzador**, P. Pegon and F. J. Molina. Transient analysis of non-linear heterogeneous structural systems enhanced with dynamic substructuring and a parallel FETI time integrator. 2016 International journal of numerical methods in engineering. (In preparation to be submitted)

### SCOPUS indexed publications

- G. Abbiati, O.S. Bursi, **E. Cazzador**, Z. Mei, F. Paolacci, P. Pegon, 2013. ”Pseudo-dynamic testing with non-linear substructuring of a reinforced concrete bridge”. SERIES Concluding Workshop joint with NEES-US Earthquake Engineering Research Infrastructures JRC Ispra, May 28-30.

- G. Abbiati, O.S. Bursi, **E. Cazzador**, R. Ceravolo; Z. Mei; F. Paolacci; P. Pegon, Pseudo-Dynamic Testing Based on Non-linear Dynamic Substructuring of a Reinforced Concrete Bridge Experimental Research in Earthquake Engineering. in Taucer, F., Apostolska, R., *Experimental Research in Earthquake*

*Engineering*, Institute for the Protection and Security of the Citizen: Springer, 2015.

**Conference proceeding publications**

- O.S. Bursi, G. Abbiati, **E. Cazzador**, Z. Mei, 2013. Numerical advances in the pseudo-dynamic testing technique with non-linear substructuring applied to a reinforced concrete bridge. Conference of the ASCE Engineering Mechanics Institute. EMI2013, August 4-7, Northwestern University, Evanston, Illinois.
- G. Abbiati, O.S. Bursi, **E. Cazzador**, Z. Mei, 2013. Numerical tools for the reduction of complex dynamic models. SERIES Concluding Workshop joint with NEES-US Earthquake Engineering Research Infrastructures, JRC Ispra, May 28-30.
- G. Abbiati, O.S. Bursi, **E. Cazzador**, R. Ceravolo, Z. Mei. Hybrid simulation of an old reinforced concrete viaduct based on nonlinear substructuring techniques Smart Monitoring Assessment and Rehabilitation of Civil Structures - SMAR 2013, September 9-11, Istanbul, Turkey.
- O.S. Bursi, G. Abbiati, M.S. Reza, **E. Cazzador**, 2013. Advances in Pseudo-Dynamic Testing of Complex Structures Based on Model Reduction Techniques. 5th International Conference on Advances in Experimental Structural Engineering, 5AESE, November 8-9, Taipei, Taiwan.
- G. Abbiati, O. S. Bursi, **E. Cazzador**, J. Molina, V. La Salandra, 2014. A Model Updating Strategy for Hybrid Simulation of a Complex Bridge. 6th edition of the World Conference of the International Association for Structural Control and Monitoring (IACSM), Universitat Politcnica de Catalunya, July 15-17. Barcelona, Spain.
- O. S. Bursi, G. Abbiati, **E. Cazzador**, P. Pegon. An Improved Parallel Partitioned Time Integration Scheme based on the Generalized-a method for Hybrid Simulation. 6th edition of the World Conference of the International Association for Structural Control and Monitoring (IACSM), Universitat Politcnica de Catalunya, July 15-17. Barcelona, Spain.

- G. Abbiati, O. S. Bursi, **E. Cazzador**, F. Paolacci and P. Pegon, 2015. Hybrid Simulation of Complex Structural Systems Based on Partitioned Time Integration Schemes. 6th edition of the International Conference on Computational Methods for Coupled Problems in Science and Engineering (COUPLED PROBLEMS 2015). May 18-20, Island of San Servolo, in Venice, Italy.
- G. Abbiati, **E. Cazzador**, I. Lanese, S. Eftekhar Azam, O.S. Bursi, and A. Pavese, 2015. Recent advances on the hybrid simulation of bridges base on partitioned time integration, dynamic identification and model updating. 6th International Conference on Advances in Experimental Structural Engineering 11th International Workshop on Advanced Smart Materials and Smart Structures Technology August 1-2, University of Illinois, Urbana-Champaign, United States
- **E. Cazzador**, M. Fassin, O.S. Bursi, F. Paolacci, O. Hechler, 2015. Performance Based Earthquake Engineering applied to composite bridges with short and medium spans and concrete cross beams. Proceedings of the ECCS - International Symposium on Steel Bridges, September14-16 Istanbul, Turkey
- M. Fassin, **E. Cazzador**, O.S. Bursi, F. Paolacci, 2015. An Innovative Mechanical Model For Steel-Concrete Connections Of Bridges Subjected To Earthquake Loadings XXV GIORNATE ITALIANE DELLA COSTRUZIONE IN ACCIAIO, October 1-3. Salerno, Italy

# CONTENTS

# LIST OF FIGURES

# LIST OF TABLES

# CHAPTER 1

# INTRODUCTION

## 1.1 Seismic performance analysis of bridges

A complete seismic performance analysis of bridges with isolation devices requires a demanding procedure that involves several steps moving from assumptions to predictions passing through analysis and experimental verifications. These phases can be summarized in the four steps of the Advanced Procedure for the Seismic Performance Analysis of Bridges (APSPAB) which are: *i*) generation of predictive FE models and selection of seismic input; *ii*) design and development of experimental tests; *iii*) improvement of FE models by means of validation and calibration procedures; *iv*) development of advanced probabilistic analyses with improved FE models. All the steps require the judgment of the engineer for both prediction and validation tasks. In grater detail, step *i* is dedicated to the numerical modelling for the prediction of structural behavior. This phase is important to localize the structure in terms of static and dynamic behavior, in purpose to design experimental tests and to propose the best seismic isolation typology. In fact, the choice of the proper device is strictly related to structure properties such as vibration periods, modal shapes and allowable displacements. The analysis requires input parameters that during step *i* are not yet available, therefore the role of the engineer becomes essential to make proper assumptions.

During step *ii* the predictive assumptions are checked by experimental tests. The most important task of this phase is the choice of the experimental procedure. In fact, in relation to what the analysis deserves the static or dynamic tests must be performed accordingly. As a result, if the interest is in the static/quasi-static behavior, the cyclic tests allow to draw conclusions about collapse mechanisms, damage evolution and energy dissipation. Conversely if the focus is testing a structure under a certain seismic/dynamic input Hybrid Simulation (HS) is the most suitable test to be performed. Anyway, during every type of test the most important task, common to cyclic and HS tests, is the positioning of an adequate number of instruments capable of quantifying the local and global unknown behavior of the structural components.

The interpretation of these experimental data is performed during step *iii*. Here in fact, the predictive numerical models are locally refined with dedicated elements able to reproduce the actual behavior recorded during the tests. This is probably the most important step during the SPAB, because allows to perform refined investigations with reduced, almost erased, approximations on the FE models.

Finally, the extension of the knowledge, obtained through step *iv*, can be performed in different manners. Each one has the unique scope to prove the effectiveness of the choices made during the previous steps, i.e. $i - iii$, such as the proposal of a structural solution and/or a structural intervention. Decisions that if not analyzed properly and deeply can generate catastrophic events. Furthermore, these numerical investigations have to include probabilistic aspects to consider the uncertainties intrinsically present in every structural problem. Currently, the most advanced techniques that allow to take into account all the cited aspects are the innovative PBEE approach (Krawinkler et al. (2001)) and the consolidated reliability time dependent analysis (Marsh and Frangopol (2008)).

## 1.2 Original scientific contributions of the thesis

APSPAB is a complete process adopted to deeply investigate the seismic response of bridges, especially when they are really complex and can not be analyzed through traditional methods. The performed research activity was focused on four main objectives: *i*) application of the APSPAB to different complex case studies; *ii*) employment of advanced testing techniques to investigate the different aspects of structural problems; *iii*) interpretation of experimental data through refined spring based numerical models with the aim to reproduce the actual behavior of the tested specimens and to extend the knowledge obtained; *iv*) application of advanced probabilistic numerical analysis based on refined FE models able to take into account the main uncertainties of the problem under investigation.

The need for assessing the seismic performance of an old reinforced concrete viaduct characterized by portal frame piers and the retrofitting based on CSBs isolators motivated the development of the RETRO Project (Paolacci (2014)). Characterized by a total span of 400 m and plain steel rebars, the Rio Torto Bridge was under designed if compared with the seismic prescriptions proposed by both Italian and European codes. The seismic retrofitting was proposed on the base of the installation of a pair of CSBs devices interposed between the deck and the cap beam of each pier portal frame. In order to simulate the dynamic response of one of the two independent roadways, a comprehensive set of HSs was designed and performed for both the *asbuilt* and isolated configurations. Predictive numerical simulations highlighted the hysteretic response of piers already at Serviceability Limit State (SLS) (Paolacci and Giannini (2012)). For this reason, nonlinear Numerical Substructures (NSs) were deemed necessary to be coupled with the two PSs, i.e. two portal frame pier, and to conduct realistic HSs. As a result, HSs of the Rio Torto Bridge were successfully implemented at the ELSA Laboratory of the Joint Research Centre of Ispra (VA), Italy. The PM method (Pegon and Magonette (2002)), which embeds subcycling capabilities, allowed for the implementation of the continuous Pseudo Dynamic Test (PDT) method. In order to simulate the degradation of physical and numerical piers a recursive offline model updating of PSs and NSs has been adopted. In addition, thanks to the copious instruments positioned on Pier #11 the degradation due to plane steel rebars has been quantified by means of two FE ABAQUS (SIMULIA (2011)) models enhanced by discrete nonlinear springs.

The novelties in the field of structural dynamic analysis introduced by the RETRO Project showed that complex systems can be tested by HS technique. In light of this additional HSs tests were performed at EUCENTRE Tress Laboratory located in Pavia (PV). The HSs based experimental campaign was dedicated to improve some still open tasks. First of all, since the variation of friction is one of the most important uncertainties in the design CSBs system the opportunity to have a rate-independent CSB device is an significative improvement. As a result, a novel prototype of CSB with asymptotic relation between friction coefficient and load rate was tested. Then, in order to reduce the approximations due to unchanging NSs, an innovative online model updating based on Unscented Kalman Filter (UKF) (Julier et al. (1995)) was implemented to improve the initial offline method adopted for the Rio Torto viaduct and to consider step by step the effects of piers degradation on the rest of the bridge. The novel updating method has been implemented thanks to a novel partitioned time integrator tailored for first order systems (Abbiati et al. (2014)) and allowed for updating the NSs parameters during each test on the base of the instantaneous response of the PSs.

Another still open task in bridge engineering is related to the optimization of costs which can be solved by the introduction of novel solutions and/or the definition of proper maintenance programs.

For the first solution, the case of functional bridges, which are systematically built to overtake city planning or transport network problems is the best choice to prove the effectiveness of a smart and low-cost structural solution. In greater detail, Steel Concrete Composite Bridges made with Hot rolled I-girders (SCCBHs) with CCB allow to save money due to several optimal constructional aspects. This solution was widely used in the non seismic prone areas but there is a lack in knowledge for the seismic response especially for high seismicity zones. As result, several cyclic tests were performed at the laboratory of the University of Trento (TN) and University of Rome TRE (Rome) to analyze the traversal and longitudinal behavior of three novel connections between steel I-girder and CCB when subjected to strong earthquakes. In addition, due to the innovative feature of the solutions, a Component-Based Mechanical Model (CMM) has been developed in an Opensees environment (Mazzoni et al. (2009)) to reproduce the behavior of these joints and to investigate the effects of these solutions when designed for different types of bridges. Finally, a part of the PBEE approach (Cornell and Krawinkler (2000)) was applied to a SCCBH case study in the isolated and non isolated configurations. This is an absolute novelty in the field of bridge engineering.

For the second solution, based on detailed maintenance programs, the case of complex steel bridges erected in extreme environments represents an interesting problem. In fact, several input parameters such as wind, corrosion or pedestrian loads act on the structure and vary during the service life becoming generally more severe. These multi-inputs effects need to be considered to define a suitable maintenance program. For these reasons, the ”Ponte del mare” foot/cycle bridge equipped with viscous dampers was selected as the fourth case study. In greater detail, it has been analyzed numerically by a reliability time dependent analysis performed in a ANSYS (2007) environment, in which the numerical simulations have been performed through Monte Carlo Simulations (MCSs) enhanced by Latin Hypercube Sampling (LHS) (McKay et al. (1979)).

## 1.3 Structure of the thesis

This Ph.D. thesis summarizes research activities performed by the author which were focused on the analysis of the seismic performance of bridges by means of the development of advanced methodological approaches to take the maximum advantage from experimental tests and to develop optimal numerical FE models. The remainder of the thesis is divided in five chapters:

- **Chapter 2**: The APSPAB adopted for the analysis of different case studies was summarized and commented. The four steps of analysis were described: the initial predictive modelling, the experimental campaign, the improvement procedure applied to FE models and the implementation of refined post-test probabilistic analyses. In greater detail, an effective procedure to improve, i.e. validate and calibrate, numerical FE models was formulated and presented.

- **Chapter 3**: The seismic retrofitting of an old RC viaduct was analyzed within the Case Study I (CSI). First, the case study was introduced and discussed for both *asbuilt* and isolated configurations. Second, the Opensees Predictive Model of Case study I (PMCSI) with relevant numerical results was introduced to support the implementation of HSs. Time history analyses justified the selection of substructuring schemes for both piers and CSBs. In greater detail, two different reduction techniques were adopted for linear and nonlinear springs. With regard to the piers the Single Degree of Freedom (S-DoF) springs were implemented on the base of a modified Bouc-Wen model (Smyth et al. (1999)), for the CSB isolation devices instead suitable S-DoF reduced models were tailored according to the state space bilinear model of Mostaghel (1999). Then, the experimental campaign and the relevant results were presented. In particular, advantages of DS to solve experimental obstacles and an offline model updating technique were described. Finally, on the base of experimental data the procedures of validation and calibration of numerical FE models, considered to investigate the effects of rebars slip, were presented. Conclusions based on the results were drawn.

- **Chapter 4**: The seismic assessment of a RC bridge was analyzed within the Case Study II (CSII). First, the case study was introduced and discussed for both isolated and non isolated configurations. Second, the Opensees Predictive Model of Case study II (PMCSII) with relevant numerical results was introduced to support the implementation of DS in the purpose of HSs. Substructuring schemes for a RC pier and a prototype of CSB were described. Then, the experimental campaign and relevant results were presented. In particular, advantages of DS to solve experimental obstacles and an online model updating technique based on UKF were discussed. On the base of experimental data the procedures of validation and calibration of a refined Opensees numerical model (Optimized Model of Case study II (IPMCSII)) were described with the relevant nonlinear time history simulations and comparison with PMCSII. Finally, conclusions were drawn.

- **Chapter 5**: The seismic assessment of a SCCBH was analyzed within the Case Study III (CSIII). First, the case study was introduced and discussed for both isolated and non isolated configurations. Second, the Opensees Simplified Model of Case Study III (SMCSIII) and Predictive Model of Case Study III (PMCSIII) with relevant numerical results was introduced to support the implementation of cyclic tests designed to analyze the seismic response of novel CCB - steel I- girder connection. Then, the experimental campaign and relevant results were discussed. In addition, on the base of experimental data the procedures of validation and calibration of numerical models were described. In greater detail, an innovative CMM of the connection was developed to analyze the local behavior of the components acting on the CCB. Finally, the CMM were used to develop an Opensees Model of CSIII enhanced by CMM (CMMCSIII) considered for the development of the hazard and structural parts of the PBEE approach. Relevant results were presented and conclusions were drawn.

- **Chapter 6**: The reliability analysis of a foot/cyclic bridge erected in extreme environment was analyzed within the Case Study IV (CSIV). First, the case study was introduced and discussed. Second, the Refined Model of Case Study IV made with Open Section Members (RMCSIVOS) developed in ANSYS environment and optimized on the base of in site experimental monitoring data was introduced and modified to obtain the equivalent Refined Model of Case Study IV made with Circular Hollow Section Members (RMCSIVCHS) suitable for the implementation of a reliability multi-input time-dependent analysis. The procedure adopted involved the analysis of the effects due to diffused and local corrosion, wind and variation of loads during the service life of the facility. The simulations were conducted by using ANSYS tools coupled with MATLAB (2012) involving Maximum Likelihood Estimation (MLE) and MCSs enhanced by LHS. Relevant results were presented and conclusions were drawn.
- **Chapter 7**:Conclusions were summarized and outlooks on future perspectives were given.

## CHAPTER 2

# ADVANCED PROCEDURE FOR SESMIC PERFORMANCE ANALYSIS OF BRIDGES - METHODOLOGY

The scope of the advanced procedure for the seismic performance analysis of bridges is to provide essential information to describe and predict the behavior of bridges composed by complex (Chapter 3, 4, 6 ) or novel (Chapter 5) structural details. The objective can not be reached without passing through the experimental data obtained from *insite* investigations or experimental tests. Furthermore, in order to have the maximum gain from these important and costly information they need to be analyzed and reproduced numerically by means of refined FE models. In greater detail, to reach the required target of reproducibility and prediction the SPAB procedure needs 4 steps: *i*) generation of predictive FE models and selection of seismic input; *ii*) design and development of experimental tests; *iii*) improvement of FE models by means of validation and calibration procedures; *iiii*) development of advanced probabilistic analyses with improved FE models. In the thesis these four steps have been developed differently in each case study. Hereinafter a general description about the methodology adopted, all the details about the different implementations and improvements considered during the analysis of each case study are described in the dedicated Chapters.

## 2.1 Step I - Generation of predictive FE models and selection of seismic input

The numerical prediction is crucial to collocate the bridge in the domain of structures and make assumptions about the magnitude and position of nonlinearities.

Generally, during this phase, material properties and geometry are defined on the base of design information and/or mechanical characterization tests. For these reasons they are modified and improved during step III on the base of updated information coming from investigations.

In greater detail, the predictive modeling is used at both global and local scale. When dedicated to global scale, it allows to identify static and dynamic properties such as deflections or fundamental periods of structures. In local scale instead, it is important to quantify roughly local nonlinearties and collapse mechanism, which are essential requirements to design the experimental campaign and to choose the proper substructure to test. Furthermore, the prediction is important to check the limits of experimental facilities and hence to choose the best scale factor to be applied to the specimen. Finally, as shown in Chapters 3 and 4, when HSs tests are performed, the predictive modelling becomes important also to set the NSs.

The selection of seismic input is an important task and it is strictly influenced by the uncertainties related to earthquake features. Each different case requires different considerations on the selection, in this thesis different approaches were used.

## 2.2 Step II - Design and development of experimental tests

The second step is dedicated to experimental tests. During the thesis, among the well-known mechanical characterization tests, other two types of tests have been used: *i*) HSs based on PDT; *ii*) Quasi-Static Cyclic Tests (QSCTs).

### 2.2.1 Hybrid simulations based on pseudo dynamic test

This typology allows to test the Physical Substructure (PS) taking into account the effects of dynamic loads due to inertia and damping. It is important when a particular structure has to be tested in a certain condition of input and components configuration. In greater detail, Hybrid Simulation with Dynamic Substructuring (HSDS) is an experimental techniques in which the overall dynamic response of a structure is evaluated merging the experimental response of one or more PSs, which are the most critical parts, with the numerical response of NSs. As written in the name, *hybrid* means that there is a numerical part and a physical part interacting during the test, this allows the simulation of a complex dynamic system thanks to advantages produced by DS. When two or more substructures are coupled two conditions need to be satisfied in the linked Degrees-of-Freedom (DoFs): *i*) compatibility of kinematic quantities and *ii*) equilibrium of forces. A numerical environment solves the NSs and the time integration of coupled equations of motion advances whilst the condition of coupling are reproduced by the actuators. As a result, dynamics of both NSs and PSs are accurately reproduced, as well as their interactions. If the structural components response is rate independent, HSDS can be conducted at extended time scales, typically $50-200$ times slower than the actual seismic input. Accordingly, inertial and damping components of restoring forces are numerically evaluated and simulated. Conversely, when rate dependent effects are significant, i.e. when CSB are part of PSs, a Real-time Testing (RT) strategy should be selected to obtain reliable simulations. If RT procedure are not available DS allows to overcome rate dependent problems by means of numerical compensation actions. As a result, costs and efforts required to conduct a shaking table test on the entire system are significantly reduced. This type of test has been used to analyze CSI and CSII with different features. In detail, relevant limitations and advantages are described in Chapters 3 and 4.

### 2.2.2 Quasi static cyclic tests

The second testing procedure is more general and provides information about all the response domain, i.e. from elastic to collapse, without direct relation with a seismic input. Since this procedure is general and uncorrelated from specific seismic input consequently there is an open discussion between researchers about the best loading protocol to be adopted to reach the collapse. As summarized in Hutchinson et al. (2011) several loading protocols have been proposed in the last years:

- **ECCS loading protocol**: European Convention for Structural Steelwork ECCS (1986) proposed a loading protocol calibrated for steel and steel concrete structures, in which nonlinear effects are significative. It is based on the definition of a yielding displacement based on a monotonic test $e_y$. The cycles are then multiple or sub multiple of the initial value of $e_y$.

- **ATC-24 loading protocol**: Applied Technology Council 24 (Applied Technology Council (ATC) (1992)) introduced a loading protocol for low cycles experimentation extended to allow the evaluation of damage developed inside the specimen. The aim is to take the maximum advantage from cycles using, if available, the damage information achieved from other specimens.

- **CUREE loading protocol**: CUREE-Caltech wood frame project (Krawinkler et al. (2001)) developed a loading protocol intended to model demands on wood structures associated with ground motions typical of most far field sites. The protocol is characterized by a symmetric pattern of $i^{th}$ interval cycles followed by a number of $(i+1)^{th}$ interval cycles that are equal to 75 % of the previous $i^{th}$ interval cycles. The decrease in cycles number per each amplitude with increasing deformation demand is caused by the observation that earthquakes impose few strong cycles then the period of the system elongates due to nonlinear behavior.

- **ISO loading protocol**: developed by the International Organization for Standardization (ISO) (2003) provides a loading protocol with the application to wood structures. Its intent is to produce data that sufficiently describes the elastic and inelastic properties, and representative demands imposed by earthquakes on structures. This general protocol is used for structural and nonstructural components.

- **FEMA 461 loading protocol**: proposed by Federal Emergency Management Agency (FEMA) (2006) is characterized by increasing amplitude, reversed cyclic displacement controlled loading. Two cycles per amplitude are uniformly applied to the specimen to represent accumulation of damage. The FEMA 461 loading protocol has been designed for application to drift sensitive nonstructural components.

- **AISC loading protocol**: suggested by American Institute of Steel Construction (AISC) (2002), its features are similar to the ISO and FEMA 461 loading protocols, with the addition of small amplitude initial cycles, and a reduction in the number of higher amplitude cycles.

- **Hutchinson loading protocol**: suggested by Hutchinson et al. (2011), the protocol is based on cycle counting and forward ordering of interstory drift time histories for representative mid and low rise building structures. The proposed drift protocols involve: *i*) selection and scaling of the ground motion; *ii*) selection of the representative structure and modelling; *iii*) calculation of the nonlinear structural dynamic response; and *iv*) derivation of amplitude and counting information.

It is evident as the loading protocol is important in the structural response, for this reason each time a Quasi-Static Cyclic Test (QSCT) is performed it has to be properly designed. This type of test has been adopted to analyze CSIII and the implementation is described in Chapter 5.

## 2.3 Step III - Improvement of FE models by means of validation and calibration procedures

The third step is the most important to replicate the experimental results and to spread the achieved knowledge. Here, the initial predictive numerical FE models are checked and improved by means of validation and calibration procedures. In greater detail, Trucano et al. (2006) define validation and calibration as follow:

- *Validation*: procedure to quantify the confidence in the predictive capability of a model through comparison of calculations with a set of benchmark data. It imply correctness of physics and for this reason it is strictly related with engineers, physicists and chemists knowledge and judgment;
- *Calibration*: procedure to adjust a set of input parameters associated with some calculations so that the resulting agreement of the model outcomes with a chosen and fixed set of benchmark data is maximized.

It is important to underline that calibration is a consequence of validation and they can not be used independently and separately. The two steps need to coexist and to interact, hence in the circumstances of poor validation, calibration should be used cautiously and with a certain pessimism about its effectiveness. Both the procedures require a set of accurate information called benchmarks with which will

be compared. The benchmark concept is a crucial point because it decides for the goodness of the model, in general it has to be chosen accurately and can not be simply associated with some experimental data. In general it is a mix between experimental data, knowledge of experts and analytical calculations. Often, for civil engineers the benchmarks are experimental data but sometimes the engineering judgment is more important.
As described in Trucano et al. (2006), it is possible to write a model as

$$M(\bar{i}) : I \rightarrow O \tag{2.1}$$

where I is the space of the input variable $\bar{i}$ which is usually a subset of m-dimensional space $R^m$, whilst O is the space of outputs. The vector of parameters can be rewritten as follow:

$$\bar{i} = (\bar{i}_{primary}, \bar{i}_{secondary}) \tag{2.2}$$

where the $\bar{i}_{primary}$ are the parameters adopted in validation phase that allow the alignment between the model and the validation benchmarks such as geometry or materials. This array has to be consistent with the actual input as materials adopted and characterized by mechanical characterization tests. The secondary part $\bar{i}_{secondary}$ is the set of parameters important for the model but useless for the alignment, these can be modified for the calibration but should remain constant during validation. In a typical civil engineering problem, the vector $\bar{i}$ reads:

$$\bar{i}_{primary} = [Materials\ \ Constitutive\ \ laws, Boundary\ \ Conditions, ...] \tag{2.3}$$

$$\begin{aligned} \bar{i}_{secondary} =[&Loading\ \ Protocol, Load\ \ Steps, \\ &Integration\ \ Algorithm, Discretization\ \ of domain, \\ &Discrete\ \ Springs, ...]. \end{aligned} \tag{2.4}$$

The benchmarks functions can be multiple and different for validation and calibration due to the specific interest of the engineer. When experimental data have been chosen as benchmarks and several similar tests were performed, some uncertainties should be taken into account. In greater detail, there are two types of uncertainties: aleatory and epistemic. The fist one is related to the randomness of some parameters, this one can not be avoided. The second is related with the lack of knowledge about the quantities or phenomena, this one can be ideally deleted by the increasing of knowledge. These uncertainties, if quantifiable, should be considered in all the components of a comparison procedures, i.e. benchmarks and calculation values.

The benchmarks function have to be consistent with the alignment parameters and can be write as:

$$B_j^{Val}(\bar{i}_{primary}) = [Sigma_{Concrete} - \varepsilon_{Concrete}, ...] \tag{2.5}$$

$$B_j^{Cal}(\bar{i}_{primary}) = [Force - Displacement \quad response, ...] \tag{2.6}$$

as can be appreciated, the index $j$ represent the possibility to have more benchmarks for validation and calibration. For example benchmark functions can be a concrete constitutive law and the experimental force-displacement for validation and calibration, respectively. In general, benchmarks functions for validation should include materials properties and local mechanisms such as rotations or local displacements; conversely, calibration benchmarks should include global behaviors such as global force-displacement response, moment-curvature or periods of vibrations. Only representative and sensible quantities should be considered, e.g.quantities that influence and modify considerably the model output. As an example, if the model dose not exhibit nonlinear behavior or steel component, the yielding stress should not be considered as a benchmark. This choice would spoil the validation and calibration error.

Once introduced these quantities the next step is the comparison, it is performed by the definition of an error function to compare output and benchmarks, it reads:

$$D^{Val}[M(\bar{i}_{primary}, \bar{i}_{secondary}), B^{Val}(\bar{i}_{primary})] \tag{2.7}$$

$$D^{Cal}[M(\bar{i}_{primary}, \bar{i}_{secondary}), B^{Cal}(\bar{i}_{primary})] \tag{2.8}$$

respectively for validation and calibration. The formulation can be generalized for multiple benchmarks functions and alignments parameters as follow:

$$D^{Val,k} \equiv D[M(\bar{i}_{primary,k}, \bar{i}_{secondary,i}), B^{Val,k}(\bar{i}_{primary})], k = 1, ..., n \tag{2.9}$$

$$D^{Cal,k} \equiv D[M(\bar{i}_{primary,k}, \bar{i}_{secondary,i}), B^{Cal,k}(\bar{i}_{primary})], k = 1, ..., n \tag{2.10}$$

When multiple benchmarks and alignment parameters are used, the total error can be written as a mean error distributed on all the set of D functions, as follows:

$$D^{Val}_{Tot} = \frac{\sum_{k=1}^{n} w_k^{Val} \cdot D^{Val,k}}{n} \tag{2.11}$$

$$D^{Cal}_{Tot} = \frac{\sum_{k=1}^{n} w_k^{Cal} \cdot D^{Cal,k}}{n} \tag{2.12}$$

where $w_k^{Val}$ and $w_k^{Cal}$ represents the weights that can be applied to the different errors for validation and calibration, respectively. The optimum point between these quantities represents the best fitting and hence the optimal model. To be consistent with the model, the parameters have to be varied in the range of uncertainties giving the priority in decreasing the validation error. The total error vector used to quantify the global difference between the model and the benchmark functions can be write as follow:

$$Err_{Tot} = [D^{Val}_{Tot}; D^{Cal}_{Tot}] \tag{2.13}$$

that define the distance between the model and the ideal *Perfect Model*.

As an examples, in Figure 2.1 are shown two models in the domain of errors. In detail, Model #1 represents a model with a good validation but a bad calibration, Model #2 the opposite and Model #3 instead represents a model that can be considered an optimal model since it is portrayed by good validation and good calibration simultaneously.

Finally, once evaluated this quantity the last part consists in the check of the model's credibility, to do this Trucano et al. (2006) proposes to apply this procedure based on Boolean check:

1. Chose a diffused quantity to be compared;
2. compute the $l^1[0, 1]$ norm of the difference between the model and the benchmark as follow:

$$D[M(\bar{i}), B(\bar{i})] = \| \rho_{model} - \rho_{ref} \|_{l^1} [0, 1] \tag{2.14}$$

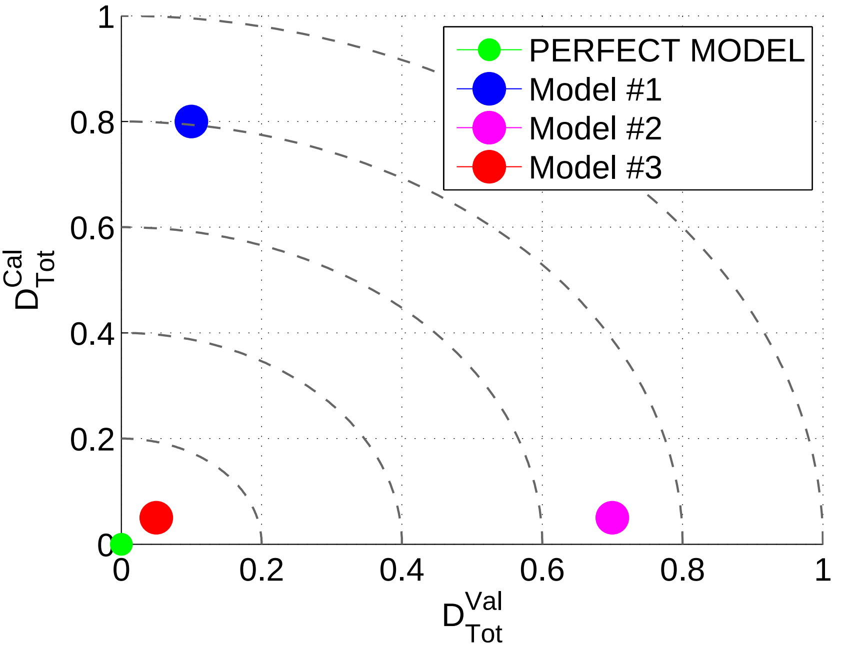

Figure 2.1: Domain of models error $Err_{Tot}$

3. define a limit $\varepsilon$;

4. the credibility of the model is verified if:

$$C^{Model} \equiv || \rho_{model} - \rho_{ref} ||_{l}1 \ [0,1] < \varepsilon \tag{2.15}$$

   otherwise the model is judged not credible.

In light of this, in the thesis was used a modelling procedure based on discrete springs. The modelling called here Springs Based Modelling (SBM) is based on the implementation of nonlinear discrete springs in crucial points of the structure and tailor their constitutive laws on the experimental outcomes. The SBM approach improves the effectiveness of the FE models and it allows to decrease the total error thanks to the good reproduction of the alignment parameters $\bar{i}_{primary}$.
Finally, the procedure can be summarized:

- **Phase 1** Definition of alignment parameters $\bar{i}$, i.e. input of the Model;

- **Phase 2** Selection of Validation benchmarks $B_i^{Val}$;

- **Phase 3** Selection of $k-th$ Validation maximum error $D_{Max}^{Val,k}$;
- **Phase 4** Selection of Calibration benchmarks $B_i^{Cal}$;
- **Phase 5** Selection of $k-th$ Calibration maximum error $D_{Max}^{Cal,k}$;
- **Phase 6[Validation Phase]** Modification of input parameters to decrease validation error $[D_{Tot}^{Val}]$;
- **Phase 7[Calibration Phase]** Modification of input parameters to decrease validation error $[D_{Tot}^{Cal}]$;
- **Phase 8** Definition of the maximum acceptable global error of the model $E_{Tot}^{Max}$;
- **Phase 10** Check the goodness of the final model by means of the classification as *believable model* or *unbelievable model* (that demand further improvements).

In the thesis this procedure is applied in CSI, CSII and CSIII to improve the FE models adopted to develop the step IV of APSPAB.

## 2.4 Step IV - Development of advanced probabilistic analysis with improved FE models

The last step is dedicated to the numerical investigations performed with the improved FE models based on the obtained outcomes. In greater detail, in the thesis, among the general FE numerical simulations two types of advanced probabilistic analyses have been implemented: *i*) PBEE framework; *ii*) reliability time dependent analysis based on MCSs and LHS. As widely described hereinafter, the fist one is the most recent and it is a design procedure able to consider all the uncertainties acting on a structure such as structural, seismic and economic uncertainties. Up to now composite bridges have never been investigated by means of PBEE, therefore the investigations presented in Chapter 5 are an absolute novelty. The second is a well-know method widely applied in structural analysis but never used for complex bridges such as CSIV. It is focused to structural investigations, economic aspects are not directly included in the calculations but the results are suitable to be translated in economic quantities such as maintenance costs.

### 2.4.1 Performance Based Earthquake Engineering Framework

The most advanced procedure to design a bridge taking into account the main uncertainties is the PBEE framework proposed by Cornell and Krawinkler (2000). In greater detail, four variables act during the procedure phases:

- *intensity measure (im)*, which represents a measure of the earthquake intensity. Different im variables can be considered, such as Peak Ground Acceleration (PGA), magnitude, etc;
- *engineering demand parameter (edp)*, which describes the structural response in term of global and local parameters, such as deformations and accelerations;
- *damage measure (dm)*, which identifies the structural damage condition;
- *decision variable (dv)*, which transforms the damage relationship into useful quantities for the economic losses evaluation.

Assuming: *i)* $G(x \mid y) = Pr(x < X \mid Y = y)$, which denotes the conditional complementary distribution function and *ii)* $dG(x \mid y)$, which denotes the derivative of the conditional complementary cumulative distribution, it is equivalent to the negative of the conditional probability density function. The PBEE procedure is applied with the following assumptions (Yang et al. (2009)):

1. $G(dm \mid edp, im) = G(dm \mid edp)$, it means that for a given edp, dm is statistically independent from im;
2. $G(dv \mid dm, edp, im) = G(dv \mid im)$, it means that for a given dm, dv is statistically independent from edp and im;
3. The structure is restored to its original condition after each damaging seismic event. Without this assumption, the state of damage of the system being subjected to subsequent earthquakes should be taken into account.

The analytical integration over all the intensity values entails:

$$\lambda(dv < DV) = \int_{im} G(dv \mid im) \mid d\lambda(im) \mid \tag{2.16}$$

with:

$$G(dv \mid im) = \int_{dm} \int_{edp} G(dv \mid dm) dG(dm \mid edp) dG(edp \mid im) \tag{2.17}$$

The mean annual rate of the decision variable DV exceeding a threshold value reads finally:

$$\lambda(dv < DV) = \int_{im} \int_{dm} \int_{edp} G(dv \mid dm) dG(dm \mid edp) dG(edp \mid im) \mid d\lambda(im) \mid \tag{2.18}$$

It is evident from Equation 2.17 that four components of performance assessment are required as shown in Figure 2.2. Specifically, the quantification of $\lambda(im)$, $G(edp \mid im)$, $G(dm \mid edp)$, $G(dv \mid dm)$ require a hazard analysis, a response analysis requires, a damage analysis and a so called loss analysis, respectively. It is evident that the quantification of $G(dv \mid im)$ requires a fully probabilistic approach. In this thesis, only the probability of exceeding of a certain edp will be quantified as shown in Chapter 5. With this scope (Kunnath (2007)), the following relationship has been adopted:

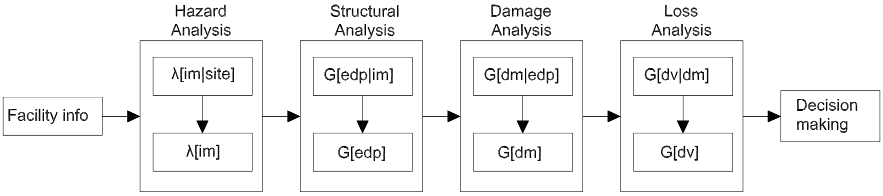

Figure 2.2: Parts of the PBEE method

$$G(edp) = \int_{0}^{\infty} G(edp \mid im) \mid \frac{d\lambda(im)}{dim} \mid dim \tag{2.19}$$

### 2.4.2 Reliability time dependent analysis based on Monte Carlo simulations and latin hypercube sampling

As stated in the work of Nowak and Collins (2000), the reliability of a structures is its ability to fulfill its design purpose for some specified design lifetime. In other words it is the probability that a structure will not fail to perform its intended function. It is important to underline that the term *failure* does not mean catastrophic events but can be associated also to the overcoming of a SLS such as deflections or rotations.

The reliability analysis allows to consider all the different uncertainties present during the constructional process:

- *Naturals uncertainties* which derive from natural predictability of loads and mechanical behavior of the materials
- *Humans uncertainties* which derive from design error due to approximations, calculations errors, communication problems, all the variations due to human interactions.

As a result, material properties of structural elements, loads and additional components acting on the structure have to be implemented in the design procedure as random variables. As a result, probability of failure can be written as follow (Holicky et al. (2005)):

$$P_f = P(E \leq R) \tag{2.20}$$

where E represents the action effect whilst R the resistance. The exact solution when both E and R are represented by two random variables can be obtained by probability integration as shown in Figure 2.3. More in detail, assuming that the event A represent the occurrence of action E in the differential interval $[x, x + dx]$, the probability of event A reads:

$$P(A) = P(x \leq E \leq x + dx) = \phi_E(x)dx \tag{2.21}$$

event B instead denote the event that R occurs within the interval $[-\infty, x]$, hence the probability of event B:

$$P(B) = P(R \leq x) = \Phi_R(x) \tag{2.22}$$

with the assumption of mutual independence of the variables E and R the differential probability of failure can be written:

$$dP_f = P(A \cap B) = P(A)P(B) = P(x \leq E \leq x + dx)P(R \leq x) = \Phi_R(x)\phi_E(x)dx \quad (2.23)$$

Finally, the integration of the quantity over all the domain $[-\infty, +\infty]$ provide the analytical probability of failure:

$$P_f = \int_{-\infty}^{\infty} \Phi_R(x)\phi_E(x)dx \quad (2.24)$$

For complex problems, this integral can not be solved analytically, as a result it is evaluated numerically passing through MCSs. In greater detail, MCS method is a procedure that allows to generate several numerical results without the need to perform additional physical tests. In fact, once defined the input distribution functions, i.e. materials and loads, these are sampled once for each simulation to obtain each time one deterministic value. In general, with traditional sampling procedure, the number of simulation has to be enough numerous especially if small probabilities of failure has to be quantified. As reported hereinafter, when a standard Monte Carlo Simulation (MCS) procedure is applied the probability of failure can be evaluated as follows:

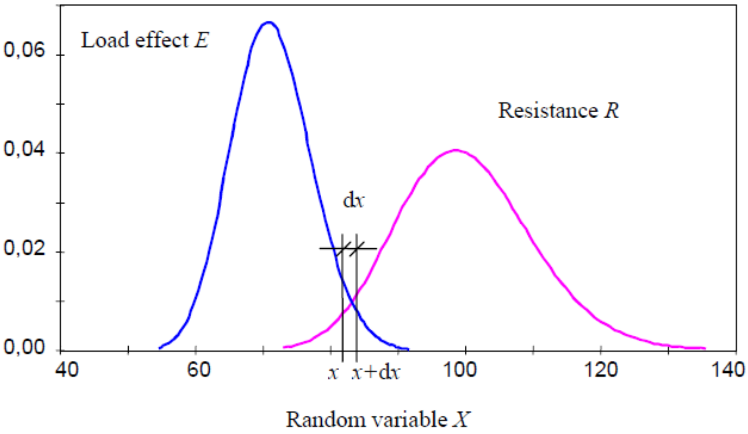

Figure 2.3: General case of probability of failure, after Holicky et al. (2005)

$$P_f = \frac{n_f}{N} \quad (2.25)$$

where N is the total number of simulations and $n_f$ the number of failures. It is clear that with a pure MCS the Equation 2.24 is not necessary anymore. Furthermore, when this type of numerical analysis is performed the probability of failure can be treated as a probability itself due to the uncertainties of numerical procedures. As a result $P_{f,True}$ can be write as:

$$E[P_f] = P_{f,True} \tag{2.26}$$

$$\sigma^2_{P_f} = \frac{1}{N}[P_{f,True}(1 - P_{f,True})] \tag{2.27}$$

$$V_{P_f} = \sqrt{\frac{(1 - P_{f,True})}{N(P_{f,True})}} \tag{2.28}$$

where $E[P_f]$, $\sigma^2_{P_f}$, $V_{P_f}$ are the expected value, variance and coefficient of variation of $P_f$, respectively. With these assumption it is possible to assume the required coefficient of variation of $P_f$ and hence evaluate the minimum number of simulations (Soong and M. (1993)):

$$N = \frac{1 - P_{f,True}}{V^2_{P_f}(P_{f,True}})) \tag{2.29}$$

With these hypothesis is evident as the number of simulations become important for the traditional structural problems in which probabilities of failure are relative small. In addition, civil engineering problems require complex and nonlinear FE models that need a significative computational time. Therefore, an effective strategy to decrease the number of simulations has to be adopted.

As an example, the MCSs method can be enhanced by LHS (McKay et al. (1979)) which is a technique to reduce the number of simulations needed to obtain meaningful probabilistic results.

In this case, the output function Y required to evaluate the $P_f$ can be written:

$$Y = f(X_1, X_2, ......X_K) \tag{2.30}$$

where $X_i$ is the $i^{th}$ input random variable for an amount of K random variables. In greater detail, the procedure develops as follows (Nowak and Collins (2000)):

1. partitions of the input probability functions $X_i$ in N equal probability intervals;
2. for each $X_i$ and each interval randomly selects a representative value, the random selection can be based on different probability functions such as uniform or normal;
3. since there are $N^K$ possible combination of these representative values, the objective of LHS is to select N combinations such that each representative values appear once;
4. to obtain the first combination, the procedure selects a value of each random variable on N intervals. Then for the second combination the value is chosen on the possible N-1 intervals, the third combination is chosen on the N-2 possible intervals. The algorithm goes like this until the number of N combinations is reached;
5. for each combination there is an output $Y_i$ function. The set of $Y_i$ need to be treated to obtain a handable probability density function, e.g. by means of the method of moments to obtain $\mu$ and $\sigma$ of a gaussian distribution.

$$\mu_Y = \frac{1}{N}\sum_{i=1}^{N} Y_i \tag{2.31}$$

$$\sigma_Y = \sqrt{\frac{\sum_{i=1}^{N}(Y_i - \mu_Y)^2}{N}} \tag{2.32}$$

Instead to use the traditional method of moments, an additional improvement is the application of MLE which allows to find the most likelihood distribution function to represent the output function Y. The method was widely applied in Chapter 6 and narrowly in Chapter 5. In greater detail, the objective is to search a parameter $\theta$ of the chosen probability function such that it allows to maximize the sample likelihood function $L_Y$.

In greater detail, the joint probability distribution of a random sample $X_1$,$X_2$,....$X_N$ can be written as:

$$f_{X_1,X_2,..X_N}(x_1, x_2, ..x_N \mid \theta) = f_{X_1}(x_1)f_{X_2}(x_2)\cdot\cdot f_{X_N}(x_N) = \prod f_X(\theta \mid x_i) \tag{2.33}$$

the sample likelihood function reads,

$$L_Y(\theta \mid x_1, x_2, ....x_N) = \prod_{i=1}^{N} f_X(x_i \mid \theta) \tag{2.34}$$

hence the MLE provide the parameter $\theta$ that maximize this function:

$$MLE = max_\theta \prod_{i=1}^{N} f_X(x_i \mid \theta) \tag{2.35}$$

As a result the output probability function has been evaluated and it is possible to evaluate the probability of failure with Equation 2.24.

The time dependency becomes part of the analysis if the simulations are performed several times considering the variation of input variables due to aging effect or modification of loads.

## CHAPTER 3

# SEISMIC RETROFITTING OF AN OLD REINFORCED CONCRETE VIADUCT BASED ON HYBRID SIMULATIONS - CASE STUDY I

### 3.1 Introduction.

This chapter was developed within the RETRO project (Paolacci (2014)). The purpose of the chapter is to describe the experimental and numerical investigations performed to study the seismic response of an existing RC bridge designed with plane steel rebars. In addition, the effectiveness of an innovative retrofitting system based on CSBs was analyzed.

In detail, CSI is a typical bridge designed with the seismic prescriptions of the middle of the 1900, for this reason it needed to be retrofitted on the base of latest seismic knowledge. The experimental campaign included hybrid tests performed by considering two piers as PSs and the remaining part of the viaduct as Numerical Substructure (NS). The prototypes of a 2-level and a 3-level one-bay RC frame piers were built at the laboratory of ELSA at the Joint Research Center of Ispra and were scaled with a factor of 1:2.5. The piers were tested by using PDT. During the tests, different configurations were considered, the original viaduct, i.e. *as built* configuration, and the retrofitted viaduct, i.e. isolated configuration. In greater detail, the objective of the project was threefold:*i*) to cover the lack of knowledge in the nonlinear behavior of portal frame piers in presence of plain steel rebars; *ii*) employment of large scale experimental test for the seismic assessment of existing bridges; *iii*) to study of the effectiveness of a seismic isolation systems based on CSBs.

Therefore, in Section 3.2 the details of CSI and the PMCSI are presented. Then, in Section 3.3 are described the experimental campaign and thefeatures of the reduced models implemented as NSs, in the same section is presented the offline model updating technique adopted to update the nonlinear parameters of the NSs to take into account the damage of the structural elements during the earthquake. After, in Section 3.4 is reported the improvement of FE models performed in the SIMULIA (2011) environment for the investigation of the local effects of the rebars bond-slip. The capability of a 3D refined model to reproduce the local mechanisms of the structural elements was compared with a lattice of Linear Variable Displacement Transducers (LVDTs) installed on the Pier #11. Finally, in Section 3.5 are reported the main conclusions.

## 3.2 Description of Case Study I

The CSI is an old RC bridge consisting of a 13 spans deck with two independent roadways sustained by 12 couples of portal frame piers as shown in Figure 3.1. Each pier is composed by two solid or hollow circular columns of variable diameter (between 120 and 160 cm), connected at the top by a cap beam and along the height at various levels, by one or more transverse beams of rectangular cross section. The height of the piers varies between 13.8 m, near the abutments, to 41 m, at the center of the bridge as reported in Table 3.1. The deck is realized by two open section RC beams 2.75 m high, as shown in 3.2(c), which are interrupted by some Gerber saddles placed at the $2^{nd}$, $7^{th}$ and $12^{th}$ span respectively, as depicted in Figure 3.2(b). The geometrical properties of the deck cross section are reported in Table 3.2. The deck is connected to each cap beam by two steel

Figure 3.1: A view of Case Study I connection of A1 highway between Florence to Bologna.

| Pier | Height [m] | Pier | Height [m] | Pier | Height [m] |
|---|---|---|---|---|---|
| #1 | 17.35 | #5 | 27.86 | #9 | 25.74 |
| #2 | 30.61 | #6 | 39.41 | #10 | 17.19 |
| #3 | 30.49 | #7 | 41.34 | #11 | 14.37 |
| #4 | 26.75 | #8 | 36.49 | #12 | 13.80 |

Table 3.1: Heights of piers of Case Study I.

dowels and to the abutments by traditional structural bearings. For these reasons the structural scheme of the bridge can be considered as simply supported. The columns have two types of cross sections: *i*) solid circular shape with diameter of

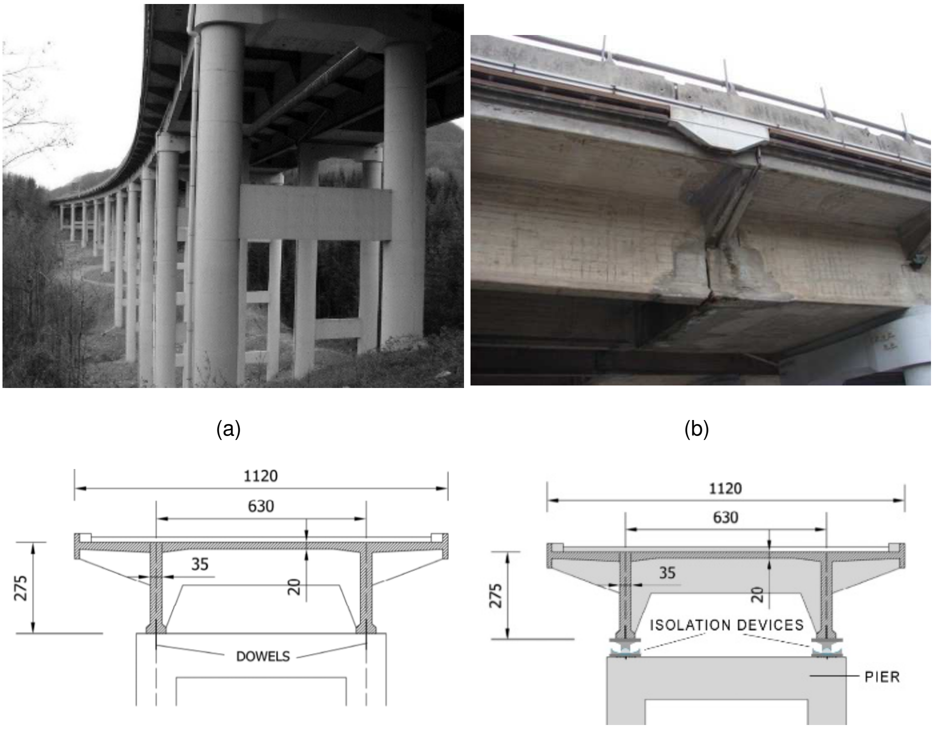

Figure 3.2: Structural details of Case Study I: a) View of the frame piers; b) View of the Gerber Saddles; c) Cross section of the *as built* bridge; d) Cross section of the isolated bridge.

| **Area [$m^2$]** | **It [$m^4$]** | **Iy [$m^4$]** | **Iz [$m^4$]** |
|---|---|---|---|
| 4.63 | 0.10 | 51.90 | 3.45 |

Table 3.2: Geometrical Properties of Case Study I.

120÷160 cm; *ii*) hollow circular shape with external and internal diameters equal to 160 cm and 100 cm, respectively. In Figure 3.3 are depicted the distribution of solid circular and hollow circular cross section columns along the bridge. In Figures 3.4 and 3.5 some structural details in full scale of piers elements and a global view with the rebars distribution of Pier #9 and #11 chosen as PSs to be tested. It is possible to appreciate the complex lattice of rebars, especially in the zones of transverse beams. In those zones there are several rebars both straight and inclined. In grater detail, Pier #9 is composed by two transversal beams with rectangular cross section of 150x40 cm and a cap beam U-shaped 120 cm high. The cross section of the columns is circular hollow with an external diameter of 160 cm and an internal diameter of 100 cm. The columns are filled with a spiral of plane steel rebars $\phi$6mm separated each 14 cm and 34 longitudinal rebars, i.e. 20 $\phi$20mm and 14 $\phi$16mm.

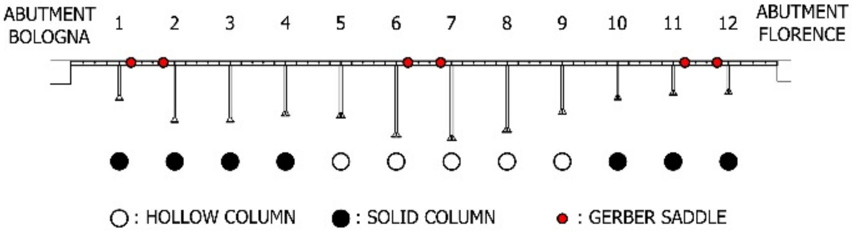

Figure 3.3: Distribution of circular and hollow sections.

Pier #11 instead has one transverse beam with a 120x40 cm cross section. As for Pier #9 the cap beam is an element U-shaped 120 cm high. The columns are solid circle cross section with a diameter of 120 cm filled with a spiral of plane steel rebars $\phi$6 mm separated each 14 cm and 16 longitudinal $\phi$20mm rebars.

Limited design data about the materials used in the bridge was available. The class of concrete should corresponds to a mean resistance of 30 MPa, while the class of

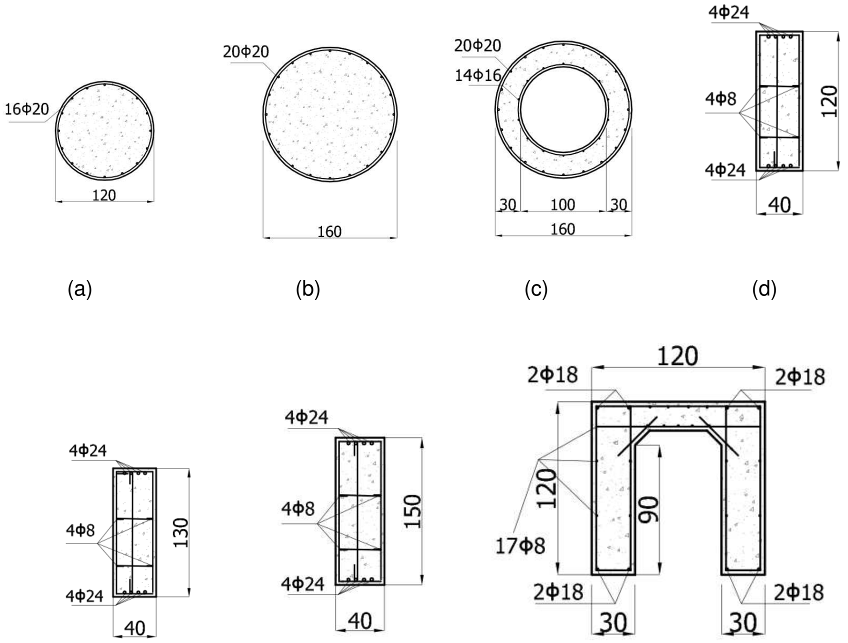

(a) (b) (c) (d)

(e) (f) (g)

Figure 3.4: Full-scale cross sections of piers elements: a) circular cross section 120 cm diameter; b) circular cross section 160 cm diameter; c) hollow circular section; d) transverse beam 120 cm high; e) transverse beam 130 cm high; f) transverse beam 150 cm high; g) cap beam section.

steel used in Italy when the bridge was constructed was AQ42, corresponding to a mean strength of 350 MPa (Paolacci (2014)).
As a result, the set of dead loads acting on the viaduct due to the described structural configuration is reported in Table 3.3.

### 3.2.1 Design of the isolation system based on concave sliding bearings

The retrofitting of the bridge was comprehensive of a couple of CSBs on each piers and the removal of the Gerber saddles. The design of the retrofitting has been carried out with a displacement-based procedure (Priestley, M.J.N. and Calvi, G.M. and Kowalsky, M.J. (2007)) focusing on two objectives: *i*) to keep the piers in the

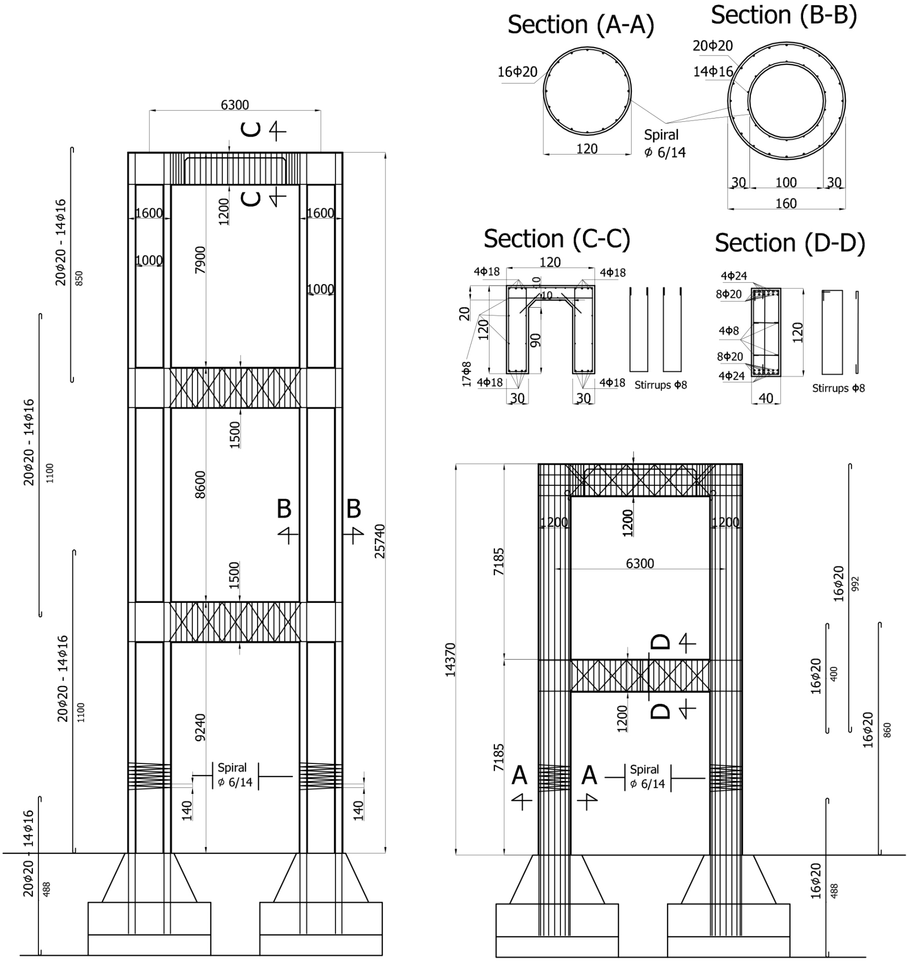

Figure 3.5: Details of Pier #9 and #11 reinforcements.

elastic o slightly inelastic range, cracking of concrete was accepted; *ii*) to minimize the displacement demand on the expansion joints located at the abutments. Currently there are three basic types of CSB commonly used for new or for existing structures:

- *CSB type I* - Single sliding surface device, that may be at the top or at the bottom of the device, connected to a spherical hinge. This device is the most adopted if the design requirements are not too much demanding.

| Element | Linear weight [$\frac{kN}{m}$] |
|---|---|
| RC deck | 112 |
| Slab | 6 |
| Stiffeners | 10 |
| Asphalt | 30 |
| Guard rail | 2 |
| Waterproof | 1 |
| Parapet | 5 |
| **Total** | **166** |

Table 3.3: Dead loads acting on the deck

- *CSB type II* - Double sliding surface device, equipped with an interposed point rocker articulation that allows relative rotations. This device is often used to minimize the plan dimensions of the isolator and to limit the vertical load eccentricity caused by the horizontal displacement.
- *CSB type III* - Triple sliding surface device, equipped with two perpendicular cylindrical articulations allowing the relative rotations. This type of device is used when a different behavior is required in the two loading directions.

The *CSB type I* was adopted herein to seismically isolate the Rio Torto bridge, which is characterized by relatively small displacements and similar responses along the lateral and transversal directions. The basic elements of the adopted CSB shown in Figure 3.6(a) are:

1. upper anchor plate;
2. sliding surface;
3. sliding material interface;
4. rotation element;
5. rotation sliding surface;
6. lower anchor plate.

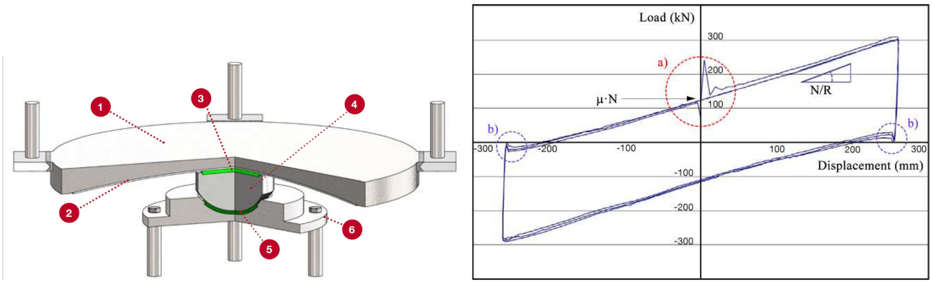

(a) (b)

Figure 3.6: Details of the CSB adopted for the seismic retrofitting: a) CSB type I (courtesy of ALGAS.p.A); b) Hysteretic behavior of the CSB obtained during dynamic tests.

From a mechanical point of view, the CSB devices is characterized by a simplified bilinear force displacement relationship assumed if the vertical load is constant:

$$V_{CSB} = \mu_f N + \frac{N}{R}\Delta_{iso} \tag{3.1}$$

where $\mu_f$ is the friction coefficient, N is the normal force, R is the device curvature radius and $\Delta_{iso}$ is the sliding displacement of the isolator. Figure 3.6(b) shows the experimental characterization tests performed on the CSB.
Typical effects of the dynamic test are shown in the Figure 3.6(b): *i*) internally to the circle a the typical variation of the friction coefficient relative to the breakaway of the motion; *ii*) in the circle b instead is possible to see the change in sign of velocity. The radius of the CSB device considered for the seismic retrofitting of the CSI is equal to 3 m whilst the design friction coefficient ($\mu_{des}$) is equal to 4%. The height of the articulated slider is 9 cm and the initial yield displacement ($\delta$) is 0.5 mm. Each pier portal frame bears a vertical load varying between 5600 kN and 5300 kN hence the vertical load N acting of the single device varies between 2800 kN and 2700 kN. The threshold shear force at the yielding of the CSB was approximately 110 kN.

### 3.2.2 Seismic Input

The East-West and the North-South components of the Emilia earthquake of 2012 were considered as SLS and Ultimate Limit State (ULS) seismic actions, respectively. Figures 3.7(a) and 3.7(b) depicts both accelerograms. The SLS accelerogram was characterized by 0.26g of PGA, whilst the ULS accelerogram by 0.27g of PGA. Relevant acceleration and displacement response spectra are compared in Figures 3.7(c) and 3.7(d).

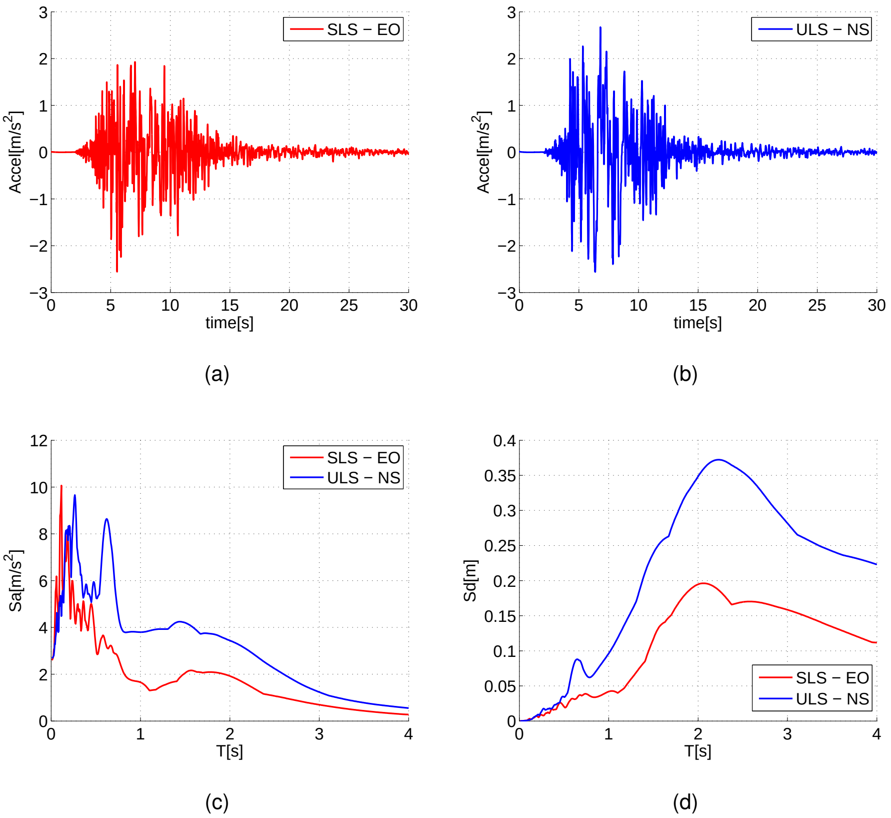

(a)

(b)

(c)

(d)

Figure 3.7: Seismic input for both SLS and ULS:a) accelerogram of the SLS ground motion; b) accelerogram of the ULS ground motion; c) acceleration response spectra; d) displacement response spectra.

### 3.2.3 Predictive FE model of Case Study I

A predictive Opensees (Mazzoni et al. (2009)) fiber-based FE model of CSI (PMCSI) able to simulate the nonlinear behavior of crucial elements of the viaduct was implemented, as presented in Paolacci and Giannini (2012). The model was developed as a support for the HSs tests. Moreover, piers were considered clamped at the base whilst abutments, of both sides of the bridge, have been assumed to be simple rested in the longitudinal direction and restrained in the transversal and vertical directions. Four rigid links were considered to take into account the offset between the center of gravity of the deck and the pier cap beam. In detail, each rigid link was considered fixed to the deck and hinged to the relevant pier, as shown in Figure 3.8(a). Gerber saddles were modelled as hinges able to transfer longitudinal and transversal actions. The deck was implemented by means of linear beam elements. Frame piers, with both circular and hollow cross sections were discretized with nonlinear fiber-based beam elements. They allowed for an accurate discretization of cross sections, reproducing the exact position and dimension of rebars inside concrete matrix with relevant constitutive laws. Figure 3.8(b) depicts the fiber-based nonlinear elements of Pier #12 characterized by solid circular cross section columns. According to Alessandri et al. (2013), the contribution of the concrete tensile strength was neglected due to the presence of plain steel rebars.

For these reasons, the *Concrete*01 material of Opensees based on the Kent-Scott-Park model was used to simulate the concrete behavior (Kent and Park (1971)). Figure 3.9(a) shows the constitutive law of the *Concrete*01 material, the maximum compressive strength $f_{cm}$ was identified equal to 26MPa with a the corresponding compressive yielding strain $\varepsilon_{c0}$ assumed equal to 0.25%. The ultimate compressive strength $f_{cu}$ and the corresponding ultimate strain $\varepsilon_{cu}$, were assumed equal to 22MPa and 0.6% respectively.

Rebars have been modelled with the *Steel*02 Opensees material according to the Menegotto-Pinto constitutive law (Menegotto and Pinto (1973)) depicted in Figure 3.9(b). The yielding stress $f_y$ was assumed equal to 360MPa, along with a Young modulus of 205000MPa; the hardening parameter b was set equal to 0.025. The

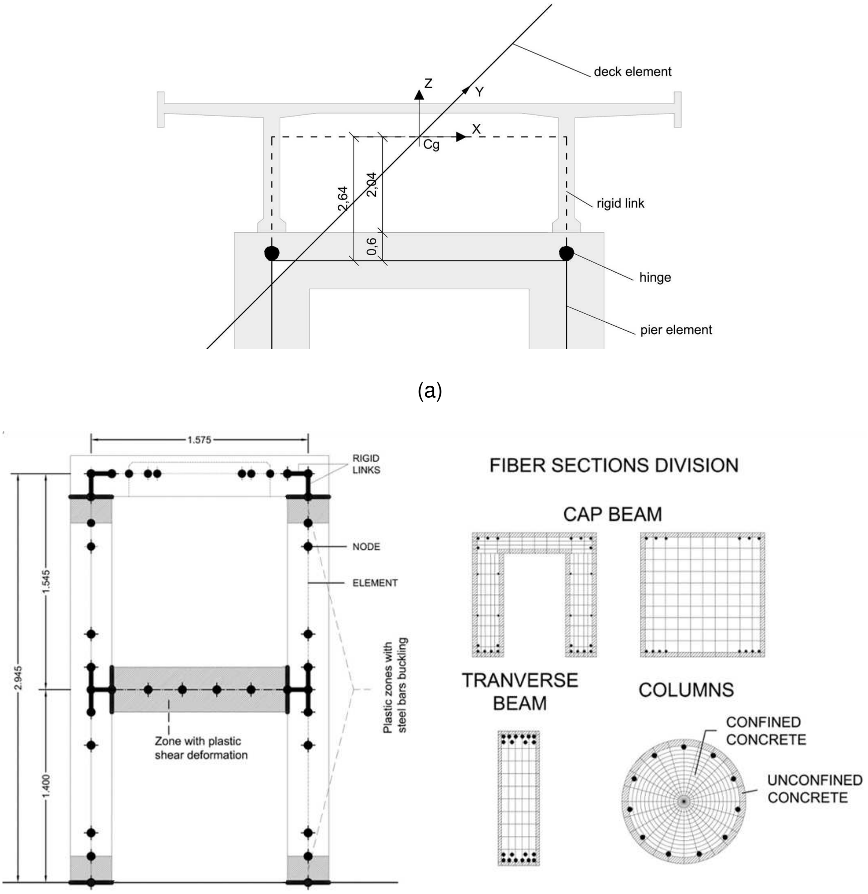

(a)

(b)

Figure 3.8: Details of the predictive model of Case Study I: a) rigid links of the deck cross section; b) fiber sections of the frame pier.

transverse beam was modelled with a nonlinear shear-strain hysteretic relationship which neglect the influence of axial forces. To do this a *hysteretic* Opensees material, depicted in Figure 3.10, was implemented according to Priestley et al. (1994) and Vecchio and Collins (1988). In greater detail, the formulation reads:

$$V_t = V_c + V_s \tag{3.2}$$

with:

$$Vc = 0.8k_d\sqrt{f_c}A_c \tag{3.3}$$

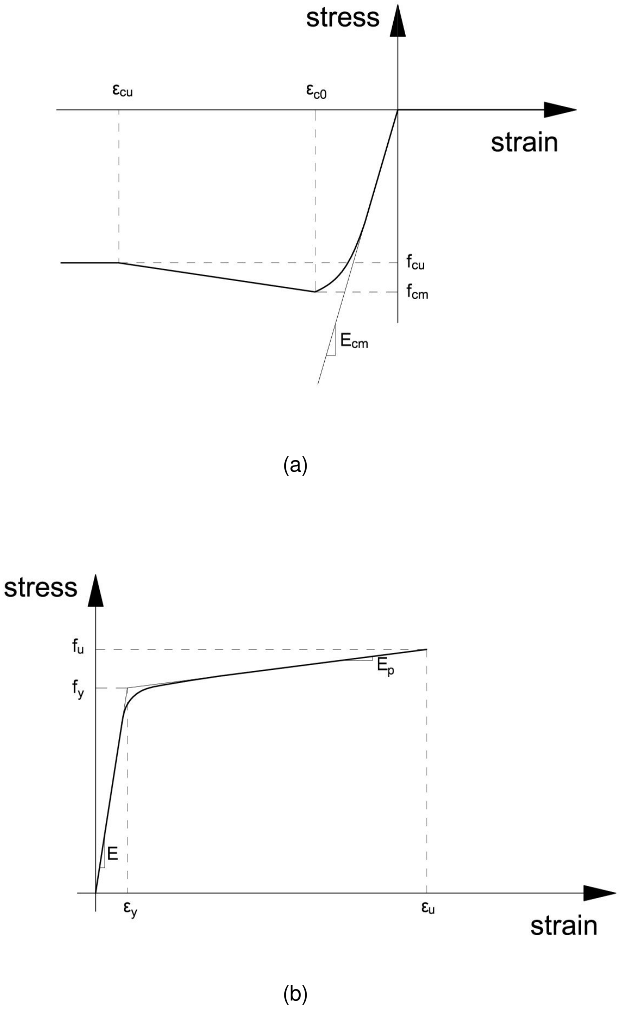

Figure 3.9: Constitutive law of Opensees materials: a) *Concrete*01; b) *Steel*02.

$$Vs = \frac{A_{sw} f_{ys} D cot(\theta)}{S_s} \tag{3.4}$$

The total shear strength $V_t$ is the sum of concrete and reinforcement contributions, $A_c$ is the cross sectional area, $A_{sw}$ and $A_{sp}$ are stirrups and inclined rebars areas, $\beta$ is the inclination angle. $s_s$ and $s_p$ are the relevant spacing and $D$ is the cross section depth. $V_c$ was set considering the curvature ductility-dependent coefficient $k_d$ equal to 0.20. Therefore, $s1p$ was assumed equal to $V_c$ , whilst

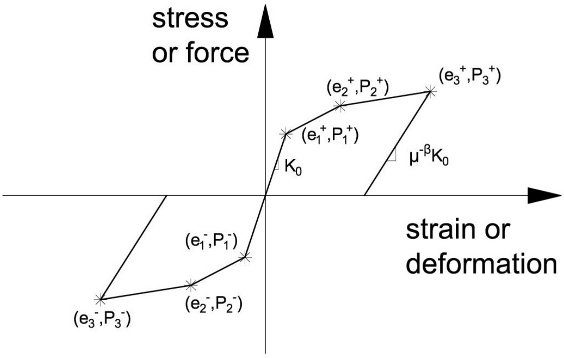

Figure 3.10: Constitutive law of *Hysteretic* Opensees material.

both *s2p* and *s3p* were assumed equal to $V_t$. Corresponding shear deformations *e1p*, *e2p* and *e3p* were assumed equal to $3.5 \cdot 10^{-4}$, $1 \cdot 10^{-3}$ and $1 \cdot 10^{-2}$, respectively. These values were implemented accordingly with the cyclic tests on the mock-up 1:4 scaled specimen of Pier #12 performed by Paolacci and Giannini (2012). The hysteretic shear material was coupled to the flexural behavior by the *sectionaggregator* Opensees command. As a result, based on the these assumptions, the dynamic properties were evaluated. In Table 3.4 are reported the first four modes of vibration of the PMCSI

In order to simulated the isolated configuration of CSI, the PMCSI was modified according to the foreseen CSBs-based seismic retrofitting. A pair of Single Friction Pendulum Bearing Opensees Element (SFPBOE) were positioned between each portal pier frame and the rigid links element supporting the deck, as shown in Figure 3.2(d). Figure 3.11 depicts the scheme of such elements; the *iNode* repre-

| Mode | Frequency [Hz] | Period [s] |
|---|---|---|
| #1 | 0.6137 | 1.629 |
| #2 | 0.6432 | 1.554 |
| #3 | 0.6576 | 1.520 |
| #4 | 1.1383 | 0.879 |

Table 3.4: Frequencies and periods of vibrations of Case Study I

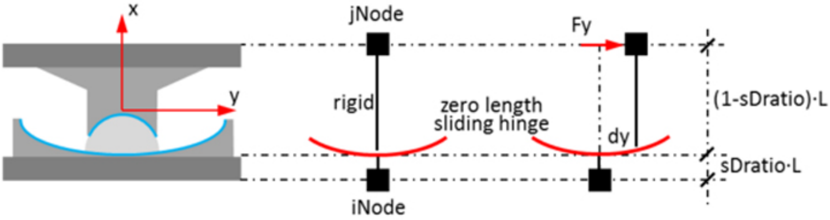

Figure 3.11: Scheme of the single friction pendulum bearing Opensees element

sents the concave sliding surface and the *jNode* represents the articulated slider. Isolators were implemented considering the effective element depth. In order to reproduce the uplift behavior of CSB, a zero tensile strength *UniaxialMaterial* was specified in the axial direction. It is important to note that rotations of the CSB surface at *iNode* affect the shear response. Finally, comprehensive set of non-linear time history analyses by means of PMCSI was carried out to estimate the dynamic response of the bridge at both the SLS and ULS. Figures 3.12(a) and 3.12(b) reports hysteretic loops relevant to Piers #9 and #11 for SLS in the *asbuilt* and isolated configurations. Displacements were measured at the cap beam level of each pier; forces refer to relevant base shear reactions along the same direction, i.e the transversa to the deck axis. As can be appreciated in Figure 3.12(b), Pier #11 shows a slight hysteretic response already at SLS. Figure 3.12 shows the benefits of the retrofitting CSBs-based isolation systems, in fact both piers remain in the elastic range for both SLS and ULS seismic intensities. This is due to the CSBs, which play a fundamental role at both limit states dissipating high levels of energy.

## 3.3 Experimental Campaign

The seismic performance analysis of the CSI in both the *asbuilt* and the isolated conditions has been investigated by means of HSs. As anticipated, in Section 3.1, 1:2.5 scale mock-up models of Piers #9 and #11 together with relevant, and equally scaled CSBs isolators were coupled to the remainder part of the bridge implemented numerically at the ELSA Laboratory of the Joint Research Centre of Ispra (VA), Italy trough a CAST3M FE model (Cast3M (2003)). The integration

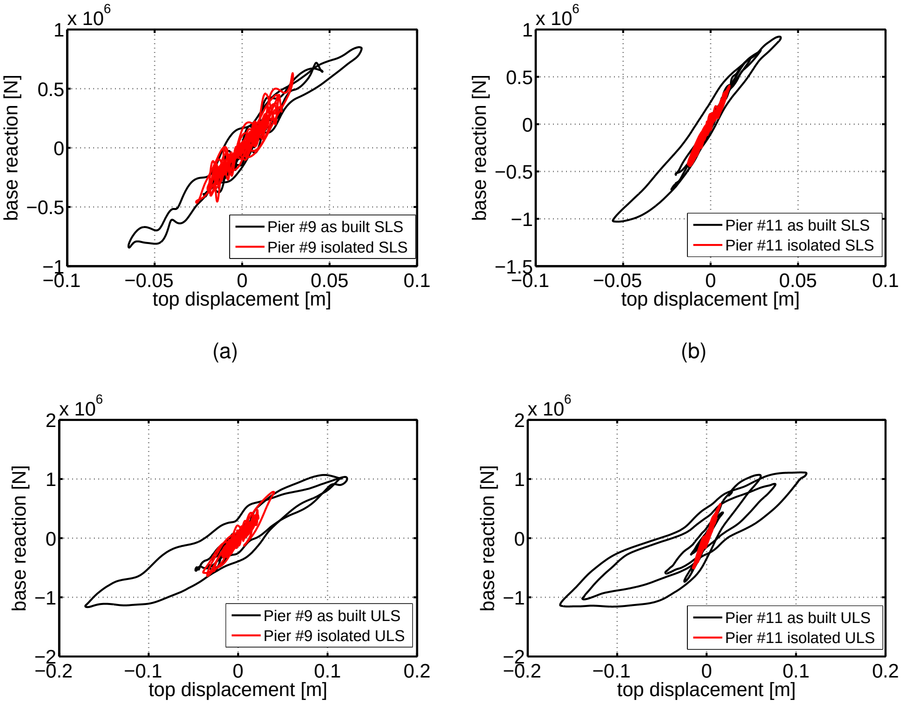

(a) (b)

(c) (d)

Figure 3.12: Numerical response of the predictive model of Case Study I, Cap beam displacement vs. base reaction force: a) Pier #9 at SLS; b) Pier #11 at SLS; c) Pier #9 at ULS; d) Pier #11 at ULS.

of the equations of motions considering the two sub-domains was performed by implementation of the PM method (Pegon and Magonette (2002)), which is suitable to solve problems with subcycling features, fundamental requirements for the implementation of this type of continuous PDT. As anticipated, the numerical domain was represented by the whole bridge except Pier #9 and #11 that represented the physical domain. In greater detail, ten piers and relevant CSBs pairs and the deck, were numerically modelled and solved by the CAST3M FE code, whilst Piers #9 and #11 with relevant pairs of CSBs were loaded through dynamic actuators. Figures 3.13(a) and 3.13(b) depict substructuring schemes adopted for the *asbuilt* and the isolated configurations, respectively. According to Figures 3.13(a) and 3.13(b), that represent the reduced scheme of the global system of NSs and PSs,

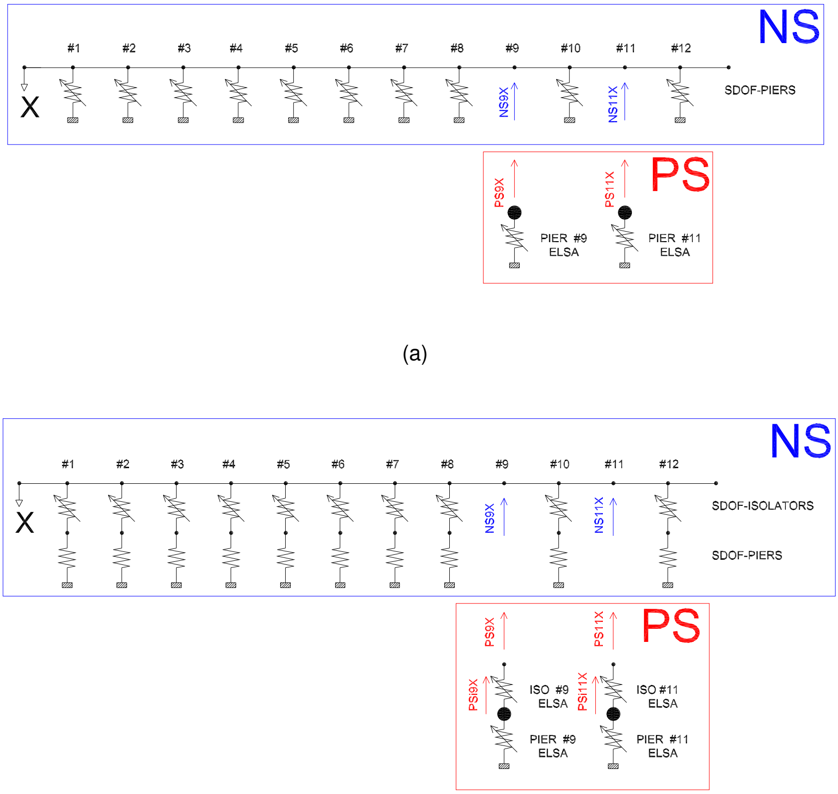

(a)

(b)

Figure 3.13: Scheme of substructures: a) *asbuilt* configuration; b) isolated configuration.

the coupling setting reads:

$$NS9X = PS9X \tag{3.5}$$

$$NS11X = PS1X \tag{3.6}$$

A total of 2-DoFs was considered for the PSs in the *asbuilt* configuration, whilst a 4-DoFs resulted for the PSs of the isolated configuration. In the second, the isolation devices were interposed ideally among deck and piers. In both the cases, substructured deck, piers and isolators were assembled to produce the complete numerical part of the CSI. Due to the complexity of the nonlinear NSs of the Rio Torto Bridge, the computational driver and the servo-hydraulic control system ran at different time rates. The PDT procedure can be implemented without particular precautions for the *asbuilt* configuration because the pier response is rate independent, for the isolated case instead, since the isolators response is dependent to the load rate, some tricks were used to overcome this dependency, as widely described in Subsection 3.3.4. As a result, the parallel partitioned time integration scheme developed by Pegon and Magonette (2002), i.e. the PM method, was considered to synchronize these two processes and to solve the equations of motion, as shown in Figure 3.14. Thanks to parallel features it enables subcycling avoiding any interpolation or extrapolation of actuator commands at the controller sampling time $\Delta_t$.

In greater detail, a coarse time step $\Delta_{tN}$ was selected for the numerical subdomain

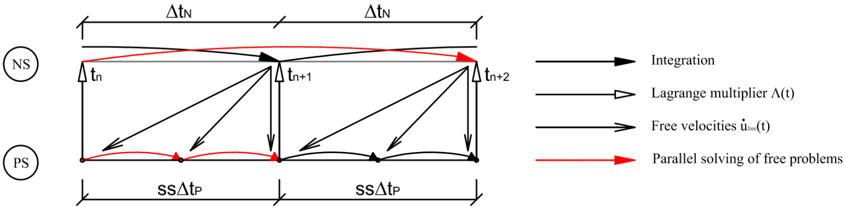

Figure 3.14: PM Method scheme.

where the NSs were solved, whilst a smaller time step $\Delta_{tP} = \dfrac{\Delta_{tN}}{ss}$, was selected for the integration of the PSs, with n represents the subcycling magnitude. As a result, displacement commands were provided to the transfer system at the controller sampling time $\Delta t = 2ms$; smooth trajectories of actuators were obtained and the continuous time PDT method was successfully implemented. Relationships about sampling times involved by the time integration setting read,

$$\Delta_{tP} = \frac{\Delta_t}{\lambda} \tag{3.7}$$

$$ss = \frac{\Delta_{tA}}{\Delta_t}\lambda \tag{3.8}$$

where $\lambda$ is the extended time scale characterizing the PDT. For the purpose of HSs of the Rio Torto Bridge the PM method, was implemented considering the parameters reported in Table 3.5.

| $\lambda$ | **ss** | $\Delta_{tN}$ | $\Delta_{tP}$ |
|---|---|---|---|
| 200 | 250 | 2.5 *msec* | 0.01 *msec* |

Table 3.5: Parameters adopted during HSs

### 3.3.1 Physical substructures

Due to the majestic size of the actual piers, i.e. 25.74 m for Pier #9 and 14.37 m for Pier #11, with the scope to fit with the facilities limitations, a scaling factor $S$ = 2.5 was applied to the piers and CSBs. In addition, the reduced dimensions of specimens allowed for saving costs for both building and removal phases.
For typical dynamic problems, the fundamental quantities to be monitored are mass, length and time; accordingly, three independent scale factors should be selected for a rigorous scaling. The solution of the dimensional problem is governed by the well-known Buckingham Theorem (Buckingham (1914)). Since gravity loads play an important role, the scale factor were applied as reported in Table 3.6 according to Kumar et al. (1997). In Figures 3.15 and 3.16 are depicted the specimens of Pier #9 and Pier #11, respectively. The first one is characterized by 3 levels and a total height of 11.50 m, the second has 2 levels and 7.00m of total height. Both specimen were provided with a 6.00x2.80x1.20 m block foundation. The scaling procedure involved also reinforcement diameters and positions. In greater detail, regard to columns of Pier #9 and #11, $\phi$8 mm and $\phi$10 mm plain steel rebars replaced full scale $\phi$ of 24 mm and $\phi$ 20 mm, respectively. Therefore, a

| **Mass** | **Length** | **Stress** | **Force** | **Stiffness** |
|---|---|---|---|---|
| $S^3$ | $S$ | 1 | $S^2$ | S |

Table 3.6: Scale factors applied to each different quantity

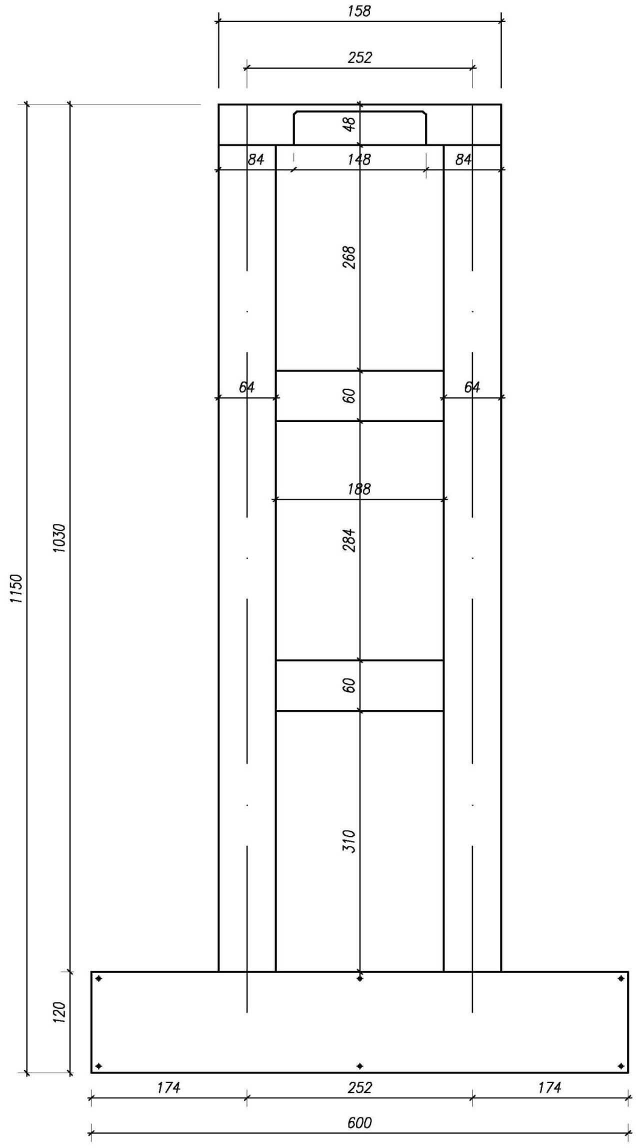

Figure 3.15: Views of the scaled Pier #9.

small approximation occurred for the $\phi$ 24 mm diameter. With regard to the transverse beams, both diameters and spacings of stirrups and inclined rebars have been scaled to reproduce the correct confinement effect. Hence, $\phi$3 mm rebars replaced the full scale $\phi$8 mm reinforcements characterizing stirrups and inclined rebars.

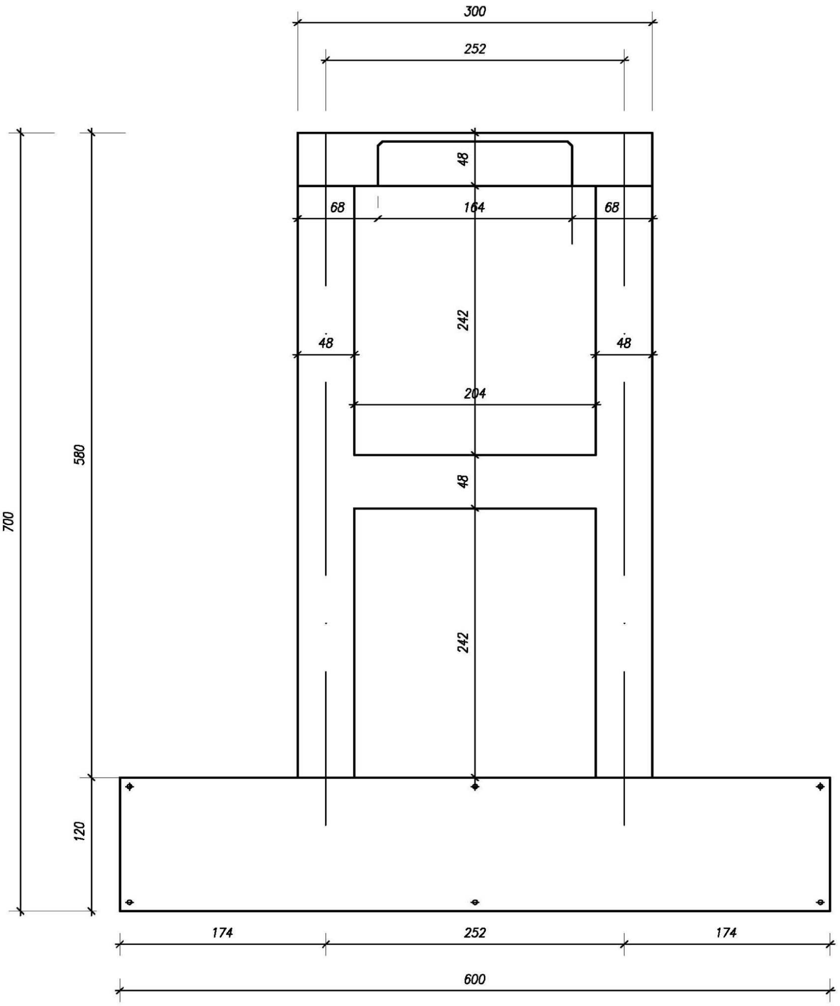

Figure 3.16: Views of the scaled Pier #11.

With regard CSBs, the foreseen full scale radius of the concave sliding surface was reduced to 1200mm, whilst the same friction coefficient equal to 4% characterized reduced devices. Drawings of the reduced CSB isolator are depicted in Figure 3.17. Each single CSB isolator was designed to support a scaled vertical load of $\frac{2800}{2.5^2} = 448kN$.

In order to perform the experimental campaign, eighteen hydraulic actuators were employed at the ELSA facility acting on the PSs. Short actuators, depicted in Figure 3.18(c), applied the vertical loads to both piers and CSBs. Long actuators,

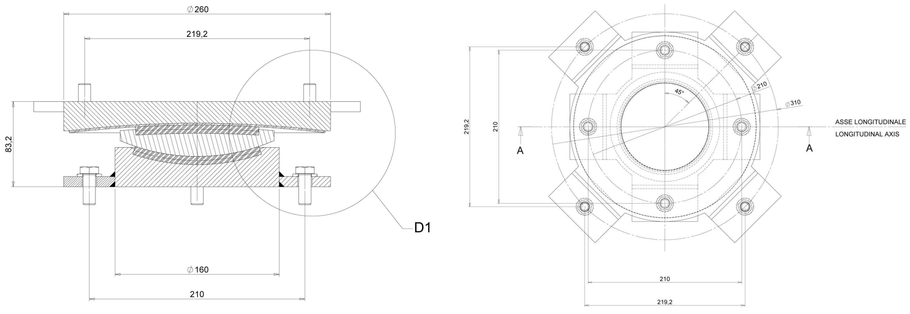

(a) (b)

Figure 3.17: Views of the scaled CSB: a) Cross section; b) Plan view.

depicted in Figure 3.18(a), provided the horizontal displacements to all PSs according to substructuring schemes presented in Subsection 3.3. Each actuator was provided with a TEMPOSONICS displacement transducer, which measured the actuator stroke, and a load cell measuring the entailing axial force; additional sensors recorded data regarding the oil pressure within the servo valve. Table 3.7 summarizes label and application of the hydraulic actuators adopted.

With regard to horizontal actuators, i.e. 2A, 3C, 1A, 3B, 3A and 4A, additional feedback HEIDENHAIN displacement transducers were applied for control purpose; they measured the absolute displacements by the connection with a fixed steel frame on the reaction floor, as depicted in Figure 3.18(c). Each single actuator and relevant measurements were managed by a dedicated SLAVE controller with the same label and running the specific PID displacement/force control algorithm. As a result, nonlinear NSs were implemented and solved exploiting the element library of the CAST3M FE code as well as its nonlinear solver. Figure 3.18 shows the complete setup installed at the ELSA laboratory.

### 3.3.2 Numerical substructures for piers

As described in detail in Abbiati (2014) the seismic loads excited mainly the four lowest global eigenmodes of the CSI avoiding the local eigenmodes. In addition, the piers were mainly loaded in the transversal direction of the deck. As a result, it was possible to model the pier with a reduced linear S-DoF. The conden-

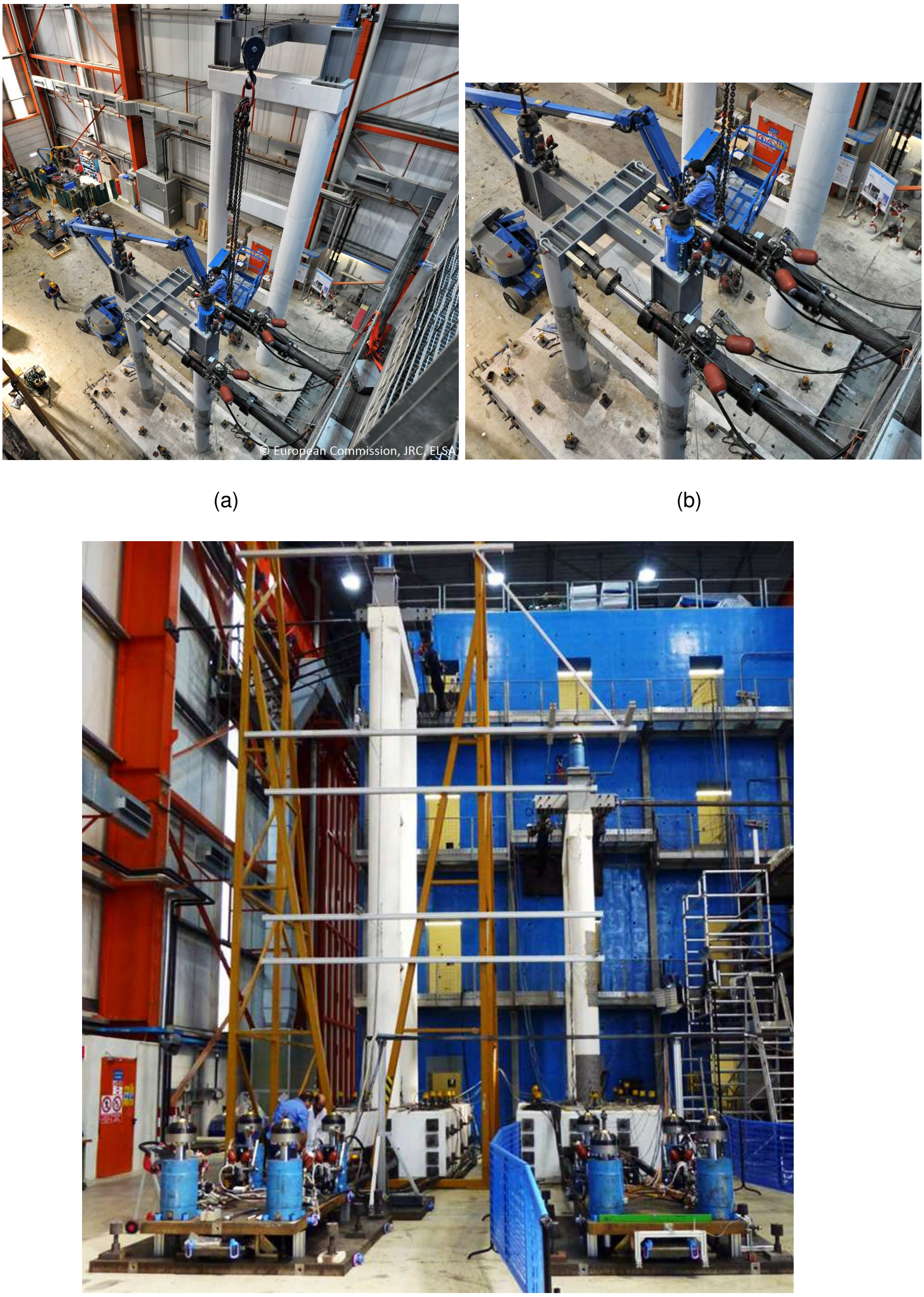

(a) (b)

(c)

Figure 3.18: Details of experimental setup.

| Pier | Type | Purpose |
|---|---|---|
| 1E,2E,3E,4E | short | vertical load on CSB of Pier #9 |
| 1D,2D,3D,4D | short | vertical load on CSB of Pier #11 |
| 1C,2C | short | vertical load on Pier #9 |
| 1B,2B | short | vertical load on Pier #11 |
| 2A,3C | long | horizontal displacement of Pier #9 |
| 1A,3B | long | horizontal displacement of Pier #11 |
| 4A | long | horizontal displacement of CSB of Pier #9 |
| 3A | long | horizontal displacement of CSB of Pier #11 |

Table 3.7: List of actuators and properties.

sation of pier matrices were performed by means of the so called Guyan reduction method (Guyan (1965)), in detail the top transversal displacement Degree-of-Freedom (DoF) of each pier was considered as master, i.e. $u_r$, whilst the others as slaves, i.e. $u_l$. The algebraic formulation is reported herein:

$$u = \begin{bmatrix} u_r \\ u_l \end{bmatrix} = \begin{bmatrix} T \end{bmatrix} u_r \tag{3.9}$$

with:

- $u_r$=master DoFs;
- $u_l$=slave DoFs;
- $T$=condensation matrix

The parameters of the S-Dof pier reads as follow:

$$K^r = T^T KT \qquad M^r = T^T \qquad F^r = T^T ML \tag{3.10}$$

with:

- $K$ and $M$ are the matrices of stiffness and mass;
- $L$ is a boolean vector that project the seismic inertial acceleration to the transversal DoF in X direction;

In order to produce the stiffness and mass matrices of the reduced model, the S-DoF scheme was implemented in ANSYS environment (ANSYS (2007)) as fully presented in Abbiati (2014). The ANSYS Guyan Model (ANSYSGM) is depicted in Figure 3.19, whilst the parameters of the reduced models evaluated by Guyan procedure are reported in Table 3.8.

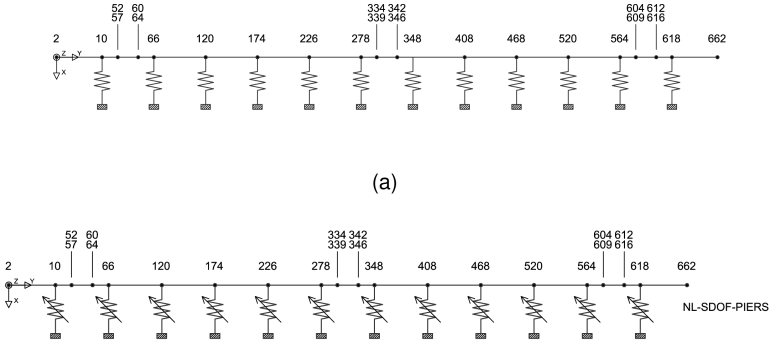

(a)

(b)

Figure 3.19: FE model equipped with reduced model of Piers for *asbuitl* configuration:a) ANSYSGM; b) NLGRM.

As depicted in Figure 3.20 the ANSYSGM has been compared with the ANSYS Simplified Model (ANSYSSM) developed and validated on the base of PMCSI. In greater detail, the check has been done by means of MAC matrix in Equation 3.3.2 reported hereinafter with optimum results.

$$MAC(\Phi_1, \Phi_2) = \frac{(\Phi_1^T \Phi_2)^2}{(\Phi_1^T \Phi_1)(\Phi_2^T \Phi_2)} \tag{3.11}$$

The nonlinear behavior of the reduced models was obtained by means of replacing the linear springs with nonlinear springs based on Bouc-Wen model. The equations governing the transition are the following:

$$Linear \quad Model \rightarrow K^r x + C^r \dot{x} + M^r \ddot{x} = f(t) - F^r a_g(t) \tag{3.12}$$

$$Nonlinear \quad Model \rightarrow r + C^r \dot{x} + M^r \ddot{x} = f(t) - F^r a_g(t) \tag{3.13}$$

| **Pier** | $K^r[\frac{kN}{m}]$ | $M^r$ **[kg]** | $F^r$ **[kg]** |
|---|---|---|---|
| #1 | 32211 | 35106 | 45034 |
| #2 | 9934 | 75300 | 103715 |
| #3 | 8834 | 80397 | 108883 |
| #4 | 11947 | 67167 | 90580 |
| #5 | 18401 | 69616 | 96933 |
| #6 | 9468 | 92891 | 132832 |
| #7 | 8426 | 99025 | 140808 |
| #8 | 11186 | 85172 | 122064 |
| #9 | 23560 | 62955 | 88393 |
| #10 | 22920 | 42569 | 56426 |
| #11 | 38140 | 39013 | 50693 |
| #12 | 42660 | 37068 | 48389 |

Table 3.8: Parameters for the linear reduced model of the pier reduced by the Guyan method.

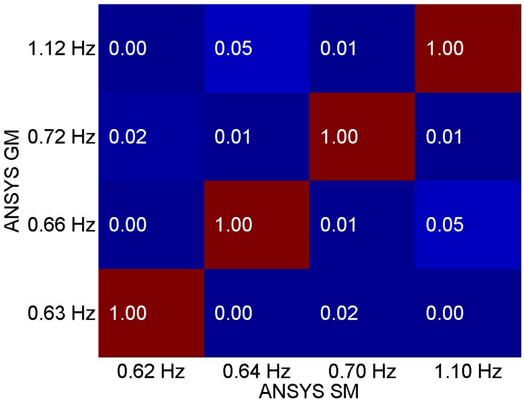

| | 0.62 Hz | 0.64 Hz | 0.70 Hz | 1.10 Hz |
|---|---|---|---|---|
| 1.12 Hz | 0.00 | 0.05 | 0.01 | 1.00 |
| 0.72 Hz | 0.02 | 0.01 | 1.00 | 0.01 |
| 0.66 Hz | 0.00 | 1.00 | 0.01 | 0.05 |
| 0.63 Hz | 1.00 | 0.00 | 0.02 | 0.00 |

Figure 3.20: MAC matrix to validate the linear reduction of the piers.

with:

$$\dot{r} = f(x, \dot{x}, r, \theta) \tag{3.14}$$

A nonlinear spring, based on a modified version of the well-known Bouc-Wen was produced. It allowed for substructuring piers at both limit states with few parameters. The differential model of the modified Bouc-Wen spring proposed for the nonlinear substructuring of CSI piers recalls the work of Smyth et al. (1999). In order to replicate the softening behavior of Opensees piers owing to material constitutive laws, the term $\frac{1}{(1+\alpha x^2)}$ was introduced.

$$\dot{f} = (\frac{\rho A}{(1+\alpha x^2)} - (\beta sign(\dot{x} f) + \gamma \mid f \mid^n))\dot{x} \tag{3.15}$$

where A, $\beta$, $\gamma$ and n are parameters of the Bouc-Wen model. *A* was assumed equal to the reduced linear stiffness $K^r$, whilst $\rho$ was introduced to represents its average degradation. In order to decrease the computational effort of resulting optimization problem, $\gamma$ was set equal to zero and *n* to one. The proposed reduced nonlinear springs characterized by these parameters were not capable of reproducing piers behavior at their full operating range, i.e. SLS and ULS. As a consequence, different nonlinear parameter sets were evaluated at each limit state. The initial elastic branch of nonlinear models capable of reproducing the hysteretic behaviour of the piers were identified on the base of the linear parameters of reduced linear S-DoF piers. For the identification of the remaining nonlinear parameters each substructured pier was considered as a standalone Single-Input-Single-Output (SISO) system. Internal forces recorded at the cap beam level from time history analysis of the PMCSI were considered as input applied to each substructured pier, whilst the cap beam level displacement response was considered as the output. A penalty function was set in terms of Normalized Root Mean Square Error (NRMSE) defined as (Abbiati (2014)):

$$NRMSE(x_{\mathrm{PMCSI}}, x_{S-DoF}) = \frac{\sqrt{\frac{1}{n}\sum_{i=1}^{n}(x_{S-DoF,i} - x_{\mathrm{PMCSI},i})^2}}{max(x_{\mathrm{PMCSI}}) - min(x_{\mathrm{PMCSI}})} \tag{3.16}$$

between displacement response histories of the reduced S-DoF pier and the Opensees PMCSI:

$$\hat{\theta} = minNRMSE(x_{\mathrm{PMCSI}}, x_{S-DoF}(\theta)) \tag{3.17}$$

At each iteration of the identification loop, the displacement response of the reduced non-linear pier $x_{S-DoF}(\theta)$ was calculated by integrating Equation 3.3.2 with

| | SLS | | | ULS | | |
|---|---|---|---|---|---|---|
| **Pier** | $\rho$ | $\alpha$ | $\beta$ | $\rho$ | $\alpha$ | $\beta$ |
| #1 | 1.00 | 1987.15 | 0.00 | 0.83 | 1942.26 | 0.10 |
| #2 | 0.67 | 32.50 | 1.17 | 0.50 | 0.19 | 2.13 |
| #3 | 0.81 | 108.82 | 1.32 | 0.96 | 215.65 | 2.19 |
| #4 | 0.66 | 125.55 | 2.51 | 0.50 | 24.98 | 3.93 |
| #5 | 0.63 | 248.94 | 1.90 | 0.68 | 338.44 | 0.60 |
| #6 | 0.79 | 161.51 | 1.25 | 0.50 | 8.66 | 1.44 |
| #7 | 0.50 | 7.94 | 1.05 | 0.50 | 8.34 | 1.94 |
| #8 | 0.59 | 44.75 | 0.58 | 0.50 | 29.30 | 1.25 |
| #9 | 0.73 | 338.32 | 0.84 | 0.95 | 1005.93 | 0.36 |
| #10 | 1.00 | 1151.93 | 0.00 | 0.59 | 387.69 | 1.58 |
| #11 | 0.79 | 919.21 | 1.84 | 0.50 | 490.84 | 1.31 |
| #12 | 0.99 | 1997.13 | 0.01 | 0.72 | 1090.46 | 3.10 |

Table 3.9: Nonlinear parameters for the reduced models of the piers identified by NRMSE.

the ode15s Matlab solver for stiff ODEs (MATLAB (2012)). As a result, Table 3.9 summarizes parameters sets for both SLS and ULS, respectively.

As can be appreciated in Table 3.9, a sensible stiffness degradation at ULS was recorded. Moreover, $\beta$ parameter, which governs of the hysteretic energy dissipation, increased in all the NSs. NRMSE between time history responses of standalone reduced piers and the PMCSI were calculated as reference parameter. In Table is gathered 3.10 the complete set of Normalized Root Mean Square Errors (NRMSEs) for both the SLS and the ULS. Figure 3.21 compares displacement responses of reduced S-DoF models of Piers #9 and #11 in the transversal direction with the PMCSI solution at both limit states. These results prove that the proposed nonlinear springs are suitable for the DS of the hysteretic piers of CSI. In Figure 3.21 a comparison in terms of displacement between the standalone reduced model of Pier #9 and #11 at SLS and PMCSI. In order to validate the effectiveness of the nonlinear substructured components for the purpose of

| | SLS | | | ULS | | |
|---|---|---|---|---|---|---|
| **Pier** | **displacement** | **velocity** | **force** | **displacement** | **velocity** | **force** |
| #1 | 0.03 | 0.04 | 0.03 | 0.03 | 0.05 | 0.05 |
| #2 | 0.06 | 0.07 | 0.04 | 0.07 | 0.09 | 0.06 |
| #3 | 0.03 | 0.05 | 0.04 | 0.07 | 0.08 | 0.07 |
| #4 | 0.06 | 0.05 | 0.03 | 0.08 | 0.08 | 0.05 |
| #5 | 0.05 | 0.06 | 0.04 | 0.06 | 0.09 | 0.08 |
| #6 | 0.03 | 0.05 | 0.05 | 0.07 | 0.06 | 0.05 |
| #7 | 0.05 | 0.06 | 0.04 | 0.09 | 0.06 | 0.06 |
| #8 | 0.03 | 0.05 | 0.04 | 0.04 | 0.06 | 0.05 |
| #9 | 0.02 | 0.06 | 0.03 | 0.05 | 0.07 | 0.08 |
| #10 | 0.02 | 0.05 | 0.03 | 0.04 | 0.06 | 0.05 |
| #11 | 0.02 | 0.04 | 0.02 | 0.07 | 0.07 | 0.06 |
| #12 | 0.02 | 0.03 | 0.02 | 0.04 | 0.04 | 0.03 |

Table 3.10: NRMSE for standalone S-DoF piers and PMCSI.

the HSs of the Rio Torto Bridge, an Nonlinear Global Reduced Model (NLGRM) of the structure was assembled again in ANSYS (2007) environment. Figure 3.19(b) depicts the scheme of the resulting global model of the Rio Torto Bridge in the *asbuilt* case with node numbering. In detail, deck matrices were imported from this ANSYSGM model based on BEAM44 elements. Nonlinear S-DoF piers acted as transversal springs. Gerber saddles were implemented by means of constraint equations defined on internal DoFs. NRMSE was calculated on displacement, velocity and acceleration responses of piers measured at cap beam levels of NLGRM model with respect to the PMCSI solution as gathered in Table 3.12.

According to Table 3.12 the proposed models well reproduced the dynamic response of the PMCSI at SLS and ULS in the *asbuilt* case. Figure 3.22 report displacement responses of Pier #9 and #11 of the reduced model of the Rio Torto Bridge in the *asbuilt* configuration at SLS and ULS, respectively. According to Tables 3.12 and Figure 3.22, the suitability of the proposed reduced models of the bridge to reproduced the dynamic response of the PMCSI at both SLS and ULS

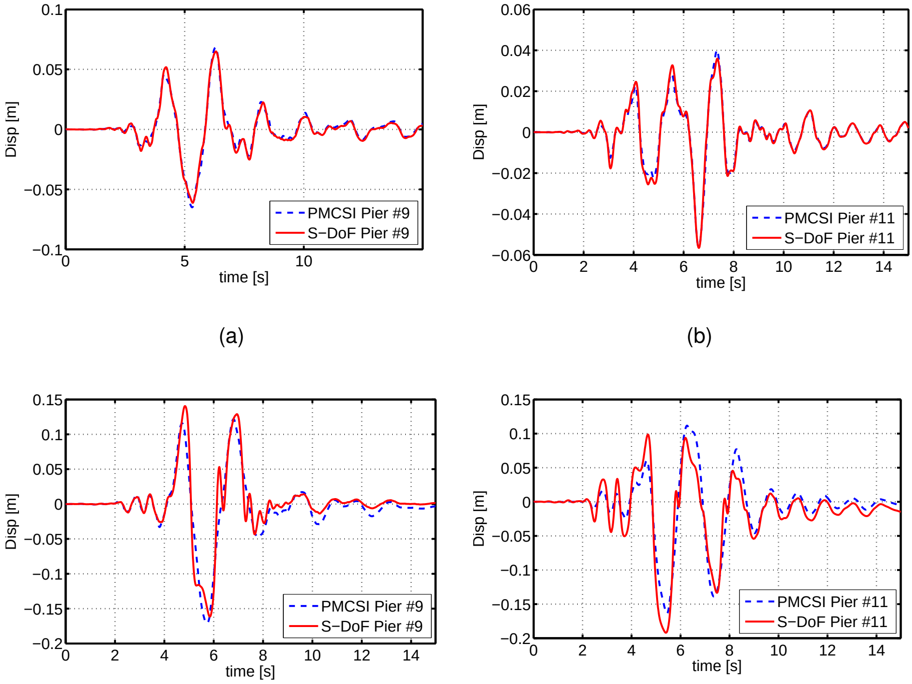

(a) (b) (c) (d)

Figure 3.21: Comparison between numerical refined PMCSI and reduced S-DoF of piers: a) Pier #9 at SLS; b) Pier#11 at SLS; c) Pier #9 at ULS; d) Pier #11 at ULS.

was proven.

### 3.3.3 Numerical substructures for concave sliding bearings

CSBs are characterized by a bilinear constitutive law that replicates the slip based behavior, as shown in Figure 3.6(b). In agreement with this, the proposed model for substructuring of isolator elements was based on the bilinear model proposed by Mostaghel (1999). Figure 3.23 shows both idealized hysteretic S-DoF oscillator and the relevant bilinear hysteretic loop. The bilinear model was able to reproduce the nonlinear behavior of the two node SFPBOE implemented in the PMCSI. The ODE set that characterizes the bilinear system of the Figure reads:

$$m\ddot{x} + c\dot{x} + \alpha k x + (1-\alpha) k u = P_0 p(t) \tag{3.18}$$

|  | SLS |  |  | ULS |  |  |
|---|---|---|---|---|---|---|
| **Pier** | **displacement** | **velocity** | **force** | **displacement** | **velocity** | **force** |
| #1 | 0.04 | 0.03 | 0.02 | 0.07 | 0.06 | 0.07 |
| #2 | 0.06 | 0.07 | 0.04 | 0.06 | 0.04 | 0.03 |
| #3 | 0.05 | 0.05 | 0.03 | 0.05 | 0.04 | 0.03 |
| #4 | 0.04 | 0.04 | 0.02 | 0.04 | 0.03 | 0.03 |
| #5 | 0.03 | 0.03 | 0.02 | 0.04 | 0.03 | 0.02 |
| #6 | 0.04 | 0.04 | 0.02 | 0.04 | 0.04 | 0.03 |
| #7 | 0.05 | 0.05 | 0.03 | 0.05 | 0.03 | 0.04 |
| #8 | 0.05 | 0.05 | 0.03 | 0.04 | 0.04 | 0.03 |
| #9 | 0.05 | 0.05 | 0.02 | 0.05 | 0.07 | 0.05 |
| #10 | 0.04 | 0.03 | 0.02 | 0.08 | 0.09 | 0.07 |
| #11 | 0.03 | 0.03 | 0.02 | 0.09 | 0.09 | 0.09 |
| #12 | 0.02 | 0.02 | 0.02 | 0.05 | 0.04 | 0.04 |

Table 3.11: NRMSE for NLGRM and PMCSI

$$\dot{u} = (\bar{N}(\dot{x})\bar{M}(u-\delta) + M(\dot{x})\bar{N}(u+\delta))\dot{x} \tag{3.19}$$

with:

$$N(x) = 0.5(1 + sign(x))(1 + (1 - sign(x))) \tag{3.20}$$

$$M(x) = 0.5(1 - sign(x))(1 - (1 + sign(x))) \tag{3.21}$$

$$\bar{N}(x) = 0.5(1 + sign(x))(1 - (1 - sign(x))) \tag{3.22}$$

$$\bar{M}(x) = 0.5(1 - sign(x))(1 + (1 + sign(x))) \tag{3.23}$$

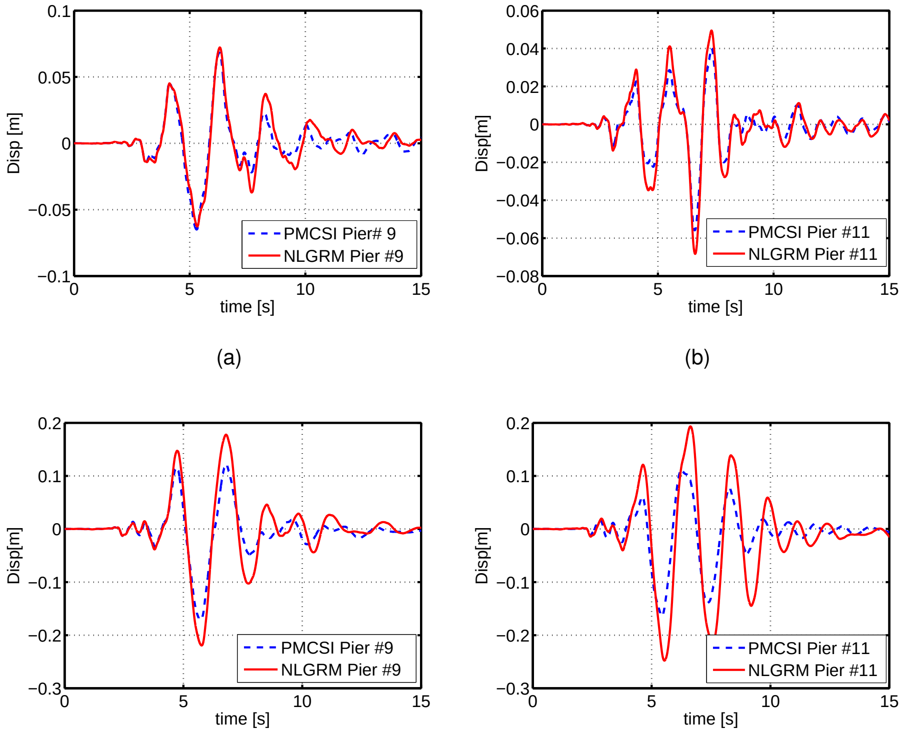

(a) (b)

(c) (d)

Figure 3.22: Validation of NLGRM of Case Study I: a) Pier #9 SLS; b) Pier #11 SLS; c) Pier #9 ULS; d) Pier #11 ULS.

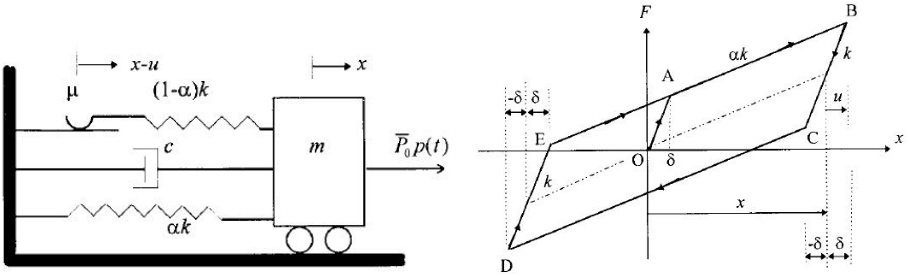

(a) (b)

Figure 3.23: Hysteretic S-DoF oscillator adopted for CSBs NSs: a) idealized model; b) hysteretic bilinear law.

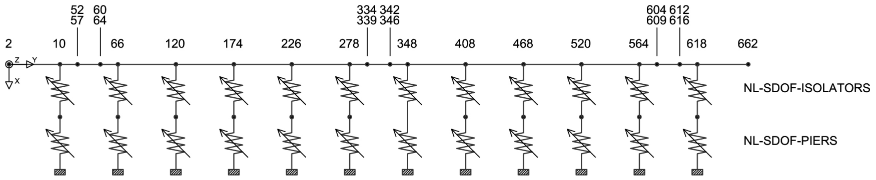

Figure 3.24: FE NLGRM model in the isolated configuration.

The information of the hysteretic system as slip displacement, were stored in the state space variable $u$. The time integration of Equations 3.18 and 3.19 defines the response of hysteretic bilinear system under a given load history $P_0 p(t)$. As can be seen, mass and damping contributions of isolators were neglected. The penalty function defined was the previously introduced NRMSE between reference and reduced restoring forces relevant to the single isolator element:

$$(\hat{k}, \hat{\alpha}, \hat{\delta}) = minNRMSE(r_{PMCSI}, r_{S-DoF}(k, \alpha, \delta)) \tag{3.24}$$

with:

$$r_{PMCSI,i} = \alpha k x_{PMCSI,i} + (1 - \alpha) k u_i \tag{3.25}$$

$$u_i = \sum_{j=1}^{i} \dot{x}_{PMCSI}, j(\bar{N}(\dot{x}_{PMCSI,j})\bar{M}(u_j - \delta) + M(\dot{x}_{PMCSI,j})\bar{N}(u_j + \delta))dt \tag{3.26}$$

In detail, $r_{S-DoF}$ is the restoring force history of the SFPBOE; $x_{PMCSI}$ and $\dot{x}_{PMCSIM}$ are the corresponding relative displacement and velocity histories, respectively. Equation 3.24 defines the penalty function for the estimation of nonlinear parameters, which are $k = 2.03e8\frac{N}{m}$ , $\alpha = 0.0046$, $\delta = 0.00050m$. The penalty function of Equation 3.24 was minimized through the Matlab *pattern search algorithm*. The same parameters were evaluated for all isolators. Even though the effect of variable vertical loads was neglected, this simplified bilinear models well reproduced the behavior of SFPBOE and were chosen as reduced mode for the HSs tests. Figure 3.24 depicts the scheme of the overall reduced model of the CSI in the isolated configuration with node numbering. The external constraints remained unchanged with respect to the *asbuilt* configuration. According to the foreseen retrofitting scheme, Gerber saddles were removed. NRMSEs were calculated on displacement, velocity and acceleration responses of piers measured at cap beam levels with respect to the PMCSI reference solution. Table 3.12 gathers the obtained values for the standalone reduced models at both limit states.

In order to validate the effectiveness of substructured components for the purpose of the HSs of the CSI in the isolated case, a reduced model of the structure was assembled (NLGRM), as depicted in Figure 3.24. Figure 3.25 compare displacements of Piers #9 and #11 of the PMCSI and the global reduced model at SLS and ULS, respectively. It was confirmed that the proposed reduced models for CSBs agreed with the PMCSI also in the isolated case. Since CSB devices carried the most of the hysteretic energy dissipation, piers were supposed to remain in the linear regime, nonlinearities were confined in the substructured isolators. Finally, due to the complexity of the NSs identification in Figure 3.26 is depicted a flowchart describing the overall procedure.

| | **SLS** | | **ULS** | |
|---|---|---|---|---|
| **Pier** | **displacement** | **force** | **displacement** | **force** |
| #1 | 0.04 | 0.22 | 0.02 | 0.12 |
| #2 | 0.10 | 0.15 | 0.02 | 0.09 |
| #3 | 0.06 | 0.16 | 0.03 | 0.10 |
| #4 | 0.03 | 0.17 | 0.04 | 0.11 |
| #5 | 0.03 | 0.17 | 0.03 | 0.11 |
| #6 | 0.04 | 0.15 | 0.03 | 0.09 |
| #7 | 0.04 | 0.16 | 0.03 | 0.08 |
| #8 | 0.05 | 0.13 | 0.03 | 0.11 |
| #9 | 0.07 | 0.12 | 0.04 | 0.09 |
| #10 | 0.07 | 0.14 | 0.04 | 0.08 |
| #11 | 0.07 | 0.18 | 0.04 | 0.12 |
| #12 | 0.10 | 0.14 | 0.04 | 0.12 |

Table 3.12: NRMSEs for NLGRM and PMCSI

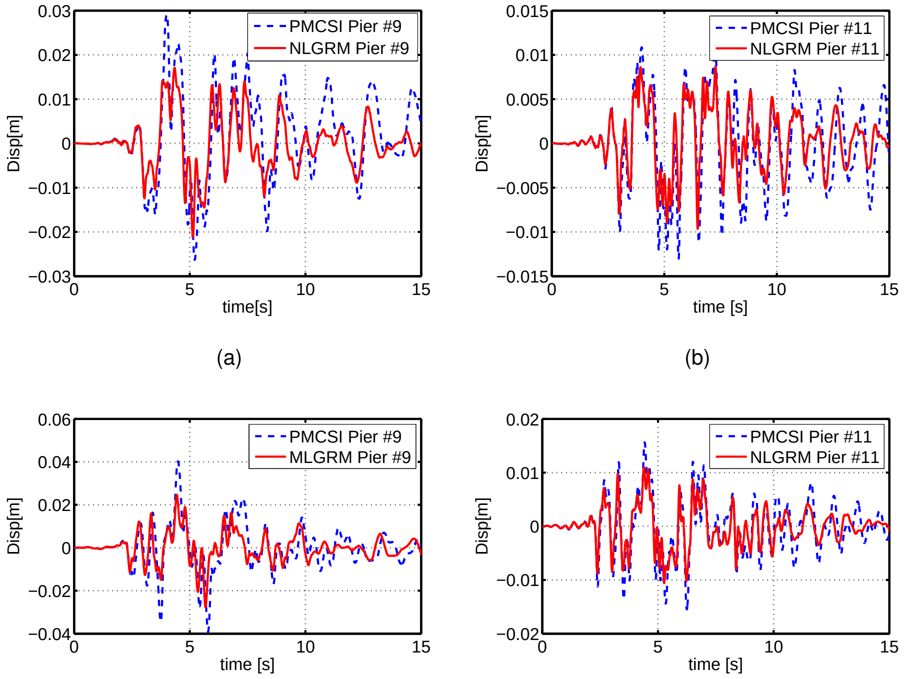

(a) (b)

(c) (d)

Figure 3.25: Validation of NLGRM of isolated Case Study I: a) Pier #9 SLS; b) Pier #11 SLS; c) Pier #9 ULS; d) Pier #11 ULS.

### 3.3.4 Friction coefficient and test velocity - Solution I

During the tests, due to the slow speed of PDT there was an alteration of the friction coefficient. In fact, in agreement with Lomiento et al. (2013) the friction coefficient can vary due to the effects of: *i*) Vertical applied load; *ii*) Sliding velocity; *iii*) Direction of motion.

$$\mu = f(\dot{\Delta}, N, \bar{u}) \tag{3.27}$$

In the case of Rio Torto Viaduct the tests were performed with a $\lambda$ factor equal to 200, it means a rate of load application 200 times slower than the actual loading produced by the earthquake, usually in the range $[100 \div 200]\ \frac{m}{s}$. Therefore, a variation of $\mu$ was expected. As depicted in Figure 3.27, the characterization tests showed a maximum and a minimum values of the coefficient equal to 8% and 2%,

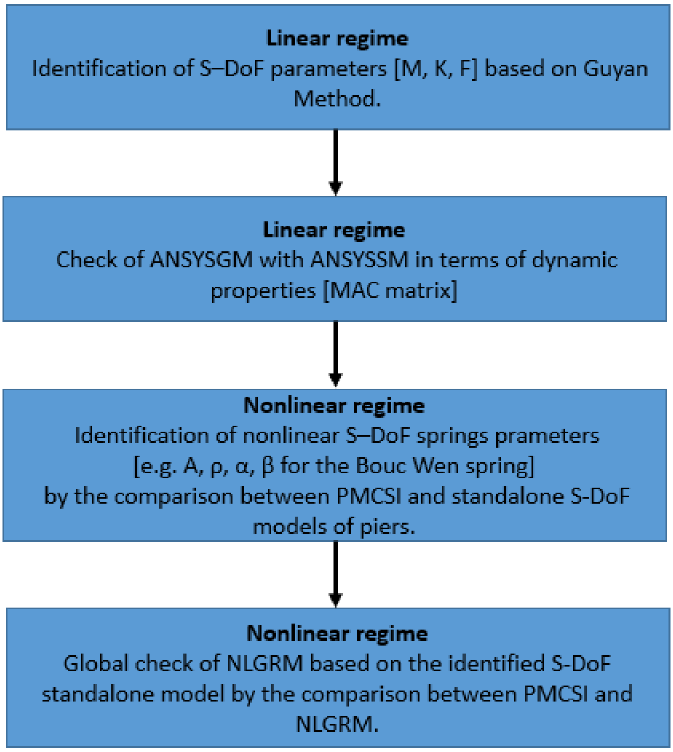

Figure 3.26: Flowchart of NSs identification procedure.

respectively. Since the design value was 4% and the identified $\mu_{test}$ for slow load rate was approximately 7% an unexpected damage could happen in the piers if the proper precautions are not taken into account. In general, this problem can be solved thanks to the advantage of DS; in fact, the vertical force on the isolator can be physically modified as well as the restoring force coming from the CSB can be corrected numerically during the test. The solution adopted during the Rio Torto tests was to modify the vertical force on the isolators in order to decrease the larger $\mu$ identified at test speed. The limit of this procedure is the alteration of the nonlinear branch of the restoring force. In fact, the refined equation of the CSB reads:

$$V = NCe^{-\frac{N}{N_r}} + \frac{N}{R}\Delta \neq \mu N + \frac{N}{R}\Delta \tag{3.28}$$

with, N actual vertical load, $N_r$ and C parameters of the CSB to be identified, R radius of the device, $\mu$ friction coefficient and $\Delta$ is the displacement of the CSB.

As can be see in Equation 3.28, the second branch is dependent to the vertical load and the surface radius. As a result, when the friction coefficient is modified by means of the application of a different vertical load, the secondary branch results to be modified. To solve this limitation it was introduced a numerical compensation to amplify the restoring force of the isolator on the base of the actual radius and expected vertical load. The post yielding stiffness considered to compensate the different vertical load was evaluated as follow:

$$k_{comp}^{Pier_i} = \frac{N_d^{Pier_i} - N_{test}^{Pier_i}}{R} \tag{3.29}$$

$$k_{test}^{Pier_i} = \frac{N_{test}^{Pier_i}}{R} \tag{3.30}$$

As a result the restoring force of the isolator transmitted to the pier was evaluated as:

$$V = \mu_{test} N_{test}^{Pier_i} + (k_{test}^{Pier_i} + k_{comp}^{Pier_i})\Delta \tag{3.31}$$

### 3.3.5 Model Updating offline.

As highlighted by Paolacci and Giannini (2012), the total amount of damage is accumulated in the piers, therefore the deck remains in the linear regime. In order to take into account of such damage during HSs, a novel offline model updating strategy was adopted. In greater detail, NSs were updated offline after each test and before the consecutive one. The parameters were identified and applied to the global model before starting the new test, then a time history of this updated model was conducted considering the seismic input of the incoming test. Finally, before starting the new test in order to reproduce the dynamic response of the updated global FE model, nonlinear parameters of reduced NSs were updated and implemented accordingly. In detail, as depicted in flowchart of Figure 3.28. Firstly, Piers #9 and #11 of PMCSI were considered as stand alone smodel and used to quantify damage experienced by corresponding specimens after a generic hybrid simulation *i*. Moreover, the maximum compressive strength $f_{cm}$ and hence also $E_{cm}$ of *Concrete*01 OpenSEES material were considered as updating parameters.

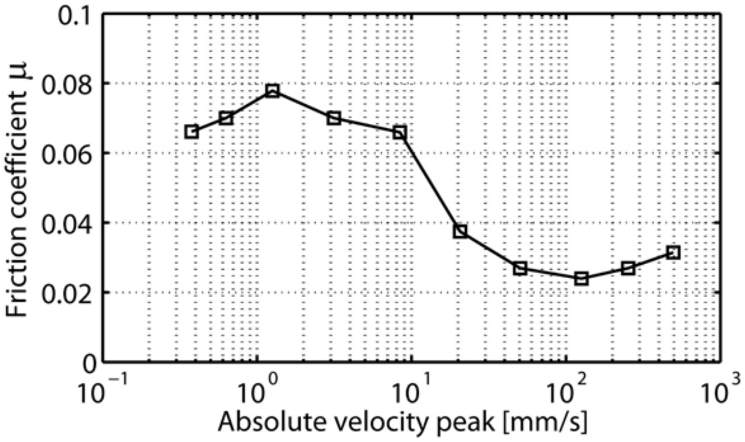

(a)

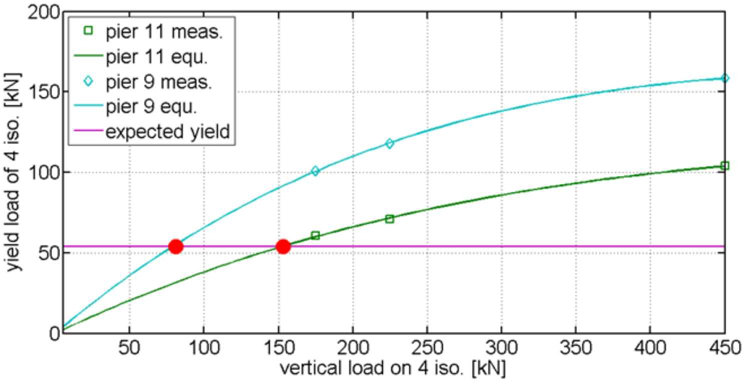

(b)

Figure 3.27: Variation of friction coefficient: a) variation due to speed; b) variation due to vertical load.

The then, the identified values on Pier #9 and #11 were applied to remaining hollow and solid cross section columns of PMCSI, respectively. A time history analysis of the updated PMCSI was successively conducted assuming the seismic input of the incoming hybrid simulation $i+1$. Finally, the results of this time history simulation were used to identify the parameters of the reduced S-DoF springs.

To systematically run this updating a numerical tool based on the *patternsearch* function was implemented in Matlab environment and carefully described in Abbiati (2014). In greater detail, it was based on a Matlab - Opensees interface;

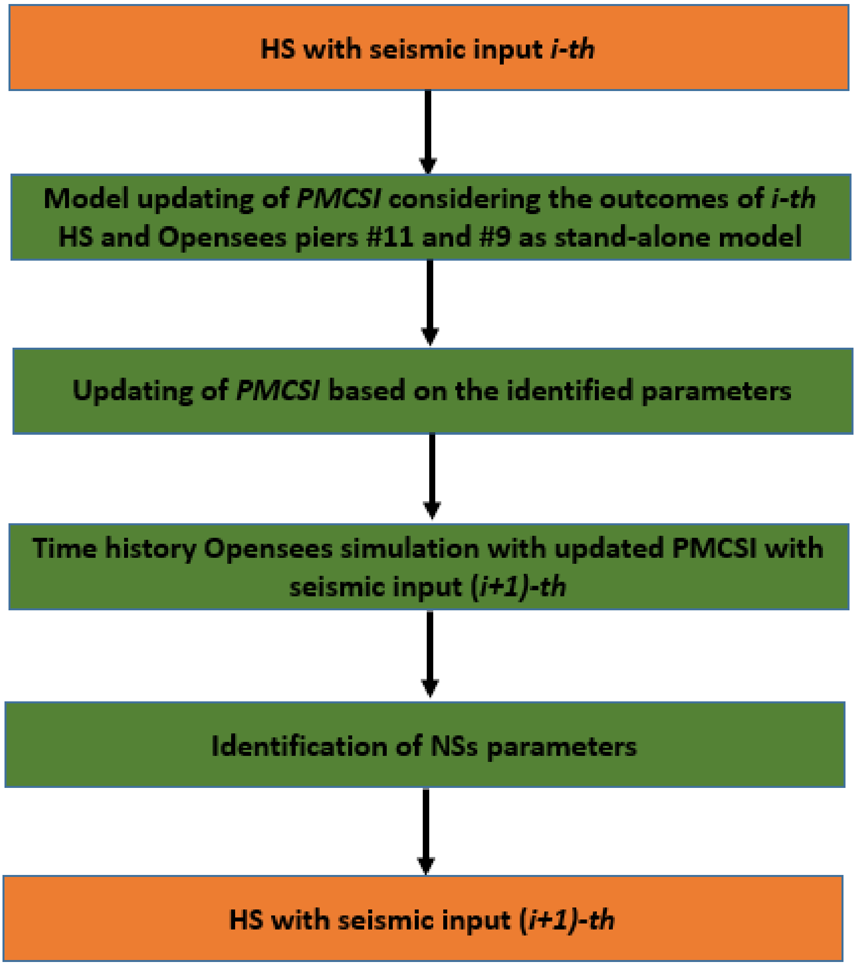

Figure 3.28: Flowchart describing the offline model updating procedure.

such interface generates the updated tcl code of the PMCSI and then runs the Opensees analysis. The procedure at each iteration update the parameters based on the *patternsearch* function which drove the selection to the optimum solution. As a results, in Figure 3.29 are reported the results of the model updating. The procedure was adopted to identify both RC piers and CSBs.

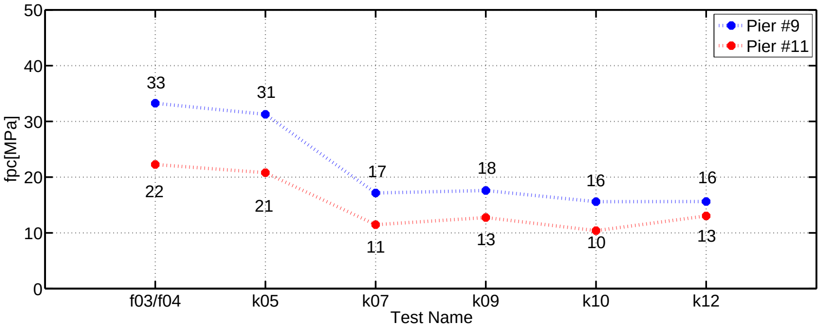

Figure 3.29: Variation of $f_{pc}$ during HSs resulted from offline model updating.

### 3.3.6 Outcomes of hybrid simulations

Hereinafter the outcomes of the HSs carried out in both *asbuilt* and isolated configurations. Displacements and forces refer to measurements of horizontal actuators magnified to the prototype scale, i.e. amplified accordingly to Table 3.6. In Table 3.13 are reported the most important tests performed at ELSA laboratory.

The dynamic response of the CSI in the linear range was investigated assuming the SLS accelerogram scaled to 10% of its PGA. In Figure 3.30 are reported the responses characterizing both PSs.

The scope of Test k07 was to analyze the response of the viaduct in *asbuilt* con-

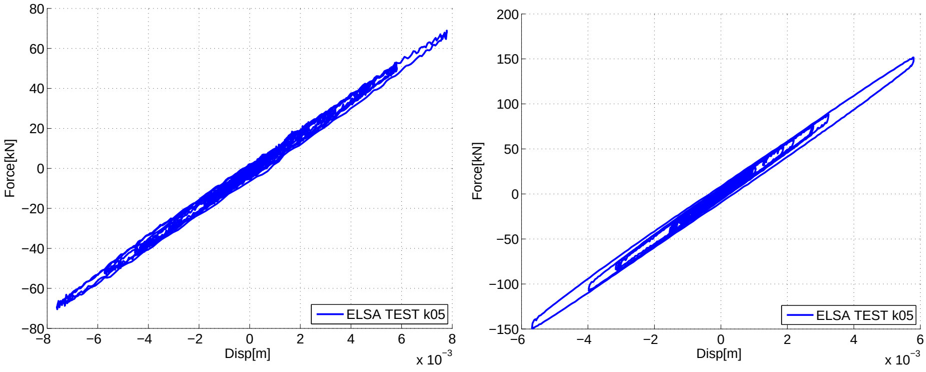

(a)

(b)

Figure 3.30: Force-displacement response of test k05: a) Pier #9; b) Pier #11.

| Label | PS | NS | Seismic input |
|---|---|---|---|
| k04 | *Piers#9and#11* | *asbuilt* | 10% SLS (12.5s) |
| k05 | *Piers#9and#11* | *asbuilt* | 10% SLS (25s) |
| k06 | *Piers#9and#11* | *asbuilt* | 10% SLS (12.5s) |
| k07 | *Piers#9and#11* | *asbuilt* | 100% SLS (6.6s) |
| l01 | *Piers#9and#11* | isolated | 100% SLS |
| l02 | *Piers#9and#11* | isolated | 100% ULS |
| n01 | *Iso.#9and#11* | isolated | 100% SLS |
| p01 | *Piers#9and#11* + *Iso.#9and#11* | isolated | 100% SLS |
| p02 | *Piers#9and#11* + *Iso.#9and#11* | isolated | 70% ULS |
| q01 | *Pier#9* + *Iso.#9* | isolated | 100% SLS |
| q02 | *Pier#9* + *Iso.#9* | isolated | 65% ULS |
| q03 | *Pier#9* + *Iso.#9* | isolated | 65% ULS |
| k09 | *Piers#9and#11* | *asbuilt* | 100% ULS |
| k10 | *Piers#9and#11* | *asbuilt* | 100% ULS |
| k12 | *Piers#9and#11* | *asbuilt* | 200% ULS |
| r01 | *Iso.#9* | isolated | 65% ULS |
| r02 | *Iso.#9* | isolated | 80% ULS |
| r03 | *Iso.#9* | isolated | 90% ULS |

Table 3.13: Testing program of hybrid tests

figuration when subjected to a SLS earthquake, therefore the 100% SLS accelerogram was applied. The global behavior overtook the elastic limit, corresponding to the formation of hairline cracks due to shear damage at the transverse beam of Piers #11 and #9. The predicted level of displacement for a slight damage condition was about 3 cm for the tall pier and 1.6 cm for the short one: during the test the short pier reached a displacement of about 3 cm, for this reason to avoid excessive damage in Pier #11 the test was stopped at 6.6 s. This was mainly due to the excessive deformability of Pier #11 with respect to the design values. Both piers experienced a markable drop of stiffness represented in first approxima-

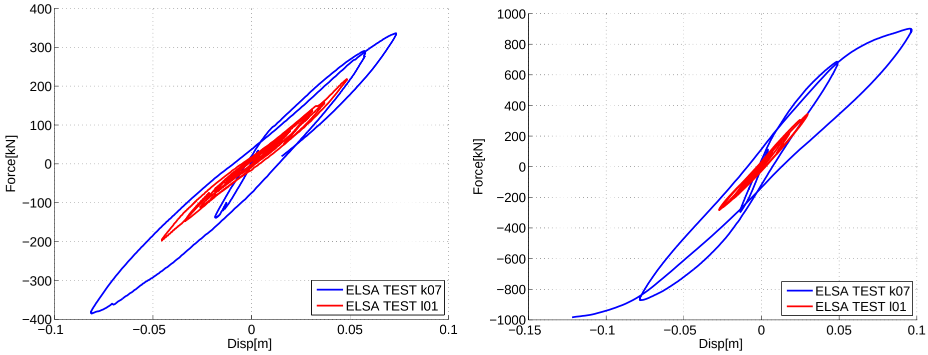

(a)

(b)

Figure 3.31: Force-Displacement of test k07: a) Pier #9; b) Pier #11.

tion with a decrease of concrete compressive strength in the PMCSI. After some investigations on the base rotations of Piers based on dedicated Linear Variable Displacement Transducer (LVDT) the drop in stiffness was attributed to slip effects due to plare rebars. The slight hysteretic loops of both specimens can be appreciated in Figure 3.31, which depicts Force-Displacement loops of both Piers #9 and #11. With regard to isolated configuration, as described in Subsection 3.3.4 the CSB isolators highlighted friction coefficients higher than design values, i.e. $\mu_{test}$ = 7% $\mu_{des}$ = 4% due to slow speed of HSs. Therefore, most significant HSs of the isolated bridge were conducted considering only NSs representing the CSB isolators. Figure 3.31 compares hysteretic loops of Piers #9 and #11 at SLS in the isolated and *asbuilt* configurations. Both piers remained in the linear regime during Test I01, hence piers were preserved even from cracks opening and propagation. These results confirm the effectiveness of the isolation system which considerably reduced maximum peaks on both piers at SLS.

Test k09 was performed to investigate the damage due to an ULS seismic event. As shown in Figures 3.32 and 3.33 both piers experienced significative nonlinearities proven by the cracks opened at the top and bottom side of piers, especially on Pier #11. Test I02 proven the effectiveness of the isolation system at ULS as shown in Figure 3.32. Hysteretic dissipation of piers was practically removed in the isolated configuration at ULS. As can be appreciated, the CSBs based retrofitting

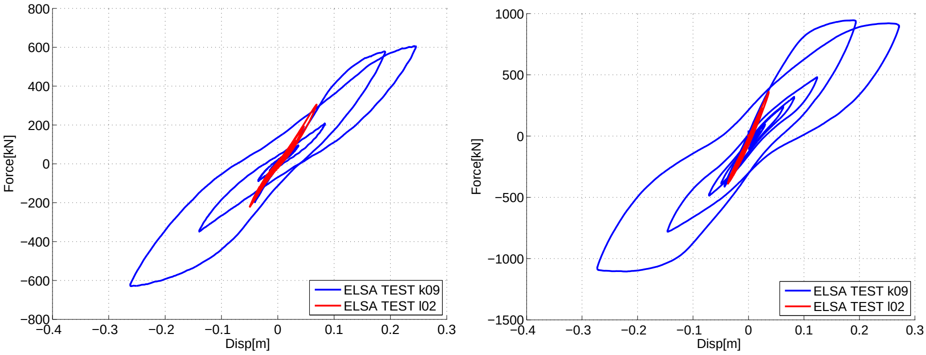

(a) (b)

Figure 3.32: Force-Displacement of test k09 and l02: a) Pier #9; b) Pier #11.

(a) (b)

Figure 3.33: Cracks opening at the top and bottom of Pier #11 after test k09.

produced a sensible drop in maximum displacement and hence piers did not accumulate damage during test l02. Further tests of the isolated configuration were conducted considering physical piers and CSB isolators. Test p01 was aimed at simulating the SLS. Since CSB isolators of Pier #11 exhibited a jagged force response, the ULS accelerogram was reduced to the 70% of its PGA value and applied through Test p02. In order to reproduce the design friction coefficient $\mu$ = 4%, reduced vertical forces were applied to physical CSBs isolators as presented in Subsection 3.3.4. Both simulations provides comparable results proving the effectiveness of DS to solve these type of experimental problems.

Then, to simulate an aftershock event, the seismic input of Test k09 was repeated during Test k10. Figure 3.34 compares hysteretic loops of Pier #9 and #11 obtained from Tests k09 and k10. As can be appreciated increasing column fix end rotations owing to higher slippage of rebars reduced hysteretic loops of piers at the second event. Finally, an amplified ULS accelerogram was applied with a PGA magnified to the 200% of its original value to see the damage due to a stronger, not considered in design phase, earthquake. According to Figure 3.35, which compares hysteretic loops of both piers of Tests k10 and k12, threshold restoring forces experienced during the earlier test were not exceeded. Nonetheless, during Test k12 both specimens experienced larger displacements approximately two times higher than peaks characterizing Test k09. Damage conditions were effectively propagated to numerical piers by means of the novel testing procedure based on offline updating. As shown in Figures 3.36, 3.37 and 3.38, both PSs experienced a consisted degradation.

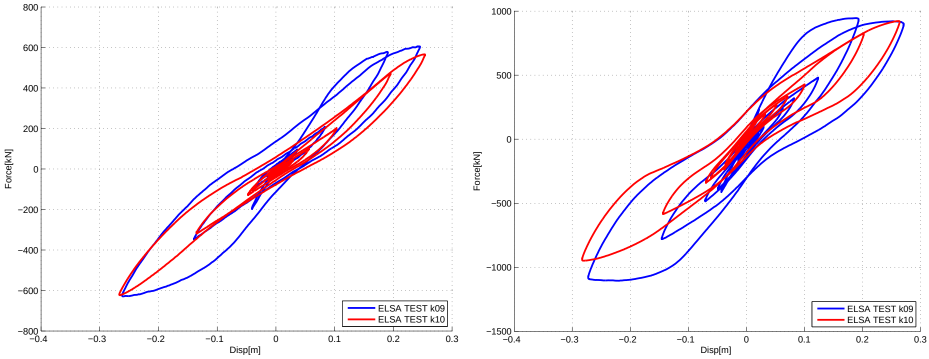

(a)

(b)

Figure 3.34: Force-Displacement of test k09 and k10: a) Pier #9; b) Pier #11.

## 3.4 Improvement of FE models based on springs-based modelling

In this section is presented the improvement procedure based on SBM approach adopted for this case study. The procedure was developed through the interpretation of experimental data provided by mechanical characterization tests and local LVDTs positioned on Pier #11. The complete set of 54 LVDTs is shown in

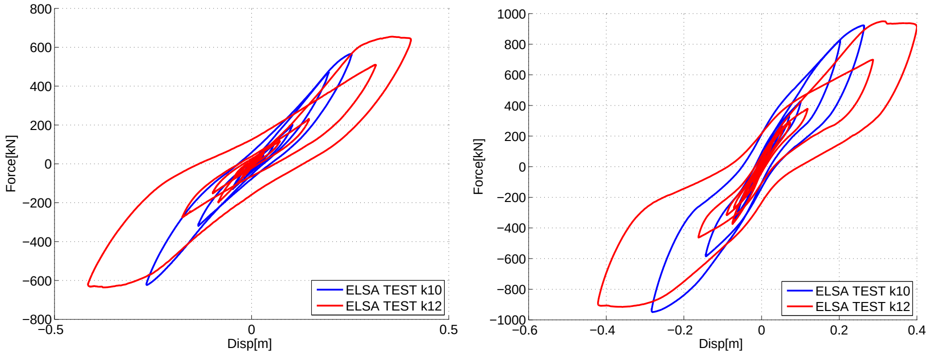

(a) (b)

Figure 3.35: Force-Displacement of test k10 and k12: a) Pier #9; b) Pier #11.

(a) (b)

Figure 3.36: Damage in the Pier #11 after k12 test: a) transverse beam damage on Pier #11; b) blow up of the transverse beam.

Figure 3.39. For the scope of this investigation, the data of the channels reported in Table 3.14 were analyzed. In grater detail, three FE models of Pier #11 have been developed in AABAQUS environment (SIMULIA (2011)): *i*) Model #1 composed by beam elements with distributed plasticity and perfectly constrained and restrained to the ground and between elements, respectively; *ii*) Model #2 with the same features of Model #1 but it is enhanced by local discrete nonlinear springs positioned at the base and top column joints; *iii*) Model #3 is a refined 3D model with all the structural details such as rebars and stirrups and enhanced by local discrete nonlinear springs identified by means of Model #2.

(a) (b)

Figure 3.37: Damage after k12 test: a) cracks opening at the top of a column in Pier #11; b) cracks pattern in the first transverse beam in Pier #9.

(a) (b) (c)

Figure 3.38: Cracks opening and buckling phenomena at the bottom section of columns after test k12: a) Pier #11; b) Pier #11; c) Pier #9.

The powerful of the SBM is widely proved in this case study thanks the ability of the springs to reproduce the actual behavior of these unknown joints affected by bond-slip effects. Due to computational effort the nonlinear discrete springs were identified through Model #2 and then imported in the Model #3.

The identification procedure started by the quantification of local rotations. In detail, they were evaluated on the base of the results provided by channels $c16-c19$, $c22-c25$, $c04-c07$ and $c10-c13$ following the traditional formulation reported hereinafter:

$$\phi_{ROTBLJ} = \frac{\Delta_{CH16} - \Delta_{CH19}}{L_{CH16-CH19}} \tag{3.32}$$

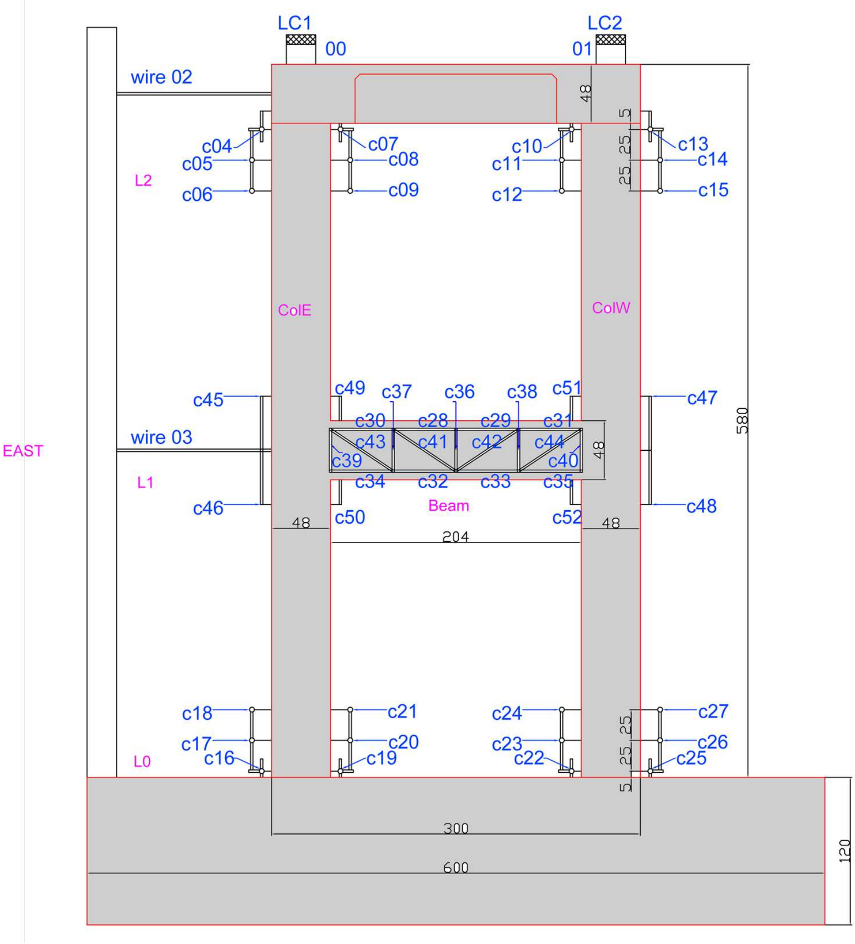

Figure 3.39: LVDTs lattice positioned on Pier #11

$$\phi_{ROTBRJ} = \frac{\Delta_{CH22} - \Delta_{CH25}}{L_{CH22-CH25}} \tag{3.33}$$

$$\phi_{ROTTLJ} = \frac{\Delta_{CH04} - \Delta_{CH07}}{L_{CH04-CH07}} \tag{3.34}$$

$$\phi_{ROTTRJ} = \frac{\Delta_{CH10} - \Delta_{CH13}}{L_{CH10-CH13}} \tag{3.35}$$

The rotations registered during test k07 have shown a semi-rigid behavior for both base and top of columns joints, as depicted in Figure 3.40. In greater detail, the

| LVDTs Position | Channels |
|---|---|
| Rotation of base left side joint (ROTBLJ) | 16,19 |
| Rotation of base right side joint (ROTBRJ) | 22,25 |
| Rotation of top left side joint (ROTTLJ) | 04,07 |
| Rotation of top right side joint (ROTTRJ) | 10,13 |
| Transverse beam top chord | 28,29,30,31 |
| Transverse beam bottom chord | 32,33,34,35 |
| Transverse beam vertical | 36,37,38,39,40 |
| Transverse beam 45° inclined | 41,42,43,44 |

Table 3.14: Summary of LVDTs considered during FE improvement process

maximum values of rotations recorded for ROTBLJ, ROTBRJ, ROTTLJ, ROTTRJ were approximately $5.5\cdot10^{-3}rad$, $6\cdot10^{-3}rad$, $7.5\cdot10^{-3}rad$ and $3\cdot10^{-3}rad$, respectively. The bending moment transmitted by each interested joints for was evaluated in first approximation following the analytical formulations of solid mechanics for a perfectly clamped system. This assumption can be accepted in firs approximation and it is valid only for the initial phase of test k07, for this reason the values identified by this preliminary hypothesis were modified during the improvement procedure. As a result, the moment-rotation envelopes reported in Figure 3.41 were obtained.

These curves were used to trace trilinear functions to be implement in the FE code. The values of each nonlinear spring, i.e. Spring of base left side joint (SPBLJ), Spring of base right side joint (SPBRJ), Spring of top left side joint (SPTLJ), Spring of top right side joint (SPTRJ), implemented in the FE models are gathered in Table 3.15.

### 3.4.1 Validation and calibration of Model #1 and Model #2

I order to save computational effort and to obtain results in a reasonable time, the first improvement step was performed on the stick models, i.e. Model #1 and Model #2. Both models were developed considering $B31$ ABAQUS elements with

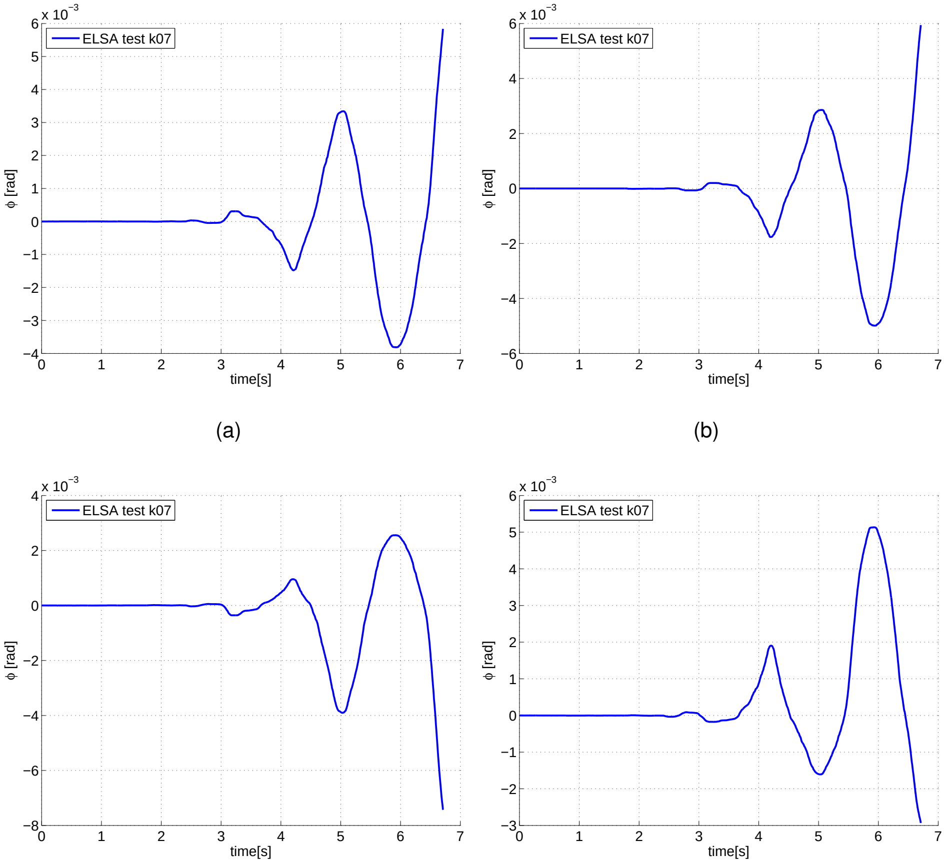

(a)

(b)

(c)

(d)

Figure 3.40: Rotations of critical joints during test k07:a)ROTBLJ; b)ROTBRJ; c)ROTTLJ; d)ROTTRJ.

distributed plasticity integrated with shear deformations and rebars elements. The models depicted in Figure 3.42 were implemented with the geometrical properties reported in Table 3.16. The columns were inserted with hollow circle cross section due to the holes made for the application of vertical loads by the actuators, i.e. 1C, 2C, 1B, 2B in Section 3.3. The materials have been set on the base of experimental characterization tests performed during the project the same presented in Section 3.2.3 (Paolacci (2014)). In greater detail, concrete was implemented with young's modulus $E_{cm} = 32000 MPa$ and strength $f_{cm} = 34 MPa$ with the constitutive law proposed in EN1992-1-1 (2005) for nonlinear problems, whilst steel rebars

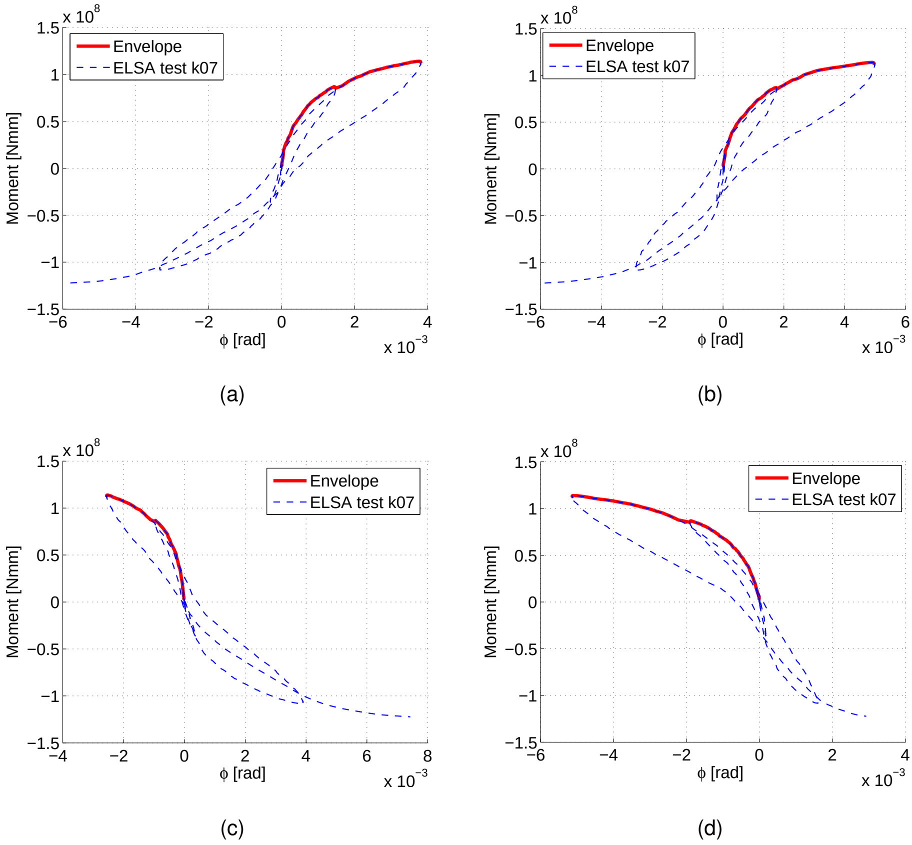

(a)

(b)

(c)

(d)

Figure 3.41: Envelopes of the moment-rotation laws at SLS: a) SPBLJ; b) SPBRJ; c) SPTLJ; d) SPTRJ.

with $E_s = 205000MPa$, $f_y = 360MPa$ and an hardening factor $\frac{E_sp}{E_s} = 0.025$. The difference between the two models can be seen in Figure 3.42, in fact, in Model #1 columns were clamped at the base and perfectly connected to cap beams whilst in Model #2 columns were connected to the ground through discrete springs as well as to the cap beam. In both models the cap beam was connected to the exact load application point by means of kinematic coupling command.

The validation phase was performed taking as benchmark function the constitutive law of concrete, $f_{cm}$ and $E_{cm}$ and the joints rotations of the RC pier, considered with the same weights, i.e. $w_k = 1$, as follows:

$$B_1^{Val} = [E_{cm}] \tag{3.36}$$

|  | **SPBLJ** | **SPBRJ** | **SPTLJ** | **SPTRJ** |
|---|---|---|---|---|
| $k_1[\frac{Nmm}{rad}]$ | $1.9 \cdot 10^{11}$ | $1.5 \cdot 10^{11}$ | $2.8 \cdot 10^{11}$ | $1.3 \cdot 10^{11}$ |
| $M_1[Nmm]$ | $3.3 \cdot 10^{7}$ | $3.3 \cdot 10^{7}$ | $3.3 \cdot 10^{7}$ | $3.3 \cdot 10^{7}$ |
| $\phi_1[rad]$ | $1.6 \cdot 10^{-4}$ | $2.1 \cdot 10^{-4}$ | $1.2 \cdot 10^{-4}$ | $2.3 \cdot 10^{-4}$ |
| $k_2[\frac{Nmm}{rad}]$ | $5.9 \cdot 10^{10}$ | $4.1 \cdot 10^{10}$ | $7.7 \cdot 10^{10}$ | $3.8 \cdot 10^{10}$ |
| $M_2[Nmm]$ | $9.5 \cdot 10^{7}$ | $9.5 \cdot 10^{7}$ | $9.5 \cdot 10^{7}$ | $9.5 \cdot 10^{7}$ |
| $\phi_2[rad]$ | $1.4 \cdot 10^{-3}$ | $1.7 \cdot 10^{-3}$ | $9.2 \cdot 10^{-4}$ | $1.8 \cdot 10^{-3}$ |
| $k_3[\frac{Nmm}{rad}]$ | $1.3 \cdot 10^{10}$ | $9.0 \cdot 10^{9}$ | $1.9 \cdot 10^{10}$ | $9.3 \cdot 10^{9}$ |
| $M_3[Nmm]$ | $1.2 \cdot 10^{8}$ | $1.2 \cdot 10^{8}$ | $1.2 \cdot 10^{8}$ | $1.2 \cdot 10^{8}$ |
| $\phi_3[rad]$ | $3.8 \cdot 10^{-3}$ | $5.0 \cdot 10^{-3}$ | $2.6 \cdot 10^{-3}$ | $5.1 \cdot 10^{-3}$ |

Table 3.15: Initial parameters identified.

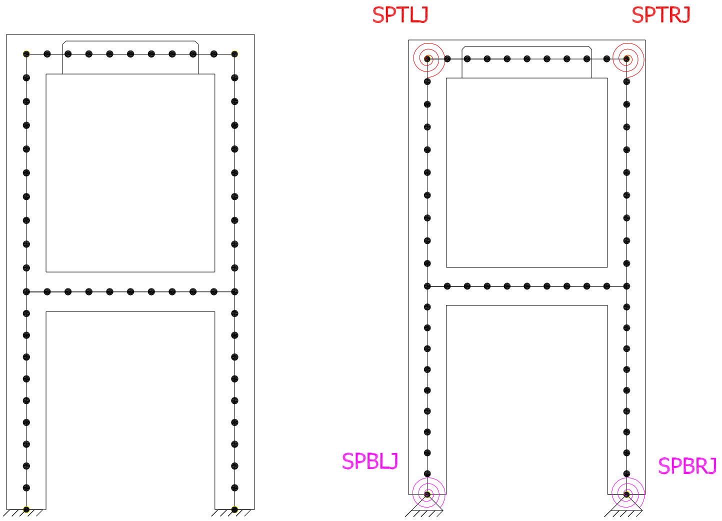

(a) (b)

Figure 3.42: Views of the stick FE models of Case Study I: a) Model #1; b) Model #2.

| Component | Sec Type | Shear Coeff | Dimensions | Material |
|---|---|---|---|---|
| Columns | Hollow Circular | $k_1$=0.53<br>$k_2$=0.53 | $r_o = 240mm$<br>$r_i = 177.5mm$ | Concrete and Rebars |
| Transverse Beam | Rectangular | $k_1$=0.85<br>$k_2$=0.85 | $b = 160mm$<br>$h = 480mm$ | Concrete and Rebars |
| Cap Beam | U-Shape | $k_1$=1<br>$k_2$=1 | $b = 480mm$<br>$h = 480mm$ | Concrete and Rebars |

Table 3.16: Geometrical Properties of Pier #11 implemented in the stick models.

$$B_2^{Val} = [f_{cm}] \tag{3.37}$$

$$B_3^{Val} = [\mathrm{ROTBLJ}] \tag{3.38}$$

$$B_4^{Val} = [\mathrm{ROTBRJ}] \tag{3.39}$$

$$B_5^{Val} = [\mathrm{ROTTLJ}] \tag{3.40}$$

$$B_6^{Val} = [\mathrm{ROTTRJ}] \tag{3.41}$$

Calibration instead was referred to the global base reaction force and top pier displacement:

$$B_1^{Cal} = [Pier\ \ Base\ \ Reaction\ \ Force - Pier\ \ Top\ \ Displacement\ \ law] \tag{3.42}$$

In this case the comparison functions used to evaluate the difference between benchmarks and FE models was the NRMSE adapted to validation and calibration cases:

$$D_i(M, B_i^{Val}) = NRMSE_i(M, B_i^{Val}) = \frac{\sqrt{\frac{1}{n}\sum_{i=1}^{n}(M - B_i^{Val})^2}}{max(B_i^{Val}) - min(B_i^{Val})} \tag{3.43}$$

$$D_i(M, B_i^{Cal}) = NRMSE_i(M, B_i^{Cal}) = \frac{\sqrt{\frac{1}{n}\sum_{i=1}^{n}(M - B_i^{Cal})^2}}{max(B_i^{Cal}) - min(B_i^{Cal})} \tag{3.44}$$

Once defined these quantities, it was possible to start with validation and calibration phases. In this case study it was decided to keep fixed the input parameters during validation phase and to modify them during calibration phase. Hereinafter is presented the procedure applied to reproduce the SLS regime. As can be seen in Tables 3.17 and 3.18 during validation phase also the calibration parameters have been monitored in order to investigate the possibility to skip the calibration phase judging the model as *Believable model* after validation. As a result, it is clear as the Model #2 is capable to represent the actual behavior without significative updating. As shown in Figure 3.43, thanks to these discrete springs the stick model is capable to reproduce the global and local behavior with an acceptable error generally smaller than 10% in terms of rotations, except for ROTTLJ that showed a larger error. Moreover for all the monitored quantities it is possible to conclude that conversely to Model #1, Model #2 was already capable to reproduce the structural behavior during validation phase, it was confirmed by the well reproduction of rotations trends. The maximum validation error was 10% against the 38% evaluated for Model #1. In addition, Model #2 can be considered believable without the need of a calibration step, in fact the calibration error is already 7%. Differently for Model #1 which registered a calibration error of 46%.

In light of this, the calibration procedure was developed to prove the potential of the SBM and the results are gathered in Tables 3.17 and 3.18. As can be appreciated, both model were capable to decrease the calibration error. Needs to be underlined that Model #1 payed an increasing of validation error equal to 16% whilst Model #2 only 5%. In both cases to reach the calibration requirements the models became less valid but with important differences in terms of error magnitude.

Calibration have been obtained differently in the two models. In grater detail, for Model #1 $E_{cm}$ and $f_{cm}$ of concrete have been reduced to 18000 MPa and 17 MPa, respectively with an unacceptable error in terms of validation. With regard to Model #2 the trilinear function of the springs were modified with a coefficient of 0.6 for point one of moment-rotation, 0.7 for the second and 0.9 for the third

| **Validated Model** #1 | | | | | | | | | |
|---|---|---|---|---|---|---|---|---|---|
| | $D_1^V$ | $D_2^V$ | $D_3^V$ | $D_4^V$ | $D_5^V$ | $D_6^V$ | $D_{Tot}^V$ | $D_1^C$ | $D_{Tot}^C$ |
| $w_k^{Val}$ | 1 | 1 | 1 | 1 | 1 | 1 | | 1 | |
| Env of k07 | 0 | 0 | 0.61 | 0.55 | 0.56 | 0.57 | 0.38 | 0.46 | 0.46 |
| **Calibrated Model** #1 | | | | | | | | | |
| | $D_1^V$ | $D_2^V$ | $D_3^V$ | $D_4^V$ | $D_5^V$ | $D_6^V$ | $D_{Tot}^V$ | $D_1^C$ | $D_{Tot}^C$ |
| $w_k^{Cal}$ | 1 | 1 | 1 | 1 | 1 | 1 | | 1 | |
| Env of k07 | 0.44 | 0.50 | 0.61 | 0.55 | 0.56 | 0.57 | 0.54 | 0.06 | 0.06 |

Table 3.17: Results of Model #1 during validation and calibration phases.

| **Validated Model** #2 | | | | | | | | | |
|---|---|---|---|---|---|---|---|---|---|
| | $D_1^V$ | $D_2^V$ | $D_3^V$ | $D_4^V$ | $D_5^V$ | $D_6^V$ | $D_{Tot}^V$ | $D_1^C$ | $D_{tTot}^C$ |
| $w_k^{Val}$ | 1 | 1 | 1 | 1 | 1 | 1 | | 1 | |
| Env of k07 | 0 | 0 | 0.05 | 0.09 | 0.42 | 0.06 | 0.10 | 0.07 | 0.07 |
| **Calibrated Model** #2 | | | | | | | | | |
| | $D_1^V$ | $D_2^V$ | $D_3^V$ | $D_4^V$ | $D_5^V$ | $D_6^V$ | $D_{Tot}^V$ | $D_1^C$ | $D_{Tot}^C$ |
| $w_k^{Cal}$ | 1 | 1 | 1 | 1 | 1 | 1 | | 1 | |
| Env of k07 | 0 | 0 | 0.14 | 0.13 | 0.55 | 0.095 | 0.15 | 0.005 | 0.005 |

Table 3.18: Results of Model #2 during validation and calibration phases-

moment values, respectively. As a result a small drop in the springs stiffness resulted as shown in Figure 3.44. The modification required in Model #2 resulted to be significative, even though smaller if compared with the required modification in Model #1. It was anyway reasonable if we consider that when the connection lose stiffness it is unable to transmit bending moment. This is exactly what the modified laws are showing. In this first example all the benefits provided by the SBM approach were shown, in fact thanks to this numerical approach it was possible to decrease the calibration error by the preservation of material properties that means preservation of local stresses and plasticity on all the pier zones. To obtain this it was accepted to have a larger error in the springs zone, this variation remains in

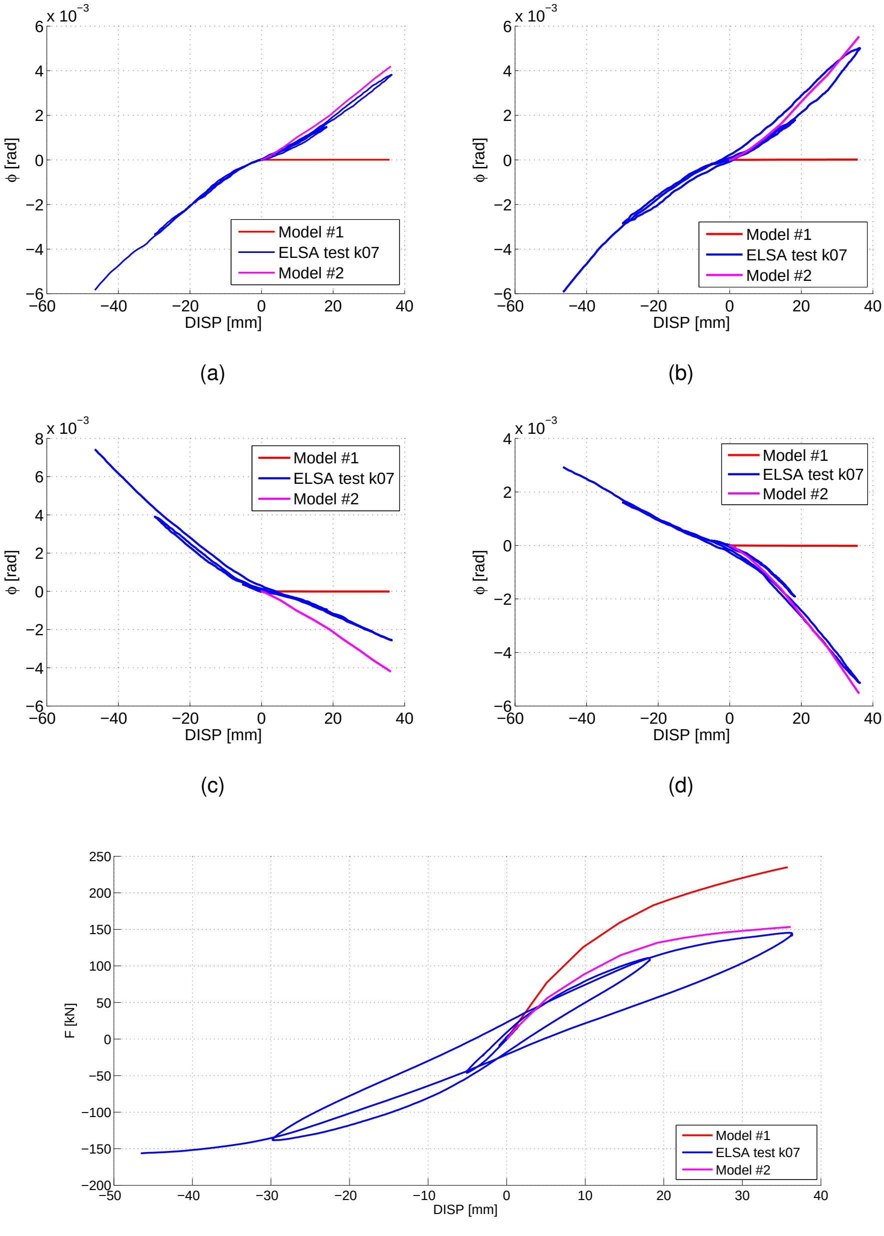

(a)

(b)

(c)

(d)

(e)

Figure 3.43: Comparison of rotations after validation step: a) ROTBLJ; b) ROTBRJ; c) ROTTLJ; d) ROTTRJ; e) Force-displacement.

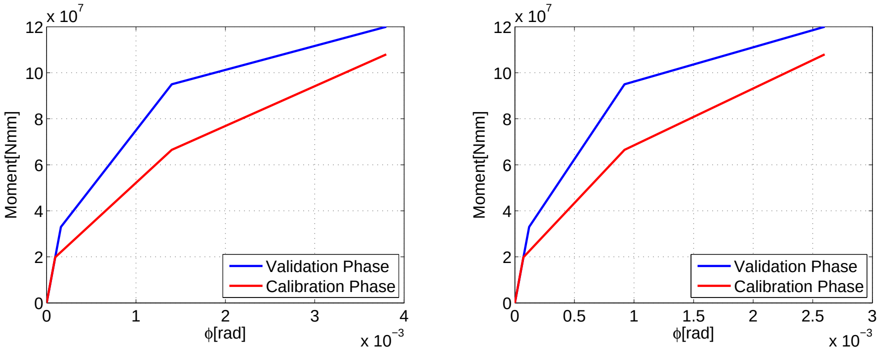

(a) (b)

Figure 3.44: Modified constitutive laws to fit calibration benchmark: a) ROTBLJ; b) ROTTLJ.

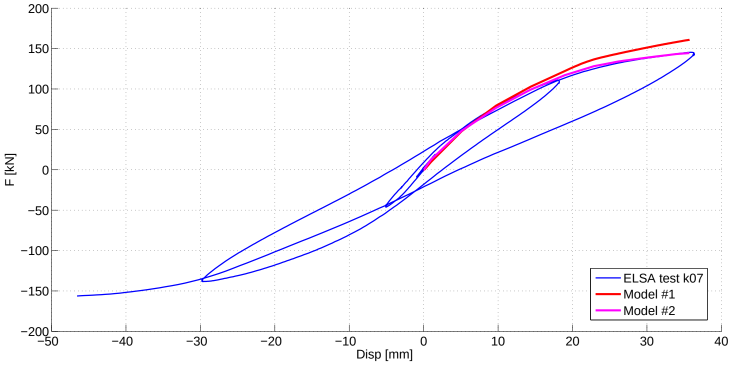

Figure 3.45: Force-displacements response of stick models after calibration phase.

an acceptable range with modifications of maximum 20% in terms of stiffness. In addition, a reduction in terms of joint stiffness was expected because of the modification of constraints condition that imply reduction of transferred moment.

Finally, in Figure 3.45 is depicted the comparison between models after calibration phase. Model #1 could have been modified more but it was decided to stop the calibration due to the unacceptable validation error that had been reached.

### 3.4.2 Validation and calibration of Model #3

The aim of Model #3 was the investigation of the local behavior of structural joints built with smooth steel rebars. In this purpose the model was enhanced by local springs identified by means of Model #2. The 3D model was implemented in an ABAQUS environment (SIMULIA (2011)). It was a mix of solid and beam elements, in fact to decrease computational effort only the critical parts were modelled in a 3D manner as depicted in Figure 3.49(a). In greater detail, the concrete columns and bottom transverse beam were modelled by $C3D8R$ solid elements, steel rebars and stirrups by $T3D2$ truss elements, as shown in Figure 3.49(b) and finally $B31$ beam elements for the pier cap beam that remains elastic during all the tests. Steel rebars and stirrups shown in Figures 3.46, 3.47, 3.48 have been carefully modelled. As a result the lattice of reinforcements depicted in Figure 3.49(b) was obtained. In first approximation the rebars and stirrups have been connected to the concrete matrix by a perfect link represented by the Embedded element command which links all the DoFs between the interested elements. The amount of elements is approximately 210000 including solid, beam and truss elements. Due to strong nonlinearities the problem could not be solved with ABAQUS/Standard but required the implementation of dynamic quasi-static procedure through ABAQUS/Explicit. Thanks to dynamic features the explicit procedure does not require the iteration to obtain the solution but it advance the kinematic state from the

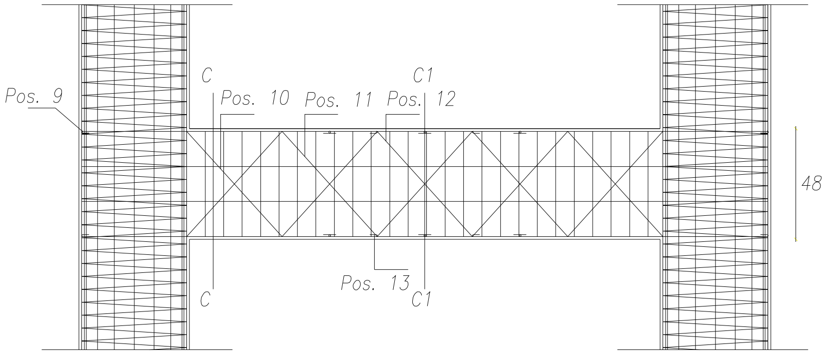

Figure 3.46: Reinforcements of the scaled transverse beam of Pier #11.

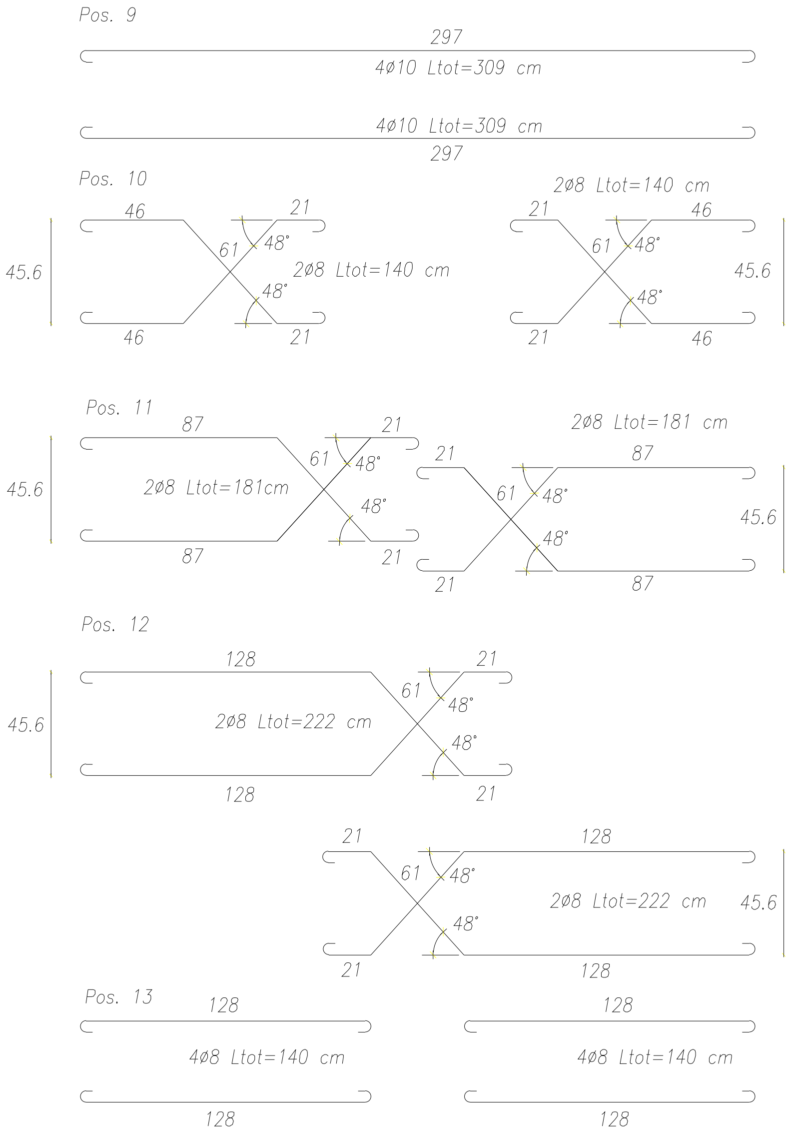

Figure 3.47: Details of the reinforcements of scaled transverse beam of Pier #11 (Pos. 9 - Pos. 13).

previous increment. This type of analysis could require several time increments. In addition it allows to optimize the use of space and memory in the computer.

In general, when this type of simulation is performed, the dynamic equilibrium

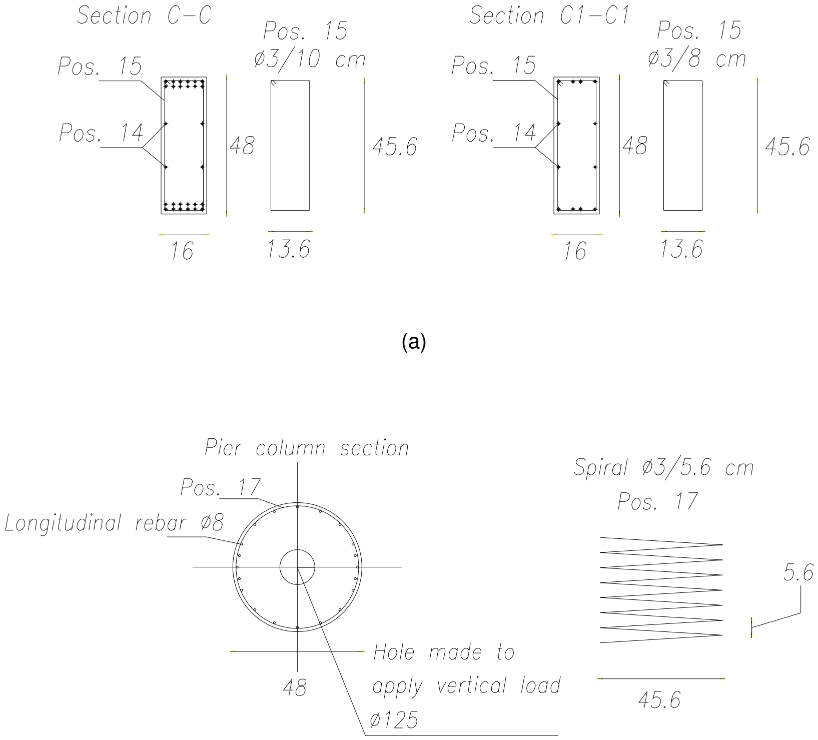

(a)

(b)

Figure 3.48: Details of the reinforcements of Pier #11: a) Transverse beam stirrups; b) Column reinforcements.

equations can be written with the inertial forces isolated from the other forces:

$$M\ddot{u} = F - I \tag{3.45}$$

where M is the mass matrix, $\ddot{u}$ is the vector of acceleration, F is the external load vector and I is the internal load vector. These equilibrium equations are completely general and are valid for the behavior of any mechanical system and contain all nonlinearities such as large deformations, nonlinear material response, contact. For a static problems it is possible to write

$$M\ddot{u} \approx 0 \tag{3.46}$$

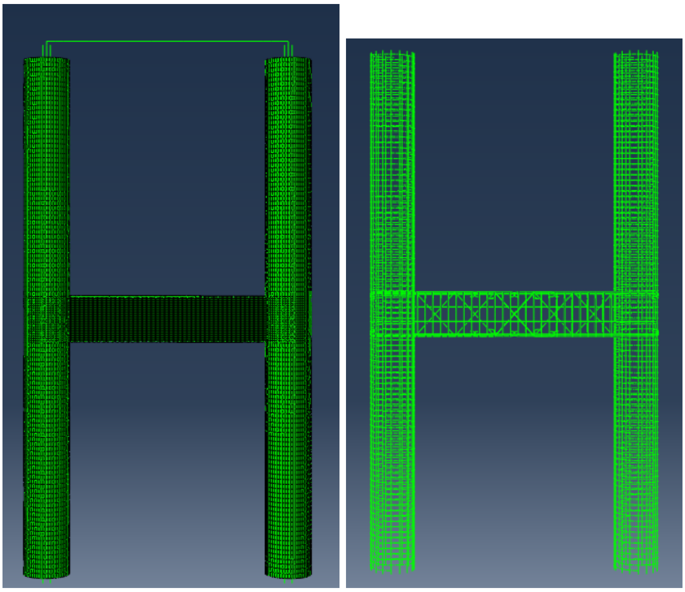
(a) (b)

Figure 3.49: Views of Model#3: a) concrete volume with C3D8R solid elements; b) rebars and stirrups implemented as T3D2 truss elements.

The explicit procedure perform the analysis by means of a large number of time/load increments. Considering the central difference integration, for each increment the solution reads,

$$(M\ddot{u})_n = (F - I)_n \tag{3.47}$$

$$(\ddot{u})_n = M^{-1}(F - I)_n \tag{3.48}$$

$$(\dot{u})_{n+\frac{1}{2}} = (\dot{u})_{n-\frac{1}{2}} + (\frac{\Delta t_{n+1} + \Delta t_n}{2}\ddot{u})_n \tag{3.49}$$

$$(u)_{n+1} = (u)_n + (\Delta t_{n+1}\dot{u})_{n+\frac{1}{2}} \tag{3.50}$$

This procedure allows to avoid convergence problems by the modification of model masses. In detail, to solve a static problem it is possible to play with masses with the aim to find the time increment suitable for the problem. This equivalent dynamic analysis with springs elements implied a very small time increment which was too small to have results in a reasonable time. As a result, the top and bottom sides of column spring, i.e. SPBLJ, SPBRJ, SPTLJ, SPTRJ, were replaced by an equivalent truss element based system.

In detail, as shown in Figures 3.50 and 3.51 a system of rigid links and multi-point constraints, i.e. MPC elements, were implemented to transfer the rotations to a couple of truss elements that provides the rotational stiffness of the joints. The axial stiffness of the truss elements were evaluated as reported hereinafter. In detail, the general moment-rotation relation reads:

$$M = k_{rot} \cdot \phi_{rot} \tag{3.51}$$

- if the base joint spring depicted in Figure 3.50(a) is considered, M can be written as,

$$M_{SPBLJ} = KBLJ1 \cdot \Delta \cdot b + KBLJ2 \cdot \Delta \cdot b \tag{3.52}$$

since $KBLJ1 = KBLJ2 = KBLJ$,

$$M_{SPBLJ} = 2 \cdot KBLJ \cdot \Delta \cdot b = 2 \cdot KBLJ \cdot b^2 \cdot \theta \tag{3.53}$$

finally, since $\theta = \phi_{rot}$

$$k_{SPBLJ} = 2 \cdot KBLJ \cdot b^2 \tag{3.54}$$

$$k_{SPBRJ} = 2 \cdot KBRJ \cdot b^2 \tag{3.55}$$

- if the base joint spring depicted in Figure 3.50(b) is considered, M can be written as,

$$M_{SPTLJ} = KTLJ1 \cdot (\Delta 1 + \Delta 2) \cdot b + KTLJ2 \cdot (\Delta 1 + \Delta 2) \cdot b \tag{3.56}$$

$$M_{SPTLJ} = KTLJ1 \cdot (\theta 1 + \theta 2) \cdot b^2 + KTLJ2 \cdot (\theta 1 + \theta 2) \cdot b^2 \tag{3.57}$$

since $KTLJ1 = KTLJ2 = KTLJ$,

$$M_{SPTLJ} = 2KTLJ \cdot (\theta 1 + \theta 2) \cdot b^2 \tag{3.58}$$

$$(\theta 1 + \theta 2) = \phi_{rot} \tag{3.59}$$

$$M_{SPTLJ} = 2KTLJ \cdot b^2 \tag{3.60}$$

$$M_{SPTRJ} = 2KTRJ \cdot b^2 \tag{3.61}$$

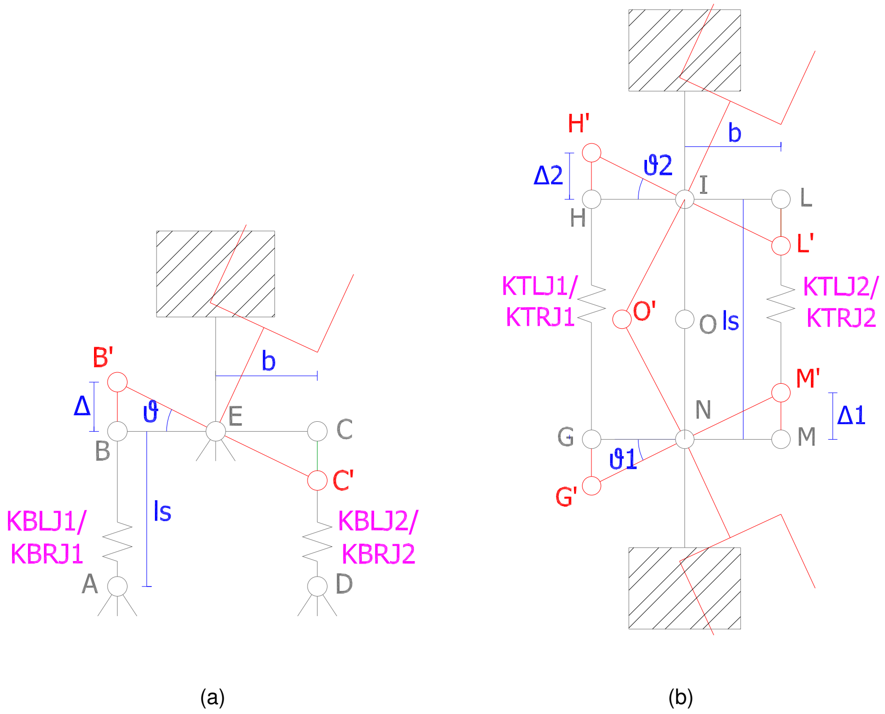

Figure 3.50: Equivalent springs implemented in Model #3: a) column base; b) column top.

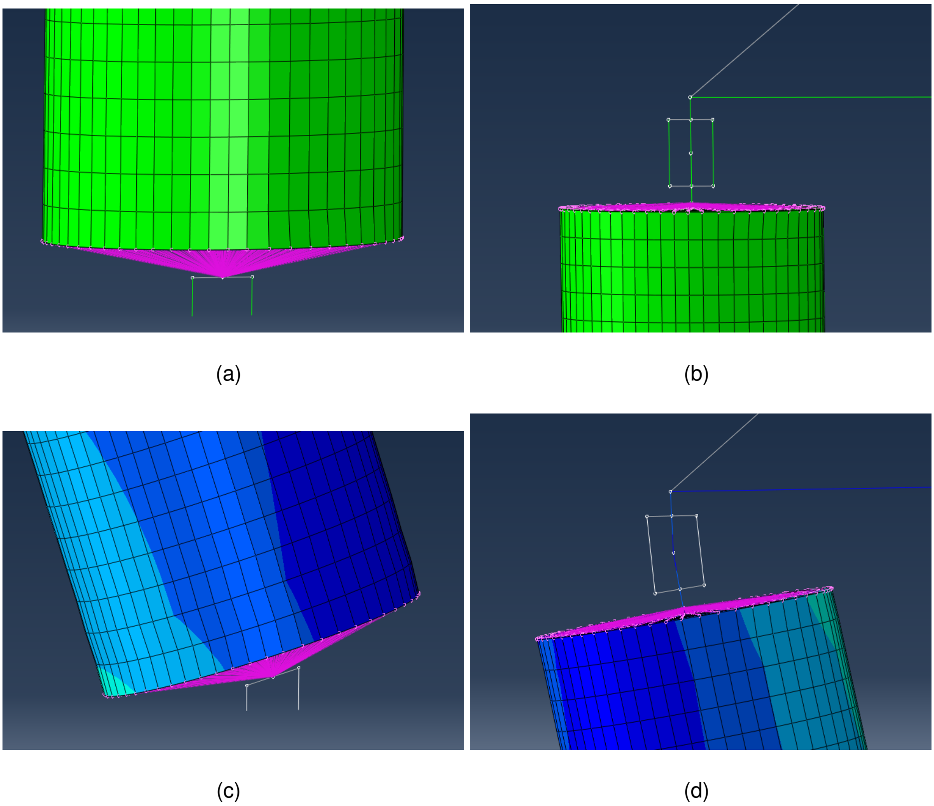
(a)
(b)
(c)
(d)

Figure 3.51: Details of Model #3: a) undeformed column base truss system; b) undeformed column top truss system; c) deformed column base truss system; d) deformed column top truss system.

In order to check the goodness of Model #3, it was run initially at SLS regime and it was validated and calibrated with the same benchmarks functions adopted for Model #1 and Model #2. In detail, for the validation phase the material properties were the same of Model #1 and Model #2, the springs constitutive laws instead were the same reported in Table 3.15, i.e. the one implemented in Model #2.
The results, reported in Table 3.19 showed the goodness of the model in both validation and calibration phases and it would not require calibration. In this case a calibration has been performed anyway and the resulted error was approximative 3%. As can be read in Table 3.19 in the 3D case, the validation errors increased, this was due to the higher general stiffness characterizing the 3D modelling. This

additional stiffness imply a major load on the springs that result in larger rotations. This means that improvements in the model are required especially by the refinement of the interaction between rebars and concrete. Even though the larger error, Model #3 remains a believable model which can be improved. Model #3 is still in evolution phase hence it will be improved, for the scope of the thesis these results have been judged satisfactory. In Figure 3.52 force displacement responses of Model #3 after both validation and calibration phases.

Few considerations can be drawn, firstly the 3D model seems to have a different behavior for large displacements if compared with stick Model #2, this is due to the nonlinear effect generated in the transverse beam. In Model #2, differently from Model #3, the transverse beam was modelled with elastic shear stiffness which did not include nonlinear shear effects. This is the reason for which the 3D model diverged from benchmark solution for displacements larger than 20 mm. In fact, from this point of the simulation the nonlinearities of transverse beam became significative calibration. Model #3 has been pushed up to ULS regime. As can be seen in Figure 3.52 the model was capable to represent the pier response also for large displacements.

Finally, to prove the effectiveness of Model #3 in the SLS regime others error functions have been evaluated considering as benchmark functions the experimental data of LVDTs.

<table>
<tr><th colspan="10"><b>Validated Model</b> #3</th></tr>
<tr><td></td><td>$D_1^V$</td><td>$D_2^V$</td><td>$D_3^V$</td><td>$D_4^V$</td><td>$D_5^V$</td><td>$D_6^V$</td><td>$D_{Tot}^V$</td><td>$D_1^C$</td><td>$D_{Tot}^C$</td></tr>
<tr><td>$w_k^{Val}$</td><td>1</td><td>1</td><td>1</td><td>1</td><td>1</td><td>1</td><td></td><td>1</td><td></td></tr>
<tr><td>Env of k07</td><td>0</td><td>0</td><td>0.21</td><td>0.18</td><td>0.98</td><td>0.37</td><td>0.28</td><td>0.04</td><td>0.04</td></tr>
<tr><th colspan="10"><b>Calibrated Model</b> #3</th></tr>
<tr><td></td><td>$D_1^V$</td><td>$D_2^V$</td><td>$D_3^V$</td><td>$D_4^V$</td><td>$D_5^V$</td><td>$D_6^V$</td><td>$D_{Tot}^V$</td><td>$D_1^C$</td><td>$D_{Tot}^C$</td></tr>
<tr><td>$w_k^{Cal}$</td><td>1</td><td>1</td><td>1</td><td>1</td><td>1</td><td>1</td><td></td><td>1</td><td></td></tr>
<tr><td>Env of k07</td><td>0</td><td>0</td><td>0.20</td><td>0.11</td><td>1.00</td><td>0.40</td><td>0.29</td><td>0.03</td><td>0.03</td></tr>
</table>

Table 3.19: Comparisons of Model #3 during validation and calibration phases.

Model #3 implemented in this manner was perfect to be used for the compari-

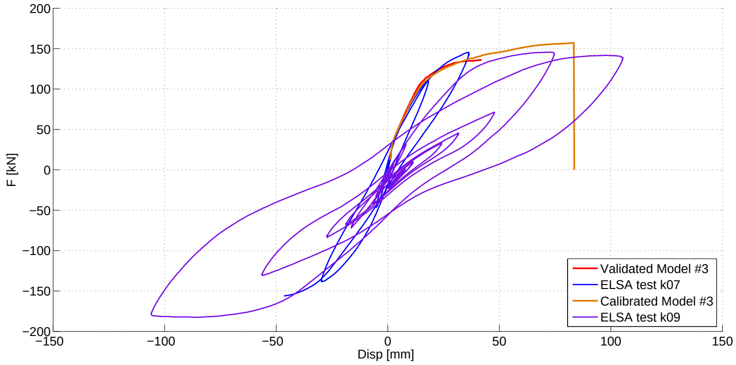

Figure 3.52: Force-displacements response of 3D model after validation and calibration phase.

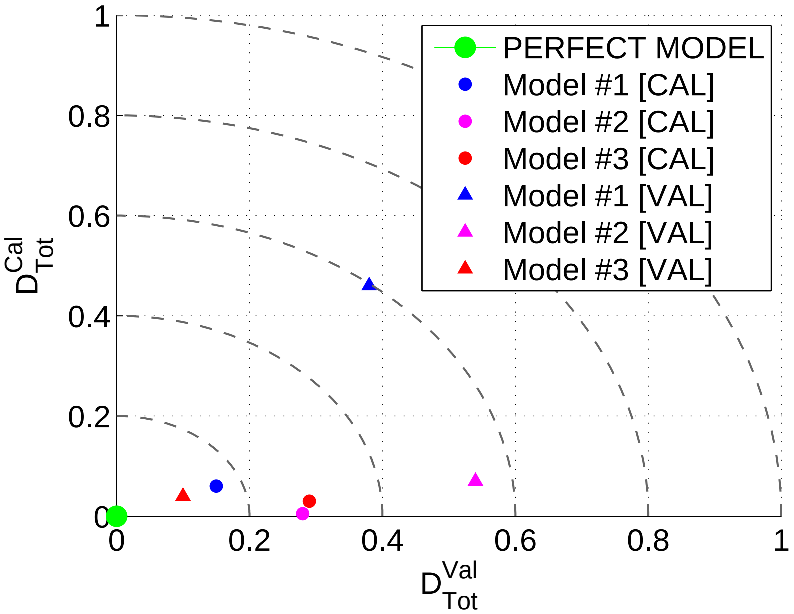

Figure 3.53: Results after calibration phase: a) force-displacements response; b) domain of errors for Case Study I.

son of displacements between the numerical and experimental results relevant to transverse beam. In grater detail, the channels between 29 and 44 were considered. The effective displacement of the LVDTs was compared with the effective

| **Calibrated Model** #3 | | | | | | | | |
|---|---|---|---|---|---|---|---|---|
| | $D^V_{c28}$ | $D^V_{c29}$ | $D^V_{c30}$ | $D^V_{c31}$ | $D^V_{c32}$ | $D^V_{c33}$ | $D^V_{c34}$ | $D^V_{c35}$ |
| $w_k^{Val}$ | 1 | 1 | 1 | 1 | 1 | 1 | 1 | 1 |
| Env of k07 | 0.32 | 0.69 | 0.63 | 0.07 | 0.13 | 0.20 | 0.09 | 0.12 |
| | $D^V_{c37}$ | $D^V_{c38}$ | $D^V_{c39}$ | $D^V_{c40}$ | $D^V_{c41}$ | $D^V_{c42}$ | $D^V_{c43}$ | $D^V_{c44}$ |
| $w_k^{Val}$ | 1 | 1 | 1 | 1 | 1 | 1 | 1 | 1 |
| Env of k07 | 0.57 | 0.32 | 0.20 | 0.15 | 0.44 | 0.16 | 0.08 | 0.30 |

Table 3.20: Comparisons of Model #3 during validation phase.

displacement between the two nodes positioned at the same coordinates as depicted in Figure 3.54(a). For the presented purpose 17 relative displacements were considered and each one was calculated with the formulation reported hereinafter:

$$L_{ini}^{POSk} = \sqrt{\bar{x}_i{}^2 + \bar{x}_j{}^2} \tag{3.62}$$

$$L_{fin}^{POSk} = \sqrt{(\bar{x}_i + \bar{u}_i)^2 + (\bar{x}_j + \bar{u}_j)^2} \tag{3.63}$$

$$\Delta^{POSk} = L_{fin} - L_{ini} \tag{3.64}$$

The set of 17 —acLVDTs monitored during the tests and reproduced with the Model#3 is reported in Figure 3.54(b). In Figure 3.55 are depicted the deformations and stresses on transverse beam at collapse, it is possible to appreciate the shear deformation which drove the element failure. In Figures 3.56, 3.57, 3.58, 3.59, are shown the comparisons between LVDTs and Model #3 for the SLS regime investigated with the calibrated Model #3.

## 3.5 Conclusions

The assessment of the seismic performances of the Rio Torto Bridge was conceived within the RETRO activity funded by the Seismic Engineering Research

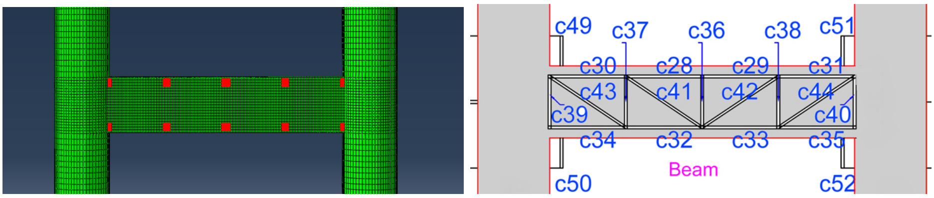

(a) (b)

Figure 3.54: Details about the positions investigated on the transverse beam: a) Model #3; b) experimetnal LVDTs lattice.

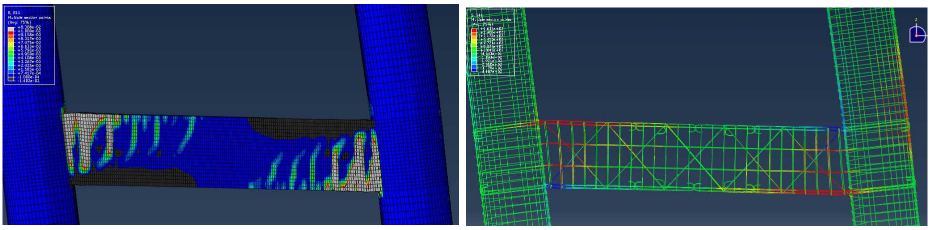

(a) (b)

Figure 3.55: Stresses on the pier transverse beam at maximum displacement of calibrated model: a) concrete; b) rebars and stirrups.

Infrastructures for European Synergies (SERIES) research project. In this chapter have been developed Steps I, II, III of APSPAB procedure in purpose to reach the objectives of the project that were: *i*) to cover the lack of knowledge in the nonlinear behavior of portal frame piers in presence of plain steel rebars; *ii*) to employ large scale experimental test for the seismic assessment of existing bridges; *iii*) to study the effectiveness of a seismic isolation systems based on CSBs.

Firstly, thanks to the huge numerical FE based investigations supported by experimental data, the effects of plane rebars have been quantified. In grater detail, two refined FE models based on SBM approach have shown the effective drop in stiffness due to the weak connection provided by the piers joints. In addition these models allowed to compare the numerical results with a set of LVDTs installed on the transverse beam with the aim to investigate locally the nonlinear effects due to shear deformations. The validation and calibration of numerical FE models allowed

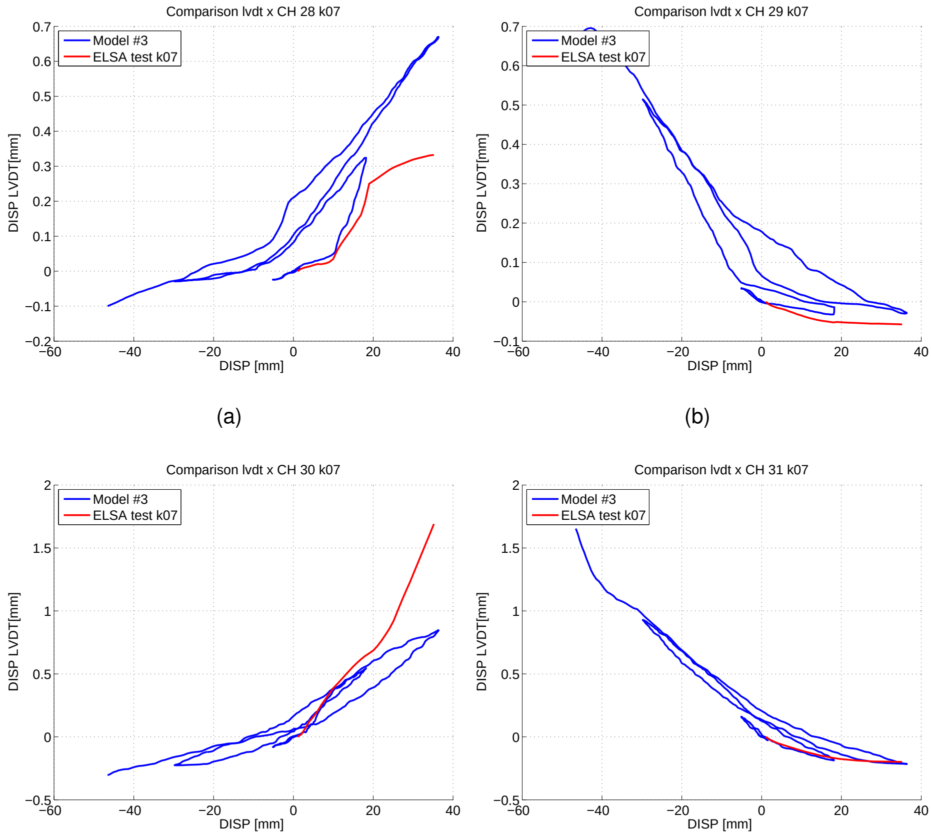

(a) (b)

(c) (d)

Figure 3.56: Comparison of local displacements on calibrated Model #3: a) channel 28; b) channel 29; c) channel 30; d) channel 31.

to identify the joints rotations and hence to quantify the effective degradation produced by plane rebars and compare it with the degradation due to the transverse beam. In fact, initially the damage of the pier was driven by nonlinear effects due to joints rotations, later once the joints lost rotational stiffness additional damaging was induced in the transverse beam.

Relevant to the second objective of the project, a set of HSs has been designed and performed at ELSA laboratory to test the Rio Torto Viaduct in both *asbuilt* and isolated configurations. In greater detail, the implementation of the tests required high speed in numerical calculations due to the needs of substructures coupling.

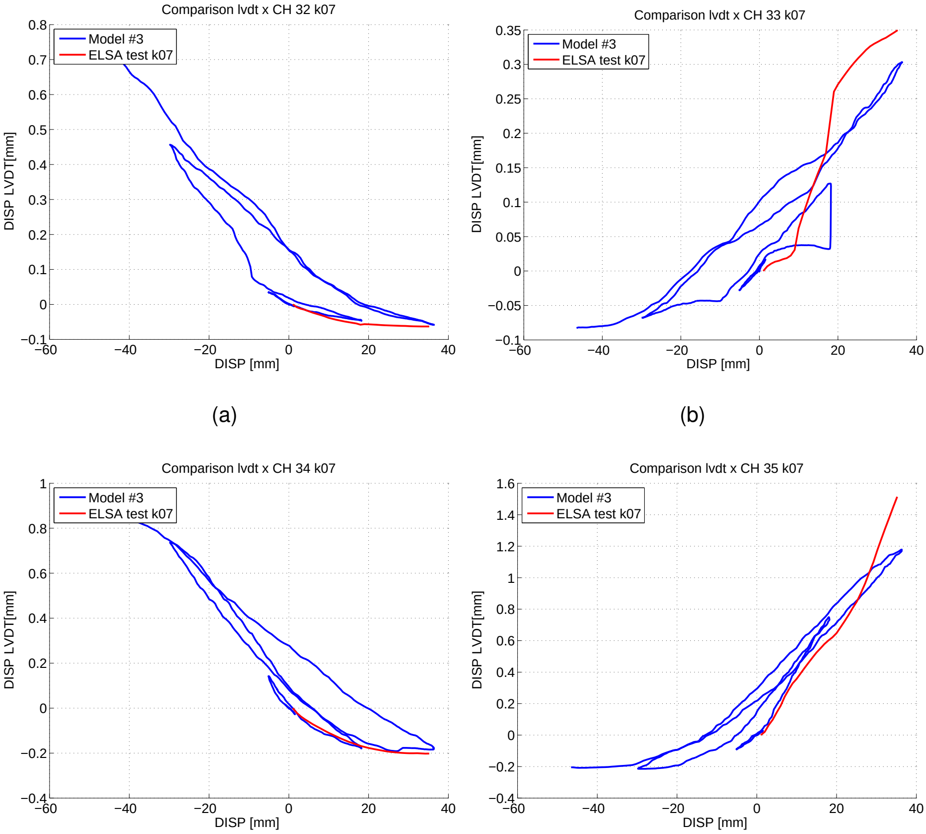

(a) (b)

(c) (d)

Figure 3.57: Comparison of local displacements on calibrated Model #3: a) channel 32; b) channel 33; c) channel 34; d) channel 35.

It resulted in the definition of nonlinear reduced models representing the NSs, which implicated additional numerical investigations to prove the effectiveness of the models choice. The final NSs setting has been reached passing through identification and optimization tools developed by interfacing different numerical/FE software. Furthermore, relevant to the structural degradation, the damage generated during tests has been taken into account by an offline model updating technique, the method allowed to update the parameters of NSs before starting each HSs test. Event though, the updating was devoted only to concrete parameters of PMCSI, the procedure has shown a considerable damage in the PSs gathered during the

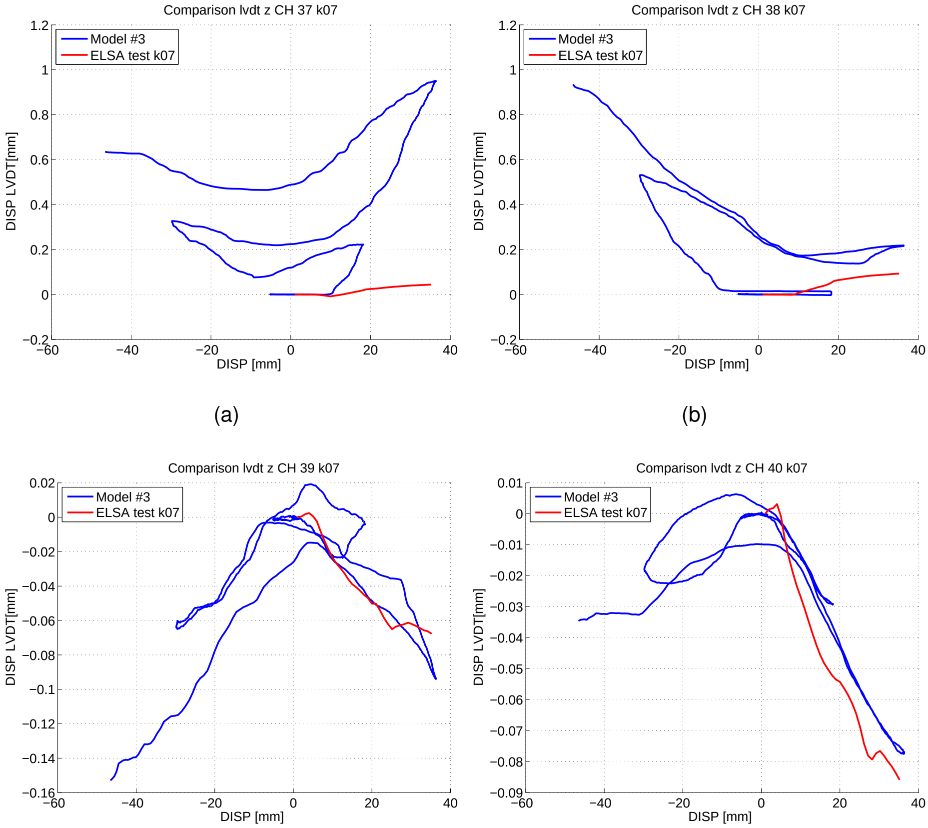

(a) (b)

(c) (d)

Figure 3.58: Comparison of local displacements on calibrated Model #3: a) channel 37; b) channel 38; c) channel 39; d) channel 40.

tests. In addition, the potential of DS has been exploited to solve the problems generated on CSBs due the slow speed of PDT procedure.

Finally, through the experimental campaign has been proven the effectiveness of the seismic CSBs based retrofitting system up to ULS earthquake. In fact when the isolated configuration has been tested piers remained in the elastic range for both SLS and ULS ground motions.

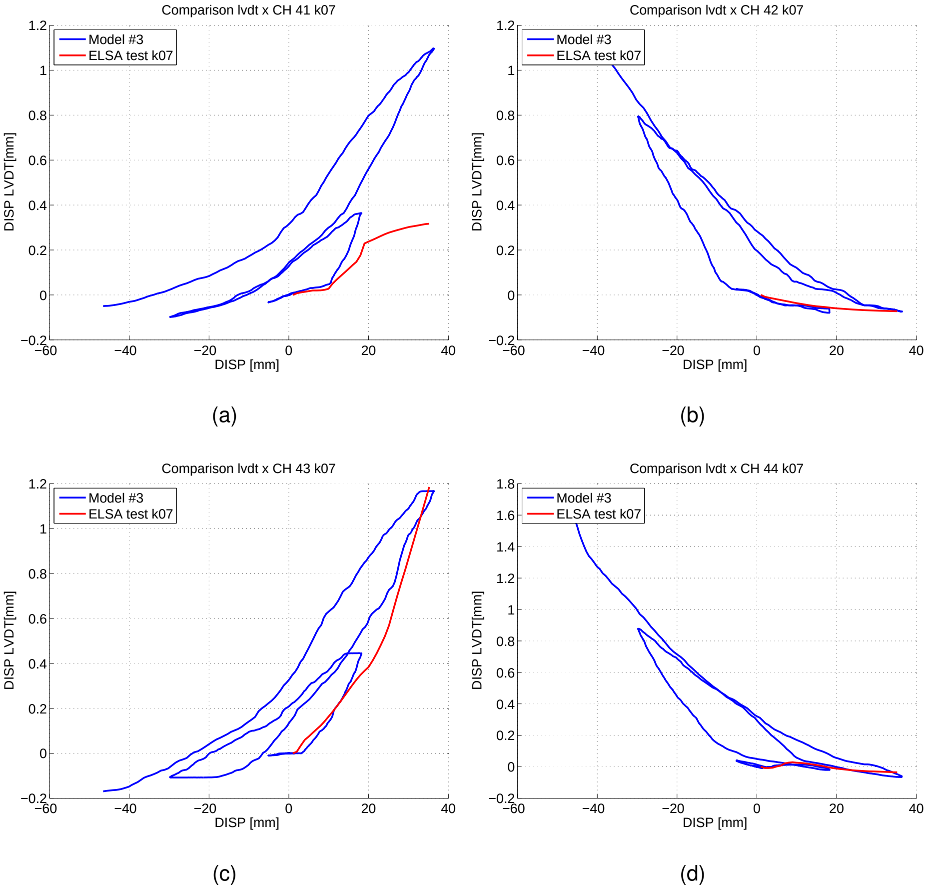

Figure 3.59: Comparison of local displacements on calibrated Model #3: a) channel 41; b) channel 42; c) channel 43; d) channel 44.

CHAPTER 4

# SEISMIC ASSESSMENT OF A REINFORCED CONCRETE BRIDGE BASED ON HYBRID SIMULATIONS - CASE STUDY II

## 4.1 Introduction

This chapter was developed within a collaboration between the University of Trento and the EUCENTRE TREES Laboratory of Pavia (Italy) in purpose to refine and develop the novelties introduced during RETRO project described in Chapter 3 and to test an innovative rate independent CSB device. In gretear detail, among the seismic assesment of the bridge, the objective of the collaboration was three fold: *i*) Test a prototype of CSB with an innovative rate indipendent behavior; *ii*) implement an online model updating based on UKF; *iii*) test a novel partitioned time integration first order scheme. Therefore, hereinafter, are reported the numerical and the experimental research activities aimed to reach these objectives.
The case study is a RC open section bridge continuous on three spans of 45 m supported by two twin hollow cross section concrete columns. A pair of novel CSBs were interposed among the deck and each pier and each abutment as a suitable seismic retrofitting scheme. An Opensees fiber-based PMCSII of the structure was implemented to support the design of the HSs based testing campaign. In grater detail, it was used to calibrate the reduced nonlinear state space models implemented for piers and CSBs. A Bouc-Wen spring (Ismail et al. (2009)) acted as NS of pier, whilst a Mostaghel bilinear state space model (Mostaghel (1999)) simulated the NSs of CSBs. In order to facilitate the inter operation between time integration and dynamic identification, a novel partitioned time integration scheme (Abbiati

(2014)) tailored to first order systems has been used and is quickly introduced. The use of this integration scheme allowed for the straightforward accommodation of the UKF as input/output dynamic identification tool. As a result, the parameters of the Bouc-Wen based S-DoF spring representing the numerical pier was identified and updated online on the basis of the physical pier response. The Eucentre dynamic Bearing Testing System (BTS) was used for the substructuring of one physical full scale CSB. The restoring force of the isolator pair was then obtained by doubling the corresponding measurements.

Therefore, in 4.2 the details of CSII and the PMCSI are presented. Then, in Section 4.3 is described the experimental campaign devoted to analyze transversal seismic actions with the description of substructures, i.e. NSs and PSs. Furthermore, the numerical compensation adopted during the tests to solve the problem of variation of yielding force on the CSBs due to friction coefficient variation is described in the same Section. The novel online model updating technique based on an UKF adopted to update the nonlinear parameters of the NSs to take into account the damage of the structural elements during the earthquake is presented in the same Section. After, in Section 4.4 is reported the improvement of FE models performed in the Opensees environment (Mazzoni et al. (2009)) to refine the PMCSII on the base of experimental data. It was performed by the application of SBM approach. Time history simulations with the improved PMCSII called (IPMCSII) have been used to compare the predictive and final numerical models, relevant results are presented in Section 4.5. Finally, in Section 4.6 are reported the main conclusions.

## 4.2 Description of Case Study II

The CSII is a fictitious RC bridge consisting of a 3 spans deck for a single independent roadways sustained by 2 twin cantilever rectangular hollow cross section piers, as shown in Figure 4.1. The deck was chosen with a geometry suitable for the existing RC 12.6 m high pier, property of EUCENTRE Laboratory shown in Figure 4.2. The open cross section of the deck has a depth of 6.7 m and it is appropriate for a 2-line urban way. The geometrical properties of the sections, i.e. pier and deck, are reported in Table 4.1. In detail, two concentric lines of $\phi$20 mm longitudinal rebars and five different positions of $\phi$12 mm stirrups represent the reinforcements of each pier section.

The CSB chose is a prototype of single sliding surface bearing. Thanks to the innovative sliding materials it guarantee an asymptotic friction coefficient for high load-rate. The radius of the device considered is equal to 3.1 m, the design friction coefficient ($\mu_{des}$) is equal to 8% and the initial yield displacement ($\delta_y$) is 1 mm. As a result, in perfect agreement with the maximum vertical load supported by the CSB, the complete set of dead loads in the serviceability condition drop on the pier a load equal to 4000 kN.

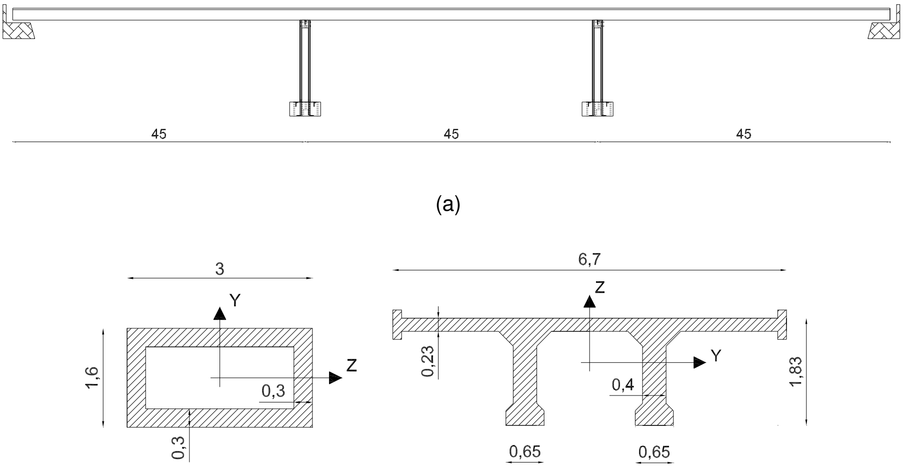

(a)

(b)

(c)

Figure 4.1: Details of Case Study II: a) lateral view of the bridge; b) cross section of pier; c) cross section of deck.

### 4.2.1 Seismic input

In order to fit with the requirements of the site of Naples the seismic input for these tests was chosen in the European Strong Motion Database. In greater detail it was chosen for soil category B with intervals of magnitude 5÷7 and epicentral distance between 0÷30 km. The selection of ground motions was performed by means of REXEL software (Iervolino et al. (2009)), assuming a lower and an upper bound of acceptable spectral acceleration relatively to the design spectrum. In

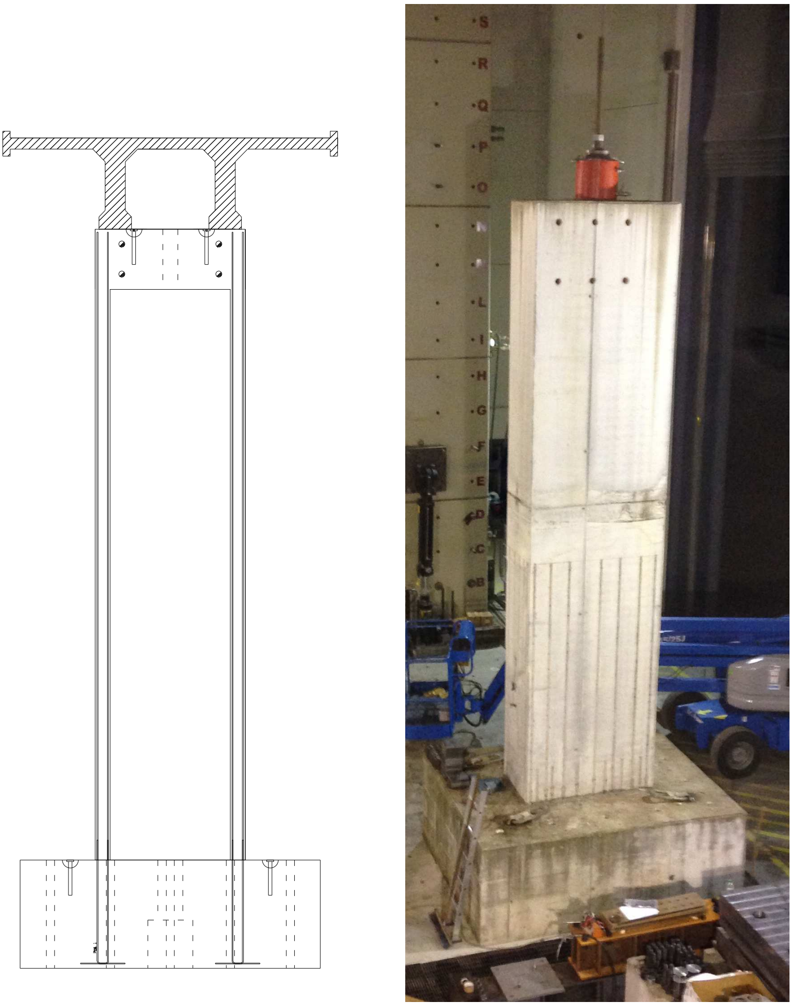

(a) (b)

Figure 4.2: View of Case Study II: a) drawing of the Pier with the deck; b) picture of the actual pier tested at the EUCENTRE TREES Laboratory.

Figures 4.3 and 4.4 are depicted the specra and the accelerograms of the selected ground motions for SLS and ULS.

|  | Deck | Pier |
|---|---|---|
| **H** | 1.83 m | 1.60 m |
| **B** | 6.70 m | 3.00 m |
| **A** | 2.78 $m^2$ | 2.40 $m^2$ |
| **Iz** | 7.20 $m^4$ | 0.82 $m^4$ |
| **Iy** | 0.85 $m^4$ | 2.40 $m^4$ |

Table 4.1: Geometrical properties of the cross sections

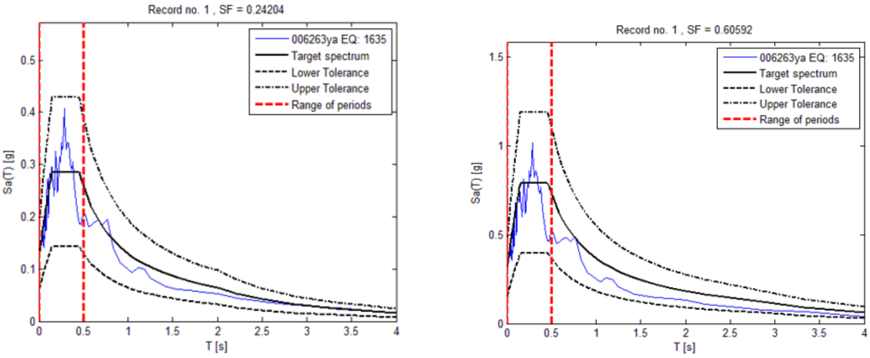

(a)

(b)

Figure 4.3: Spectra of the selected accelerograms: a) SLS; b) ULS.

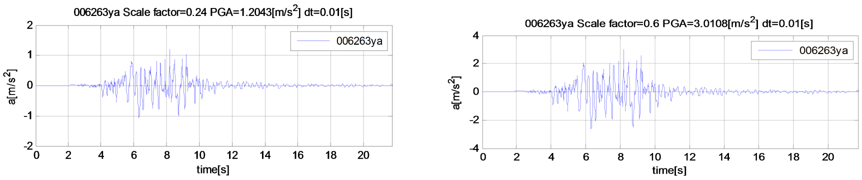

(a)

(b)

Figure 4.4: Accelerograms selected: a) SLS; b) ULS.

### 4.2.2 Predictive FE model of Case Study II

In order to implement continuous PDT, a PMCSII was implemented in the Opensees environment (Mazzoni et al. (2009)). Linear beam elements were selected to model the deck, whilst fiber-based nonlinear elements were considered for the piers; translational DoFs of both abutments were fixed whilst rotations released. Nonlinear fiber-based beam elements allowed for an accurate discretization of cross sections as well as for positions and dimensions of rebars. The offset between the pier cap and the deck gravity center has been considered by means of rigid links, as shown in Figure 4.5.

The appropriate materials were implemented on the basis of a previous experimental campaign on the considered 1:2 scale mock-up specimen of Pier #1, in which QSCTs were performed (Peloso and Pavese (2009)). Since have been used rough steel rebars, the contribution of the concrete tensile strength was considered. Therefore, the *Concrete*02 material of Opensees, was employed to simulate concrete behavior with the constitutive law depicted in Figure 4.6. In detail, it was assumed a the maximum concrete strength $f_{cm}$ = 55MPa with a corresponding deformation $\varepsilon_{c0}$ = 0.4%; an ultimate concrete strength $f_{cu}$ = 44MPa with a relevant deformation $\varepsilon_{cu}$ = 0.6% and finally a tensile strength $f_t$ = 5.5MPa. Rebars were represented by the *Steel*02 material, shown in Figure 3.9(b) with $f_y$ = 525MPa, along with $E$ = 200000MPa and hardening ratio $\frac{Ep}{E} = 0.015$. As a result, in agreement with the assumptions adopted, the periods of the first five modes of vibration of the bridge in the non isolated configuration are reported in Table 4.2.

CSB devices were implemented in Opensees software by using SFPBOE with nominal radius, friction coefficient and yielding slip equal to 3.1 m, 8% and 1 mm, respectively. SFPBOE embed a physical model that replicates the slip mechanism

| **PMCSII** | |
|---|---|
| **Mode** | **Period [s]** |
| **#1** | 0.639s |
| **#2** | 0.500s |
| **#3** | 0.392s |
| **#4** | 0.344s |
| **#5** | 0.320s |

Table 4.2: Periods of vibration of the PMCSII

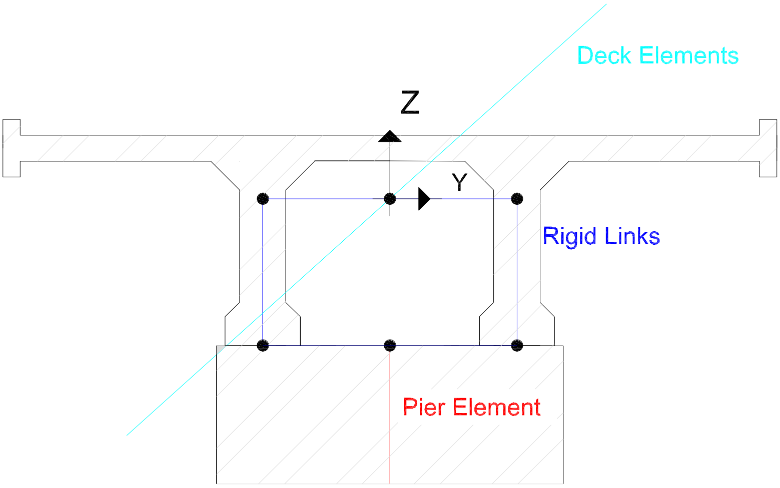

Figure 4.5: Modelling of the deck-pier connection by means of rigid links.

of CSB isolation devices as shown in Figure 3.11. Mono directional time history

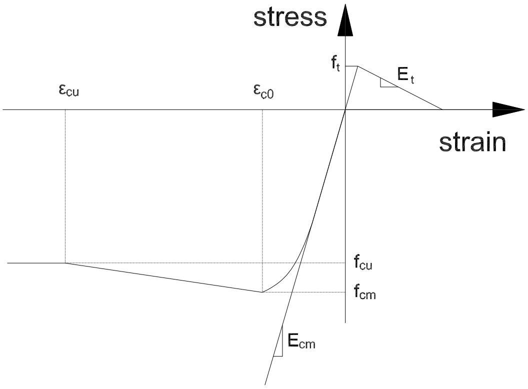

Figure 4.6: Constitutive law of *Concrete*02 Opensees material.

simulations were performed in the range 0.12-0.9g of PGA by the application of the seismic input in the traversal direction of the deck, in agreement with the direction of the HSs. As can be appreciated in Figure 4.7, the seismic response in the non isolated configuration showed a linear elastic response for the SLS earthquake. A reduced damage was recorded during the ULS simulation. The strongest simula-

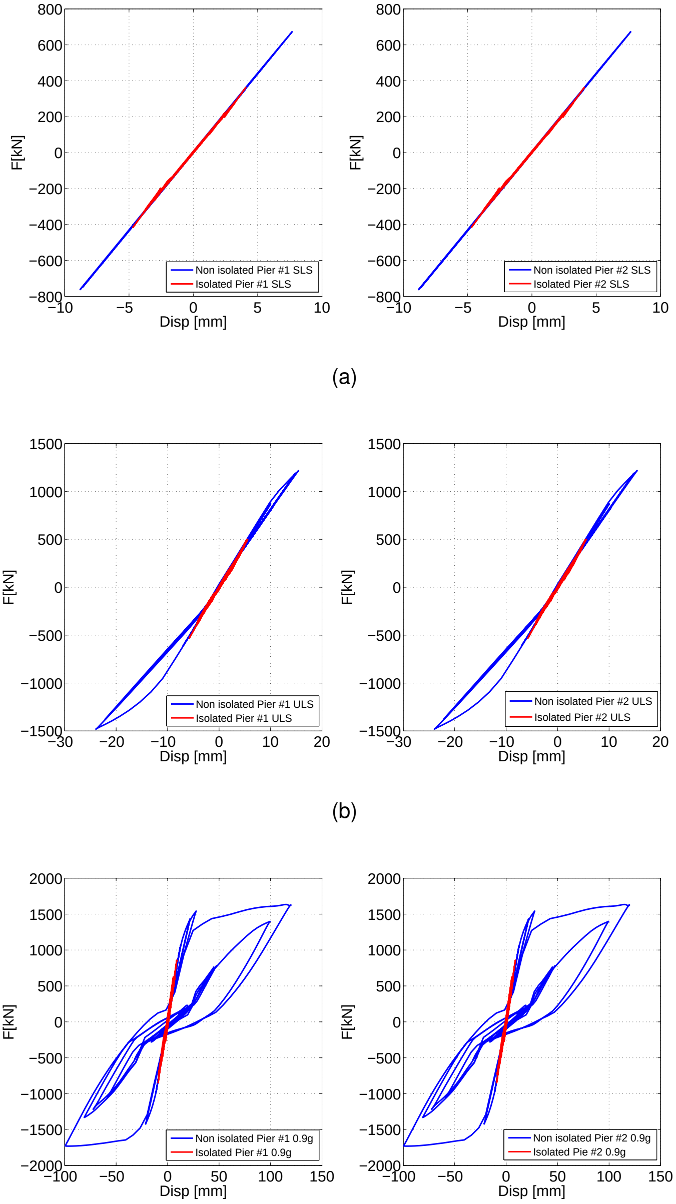

(a)

(b)

(c)

Figure 4.7: Numerical results of PMCSII: a) PGA of 0.12g (SLS); b) PGA of 0.3g (ULS); c) PGA of 0.9g.

tion with PGA equal to 0.9g has shown a wide damage pattern that correspond to the generation of a plastic hinge on the piers base. The simulations relevant to the isolated case, showed the benefit of the CSBs based system, in fact the pier response remained in the elastic range for all the intensities considered, i.e. SLS, ULS and 300% ULS.

The PMCSII was used to set the simplified models for the design of the numerical substrucure of the HSs. The same procedure described in Section 3.3 and Figure 3.26 has been adopted.

## 4.3 Experimental campaign

The scheme of the test setup implemented at the EUCENTRE TREES Lab, evolution of a previously implemented HS testing system Lanese (2012), is shown in Figure 4.8. Both time integrator and UKF were implemented in the xPC Target MATLAB (2012). The MTS standard (for the Pier#1 actuator) and customized (for the CSB) controllers are used as secondary inner-loop control to impose the calculated displacement to the specimen and measure corresponding restoring forces. The xPC Target and MTS controller communicate via analogical signals. The numerical domain, representing the NSs set was composed by the whole bridge, one pier and the relevant CSBs. The PSs set was composed by the RC pier and the

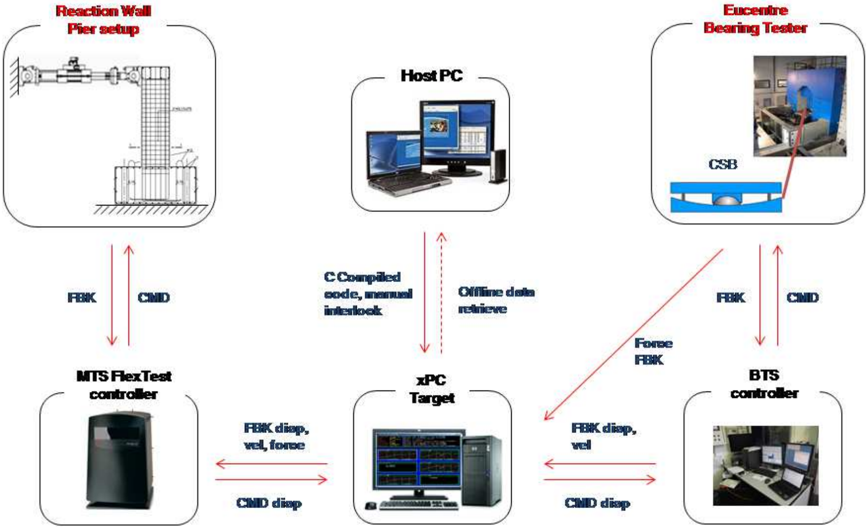

Figure 4.8: EUCENTRE TREES Lab hybrid simulation system scheme.

relevant CSBs doubled numeircally during the tests.

Figure 4.9 depicts the schemes of both the non isolated and the isolated global reduced models of CSII. As can be appreciated from Figure 4.9, Pier #1 was substructured in the laboratory together with the related CSBs.

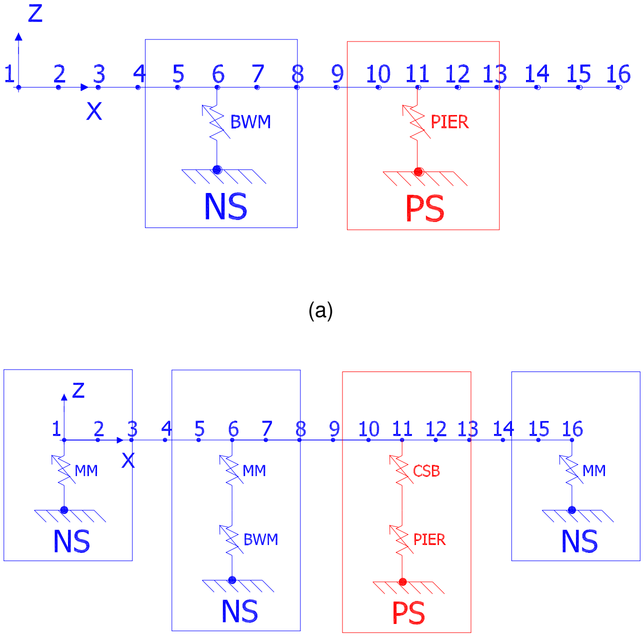

(a)

(b)

Figure 4.9: Substructuring scheme of Case Study II: a) non isolated configuration; b) isolated configuration.

### 4.3.1 Partitioned time integrator algorithm

Since the same Bouc-Wen model was used for both the simulation of the NS of pier and the dynamic identification of the physical pier, a partitioned time integrator tailored to first order system was selected. Therefore, the following semi-discretized equation of motion describe the problem:

$$M\dot{y} + G(y) = F(t) \tag{4.1}$$

with

$$y = \begin{bmatrix} x \\ \dot{x} \end{bmatrix} \tag{4.2}$$

$$M = \begin{bmatrix} I & 0 \\ 0 & m \end{bmatrix} \tag{4.3}$$

$$G(y) = \begin{bmatrix} -I \\ r \end{bmatrix} \tag{4.4}$$

$$F(t) = \begin{bmatrix} 0 \\ f(t) \end{bmatrix} \tag{4.5}$$

In detail, I is the identity matrix, whilst r is the generic nonlinear restoring force vector and m is the mass matrix of the system; x and $\dot{x}$ are displacement and velocity state components, and f(t) is the external load. In the case of hysteretic restoring force models, the state vector can be easily extended to accommodate additional memory variables. In order to embed favorable user-controlled algorithmic, a Modified version of G-$\alpha$ was considered as basic monolithic integrator for the development of a novel partitioned time integration scheme for hybrid systems (Abbiati (2014)). The algorithm relies on velocity-like quantities $v_n$ that consist of low-pass filtered $\dot{y}_n$. As a result, the state vector is extended to embed both discretized state variables $y_n$ and velocity-like quantities $v_n$. The following equations summarize the time integration procedure of the Modified version of G-$\alpha$ method:

$$M\dot{y}_{n+1} + G(y_{n+1}) = F_{n+1} \tag{4.6}$$

$$y_{n+1} = y_n + v_n(1-\gamma)\Delta t + v_{n+1}\gamma\Delta t \tag{4.7}$$

$$(1-\alpha_m)v_n + \alpha_m v_{n+1} = (1-\alpha_f)\dot{y}_n + \alpha_f \dot{y}_{n+1} + o(\Delta t^2) \tag{4.8}$$

This algorithm is equivalent to its progenitor, i.e. the G-$\alpha$, in terms of stability, accuracy and spectral properties, but is amenable to hybrid implementations.
The coupling scheme of the Modified PH method proposed by Brun et al. (2014) was adopted. As well as its progenitor, the proposed algorithm is prone to parallel implementations, where free problems advance simultaneously on both subdomains. The task sequence of the Modified PH-method was completely inherited and is depicted in Figure 4.10.

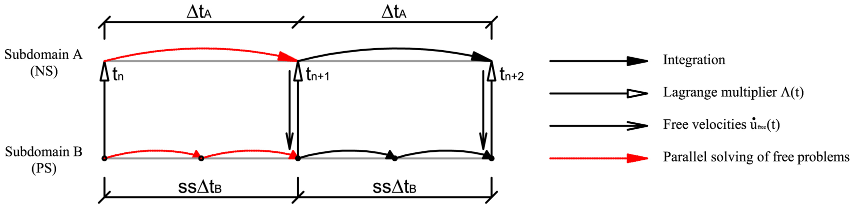

Figure 4.10: Task sequence of the Modified PH-MG-$\alpha$ method.

A coarse time step $\Delta t_A$ was applied to Subdomain A, whilst a fine time $\Delta t_B$ to Subdomain B. Since the link problem is solved at coarse time steps only, interpolated free quantities of Subdomain A are not needed to advance in the solution on Subdomain B. With regard to HSs , Subdomain B always refers to the PS, where displacement commands are generated at the controller rate. Conversely, Subdomain A refers to the NS, which needs more computational resources and thus larger solving times. Accordingly, discretized coupled equations of motion read,

$$\begin{cases} M_A \dot{Y}^A_{SS} + G_A(Y^A_{SS}) + L_A \Lambda_{SS} = F^A_{SS} \\ M_B \dot{Y}^B_k + G_B(Y^B_k) + L_B \Lambda_k = F^B_k \\ B_A \dot{Y}^A_{SS} + B_B \dot{Y}^B_{SS} = 0 \end{cases} \tag{4.9}$$

where $k = [1, 2, , SS]$ and the subcycling parameter SS is defined as $\frac{\Delta t_A}{\Delta t_B}$. Boolean matrices $L^m$ and $B^m$ localize Lagrange multipliers as interface loads and coupling DoFs, respectively. In order to preserve the stability of underlying monolithic integrators, the compatibility was force on state variable rates, which physically correspond to interface velocities. Accordingly $L^{m^T} = [(0^T \; I^{m^T})]$ and $B^m = [(I^{m^T} \; 0)]$, where $I^m$ is a row-wise Boolean matrix that collocates all interface DoFs on the subdomain m-th. At each coarse time step $\Delta t_A$, the equation of motion of both subdomains are solved independently. Refer to Abbiati et al. (2014) for a detailed description of the solution procedure.

### 4.3.2 Physical substructure for pier

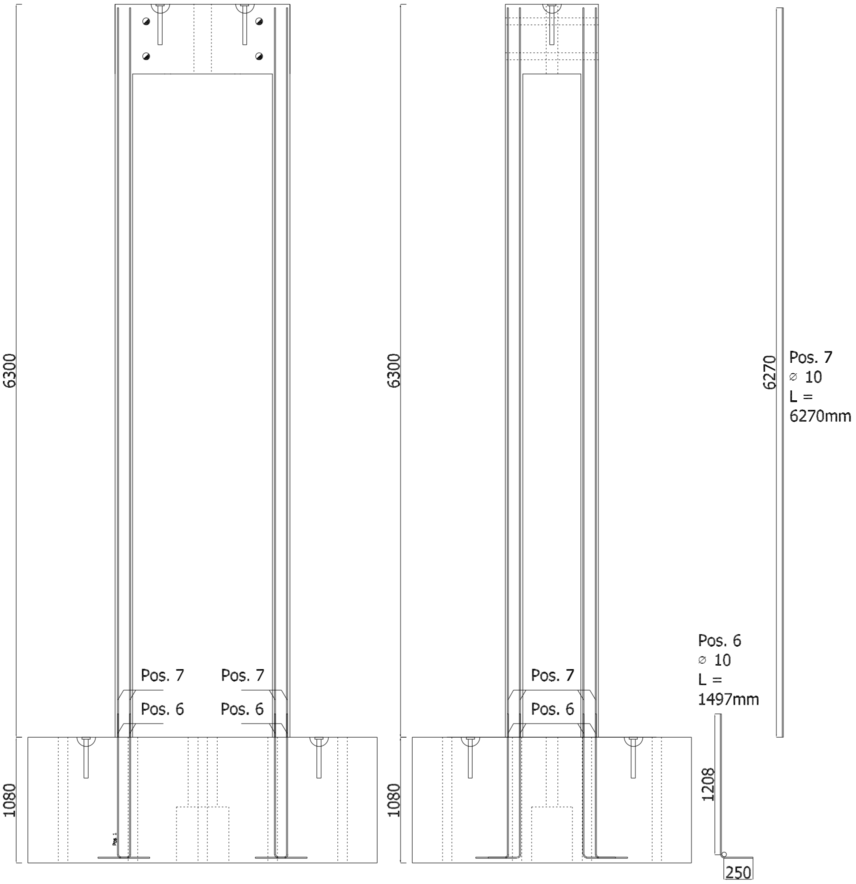

Figure 4.11: Global view of the scaled pier.

A 1:2 scale specimen of one pier has been realized and used as PS. As depicted in Figures 4.11 and 4.12 all the geometrical quantities of the actal full-scale pier have been halved. The scaling included both global dimensions and reinforcements, in fact the full scale rebars and stirrups have been modified and became,

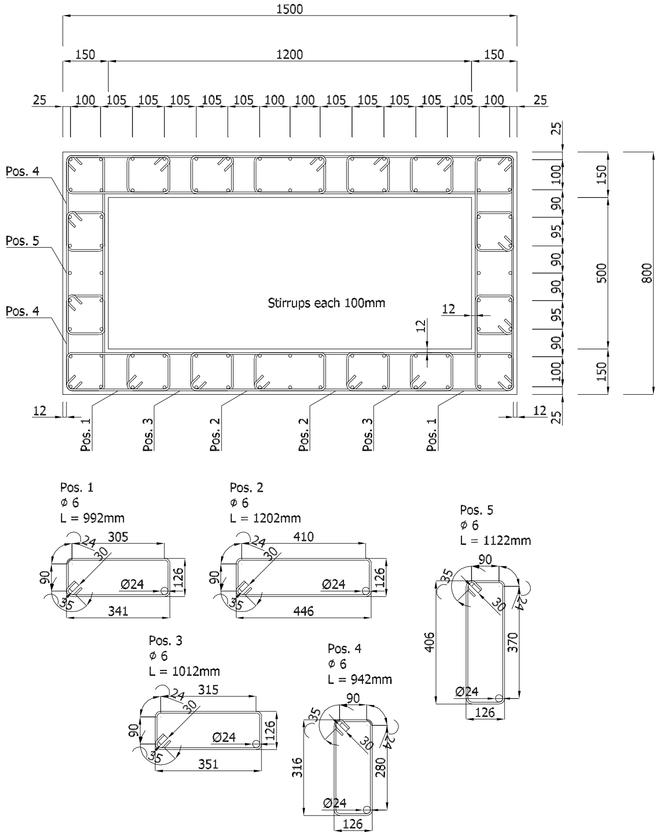

Figure 4.12: Scaled pier cross section.

$\phi$10 mm and $\phi$6 mm for longitudinal rebars and stirrups, respectively.

As shown in Figure 4.14(a), The RC Pier#1 was fully restrained at the base by 14 Diwidag post-tensioned $\phi$42 steel bars, while a pin-connection was realized between horizontal actuator and pier cap. The horizontal load has been applied through a 1000 kN dynamic actuator, acting on a post-tensioned system made of two 150 mm thick steel plates positioned on the two sides of the pier cap in the direction of motion (4.14(b)).

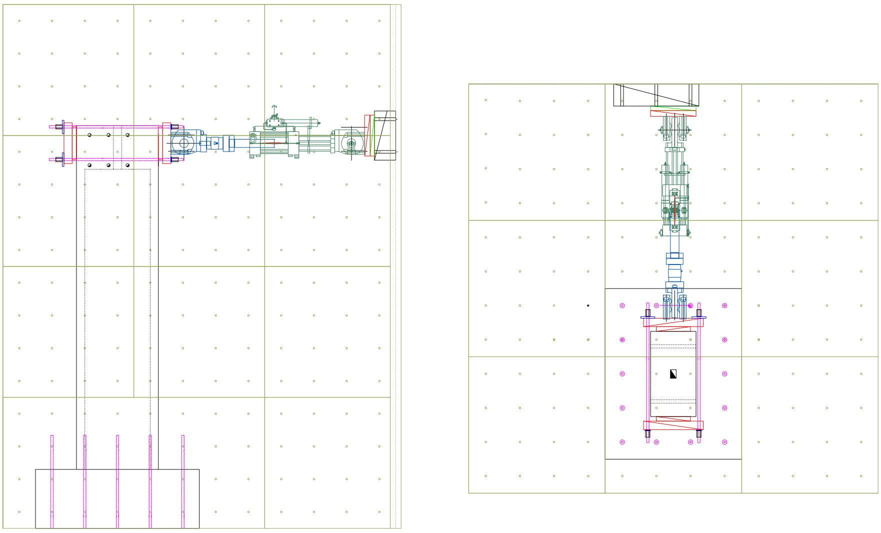

(a) (b)

Figure 4.13: View of the pier PS

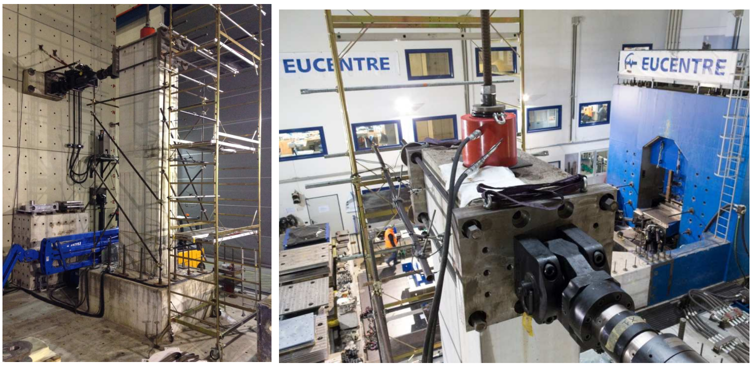

(a) (b)

Figure 4.14: RC Pier#1 test setup

### 4.3.3 Physical substructure for concave sliding bearings

Since the scaling of CSBs produces distortions, because of the modified surface radius, the non-uniform contact pressure, etc., a full-scale specimen was considered. The vertical load due to the self-weight of the bridge deck was kept constant and equal to 2000 kN, while horizontal and vertical displacements, univocally related by the surface curvature, are imposed with the EUCENTRE TREES Lab BTS (Peloso and Pavese (2009)). During open loop tests, the raw shear force of the specimen is measured from horizontal actuators, and then processed afterwards to remove the machine inertia and friction to obtain the device response. This procedure is not compatible with the hybrid simulation requirements, where the restoring force of the specimen has to enter the time integration loop step by step. To this end, a dedicated new restoring force measurement system has been realized as shown in Figure 4.15. The system is made of a steel plate laying on a Teflon layer and surrounded by 8 ring-shaped load cells; because of the negligible friction force at the base, the pre-stressed compression cells directly give the specimen restoring force in two orthogonal plane directions. As result, all the geometrical quantities of the CSB were the same as the design full scale prototype. In Figure 4.16 are shown a view of CSB itself and the same device positioned in the BTS at EUCENTRE ready to be tested.

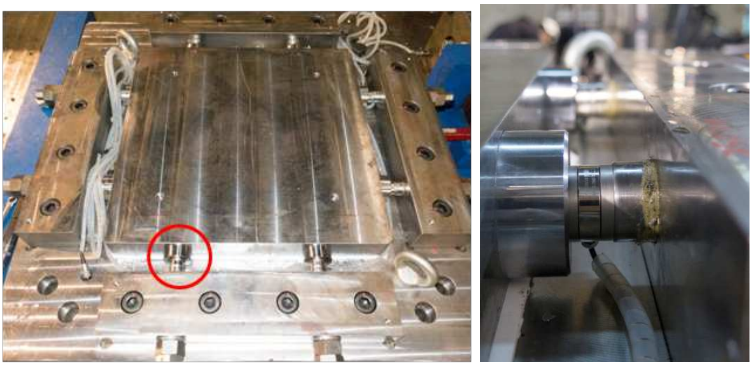
(a) (b)

Figure 4.15: CSB direct measurement load cell

### 4.3.4 Numerical substructure for pier

An ANSYS Simplified Model of CSII (ANSYSSMCSII) has been implemented to obtain the mass and stiffness matrix for the tests, the model was a modified version of PMCSII. In detail, it was composed by 20 nodes and 17 elements as

(a) (b)

Figure 4.16: View of the CSB: a) CSB during positioning phase; b) CSB positioned under the BTS.

shown in Figure 4.17. In particular the system of rigid links implemented in PMCSII was reduced to a simple connection based on coupled DoFs command between two nodes, i.e. 6-17 and 11-19.

The identification procedure was similar to the one adopted to analyze CSI and

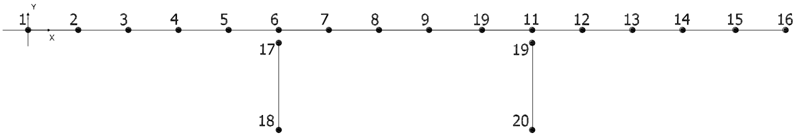

Figure 4.17: View of the simplified model.

it was based on the comparison between S-DoF springs and numerical results of PMCSII, with the same procedure shown in Figure 3.26. In grater detail, a linear deck was assumed whilst the nonlinear restoring force owing to the lateral displacement of each single pier was simulated by means of the well-known Bouc-Wen model (Ismail et al. (2009)).

Firstly, a linear reduction was performed by the Guyan method (Guyan (1965)) to evaluate the reduced parameter for the linear response. Then, the nonlinear Bouc-Wen model based spring was implemented to simulate the nonlinear behavior of the piers when subjected to strong earthquakes. The formulation of the hysteretic

| **Pier** | $\mathbf{K^r[N/m]}$ | $\mathbf{M^r[kg]}$ |
|---|---|---|
| **#1** | $9.15 \cdot 10^7$ | $3.67 \cdot 10^4$ |

Table 4.3: Parameters for the linear reduced model of the pier by the Guyan method

restoring force in differential form reads,

$$r = \int_0^t \dot{r} d\tau \tag{4.10}$$

$$\dot{r} = [A - (\beta sgn(\dot{x}r) + \gamma) \mid r \mid^n]\dot{x} \tag{4.11}$$

where $\beta$, $\gamma$ and n are model parameters, whilst $\dot{x}$ and $\dot{r}$ are the velocity and the restoring force rate, respectively. It can be appreciated the difference with the reduced model adopted in CSI, in this one the degradation of the linear stiffness was not considered with a dedicated coefficient. The identification pre test, used as a starting setting updated by means of UKF, was based on the NRMSE introduced in equation 3.3.2, in detail the minimization of the error between the numerical response of PMCSII and the S-DoF have been performed. The identification involved the nonlinear parameters k, and $\gamma$; conversely, $n$ was set to constant and equal to 1. In Table 4.4 are reported the initial values that were updated by the UKF based online updating procedure.

| | **SLS** | | |
|---|---|---|---|
| **Pier** | $\mathbf{A[\frac{N}{mm}]}$ | $\beta$ | $\gamma$ |
| **#1** | $9.15 \cdot 10^7$ | 1 | 40 |

Table 4.4: Nonlinear parameters for the reduced models of the pier identified by NRMSE

### 4.3.5 Numerical substructure for concave sliding bearings

The state space model proposed by Mostaghel (1999) was selected for reproducing the DS of isolator elements. The expression of the nonlinear restoring force of a nondegenerating bilinear element is given in Subsection 3.3.3. Parameters $\alpha$, k, and $\delta$ were tuned based on the characterization tests performed at the EUCENTRE laboratory before the HSs campaign and presented in Subsection 4.3.6. As a results, the parameters identified by NRMSE are: $\alpha$ = 0.0045, $k = 150136\frac{N}{mm}$, $\delta = 0.73mm$. The response of the paired CSB devices is represented by one single full-scale CSB, considering a constant vertical load representative of the average conditions of the isolation system.

### 4.3.6 Friction coefficient and test velocity - Solution II

One of the objective of the project was to test an innovative CSB device with an asymptotic behavior in terms of friction coefficient and load rates. Because of the prototype condition of the CSB device several experimental tests have been performed as reported in Table 4.5. In Figures 4.18(a), 4.18(b), 4.18(c) are depicted the results of some tests performed at different load rate. Then, in Figure 4.18(d) the variation of $\mu$ with the load rate, as can be appreciated for high speeds the behavior become asymptotic to the design value of 8%. Even thought the asymptotic behavior, some issues related to low speed of the PDT still remain. The asymptotic behavior was proven for large load rates but showed a significative variation of it for small load rates. In these condition the problem is the opposite of CSI, in fact during test friction coefficient $\mu_{test}$ resulted to be smaller than the design value. In light of this, to compensate the velocity effect on the CSB, the following equation was considered to modify the restoring force recorded by the load cell positioned on the isolator before sending it to the algorithm:

$$F_{ALG} = F_H \frac{\mu_{des}}{\mu_{test}} - \frac{F_V D_H}{R_{eq}} \left(\frac{\mu_{des}}{\mu_{test}} - 1\right) \tag{4.12}$$

where $F_{ALG}$ is the CSB restoring force computed and sent to the algorithm, $F_H$ is the horizontal restoring force of the CSB, $F_V$ is the vertical load on the CSB, $\mu_{des}$ is the design friction coefficient equal to 8%, $\mu_{test}$ is the friction coefficient at test

| **Test name** | **Amplitude [m]** | **Load rate [$\frac{m}{s}$]** | **Frequency [Hz]** | **Vertical load [MN]** | $\mu$ [%] |
|---|---|---|---|---|---|
| **ciso25** | ±0.050 | 0.001 | 0.005 | 2 | 4.3 |
| **ciso26** | ±0.050 | 0.005 | 0.03 | 2 | 5.7 |
| **ciso27** | ±0.050 | 0.010 | 0.05 | 2 | 6.3 |
| **ciso28** | ±0.100 | 0.020 | 0.05 | 2 | 6.9 |
| **ciso29** | ±0.100 | 0.050 | 0.13 | 2 | 7.5 |
| **ciso30** | ±0.100 | 0.100 | 0.25 | 2 | 7.9 |
| **ciso31** | ±0.100 | 0.200 | 0.50 | 2 | 8.0 |

Table 4.5: Characterization tests on CSBs performed at the EUCENTRE TREES Laboratory.

velocity in this case equal to 6%, $D_H$ is the horizontal displacement of the CSB, and $R_{eq}$ is the CSB equivalent radius.

### 4.3.7 Model updating online based on a Unscented Kalman Filter

As anticipated, another great advantage of partitioned time integration is that the algorithm provides the interface Lagrange multiplier set at each time step. This means that both input and output loads acting on each subdomain are available. Accordingly, the implementation of any input/output identification tools aimed at characterizing the parameter of a single subdomain is straightforward. In the present implementation, the seismic load acting of the condensed physical pier was moved to the deck. In this way, the original dynamics of the bridge was preserved, but Lagrange multipliers were the unique load acting on the physical pier. The presented approach is very suitable for accommodating gray box identification tools (Ljung (1999)), where both the model structure and input and output quantities are available, as depicted in Figure 4.19. In fact, Lagrange multipliers $\Lambda_k$ completely characterize the input load acting on the subdomain B. As a result, the UKF was selected in this particular case (Wu and Smyth (2007)).

In greater detail, UKF is the result of an evolution of estimation methods, initially

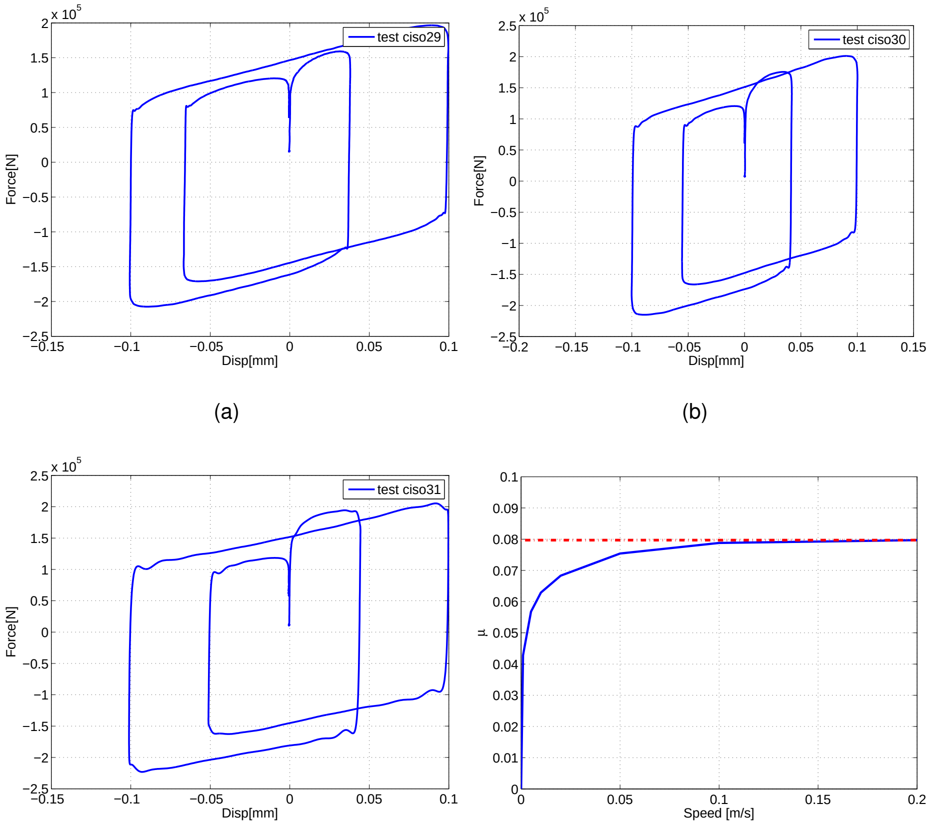

(a) (b)

(c) (d)

Figure 4.18: Characterization tests on CSBs: a) ciso29; b) ciso30; c) ciso31; d) asymptotic behavior of CSB prototype.

Kalman (1960) proposed the Kalman Filter, a filter for the estimation of state of stochastic linear systems based on the addition of Gaussian noise to processes and estimation. Successively Mariani and Corigliano (2005) extended the filter to take in to account nonlinearties based on the linearization of nonlinear function (Extended Kalman Filter (EKF)). Finally, since the EKF suffered limitations in term of nonlinear estimation, Julier et al. (1995) introduced the UKF. The innovation was the modification of the linearization process. In fact in the UKF, the evolution of a state variable is approximated with a Probability Density Function (PDF) of the state variable itself. Superior accuracy of the UKF compared to the EKF drives the decision for the estimation filter. Detailed comparative studies of the recursive

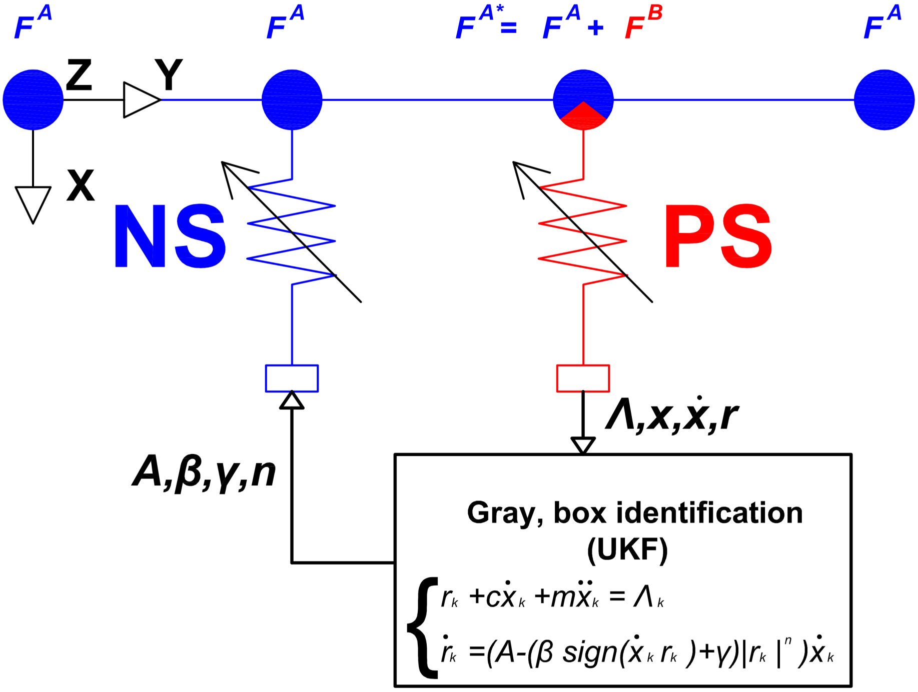

Figure 4.19: Details about UKF implementation.

Bayesian filters are presented in Azam (2014).

Within the scope of the HSs, the objective was online and real-time estimation of states and parameters of the physical pier for providing input for the numerical part of the test. In greater detail, the procedure can be generalized considering the non-linear state-space model reported hereinafter (Wan and Van der Merwe (2000)), which represents the dual estimation problem:

$$z_{k+1} = F(z_k, \theta_k, v_k) \tag{4.13}$$

$$y_{k+1} = H(z_k, n_k) \tag{4.14}$$

$F$ denotes a function of the state $z_k$ and model parameters $\theta_k$ to obtain $z_{k+1}$. $H$ represents the state and the observable part of the system, at any given time instant. $v_k$ and $n_k$ are zero mean uncorrelated Gaussian processes. In the case of CSII restoring force and displacement of the PS are observed quantities. Lagrange multipliers are the loading term.

The aim of the UKF, beyond estimating hidden part of the state vector, would be the calibration of system model parameters in an online fashion. Based on the information contained in the latest observation $y_{k+1}$, the algorithms update previous knowledge of the parameter $\theta_k$ to obtain $\theta_{k+1}$. To accomplish this goal, the parameter vector $\theta_{k+1}$ is augmented into the state vector $x_{k+1} = [z_{k+1} \ \theta_{k+1}]^T$, and the following process equation is added to the initial set of state-space equations:

$$\theta_{k+1} = \theta_k + v_k^{\theta} \tag{4.15}$$

The main notion behind this extra equation is to allow variations of the unknown parameters of the system in time, so that by starting from an initial guess the estimates converge into an unbiased estimate. The variations of the parameter vector over time is facilitated via an additive white Gaussian fictitious noise $v_k^{\theta}$ to parameter evolution; the intensity of such a noise should be appropriately adjusted, for obtaining accurate estimates. The state-space equation governing evolution of the augmented state reads:

$$x_{k+1} = F(x_k, v_k) \tag{4.16}$$

$$y_{k+1} = H(x_k, n_k) \tag{4.17}$$

The algorithm of UKF, implemented adopting the unscented transformation (Eftekhar Azam et al. (2012), Wan and Van der Merwe (2000)), is reported hereinafter:

1. Initialize with:

$$\hat{x}_0 = E[x_0] \tag{4.18}$$

$$P_0 = E[(x_0 - \hat{x}_0)(x_0 - \hat{x}_0)^T] \tag{4.19}$$

$$\hat{x}_0^a = E[x^a] = \begin{bmatrix} \hat{x}_0^T & 0 & 0 \end{bmatrix}^T \tag{4.20}$$

$$P_0^a = E[(x_0^a - \hat{x}_0^a)(x_0^a - \hat{x}_0^a)^T] = \begin{bmatrix} P_0 & 0 & 0 \\ 0 & P_v & 0 \\ 0 & 0 & P_n \end{bmatrix} \tag{4.21}$$

2. For $k = 1, ...., N_{tstep}$

- Calculate Sigma Points:

$$\chi_{k-1}^a = \left[\hat{x}_{k-1}^a \quad \hat{x}_{k-1}^a \pm \sqrt{(L+\lambda)P_{k-1}^a}\right] \tag{4.22}$$

- Time Update:

$$\chi_{k|k-1}^x = F[\chi_{k-1}^x, \chi_{k-1}^v] \tag{4.23}$$

$$\hat{x}_k^- = \sum_{i=0}^{2L} W_i^{(m)} \chi_{i,k|k-1}^x \tag{4.24}$$

$$P_k^- = \sum_{i=0}^{2L} W_i^{(c)} [\chi_{i,k|k-1}^x - \hat{x}_k^-][\chi_{i,k|k-1}^x - \hat{x}_k^-]^T \tag{4.25}$$

$$\Upsilon_{k|k-1} = H[\chi_{k|k-1}^x, \chi_{k-1}^n] \tag{4.26}$$

$$\hat{y}_k^- = \sum_{i=0}^{2L} W_i^{(m)} \Upsilon_{i,k|k-1} \tag{4.27}$$

- Measurement update Equations:

$$P_{\tilde{y}_k, \tilde{y}_k} = \sum_{i=0}^{2L} W_i^{(c)} [\Upsilon_{i,k|k-1} - \hat{y}_k^-][\Upsilon_{i,k|k-1} - \hat{y}_k^-]^T \tag{4.28}$$

$$P_{x_k, y_k,} = \sum_{i=0}^{2L} W_i^{(c)} [\chi_{i,k|k-1} - \hat{x}_k^-][\Upsilon_{i,k|k-1} - \hat{y}_k^-]^T \tag{4.29}$$

$$K = P_{x_k, y_k} P^{-1}_{\tilde{y}_k, \tilde{y}_k} \tag{4.30}$$

$$\hat{x}_k = \hat{x}^-_k + K(y_k - \hat{y}^-_k) \tag{4.31}$$

$$P_k = P^-_k - K P_{\tilde{y}_k, \tilde{y}_k} K^T \tag{4.32}$$

- Implementation of updated parameters in NSs

where:

- $\lambda$ is a scaling parameters:

$$\lambda = \alpha^2 (L + \kappa) - L \tag{4.33}$$

- L is the dimension of the augmented state
- $P_v$ is the process noise covariance
- $P_n$ is the measurement noise covariance
- $\chi_i$ sigma vectors evaluated as follows:

$$\chi_0 = \bar{x} \tag{4.34}$$

$$\chi_i = \bar{x} + (\sqrt{(L + \lambda) P_x})_i \qquad i = 1, ..., L \tag{4.35}$$

$$\chi_i = \bar{x} - (\sqrt{(L + \lambda) P_x})_i \qquad i = 1, ..., 2L \tag{4.36}$$

with $\bar{x}$ and $P_x$ mean and covariance of random variable x.

- $W_i$ weigths evaluated as follows:

$$W_0^m = \frac{\lambda}{L + \lambda} \tag{4.37}$$

$$W_0^c = \frac{\lambda}{L + \lambda} + 1 - \alpha^2 + \beta \tag{4.38}$$

$$W_i^m = W_i^c = \frac{1}{2(L + \lambda)} \qquad i = 1, ..., 2L \tag{4.39}$$

In this particular case a Bouc-Wen model was used to identify the pier response and to simulate the numerical one. As a result Equations 4.16 and 4.17 were defined as:

$$r + c\dot{x} + m\ddot{x} = \Lambda \tag{4.40}$$

$$\dot{r} = [A - (\beta sgn(\dot{x}r) + \gamma) \mid r \mid^n]\dot{x} \tag{4.41}$$

$$\theta = A \tag{4.42}$$

### 4.3.8 Outcomes of hybrid simulations

The main results of the experimental campaign are summarized hereinafter. In this respect, Table 4.6 reports the list of main tests and related substructures settings. As can be appreciated, in order to validate the implementation, first, low PGA level tests were conducted in the isolated configuration, i.e. HE 49. The structural behavior is clearly linear due to the small seismic load, in fact the maximum displacement is approximately 3 mm. Then, three tests have been performed in the non isolated configuration from 0.25 to 0.75 g of PGA levels. As shown in Figures 4.21 and 4.22 test HE 51 and HE 52 did not produce considerable damage whilst test HE 53 damaged considerably the pier. In order to prove the effectiveness of

| Test Name | Configuration | Time Scale $\lambda$ | PGA [g] | PS |
|---|---|---|---|---|
| HE 49 | ISOLATED | 256 | 0.03 | *Pier#1* + *Iso#1* |
| HE 51 | NON ISOLATED | 128 | 0.25 | *Pier#1* |
| HE 52 | NON ISOLATED | 128 | 0.35 | *Pier#1* |
| HE 53 | NON ISOLATED | 128 | 0.50 | *Pier#1* |
| HE 54 | ISOLATED | 256 | 0.25 | *Pier#1* + *Iso#1* |
| HE 55 | ISOLATED | 256 | 0.35 | *Pier#1* + *Iso#1* |
| HE 57 | ISOLATED | 256 | 0.50 | *Pier#1* + *Iso#1* |
| HE 58 | ISOLATED | 256 | 0.75 | *Pier#1* + *Iso#1* |
| HE 60 | NON ISOLATED | 128 | 0.50 | *Pier#1* |
| HE 65 | NON ISOLATED | 128 | 0.75 | *Pier#1* |
| HE 68 | NON ISOLATED | 256 | 0.85 | *Pier#1* |

Table 4.6: Testing program.

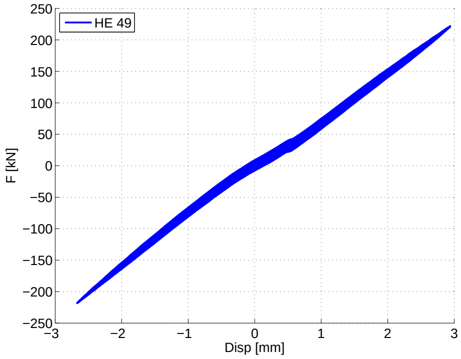

Figure 4.20: Hysteretic loops of the physical pier restoring force measured at the top level during tests HE 49.

the proposed retrofitting in this range of PGA, the same tests were conducted in the isolated configuration, i.e. HE 54, HE 55, HE 56. As shown in Figures 4.21 and 4.22 the retrofitting system is suitable for earthquakes stronger than ULS intensity. Finally, the bridge was simulated in the non isolated configuration for very strong seismic events up to 0.85 g of PGA level. In Figure 4.23 is shown the response of the pier during test HE 68, the strong nonlinear behavior was a clear proof of the irreparable damage. As can be appreciated in Figure 4.20, the proposed seismic isolation scheme strongly reduced the transversal response of piers, which remained in the linear range in the isolated case.

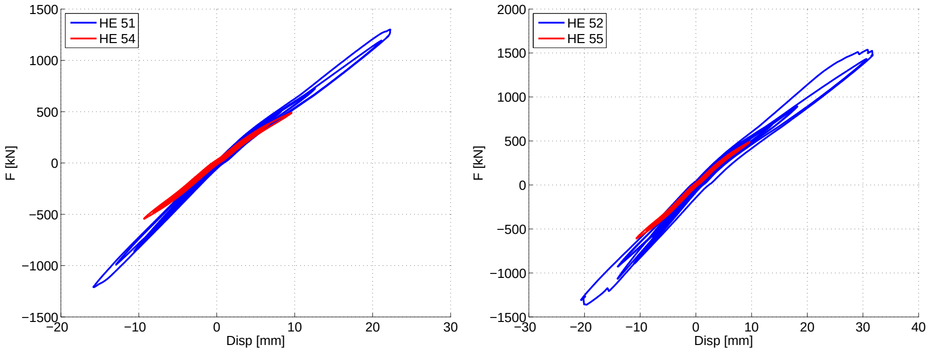

(a) (b)

Figure 4.21: Hysteretic loops of the physical pier restoring force measured at the top level during tests: a) HE 51 and HE 54; b) HE 52 and HE 55.

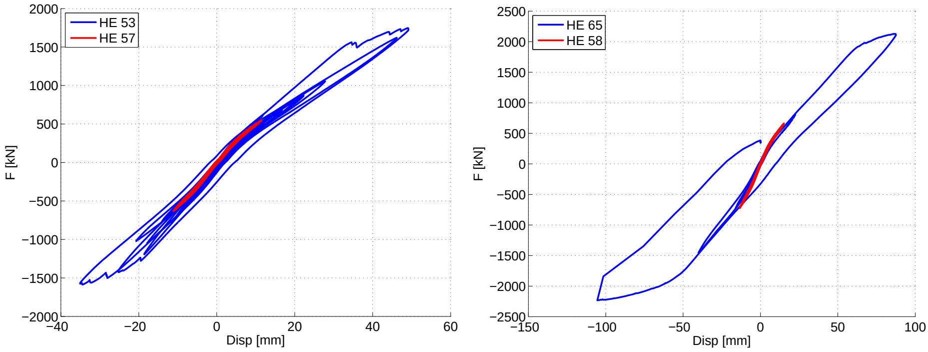

(a) (b)

Figure 4.22: Hysteretic loops of the physical pier restoring force measured at the top level during tests: a) HE 53 and HE 57; b) HE 65 and HE 58.

Figure 4.24(a) depicts the time history of the estimated parameter A during test HE 60, which was conducted assuming a PGA level equal to 0.50 g. As can be appreciated the initial value of A was updated after the previously tests, as a result it was different from the one gathered in Table 4.4. With regard to the same

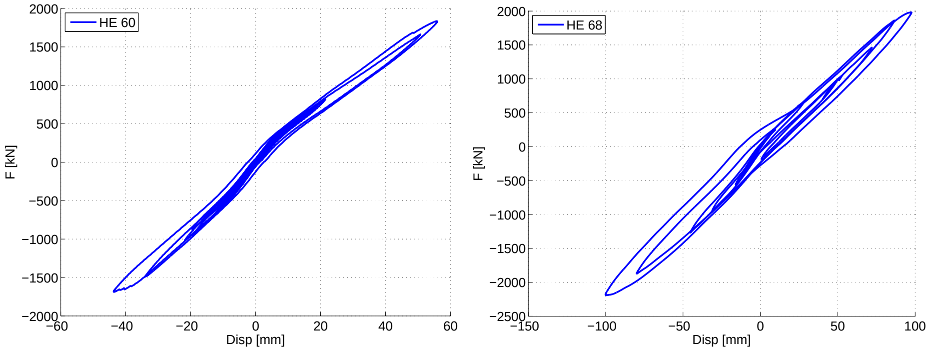

(a) (b)

Figure 4.23: Hysteretic loops of the physical pier restoring force measured at the top level during tests HE 60 and HE 68.

test, Figure 4.24(b) compares the hysteretic loops of the restoring forces of both the physical and the numerical piers. As can be appreciated the UKF captured the stiffness degradation of the physical pier that was applied to the numerical pier.

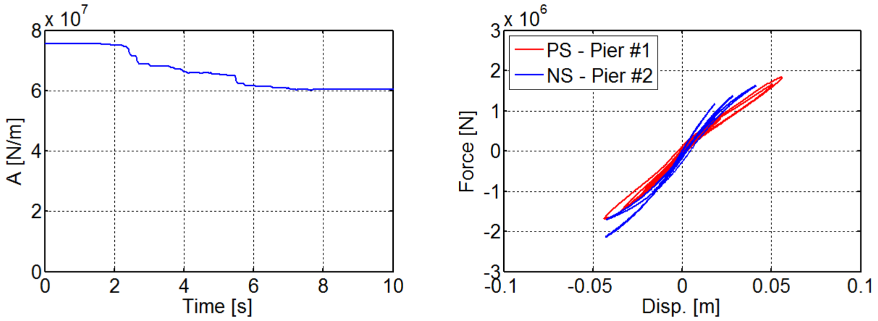

(a) (b)

Figure 4.24: Results of test HE 60: a) time history of the estimate of the parameter A of the Bouc-Wen spring obtained with the UKF; b) comparison of the hysteretic loops related to the transversal response of both the numerical and the physical piers.

### 4.4 Improvement of FE models based on springs-based modelling

In this section is presented the improvement procedure based on SBM approach adopted for this case study. The procedure was developed through the analysis of the information provided by mechanical characterization tests for materials and local LVDTs response for the local behavior of the RC pier. The complete set of 29 LVDTs is shown in Figure 4.25. For the scope of this investigation, the data of channels 10, 12, 20, 22 were analyzed.

In greater detail, two FE models of the RC pier have been implemented in Opensees environment: *i*) Model #1 with the same features of the PMCSII shown in Subsection 4.2.2 and developed with nonlinear fiber-based elements; *ii*) Model #2 with the same features of Model #1 except for a discrete spring positioned at the pier base with the aim to simulate the real behaviour of the base joint. In greater detail, the spring took into account the actual moment-rotation response of the base section. As anticipated in Section 2.3 the identification of local behavior allowed to optimize the updating process and decrease the demand of calibration tuning. The two models, shown in Figure 4.26, have been implemented with the mechanical properties presented in Section 4.2 on the base of the previous tests presented by Peloso and Pavese (2009). Therefore, the unique difference between the two FE models is the presence of the discrete based spring. The two nodes involved in the spring implementation were set as completely coupled for displacements and rotations, except for the rotation along X direction, i.e. the one involved in the out of plane seismic action.

Since two sets of LVDTs were positioned on the two sides of the pier, the moment-rotation law of the discrete spring was evaluated by means of the following equations. Firstly the Rotation of base joint (ROTBJ) was evaluated:

$$ROTBJ = \frac{\frac{\Delta_{CH10}-\Delta_{CH12}}{L_{CH10-CH12}} + \frac{\Delta_{CH20}-\Delta_{CH22}}{L_{CH20-CH22}}}{2} \tag{4.43}$$

Then, the moments transferred to the pier base was quantified as:

$$M_{Base} = RF_{Actuator} \cdot L_{Pier} \tag{4.44}$$

where $RF_{Actuator}$ is the reaction force recorded by the actuator load cell, whilst $L_{Pier}$ is the total high of the pier.

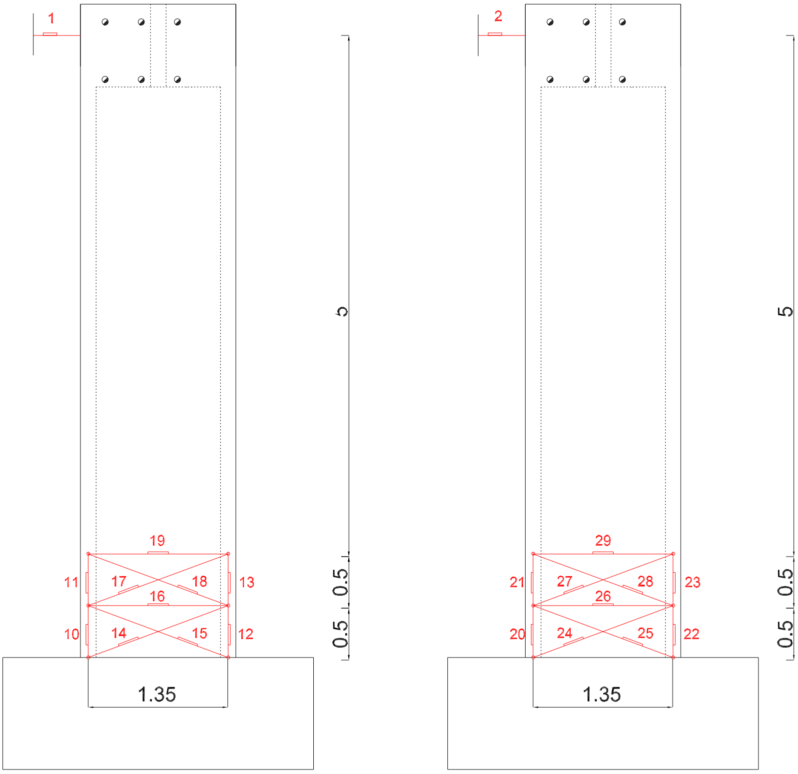

Figure 4.25: Set of LVDTs installed on the pier.

As a result, the values of the trilinear law are reported in Table 4.7 and depicted in Figure 4.27.

| **SPB** | | | | | |
|---|---|---|---|---|---|
| $k_1[\frac{Nmm}{rad}]$ | $2.5 \cdot 10^{14}$ | $k_2[\frac{Nmm}{rad}]$ | $4.4 \cdot 10^{13}$ | $k_3[\frac{Nmm}{rad}]$ | $1.4 \cdot 10^{13}$ |
| $M_1[Nmm]$ | $4.9 \cdot 10^{9}$ | $M_2[Nmm]$ | $1.6 \cdot 10^{10}$ | $M_3[Nmm]$ | $1.9 \cdot 10^{10}$ |
| $\phi_1[rad]$ | $2.0 \cdot 10^{-5}$ | $\phi_2[rad]$ | $2.7 \cdot 10^{-4}$ | $\phi_3[rad]$ | $4.8 \cdot 10^{-4}$ |

Table 4.7: Values of the trilinear approximation of moment rotation law of SPB.

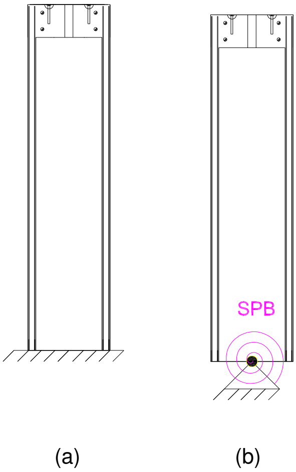

Figure 4.26: View of the two FE stick models: a) Model #1; b) Model #2.

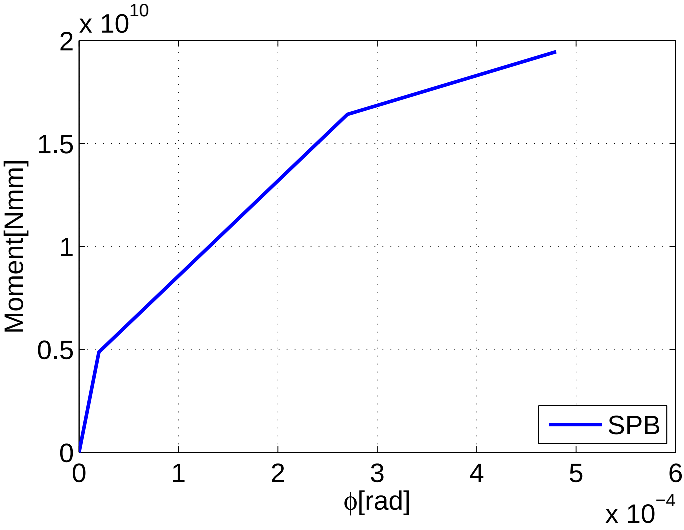

Figure 4.27: Constitutive law of the base spring

### 4.4.1 Validation and calibration of Model #1 and Model #2.

In this Subsection is presented the procedure of validation and calibration of the numerical models. The validation phase was performed taking as benchmark functions the constitutive law of concrete, i.e. $\varepsilon_{peak}$ and $f_{cm}$, and the ROTBJ of RC pier as follows:

$$B_1^{Val}(\bar{i}) = [\varepsilon_{c0}] \tag{4.45}$$

$$B_2^{Val}(\bar{i}) = [f_{cm}] \tag{4.46}$$

$$B_3^{Val}(\bar{i}) = [ROTBJ] \tag{4.47}$$

The calibration instead was defined on the based of the global quantity relevant to the law of base reaction force and top pier displacement, that reads as follows:

$$B_1^{Cal}(\bar{i}) = [Pier\ \ Base\ \ Reaction\ \ Force - Pier\ \ Top\ \ Displacement\ \ law] \tag{4.48}$$

In this case the error between the model and the benchmark functions has been evaluated througth the NRMSE:

$$D_i(M, B_i^{Val}) = NRMSE_i(M, B_i^{Val}) = \frac{\sqrt{\frac{1}{n}\sum_{i=1}^{n}(M - B_i^{Val})^2}}{max(B_i^{Val}) - min(B_i^{Val})} \tag{4.49}$$

$$D_i(M, B_i^{Cal}) = NRMSE_i(M, B_i^{Cal}) = \frac{\sqrt{\frac{1}{n}\sum_{i=1}^{n}(M - B_i^{Cal})^2}}{max(B_i^{Cal}) - min(B_i^{Cal})} \tag{4.50}$$

In order to cover both linear and nonlinear ranges, validation was performed by the comparison of FE models with tests HE 51, HE 52, HE 53, HE 60. As can be appreciated in Tables 4.8 and 4.9 both models showed a good agreement with the calibration benchmarks functions, in fact the error remain below 3.5%. In purpose of civil engineering problems and tolerances this error magnitude is surly acceptable. Even thought this good response, Model #1 showed errors twice the ones of Model #2. Therefore, a calibration procedure was applied to Model #1.
In greater detail, the calibration was performed by the comparison of Model #1 with tests HE 53 and HE 60 as shown in Table 4.8. With regard to test HE 53 the $\varepsilon_{c0}$ of concrete was magnified with a coefficient 1.2. As a result, the calibration error

| **Validated Model #1** | | | | | | |
|---|---|---|---|---|---|---|
| | $D_1^V$ | $D_2^V$ | $D_3^V$ | $D_{tot}^V$ | $D_1^C$ | $D_{tot}^C$ |
| $w_k^{Val}$ | 1 | 1 | 1 | | 1 | |
| HE 51 | 0 | 0 | 0.168 | 0.056 | 0.019 | 0.019 |
| HE 52 | 0 | 0 | 0.215 | 0.072 | 0.022 | 0.022 |
| HE 53 | 0 | 0 | 0.172 | 0.057 | 0.026 | 0.026 |
| HE 60 | 0 | 0 | 0.161 | 0.054 | 0.032 | 0.032 |
| **Calibrated Model #1** | | | | | | |
| | $D_1^V$ | $D_2^V$ | $D_3^V$ | $D_{tot}^V$ | $D_1^C$ | $D_{tot}^C$ |
| $w_k^{Cal}$ | 1 | 1 | 1 | | 1 | |
| HE 53 | 0.20 | 0 | 0.202 | 0.133 | 0.018 | 0.018 |
| HE 60 | 0.10 | 0.18 | 0.1924 | 0.156 | 0.017 | 0.017 |

Table 4.8: Results of improvement procedure relevant to Model#2.

| **Validated Model #2** | | | | | | |
|---|---|---|---|---|---|---|
| | $D_1^V$ | $D_2^V$ | $D_3^V$ | $D_{tot}^V$ | $D_1^C$ | $D_{tot}^C$ |
| $w_k^{Val}$ | 1 | 1 | 1 | | 1 | |
| HE 51 | 0 | 0 | 0.107 | 0.036 | 0.017 | 0.017 |
| HE 52 | 0 | 0 | 0.145 | 0.048 | 0.015 | 0.015 |
| HE 53 | 0 | 0 | 0.122 | 0.041 | 0.016 | 0.016 |
| HE 60 | 0 | 0 | 0.158 | 0.053 | 0.019 | 0.019 |
| **Calibrated Model #2** | | | | | | |
| | $D_1^V$ | $D_2^V$ | $D_3^V$ | $D_{tot}^V$ | $D_1^C$ | $D_{tot}^C$ |
| $w_k^{Cal}$ | 1 | 1 | 1 | | 1 | |
| HE 53 | 0 | 0 | 0.122 | 0.041 | 0.016 | 0.016 |
| HE 60 | 0 | 0 | 0.158 | 0.053 | 0.019 | 0.019 |

Table 4.9: Results of improvement procedure relevant to Model#2.

decreased from 2.6% to 1.8%; conversely, validation error increased reaching an

amount of 16% more that twice if compared with the initial evaluated after validation phase, i.e. 5.4%. The calibration based on test HE 60, required a modification of the $\varepsilon_{c0}$ and $f_{cm}$ of concrete that were magnified with a factor equal to 1.1 and 1.18, respectively. In Figure 4.28 are depicted the comparisons between models and experimental data in terms of both reaction force and rotations.
Conversely to Model #2, in Model #1 only materials parameters can be modified, as a results a calibration procedure presented before produces an increasing of validation error that classify the model as *unbelieveable*. In Figure 4.29 it is possible to see a graphical representation of the error domain and the position based on the couple [$D^V_{Tot}$;$D^C_{Tot}$] of the two models in comparison with the ideal perfect model.

## 4.5 Numerical simulations with the improved FE model

Finally, the identified Model #2 was implemented in the PMCSII. It means that the piers of the Opensees model were endowed with the validated SPB spring with the constitutive law reported in Figure 4.27. As a result, representative simulations of the updated model (IPMCSII) were performed at both SLS and ULS intensities. As can be appreciated in Figure 4.30 both simulations showed a drop in stiffness with respect to the previous PMCSII numerical results. These are a significative results because quantify the error between the two models and hence the error in terms of substructures settings adopted at the beginning of HSs. Thanks to UKF based online model updating, the effects of this error were completely deleted.

## 4.6 Conclusions

The seismic assessment of a two piers RC bridge in both the isolated and the non isolated configurations, was conducted at the EUCENTRE TREES Laboratory of Pavia (Italy) by means of HSDS testing campaign. The EUCENTRE TREES Lab BTS, which has been initially designed to carry out standard qualification tests in force and/or displacement control of isolation devices, was used to substructure a CSB and apply the correct boundary conditions in terms of vertical load and horizontal displacement. In greater detail, the seismic assessment of the structure, have been developed by means of Step I, II and III and partially IV of SPAB pro-

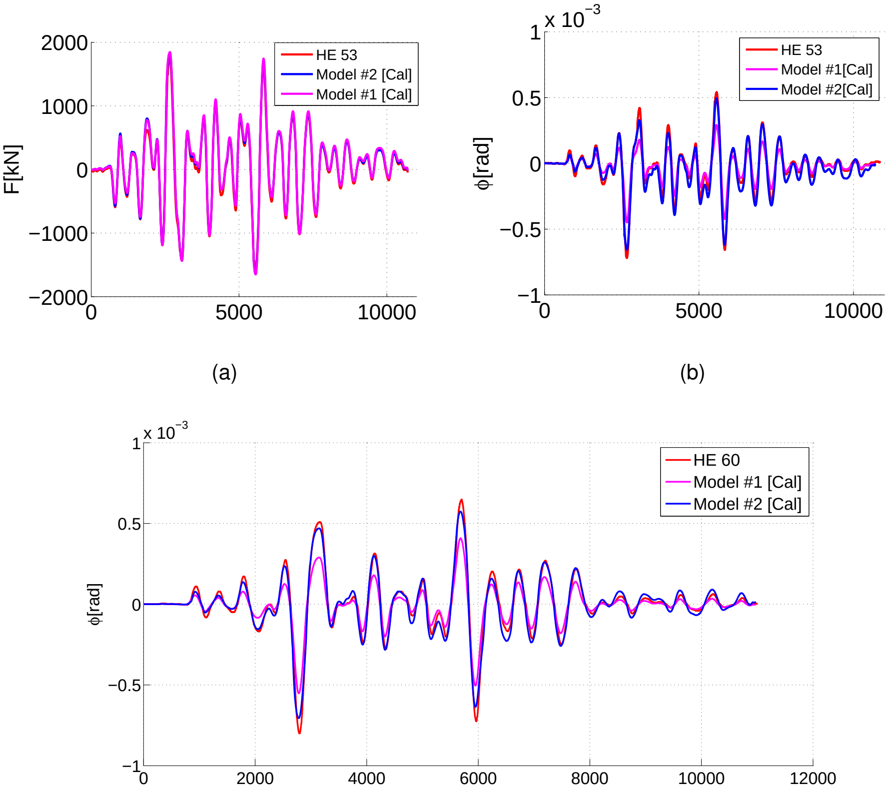

(a)

(b)

(c)

Figure 4.28: Check of the goodness of the models: a) comparison of reaction forces; b) comparison of rotations during test HE 53; c) comparison of rotations during test HE 60.

cedure. Four tasks have been investigated: *i*) the effectiveness of a prototype of CSB with an innovative rate independent behavior; *ii*) the advantage of a novel partitioned time integration first order scheme; *iii*) the improvements produced by an online model updating based on a UKF.

Firstly, a prototype of CSB has been characterized and the used during HSs. In detail, the expected rate independent behavior for high speed was proven, and hence it is the perfect candidate for the application in challenging civil engineers problems. In fact, it allowed to keep the piers in elastic regime also for strong earthquakes as shown in the experimental results.

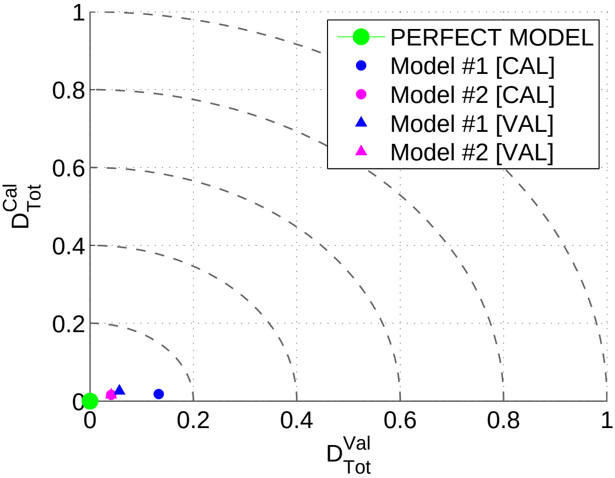

Figure 4.29: Positions of FE models in the domain when compared with HE 53 experimental test.

Then, a novel first order partitioned time integration scheme has been used during the HSs. The advantage are strictly related to the possibility to implement an online model updating procedure.

Finally, in order to simulate a consistent degradation between the twin physical and numerical piers, the UKF was used as an online dynamic identification tool. A novel parallel partitioned time integrator tailored to first order systems allowed for the straightforward accommodation of the filter. The implementation of this novel updating procedures improved the initial offline technique. In greater detail, thanks to the advantage of considering the damage step by step during the tests it practically deleted the approximations generally intrinsically present in typical HSs based on an offline model updating procedure.

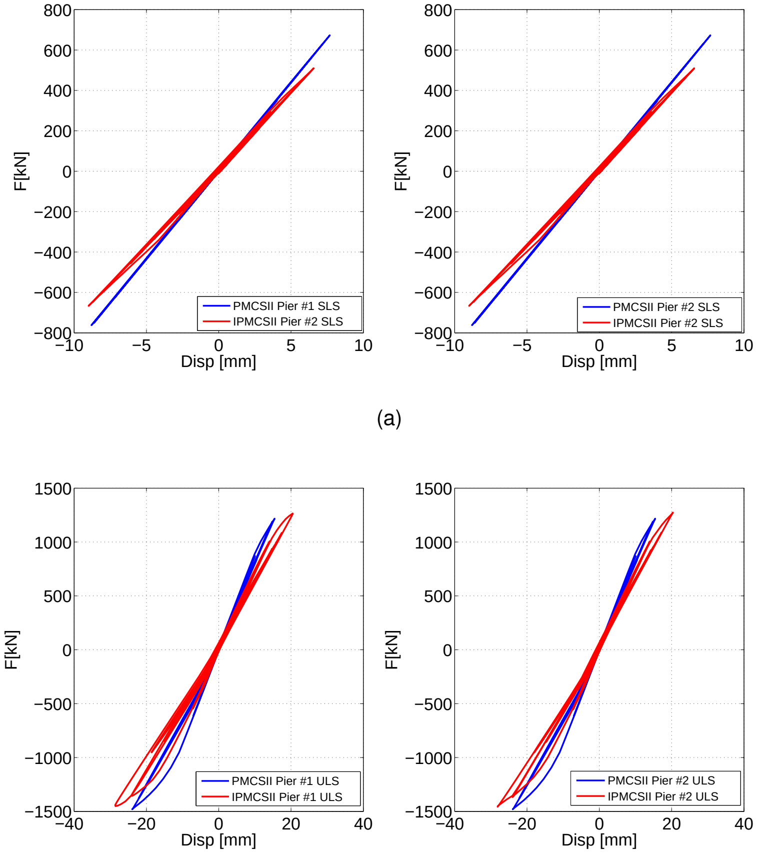

(a)

(b)

Figure 4.30: Comparison between updated numerical models: a) SLS regime; b) ULS regime.

## CHAPTER 5

# SEISMIC DESIGN AND ASSESSMENT OF A COMPOSITE STEEL-CONCRETE BRIDGE BASED ON CYCLIC TESTS - CASE STUDY III

### 5.1 Introduction

This chapter was developed within the SEQBRI Project (Paolacci et al. (2015)), in which the seismic design and assessment assessment of novel structural joints for composite bridges have been investigated on the base of QSCTs and a fully probabilistic analysis. The aim of the research study was twofold: i) to investigate the seismic response of a novel connection between the CCB and the steel I-girder beam; ii) to apply the fully probabilistic PBEE to a functional composite bridge designed according to Eurocodes.

In particular, a typical SCCBH with two 20 m length spans was selected as case study. In addition, the installation of a seismic isolation system based on Lead Rubber Bearings (LRBs) between the CCB and the supports, i.e. abutments and pier, was proposed as seismic isolation system to preserve the damage generation in the CCB.

In order to simulate the seismic response of the structural joints an experimental campaign was designed and performed at the University of Trento and at the University of RomaTRE, with the aim to test the transversal and longitudinal behaviors, respectively. This chapter is focused on the analysis of transversal behavior, hence the results of the experimental tests performed at the University of Trento were considered.

Therefore, in Section 5.2 the CSIII is introduced and both non isolated and isolated configurations are discussed. In the same section, the SMCSIII and PMCSIII developed to support the design of experimental tests are presented. They were used in particular to chose the best testing protocol to be used during the experimental campaign. Later, in Section 5.3 the experimental campaign is presented with the relevant results. Then, in Section 5.4 is presented the improvement of FE models which included the not only the tested specimen but also the experimental setup that showed an unforeseen flexibility. In detail, a CMM of the connection between the Steel Concrete Composite (SCC) section and the CCB, based on the component method widely used in EN1993-1-8 (2005) has been developed. The mechanical model has been fully implemented in the Opensees environment (Mazzoni et al. (2009)) and validated on the base of experimental outcomes. Finally, in Section 5.5 the application to CSIII of the structural part of PBEE approach is presented. Conclusions are reported in Section 5.6.

## 5.2 Description of Case Study III

The CSIII is a bridge in the category of short and medium span SCCBH. This type of facilities are popular due to their economic benefits and short construction times (Paolacci et al. (2015)). Moreover, they are very adequate for seismic areas because of their limited weight. In general, SCCBHs for small and medium spans - range between 25 m and 40 m - exhibit several advantages in terms of: *i*) simple erection methods because of no steelwork on site; *ii*) low structural weights and limited foundations and settlements of supports; *iii*) no pre-stressing in concrete slab; *iv*) short construction on site and therefore, over passing of existent railways or highways with minimized traffic restrictions.*v*) small total depth of composite section. Favorable consequences of the aforementioned properties are several, e.g. highly resistance to earthquake, high durability, minimal overall costs, high demolition and recycling capability.

In Figure 5.1 are shown the CCB solutions proposed by DIN-FB 104 (2009) widely used for non seismic prone areas. In Figure 5.2 an application of CCB solution for a SCC bridge erected in Poznan (Poland). Concrete Cross Beams (CCBs) provide continuity between the spans over support by the use of: *i*) vertical end steel plates that allow to introduce the compression of the lower flange and transfer the shear

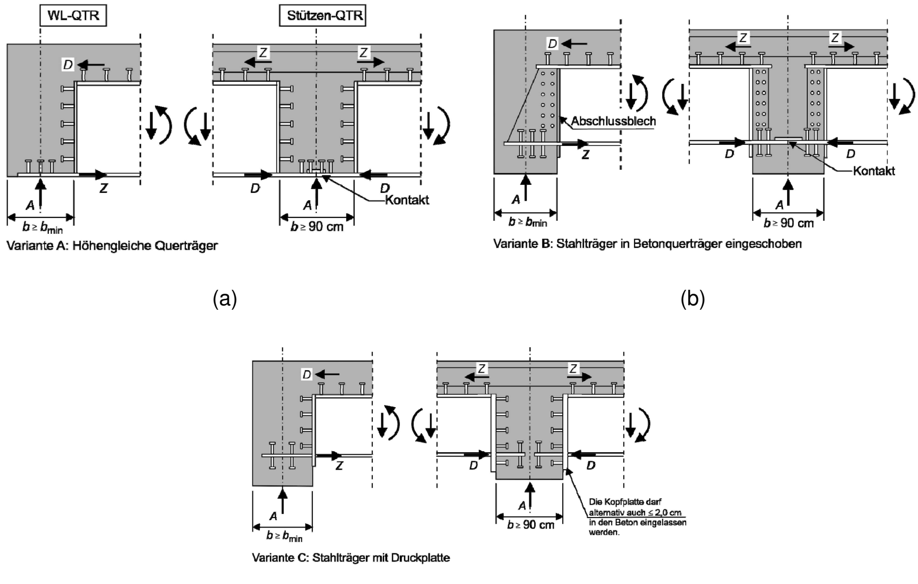

(a)

(b)

(c)

Figure 5.1: CCBs proposed in DIN-FB 104 (2009).

(a)

(b)

Figure 5.2: Dolna Wilda bridge realized with CCB (Poznan (Poland)).

loads via shear studs into the concrete cross beam; *ii*) additional reinforcing bars in the deck slab to transfer the tension force over the concrete cross beam into the adjacent slab. During concreting phase of the CCB, the loads due to structural weight of steel girders, form-work and wet concrete are carried by simply supported beams. After concrete hardening, moment resistance is provided over the support and subsequent loads are supported by continuous girders. Thus hogging bending is produced over supports only for super-imposed dead loads and variable actions. The following advantages are the result of the construction method:

- the longitudinal girders are erected as single span girders which reduces the hogging moment for the crack width design, increases the sagging moment and therefore the design is optimized and enables an independent erection of each span, thus a minimization of the traffic interference;
- there is no need for welded or bolted splices, therefore no special skilled workers are needed on the construction site as the steelwork parts of the composite beams are prepared in factory and the tolerances of concreting work need only to be respected.

In detail, CSIII is devoted to the typical two span straight overpasses. The bridge is 40 m long and consists of 2 spans of 20 m as shown in Figure 5.3. The road cross section is a typical cross section and has a 6.50 m wide carriageway, supporting two traffic lanes, and two sidewalks of 2.05 m each one. In total, the width of the cross section of the deck is 10.60 m. The wall type pier clear height is 7 m with a section of 0.60 m thick and 7 m wide as depicted in Figure 5.4. The wall type is adopted, in order to avoid vulnerability from potential vehicle collision. Finally, the pier's foundation are deep type.

The concrete slab is 0.25 m thick, and is supported by four main I-girders HLB 600 sections made with hot-rolled S460M steel, with 2.65 m in-between distance. The steel girders are fixed to an end reinforced CCB 0.60 m wide. By this diaphragm, the deck is simply supported on elastomeric Lead Rubber Bearing (LRB) isolators and structural bearings respectively for the isolated and non isolated case. On the intermediate section, the steel girders are fixed to intermediate reinforced CCB 0.90 m wide and the connection between the intermediate CCB and the pier is the same of the abutments in both configurations. The design values of materials properties are listed in Table 5.1. Loads were assigned in accordance with EN1990-2 (2002). In addition to dead and thermal loads, traffic loads (LM1, LM2 and LMF3) and 1cm soil settlement were taken into account as well as seismic actions according to EN1998-1 (2005) and EN1998-2 (2005)). As a result, the complete set of loads acting on CSIII are reported in Table 5.2.

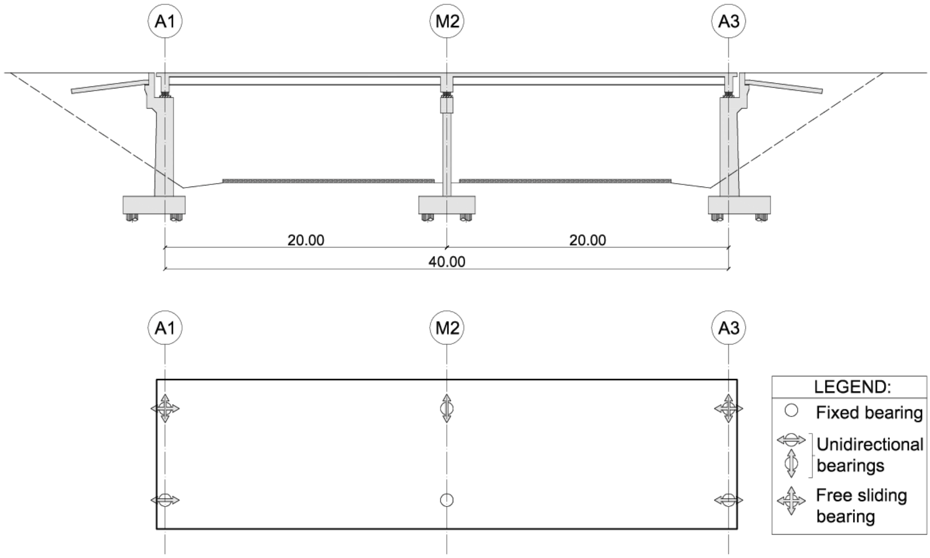

Figure 5.3: Longitudinal view of Case Study III in the non isolated configuration.

| Component | Material |
|---|---|
| Structural Steel | S460M |
| Concrete | C35/45 |
| Reinforcements | B450C |
| Shear Studs | Nelson type S235-J2G3+C450 |

Table 5.1: Materials properties of Case Study III.

### 5.2.1 Novel concrete cross beam joint solutions

In this section are presented three beam-to-beam joints for SCC bridge beams proposed in the SEQBRI Project (Paolacci et al. (2015)). In order to fit with the advantages described in Section 5.2, the design are intended to be economical and easily implemented on the work site, paying special attention to avoid outdoor weldings as proposed in the National MIKTI french project (MIKTI (2008)).

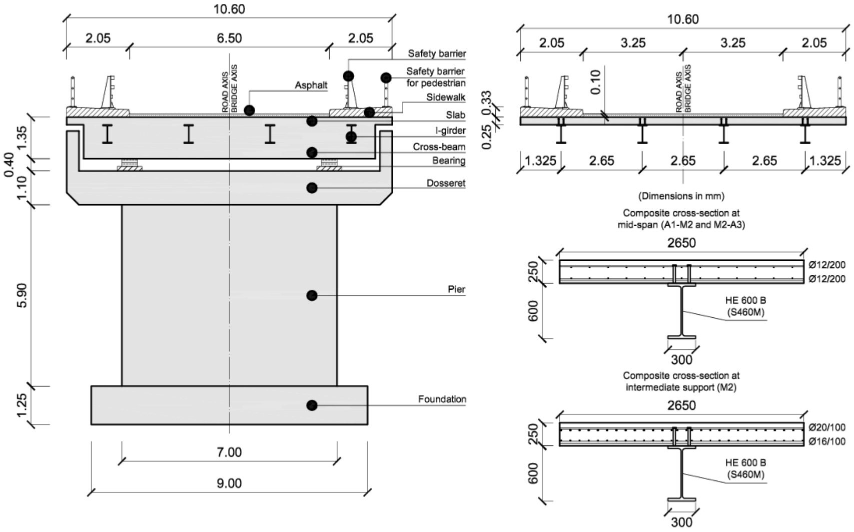

Figure 5.4: Structural Details of Case Study III.

#### 5.2.1.1 Variant C of DIN FB 104

The first type of joint, named Variant C is a reproduction of the joint proposed in the German codes (DIN-FB 104 (2009)). In this solution, as shown in Figure 5.5, the steel girder ends to a head plate. The bottom flange protrudes inside the CCB for less than half of its width. Since the flanges of steel I-girders are not connected to each other, for the hogging moment case, compression forces are transferred to the concrete . Tensile forces, in the sagging moment case, i.e. seismic case, are instead transferred through shear studs vertically disposed on the bottom flange protrusion. The flow of forces between concrete deck and steel beam is ensured by studs arranged on the girders top flange, subdivided in two rows of welded Nelson studs. Shear studs on the head plate transfer forces to the CCB.

#### 5.2.1.2 DOMI-I

Detail type DOMI-I is similar to DIN FB 104 variant B (DIN-FB 104 (2009)), although some important differences need to be pointed out as shown in Figure 5.6. First, the steel girder head plates are confined at the bottom flange region. Forces are transferred through contact (compression) or through shear studs (ten-

| **Component** | **V**[$mm^3$] | **Peso**[$N$] | **Mass**[$Ton$] | **Load**[$N/mm$] |
|---|---|---|---|---|
| Concrete Slab | $1.06 \cdot 10^{11}$ | $2.65 \cdot 10^{6}$ | $2.70 \cdot 10^{2}$ | 66.25 |
| CCB A1 | $7.00 \cdot 10^{9}$ | $1.75 \cdot 10^{5}$ | 17.82 | 4.37 |
| CCB M2 | $7.00 \cdot 10^{9}$ | $1.75 \cdot 10^{5}$ | 17.82 | 4.37 |
| CCB A3 | $1.05 \cdot 10^{10}$ | $2.62 \cdot 10^{5}$ | 26.75 | 6.56 |
| Sidewalk 1 | $2.46 \cdot 10^{10}$ | $6.15 \cdot 10^{5}$ | 62.69 | 15.36 |
| Sidewalk 2 | $2.46 \cdot 10^{10}$ | $6.15 \cdot 10^{5}$ | 62.69 | 15.36 |
| Asphalt | $2.60 \cdot 10^{10}$ | $6.24 \cdot 10^{5}$ | 63.61 | 15.60 |
| Steel Girder 1 | $1.08 \cdot 10^{9}$ | $8.48 \cdot 10^{4}$ | 8.64 | 2.12 |
| Steel Girder 2 | $1.08 \cdot 10^{9}$ | $8.48 \cdot 10^{4}$ | 8.64 | 2.12 |
| Steel Girder 3 | $1.08 \cdot 10^{9}$ | $8.48 \cdot 10^{4}$ | 8.64 | 2.12 |
| Steel Girder 4 | $1.08 \cdot 10^{9}$ | $8.48 \cdot 10^{4}$ | 8.64 | 2.12 |
| **Tot Deck** |  | $5.46 \cdot 10^{6}$ | **556.09** | **136.38** |
| Pier | $2.73 \cdot 10^{10}$ | $6.83 \cdot 10^{5}$ | 69.57 | 105 |
| Pier’s Cap Beam | $1.05 \cdot 10^{10}$ | $2.62 \cdot 10^{5}$ | 26.74 | 40.36 |
| **Tot Pier** |  | $9.45 \cdot 10^{5}$ | **96.31** | **145.36** |
| **Tot CSIII** |  | $6.40 \cdot 10^{6}$ | **652.41** |  |

Table 5.2: Dead loads acting on the Case Study III.

sion) to the CCB. Head plate thickness has to be chosen according to design force intensity. Another particular aspect of the configuration is represented by the steel girders web extending into the CCB. Shear studs are arranged over the entire area and are subjected to pure shear, in fact they have been designed for entire shear force. The web is provided with holes for the placement of the CCB reinforcements. This detail type is designed for the seismic case in which the bottom steel flanges in light tension or remains in compression.

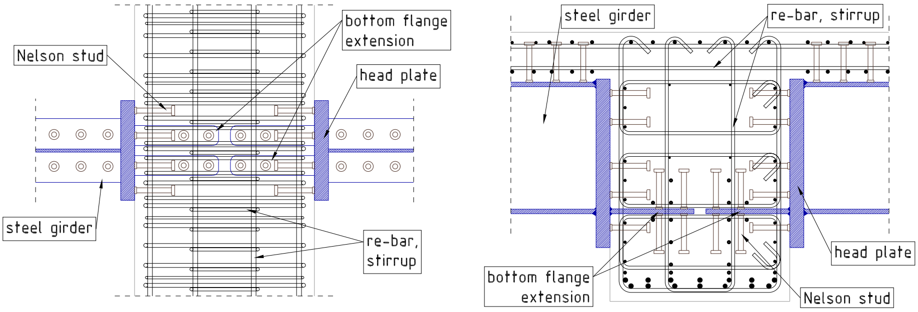

(a) (b)

Figure 5.5: Views of DIN FB 104 Variant C joint type: a) upside view; b) lateral view.

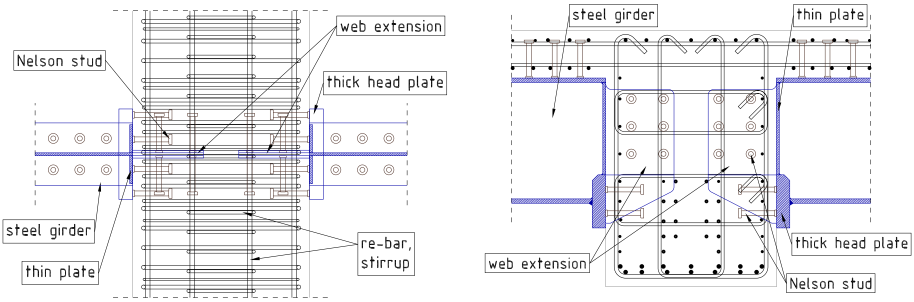

(a) (b)

Figure 5.6: Views of DOMI-I joint type: a) upside view; b) lateral view.

#### 5.2.1.3 DOMI-II

Detail type DOMI-II differs from the aforementioned DOMI-I configuration in the bottom steel flange connection, as shown in Figure 5.7. In fact, while compression forces are again transferred through contact via a thick head steel plate, tension is absorbed by four prestressed anchor bars. Shear forces are transferred through studs arranged on both sides of the steel beam web extension, whereas studs on the top flange transfer tensile and compression forces. This detail type is designed for bottom steel flanges where tension forces become significant during the seismic event and the use of shear studs proposed in the first solution, i.e. Variant C of DIN FB 104, is uneconomical. Bridges with a monolithic connection between CCB and pier can be subjected to this stress state.

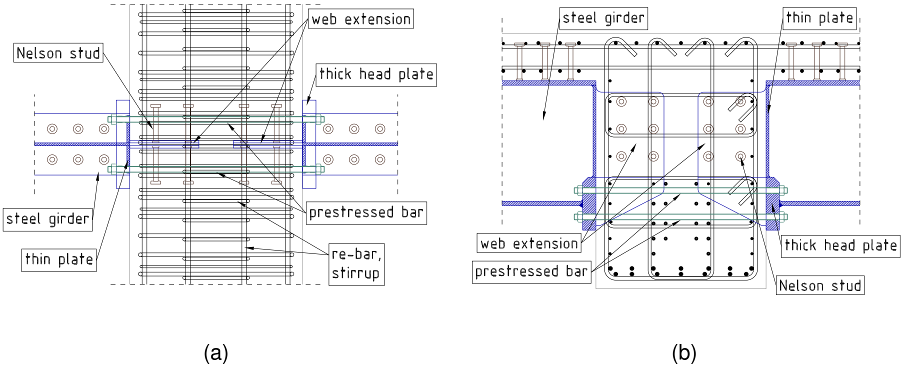

(a) (b)

Figure 5.7: Views of DOMI-II joint type: a) upside view; b) lateral view.

### 5.2.2 Simplified FE model of Case Study III

In order to perform a preliminary analysis and to design the proper isolation device a SMCSIII was implemented in the Opensees environment (Mazzoni et al. (2009)). The model is composed by a line of elements representing the equivalent section of the deck, and 2 vertical element to represent the pier as shown in Figure 5.8. In addition, several rigid links were implemented to consider the actual spatial position of the gravity centers of elements, i.e. deck and pier. The pier was clamped at the base whilst the deck, for the non isolated configuration, was hinged at the abutments for transversal loadings. The composite beams and the CCB have been considered perfectly connected. In this model only linear elastic elements, i.e. *elasticbeamcolumn*, of the Opensees library were implemented and for each one were assigned the geometrical properties reported in Table 5.3. The total mass and loads of the deck and pier were evaluated as reported in Table 5.2. As a result, in serviceability conditions, the deck drop on each abutment and on the pier a vertical load of 1020 kN and 4350 kN, respectively.

These reaction forces were used for the design of the isolation system. In greater detail, the selected device is the $LRB-S500/100-110$ produced by FIP-Industriale,

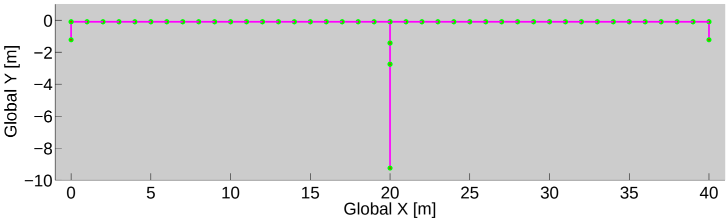

Figure 5.8: Global view of SMCSIII.

| | $Area[mm^2]$ | E[MPa] | $I_y[mm^4]$ | $I_z[mm^4]$ | $I_t[mm^4]$ |
|---|---|---|---|---|---|
| **DECK** | $3.28 \cdot 10^6$ | $3.60 \cdot 10^5$ | $1.40 \cdot 10^{11}$ | $2.50 \cdot 10^{11}$ | $2.15 \cdot 10^{11}$ |
| **PIER** | $4.20 \cdot 10^6$ | $3.60 \cdot 10^5$ | $1.72 \cdot 10^{13}$ | $1.26 \cdot 10^{11}$ | $4.99 \cdot 10^{11}$ |

Table 5.3: Geometrical properties of the elastic sections implemented in SMCSIII.

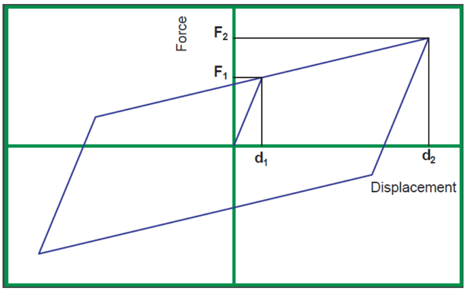

Figure 5.9: Constitutve law of LRB-S 500/100-110.

| $V[kN]$ | $K_e[kN/mm]$ | $\xi[\%]$ | $F_2[kN]$ | $F_1[kN]$ | $d_2[mm]$ | $d_1[mm]$ | $K_v[kN/mm]$ |
|---|---|---|---|---|---|---|---|
| 2700 | 1.94 | 35 | 162 | 106 | 83 | 8 | 1164 |

Table 5.4: LRB Properties.

it means a device with 500 mm of diameter, a total rubber layer of 100 mm and a lead core with a diameter of 110 mm. The mechanical properties of the device are reported in Table 5.4 and the constitutive law is depicted in Figure 5.9. The benefits of the isolation system were evaluated in first approximation by the implementation of the equivalent properties, evaluated as follows:

$$K_e = \frac{F_2}{d_2} \tag{5.1}$$

$$\xi_d = \frac{2}{\pi}[\frac{F_1}{F_2} - \frac{d_1}{d_2}] \tag{5.2}$$

In Table 5.5 are reported the periods of vibration of the first 5 modes for both non isolated and isolated configurations. It is evident as the seismic isolation system allowed to increase the periods and hence decrease the seismic actions on the bridge.

| **Period [s]** | | |
|---|---|---|
| **Mode** | **SMCSIII - Non isolated** | **SMCSIII - Isolated** |
| **#1** | 0.897 | 1.912 |
| **#2** | 0.405 | 1.904 |
| **#3** | 0.262 | 1.046 |
| **#4** | 0.103 | 0.373 |
| **#5** | 0.082 | 0.264 |

Table 5.5: Periods of vibration of the non isolated and isolated SMCSIII.

### 5.2.3 Predictive FE model of Case Study III

In order to support and design the cyclic tests a stick FE model PMCSIII able to simulate the seismic response of the bridge was set in the Opensees environment (Mazzoni et al. (2009)). The model, depicted in Figure 5.11, was implemented with the design material properties.

Two lines of elements were implemented to model the presence of the concrete slab and the steel I-girders. The two lines of elements were connected each other and with the CCB by means of rigid links. Furthermore, each CCB was connected

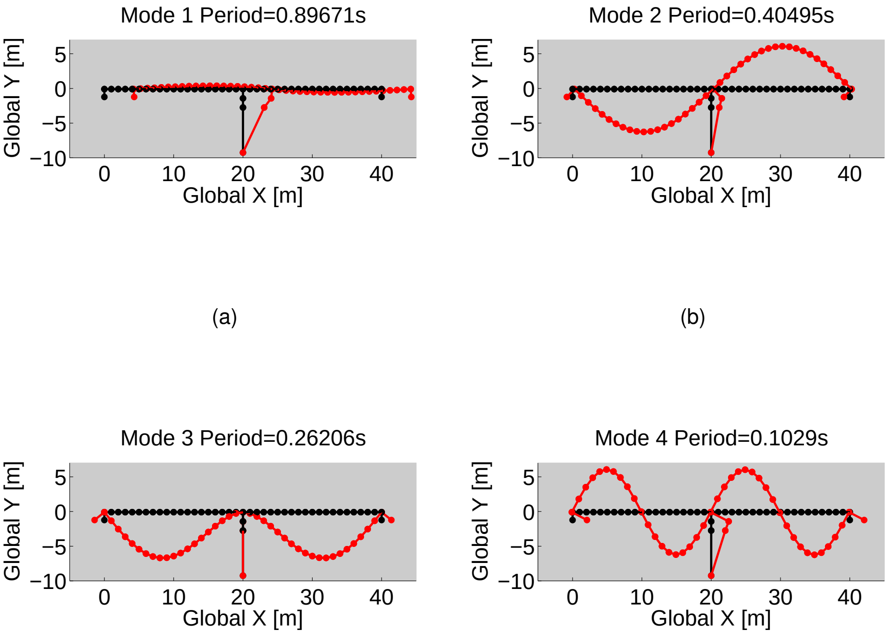

(a) (b)

(c) (d)

Figure 5.10: Mode shapes of SMCSIII in the non isolated configuration: a) $1^{st}$ *Mode*; b) $2^{nd}$ *Mode*; c) $3^{rd}$ *Mode*; d) $4^{th}$ *Mode*.

to the relative support by additional rigid links with the aim to reproduce the offset between CCB itself and the structural bearings. The concrete slab, steel I-girder and the pier were discretized with nonlinear beam fiber section elements. They allowed for an accurate discretization of the cross section, reproducing the exact position and dimension of reinforcing bars and concrete with relevant constitutive laws. Then, the pier was considered clamped at the base whilst the constraints on the abutments were set with two different configurations, the one relevant to the non isolated case reported in Figure 5.3 and the one for the isolated case in which all the DoFs in the deck's plane were considered constrained with the isolator stiffness.

Concrete tensile strength was not considered, as consequence, the Kent-Scott-

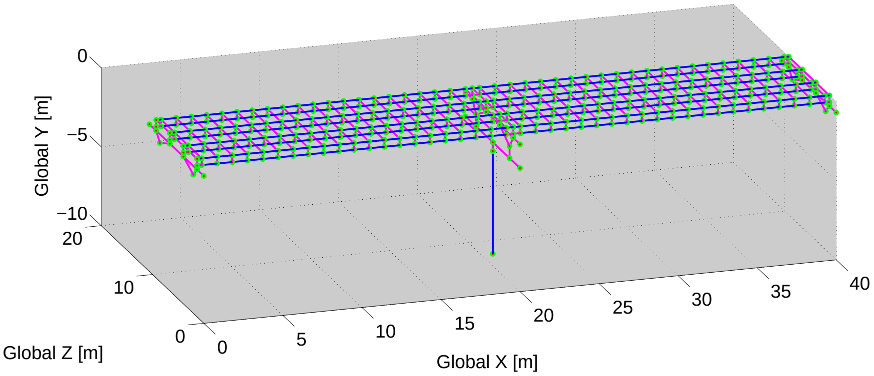

Figure 5.11: Global view of PMCSIII.

Park model was employed to simulate the concrete behavior (Kent and Park (1971)) that is implemented in the *Concrete*01 Opensees material. According to Figure 3.9(a), a first parabolic branch reaches the maximum compressive strength $f_{cm}$ which was assumed equal to 43 MPa; the corresponding compressive strain $\varepsilon_{c0}$ was assumed equal to 0.2%. Then a decreasing linear branch connects the maximum compressive strength $f_{cm}$ and the ultimate compressive strength $f_{cu}$, which was assumed equal to 34 MPa with a corresponding ultimate strain $\varepsilon_{cu}$ of 0.6%. Reinforcing bars were modelled according to the Menegotto-Pinto constitutive law (Menegotto and Pinto (1973)), which is implemented in the *Steel*02 Opensees material, as depicts in Figure 3.9(b). According to the code, $f_y$ was assumed equal to 450 MPa, with a Young's modulus of 210000 MPa, the hardening parameter identified as the ratio $b = \frac{E}{E_p}$ was set as 0.0025. The same material type was implemented for the structural steel with $f_y$, $E$ and $b$ equal to 460 MPa, 210000 MPa and 0.0025 respectively. A shear-strain relationship was assumed for the shear nonlinear behaviour of the concrete wall type pier, it consists in a trilinear curve implemented by means of the Opensees *Hysteretic* material which constitutive relationship is depicted in Figure 3.10. In detail, forces were obtained according to the formulation proposed by Vecchio and Collins (1988) and Collins et al. (1996) based on the Modified Compression Field Theory. The total shear strength $V_t$ is the sum of concrete and reinforcement contribution, i.e.

$$V_t = V_c + V_s \tag{5.3}$$

with:

$$Vc = 0.8k_d\sqrt{f_c}A_c \tag{5.4}$$

$$Vs = \frac{A_{sw}f_{ys}Dcot(\theta)}{S_s} \tag{5.5}$$

where: $f_c$ is the compressive concrete strength and $f_{ys}$ is the steel yield strength the values considered are the same implemented in the fiber elements of wall type pier, i.e. $f_{cm}$ and $f_y$ respectively. $A_c$ is the cross section area, $A_{sw}$ is the area of stirrups with the relevant spacing $S_s$. $D$ is the cross section effective depth. For the calculation of $V_c$, the curvature ductility-dependent parameter $k_d$ was set equal to 0.2. According to Figure 3.10, $e1^+$ was set equal to $V_c$, whilst both $e2^+$ and $e3^+$, corresponding shear deformations were set as $\frac{V_c}{G_c A_{shear}}$, 0.0045 and 0.02 respectively according to Kelly (2004). The hysteretic material was coupled to the flexural behaviour by using the *sectionaggregator* OpenSEES command; that allows to consider at the same time the flexural and shear effects. To simulate the presence of the isolation system, two *elastomericBearingPlasticity* Opensees elements were interposed between the abutments and the deck and between the pier and the deck. The constitutive law and the scheme of the element are shown in Figure 5.12(a). In order to best fit the constitutive law of the $LRB - S500/100 - 110$ FIP-Industriale isolator, the Opensees parameters were set as follow:

$$K_{init} = \frac{F_1}{d_1} \tag{5.6}$$

$$\alpha_1 = \frac{K_2}{K_1} \tag{5.7}$$

$$K_2 = \frac{F_2 - F_1}{d_2 - d_1} \tag{5.8}$$

$$\alpha_2 = 0 \tag{5.9}$$

$$\mu = 0 \tag{5.10}$$

with $F_1$, $d_1$, $F_2$, $d_2$ reported in Table 5.4. In Figure 5.12(b) is shown the comparison between the constitutive FIP-Industriale catalog and the implemented constitutive laws of the LRB isolator.

The PMCSIII was compared with the SMCSIII in terms of dynamic properties. In Figure 5.13 are depicted the modal shapes of the PMCSIII, as can be appreciated there is a good agreement with SMCSIII in terms of both modal shapes and periods of vibration. Therefore, the PMCSIII was chose as the predictive model to evaluate the seismic response of the bridge and to choose the proper testing protocol for the experimental campaign presented in Section 5.3.

As a result, a set of numerical simulations were performed considering a ground motion in agreement with the target spectrum of EN1998-1 (2005) as shown in Figure 5.14. The chosen ground motion was then scaled to amplify the intensity. The objective was to investigate the applicability of a damage related cyclic testing protocol. In literature can be found several works describing different procedures to be adopted considering the damage of the structure and the actual seismic response of the involved components. As an example, the method proposed by Hutchinson et al. (2011), is based on the evaluation of the damage of the structure subjected to a seismic event by the reproduction of this damage through weighting properly the amplitudes of each load cycle.

For this case study, the numerical results showed a good response of the bridge for design seismic loadings in both isolated and non isolated configurations as can be appreciated in Figure 5.15(a) and 5.15(b). The simulations have shown the reliability of these type of bridges for high seismic prone areas but local connection features still require additional investigations. In addition, because of the small damage recorded for the design earthquake, the method proposed by Hutchinson et al. (2011) can not be representative of this case study. As a result, has been decided to characterize the behavior of the joint up to collapse independently of

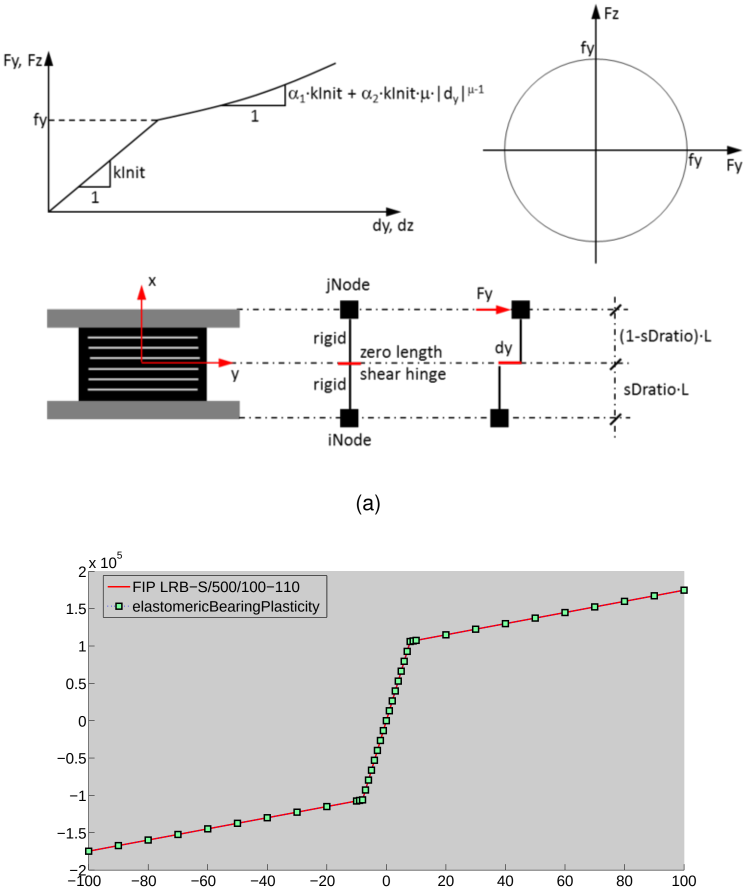

(a)

(b)

Figure 5.12: *elastomericBearingPlasticity* OpenSEES element: a) view of the element; b) constitutive law implemented in OpenSEES.

seismic actions through the standard procedure for steel structure proposed by ECCS (1986). In Figures 5.15(c) and 5.15(d)can be appreciated the benefits of the isolation system also for strong earthquakes, up to 1.5g of PGA.

## 5.3 Experimental Campaign

As anticipated in Section 5.1, the target of the experimental campaign performed at the University of Trento was to investigate the response of each single

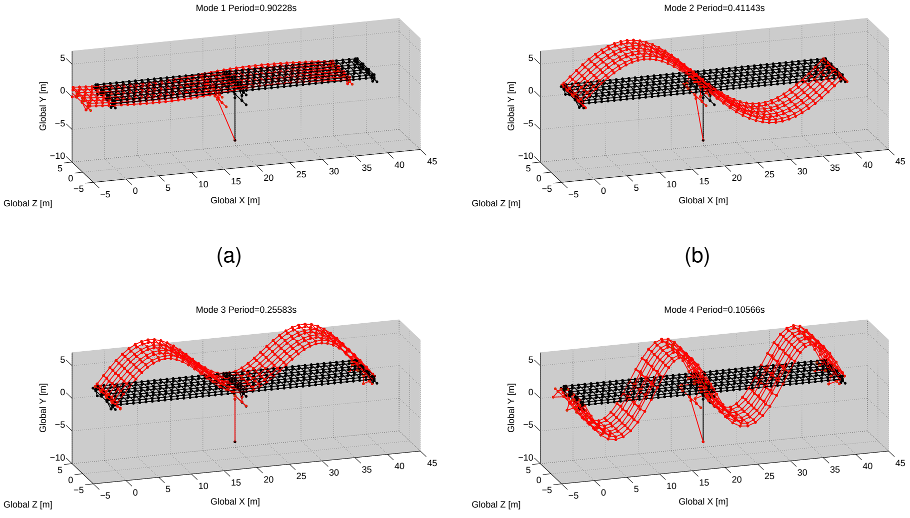

(a) (b)

(c) (d)

Figure 5.13: Mode shapes of PMCSIII in the non isolated configuration: a) $1^{st}$ *Mode*; b) $2^{nd}$ *Mode*; c) $3^{rd}$ *Mode*; d) $4^{th}$ *Mode*.

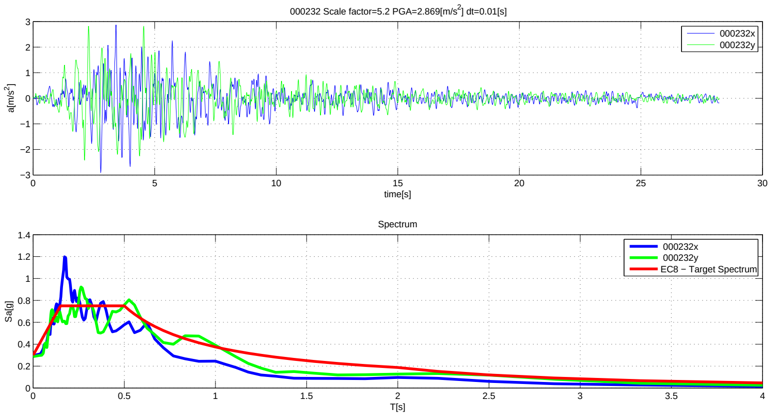

Figure 5.14: Ground motion for the preliminary simulation at 0.3g of PGA.

intermediate SCC - CCB connection in the case of transversal loadings. A substructure of the composite deck, derived from a representative part of the overall bridge was extracted as shown in Figure 5.16. In order to reach the failure of the substructure with the available laboratory facilities, a scale factor $S = 2$ was con-

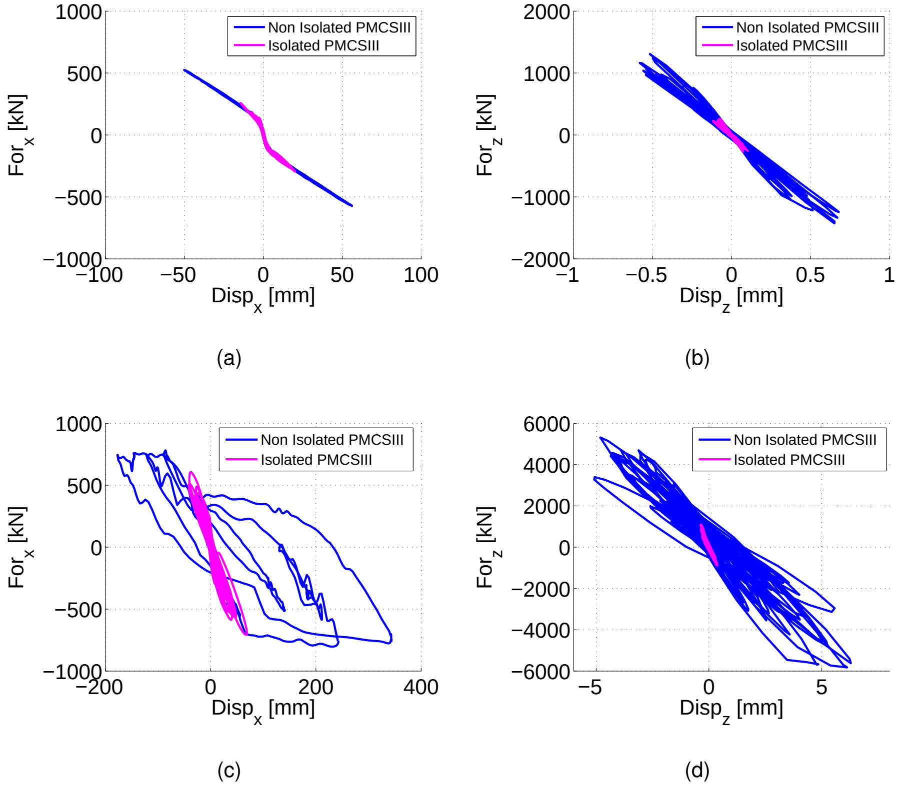

(a)

(b)

(c)

(d)

Figure 5.15: Numerical results of the RMCSIII:a-b)0.3g PGA ground motion; c-d) 1.5g PGA ground motion.

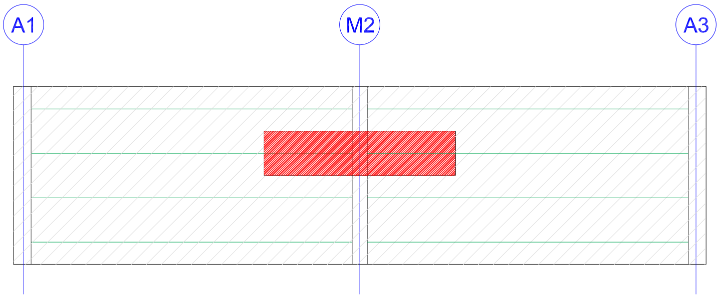

Figure 5.16: Position of the selected substructure on the bridge deck.

sidered according to the procedure proposed by Kumar et al. (1997). In particular, since the specimen was made of the same material as the prototype the stress

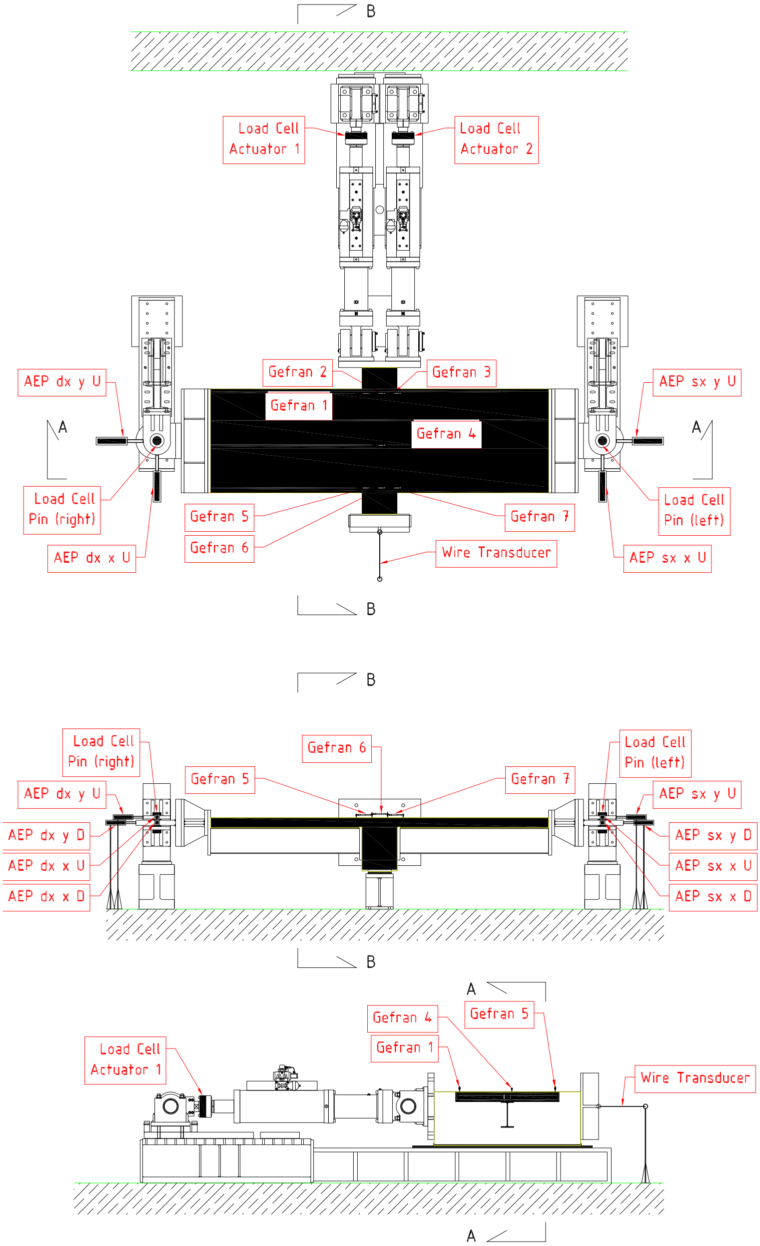

Figure 5.17: Experimental setup of transversal loadings tests.

identities $\sigma_{prot} = \sigma_{spec}$ was preserved. As a result, each quantity was scaled with the scale factors reported in Table 5.6.

The complete testing program was defined with the aim to test all the proposed

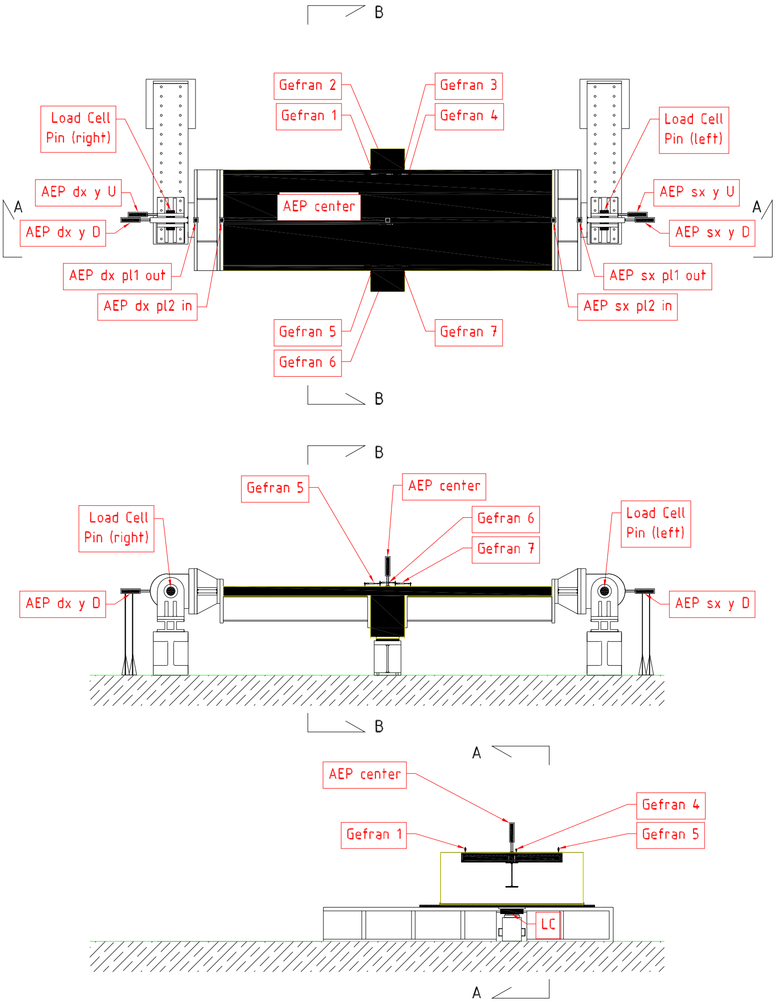

Figure 5.18: Experimental setup of vertical loading tests (Residual capacity).

| **Mass** | **Length** | **Stress** | **Force** | **Stiffness** |
|---|---|---|---|---|
| $s^3$ | $s$ | 1 | $s^2$ | s |

Table 5.6: Scale factors applied to each quantity.

joint solutions, as reported in Table 5.7. The setup configuration designed for the transversal test campaign is depicted in Figure 5.17. The substructured specimen was characterized by a center of gravity aligned with the two hinges at the bound-

| Test Name | Testing Protocol | Load direction | CCB Type |
|---|---|---|---|
| SQ1M | Monotonic | Transversal | Var. C DIN FB 104 |
| SQ2M | Monotonic | Transversal | DOMI - I |
| SQ3M | Monotonic | Transversal | DOMI - II |
| SQ1C | Cyclic | Transversal | Var. C DIN FB 104 |
| SQ2C | Cyclic | Transversal | DOMI - I |
| SQ3C | Cyclic | Transversal | DOMI - II |
| SQ3V | Monotonic | Vertical | DOMI - II |

Table 5.7: Testing program of the tests performed at the University of Trento.

aries this layout reproduces the substructures located on the neural axes of the deck. For the last test, that was conceived to investigate the residual vertical load-carrying capacity of the specimen already subjected to a certain level of damage, some modifications of the setup were needed, as schematically depicted in Figure 5.18.

Two electro-hydraulic actuators each of 1000 kN capacity, equipped with two load cells, indicated as *LoadCellActuator* 1 *and* 2 in Figure 5.17, applied the required displacement to the CCB by means of a thick steel plate. A steel stub with two layers of Teflon on its upper surface supported the bottom face of the CCB. The edges of the concrete slab were connected to steel pin hinges, i.e. *Load Cell Pin left* and *right* placed on a distance of $L_{hinge}$ = 5.70 m, by mean of a steel beam. The hinges were connected to the strong floor through heavy steel beam basements.

With the aim to record main deformations in the acute areas of each specimen, several sensors were installed. In particular, seven *Gefran* sensors were used to measure cracks opening in the interface between the concrete slab and the CCB, the sensors are LVDTs. With reference to both the DIN FB104 Variant C and the DOMI-I joint type, 22 strain gauges were applied on flanges of steel I-girders, steel re-bars and Nelson studs inside the CCB. Differently for the DOMI-II joint type, 19 strain gauges were placed inside the connection.

For the last test (SQ3V), as shown in Figure 5.18, vertical stiff columns were replaced by two stiff steel plates. The pin-hinges at the end of the specimen were turned 90° to reproduce the vertical case constraints. The load was applied to the specimen thought a vertical hydraulic jack of 1000 kN capacity, placed at the bottom of the CCB. A Load Cell (LC) and a steel plate were inserted between the jack and the CCB.

### 5.3.1 Loading protocols and test results

The experimental campaign was composed by two parts: *i*) transversal tests, monotonic and cyclc; *ii*) vertical monotonic test on the damaged SQ3C substructure to evaluate the residual capacity.
Firstly, mechanical characterization tests were performed to characterize each component as shown in Table 5.8.

Then, in order to evaluate both the yield displacement and the maximum ductility of the specimens, monotonic tests were carried out. Relevant force-displacement relationships are shown in Figure 5.19(a). Maximum values of force, moment and displacement, shown in Table 5.9 are comparable for all the three types of connections. These results showed that the out-of-plane capacity of specimens was governed by the concrete slab and the collapse mechanism mainly developed in that zone excluding effects related to the joint type.

| **Steel** | | | | **Concrete** | |
|---|---|---|---|---|---|
| **Steel Component** | **$f_y$[MPa]** | **$E_0$[MPa]** | **b[$-$]** | **$R_{cm}$[MPa]** | 60 |
| **SteelB450C $-\phi$8** | 527 | 196882 | 0.008 | **$f_{cm}$[MPa]** | 52 |
| **SteelB450C $-\phi$10** | 537 | 198264 | 0.008 | **$f_{cu}$[MPa]** | 42 |
| **Steel S460M flange** | 522 | 191650 | 0.006 | $\varepsilon_{co}$ | 0.0028 |
| **Steel S460M - web** | 538 | 203735 | 0.004 | $\varepsilon_{cu}$ | 0.0067 |
| **Steel10.9$\phi$16** | 776 | 203750 | 0.031 | **$E_{cm}$[MPa]** | 36050 |

Table 5.8: Mechanical properties of steel and concrete.

The loading protocol for cyclic tests was chosen after a preliminary analysis of the actual displacement of the bridge under seismic loading as described in Subsection 5.3.1. The investigations owing to small damage induced by the design earthquake suggested to apply a traditional ECCS loading protocol ECCS (1986) for steel elements shown in Figure 5.20(b). The procedure, adapted to SCC elements was derived on the basis of the yielding displacement $e_y^+$ of a monotonic response, calculated as indicated in Bursi et al. (2002) and schematically depicted in Figure 5.20(a). In order to conveniently define the yield displacement $e_y$, a yield limit state characterized by the displacement $e_y^+$ as well as by the corresponding reaction force $P_y^+$ must be defined. Such quantities have been traced on the linear branch of each response envelope obtained from monotonic tests, i.e. SQ1M, SQ2M, SQ3M. The trilinear approximation of each curve is evaluated on the basis of the equivalence between the dissipated energy and the best curve fitting between the actual nonlinear response and the idealized trilinear approximation up to ($e_{max}^+$, $P_{max}^+$). In a greater detail, a value of $e_y^+ = 7.98mm$, i.e. the lowest one between the three monotonic responses was selected. Since the monotonic failure displacement was about $40mm$, $6e_y = 48mm$ appeared to be enough to capture the collapse of specimens subjected to cyclic loading.

As in monotonic tests, the outcomes were fully comparable, as shown in Table 5.9. In a greater detail, mainly due to a different damage distribution both in tension and compression areas of the CCB, larger values of displacements were achieved with respect to monotonic tests, as depicted in Figure 5.19(c) and Figure 5.19(d). The first two tests SQ1C and SQ2C were carried out till failure. Conversely, the scope of the SQ3C/V was twofold: *i*) to reach a certain limit state in the deck corresponding to a repairable damaged condition (SQ3C), defined as 50% of spalling strain after Mackie et al. (2008) ; *ii*) to evaluate the vertical residual load-carrying capacity of the deck subjected to quasi-permanent lading combination(SQ3V).

The values of vertical loads required to reach all the SLS foreseen in EN1990-2 (2002) were evaluated. In detail, it can be observed that all SLS corresponding to the quasi-permanent (q/p), frequent (freq) and characteristic (char) loading combinations did not damage the deck, in fact were carried in the linear regime of the specimen. In addition, also the ULS combination foreseen in EN1990-2 (2002) left the specimen SQ3V in its linear regime, as shown in Figure 5.21(a).

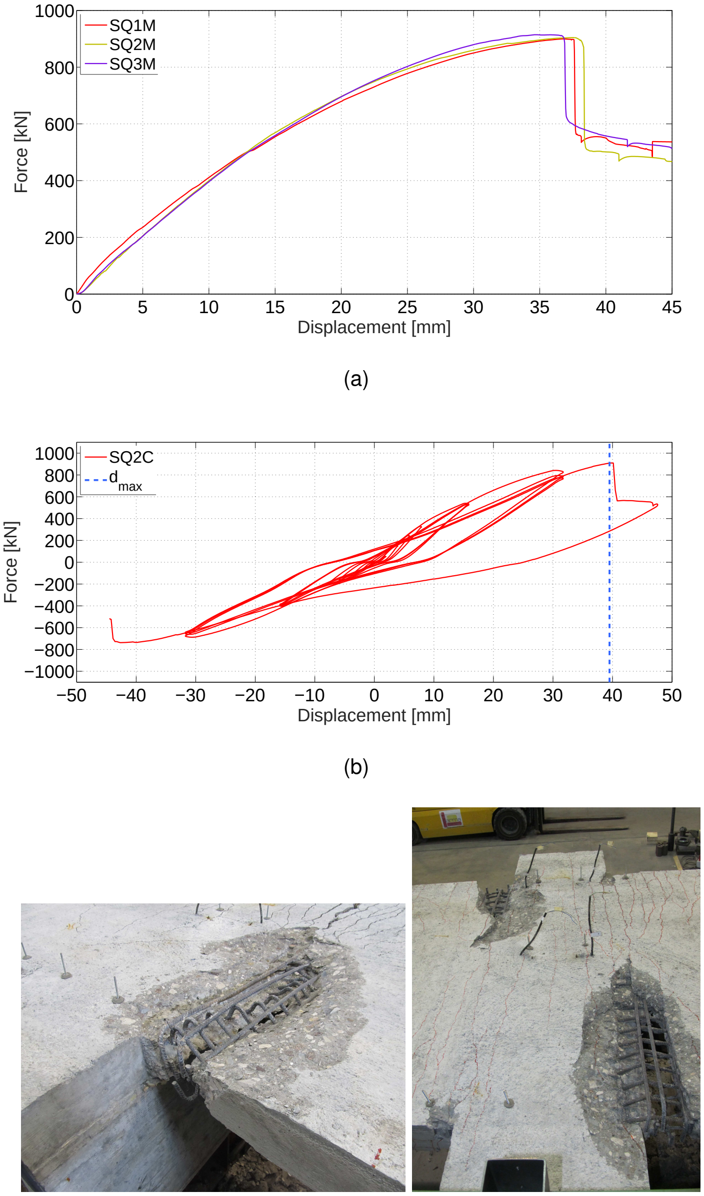

(a)

(b)

(c)

(d)

Figure 5.19: Experimental results in the scale of specimen: a) comparison between monotonic tests; b) results of the SQ2C test; c) view of the SQ3M specimen at collapse; d) view of the SQ2C specimen at collapse.

| Test | $F_{MAX}[kN]$ | $d_f[mm]$ | $M_{MAX}[kNm]$ |
|---|---|---|---|
| SQ1M | 906 | 37.6 | 1291 |
| SQ2M | 922 | 38.3 | 1314 |
| SQ3M | 922 | 36.8 | 1314 |
| SQ1C | 964 | 42.4 | 1373 |
| SQ2C | 948 | 40.1 | 1350 |
| SQ3C | 859 | 30.3 | 1224 |

Table 5.9: Forces and displacements in the scale of specimen of each test at collapse.

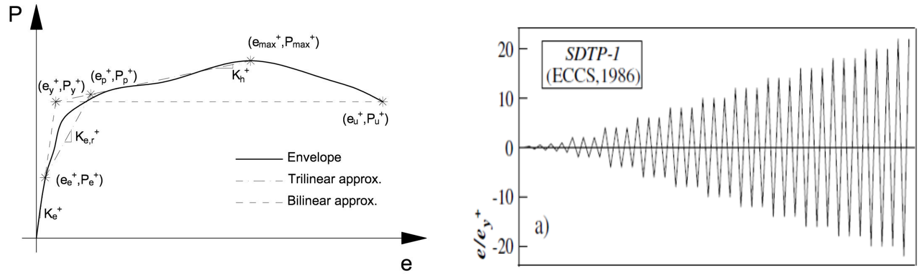

(a) (b)

Figure 5.20: Loading protocol: a) envelope proposed by Bursi et al. (2002); b) ECCS procedure (after ECCS (1986)).

## 5.4 Improvement of FE models based on springs-based modelling

In this cases study the improvement procedure resulted to be very challenging due to the multiple effects conditioning the experimental steps.

Firstly, due to the high stiffness of the specimen ($\approx 215000N/mm$), the setup flexibility during the tests could not be neglected. For this reason, a system of discrete springs was used to explain some unexpected setup deformations.

Secondly, the specimen itself showed a local characteristic behavior in the connection zone between CCB and concrete slab that suggested the implementation of a CMM.

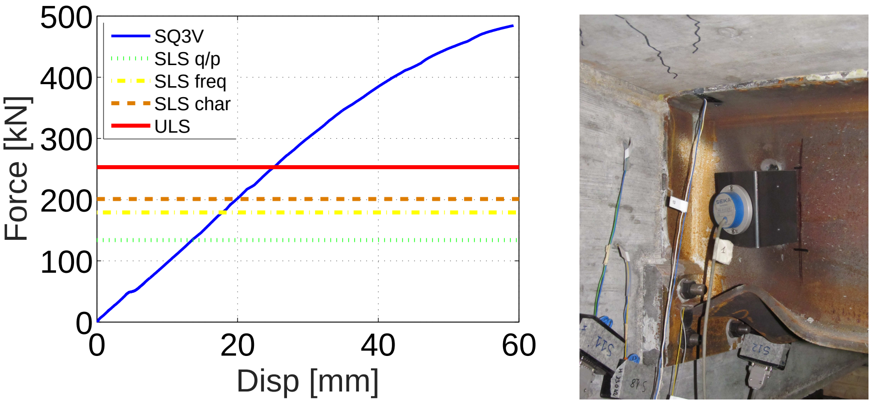

(a)

(b)

Figure 5.21: Experimental results relevant to SQ3V: a) force-displacement; b) instability of the bottom flange after specimen collapse.

The analysis was focused on DOMI-II connection which was the most interesting and innovative joint solution.

### 5.4.1 Evaluation and implementation of setup flexibility

The first phase of improvement procedure has been devoted to the evaluation and implementation of setup flexibility.

The flexibility effects disclosed by the analysis of force-displacement responses of tests, in fact, as can be appreciated in Figure 5.22 the external wire transducer (WT) recorded a smaller displacement if compared with the Temposonic transducer of the actuators. In meant that some differential displacements happened during the tests. Along this line, the DoFs chosen to investigate this flexibility problem were the ones shown in Figure 5.23(a) and equivalent to the one monitored with additional instruments positioned before the SQ3C test. They allowed to evaluate the deformations of the different components of the test setup. In greater detail, the deformations of the bolted joint between the upper part of the hinge and the ground ($U3$ and $U5$), the deformations of the hinges itself ($U4 - U3$ and $U6 - U5$) and the longitudinal opening of the hinges ($U7$ and $U10$). In Figure 5.24 are shown the effects of the additional deformations of the setup on the test SQ3C outcomes. If compared with Figure 5.22 it can be appreciated as also the components inside

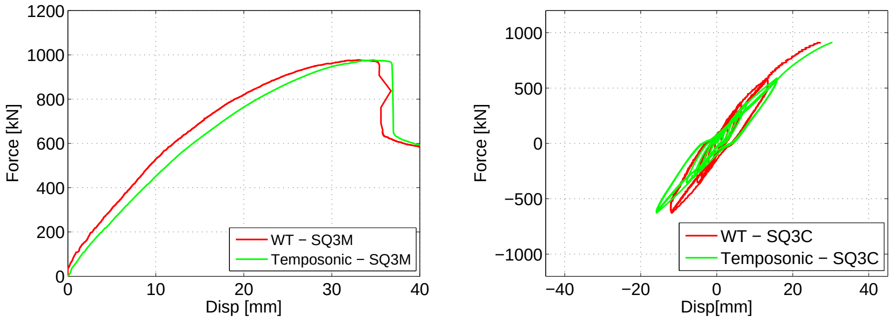

(a) (b)

Figure 5.22: Force displacement results of SQ3 tests (DOMI-II type joint): a) monotonic test; b) cyclic test.

the hinges deformed spoiling the global outcomes. As a result, the global stiffness of the substructure was apparently reduced.

To overpass these problem, the relative displacements described before, combined with the *Load Cell Pin left* and *right* outputs allows to define 6 different springs able to reproduce the actual behavior of the experimental setting, i.e. 3 on the right side and 3 on the left side of the setup, as shown in Figure 5.23(b). In detail, these springs were implemented through trilnear approximation laws with values reported in Table 5.10. The constitutive laws of the 4 springs parallel to the applied loads are shown in Figure 5.25. These springs, represented a fundamental results required for the analysis of the experimental outcomes and were used to validate the CMM described in Section 5.4.2. Since the flexibility of the setup involved mainly the translational DoFs (parallel to the loads), it was possible to conclude that the effects did not affect the global response of specimens and the relevant collapse local mechanism were preserved.

To prove the effectiveness of this equivalent system of springs a quick analytical calculation has been done assuming the springs as a series springs system. The objective was to reproduce the global behavior depicted in Figure 5.22(a) especially the curve based on the temposonic data. That curve in fact includes all the unexpected deformation of the setup.

Firstly, the global stiffness provided by that curve was evaluated considering the

| **Spring name** | **K1a** | **K2a** | **K1b** | **K2b** | **K1c** | **K2c** |
|---|---|---|---|---|---|---|
| **Dof** | $U_7$ | $U_{10}$ | $U_3$ | $U_5$ | $U_4 - U_3$ | $U_6 - U_5$ |
| $K_1[\frac{kN}{mm}]$ | 103.7 | 339 | 1011.7 | 210.5 | 175.7 | 64.3 |
| $F_1$[kN] | 5.2 | 20 | 17.2 | 86.5 | 101 | 24 |
| $d_1$[mm] | 0.053 | 0.059 | 0.017 | 0.411 | 0.575 | 0.373 |
| $K_2[\frac{kN}{mm}]$ | 136 | 14.76 | 505.9 | 153.6 | 600 | 406.6 |
| $F_2$[kN] | 77.5 | 59 | 128 | 179 | 110 | 209 |
| $d_2$[mm] | 0.581 | 2.706 | 0.236 | 1.013 | 0.590 | 0.828 |
| $K_3[\frac{kN}{mm}]$ | 36.9 | 21.73 | 270.7 | 247 | 1200 | 390 |
| $F_3$[kN] | 108 | 68 | 428 | 451 | 428 | 452 |
| $d_3$[mm] | 1.406 | 3.12 | 1.344 | 2.114 | 0.855 | 1.45 |

Table 5.10: Parameters identified to represent the flexibility of the setup.

reaction force at the initial steps of the test, equivalent to a displacement of 1 mm. As a result the initial experimental stiffness can be written:

$$K_{ini-SQ3M} = \frac{RF_{1mm}}{1mm} \approx 65\frac{kN}{mm} \tag{5.11}$$

Then, it was possible to quantify an analytical stiffness expected from the geometry of the specimen, in this case evaluated considering only the concrete slab that provides the larger contribute in term of inertia along the strong axes of specimen for the initial steps of load:

$$K_{an} = \frac{48EI}{L^3} = \frac{48 \cdot 34000 \cdot \frac{125 \cdot 1325^3}{12}}{5700^3} = 213\frac{kN}{mm} \tag{5.12}$$

Now, the springs of the setup acting in the transversal direction can be rewritten as follow:

$$K_b = K1b + K2b = 1011.7 + 210.5 = 1222\frac{kN}{mm} \tag{5.13}$$

$$K_c = K1c + K2c = 175.7 + 64.3 = 240\frac{kN}{mm} \tag{5.14}$$

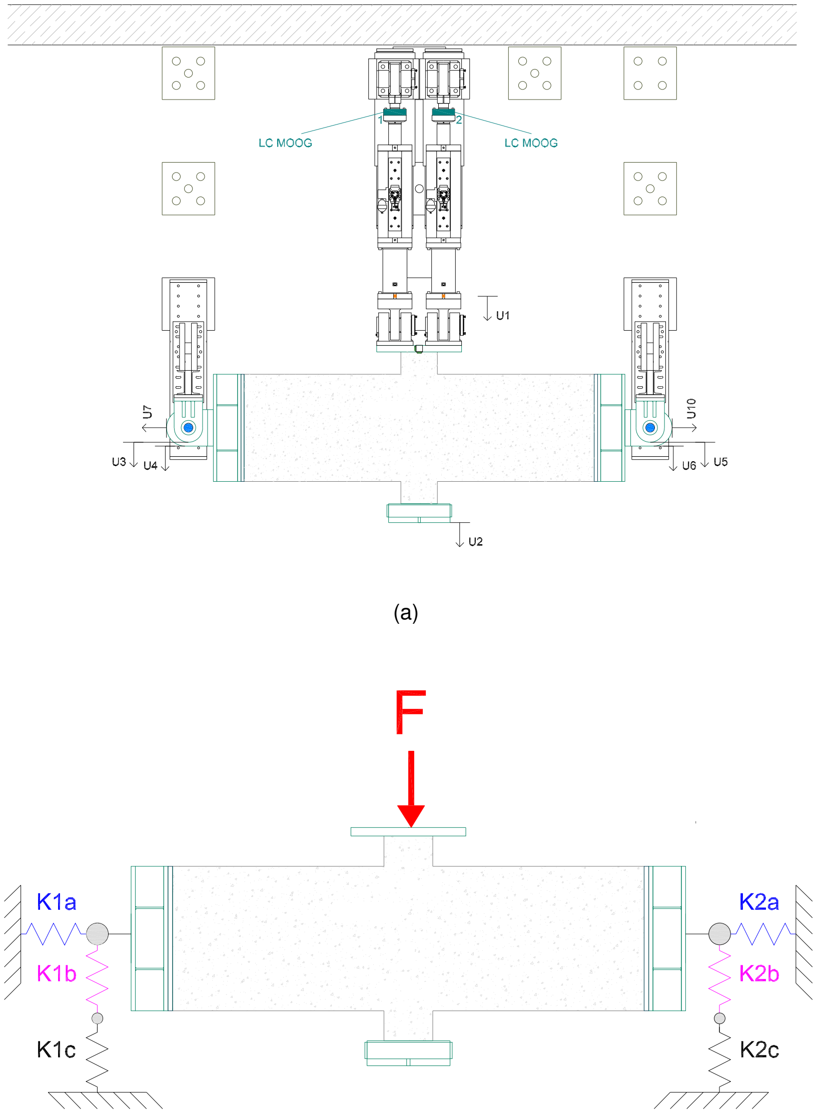

(b)

Figure 5.23: View of the substructure with additional instruments: a) additional degrees of freedom monitored during the test; b) idealization of the setup with the ideal springs

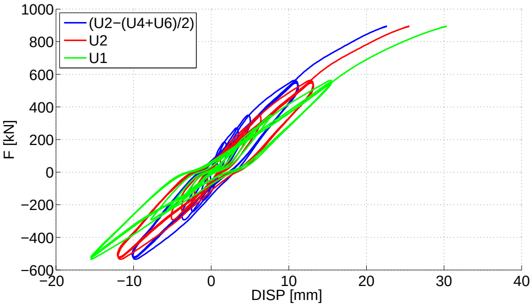

Figure 5.24: Effects of the setups' deformability

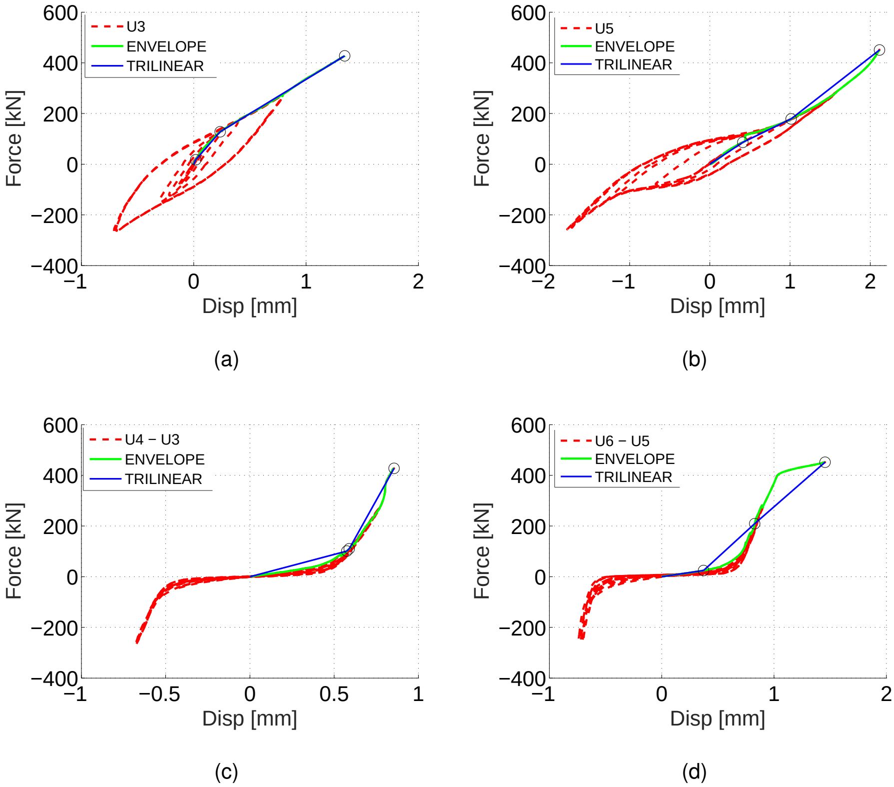

(a)

(b)

(c)

(d)

Figure 5.25: Experimental data relevant to the most important Dofs to evaluate the setup deformability: a) K1b; b) K2b; c) K1c; d) K2c.

The global stiffness of a general in series system can be quantified as:

$$K_{sys} = (\sum_{i}^{ns} \frac{1}{K_i})^{-1} \tag{5.15}$$

where *ns* represents the number of springs in the system. Finally, the global stiffness of the equivalent system was evaluated as follows:

$$K_{sys} = (\frac{1}{Kb} + \frac{1}{Kc} + \frac{1}{Kan})^{-1} = 103\frac{kN}{mm} \approx K_{ini-SQ3M} \tag{5.16}$$

As can be appreciated the stiffness of the series system is very close the one evaluated by the experimental test SQ3M, it meant that the spring system was suitable to explain the problem of setup flexibility. These additional springs allowed to compare the FE models with the whole set of experimental data also for the tests in which the differential displacements were not recorded properly.

### 5.4.2 A Component-Based Mechanical Model for bridge connections

A CMM of the DOMI-II type connection shown in Figure 5.7 has been implemented in the Opensees environment (Mazzoni et al. (2009)). It has been derived from the components approach employed in EN1993-1-8 (2005) to evaluate both strength and initial stiffness of steel joints in buildings. As already anticipated in Section 5.3 the flexibility of the setup was considered by means of additional discrete elements capable of encompassing the boundaries of the testing equipment. In Figures 5.26(a) and 5.26(b) are depicted a views of the CMM and a 3D view of the specimen and the setup, respectively. Therefore, to model the substructure, nonlinearities have been explicitly considered for the concrete slab, steel girders, Nelson studs and prestressing Dywidag bars. In this respect, two different nonlinear elements have been employed: *i*) fiber-based elements for the element outside the CCB; and *ii*) nonlinear springs, i.e. *ZeroLength* Opensees elements for the elements close and inside the CCB. The nonlinearity of concrete in the fiber-based elements has been considered by means of the *Concrete*01 material, relevant stress strain relationship is based on the Kent-Scott-Park concrete model with no tensile strength as depicted in Figure 3.9(a). In order to best fit the behavior of the slab close to the CCB, the tensile strength has been considered only for *ZeroLength* elements, i.e. internal elements of CCB. Youngs modulus, strength and strain compression values for concrete have been evaluated and then implemented using experimental data gathered in Table 5.8 and accordingly with CEB-FIP (1993).
The mechanical behavior of both steel rebars and girders has been modelled tak-

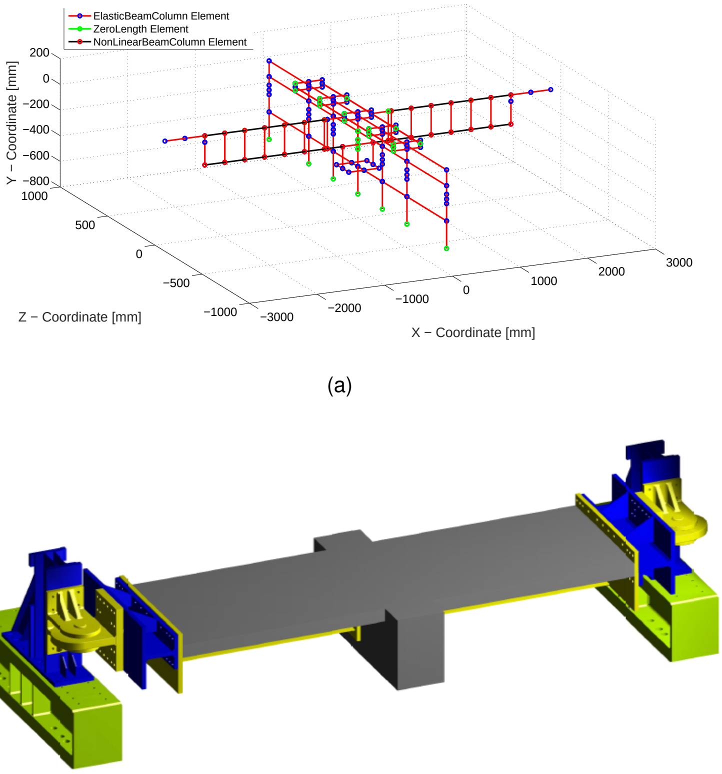

(a)

(b)

Figure 5.26: View of the substructure considered for the definition of component-based mechanical model: a) view of the elements; b) 3D view.

ing into account mechanical properties reported in Table 5.8. Therefore, components have been separately implemented for steel webs, flanges and different rebar types. For fiber-based elements, the *Steel*02 material based on the Giuffr-Menegotto-Pinto was implemented. In this respect, Table 5.8 reports the input parameters implemented in Opensees, i.e. the yield strength $f_y$, the initial elastic modulus $E$, the strain-hardening ratio $b$, as shown in Figure 3.9(b). The transition from elastic to plastic branches is governed by three parameters, i.e. $R_0$, $C_{R1}$ and $C_{R2}$ set as 15, 0.925 and 0.15, respectively. The strength of each Nelson stud has been calculated according to EN1994-1-1 (2006) and EN1994-2 (2006) whilst the related nonlinear behavior has been evaluated by means of the shear load-slip relationships proposed by Gattesco and Giuriani (1996). Rigid links have been used to model the vertical head plates welded on steel girders and directly in contact with the transverse CCB. The stiffness of the CCB has been evaluated assuming the compressive force coming from the girder acting uniformly on a surface equal to the area of the vertical head plate. Moreover, the two layer of prestressing bars in the bottom area of the CCB have been modelled by means of two *ZeroLength* elements per each side of CCB. The complete set of components considered in both the CMM and the remaining part of the substrucure are shown in Figures 5.27(a) and 5.27(b) and reported in Table 5.11. The interaction between simplified spring-based elements and fiber-based elements, i.e. the concrete slab and the steel girders outside the CCB have been implemented by using rigid links. Differently from elements endowed with fibre section, a force-displacement relationship was required for *ZeroLength* elements as the one depicted in Figure 3.10. Therefore, the group of springs composed of $TC1t[\phi 10 rebars]$, $TC1b[\phi 8 rebars]$ and $TC2$ shown in Figure 5.27(a) includes the properties of part of rebars and of concrete slab. From Figure 5.27(b) a reader can observe that 5 group of the aforementioned springs were needed to cover the whole slab width. Hereinafter is reported the formulation of the constitutive law relevant to each component.

| **Name** | **Description** | **Direction** |
|---|---|---|
| $TC1t$ | Concrete and re-bars top layer axial response in the slab | X |
| $TC1b$ | Concrete and re-bars bottom layer axial response in the slab | X |
| $TC2$ | Shear of the concrete slab | Z |
| $TC3u$ | Shear on the upper group of studs of the inner plate | X |
| $TC3l$ | Shear on the lower group of studs of the inner plate | X |
| $TC4$ | Shear on all the studs of the inner plate | Y |
| $TC5$ | Shear on the inner plate | Z |
| $TC6$ | Prestressing bars and compression zone of CCB | X |

Table 5.11: Main components of the component-based mechanical model.

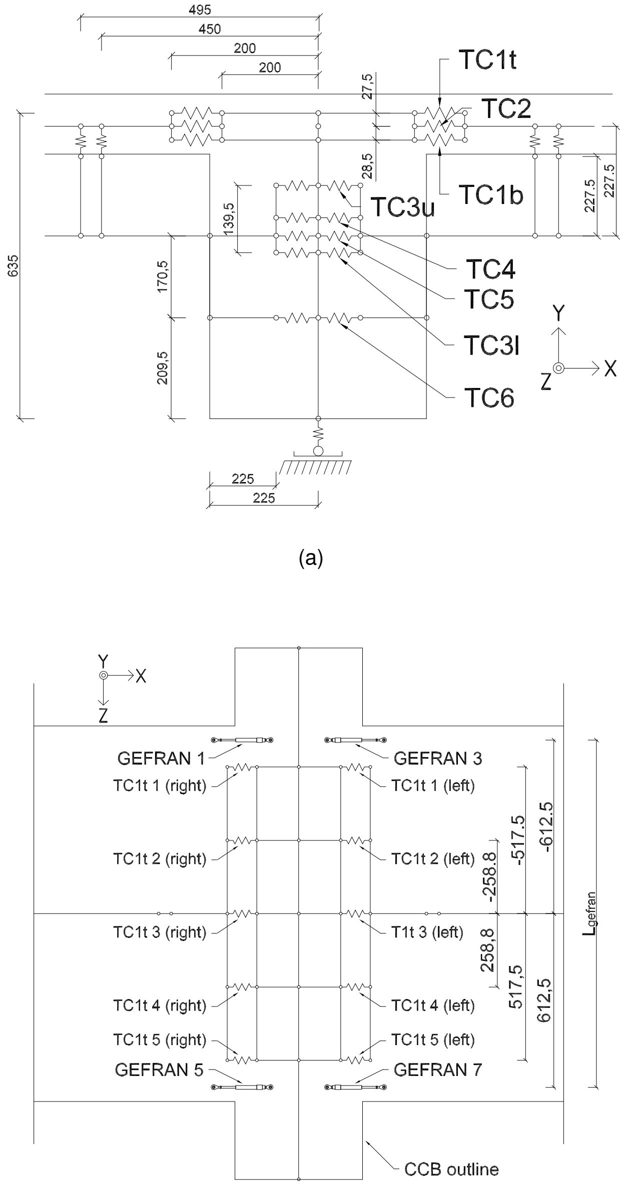

(a)

(b)

Figure 5.27: Views of the the component-based mechanical model: a) frontal view; b) in plane view.

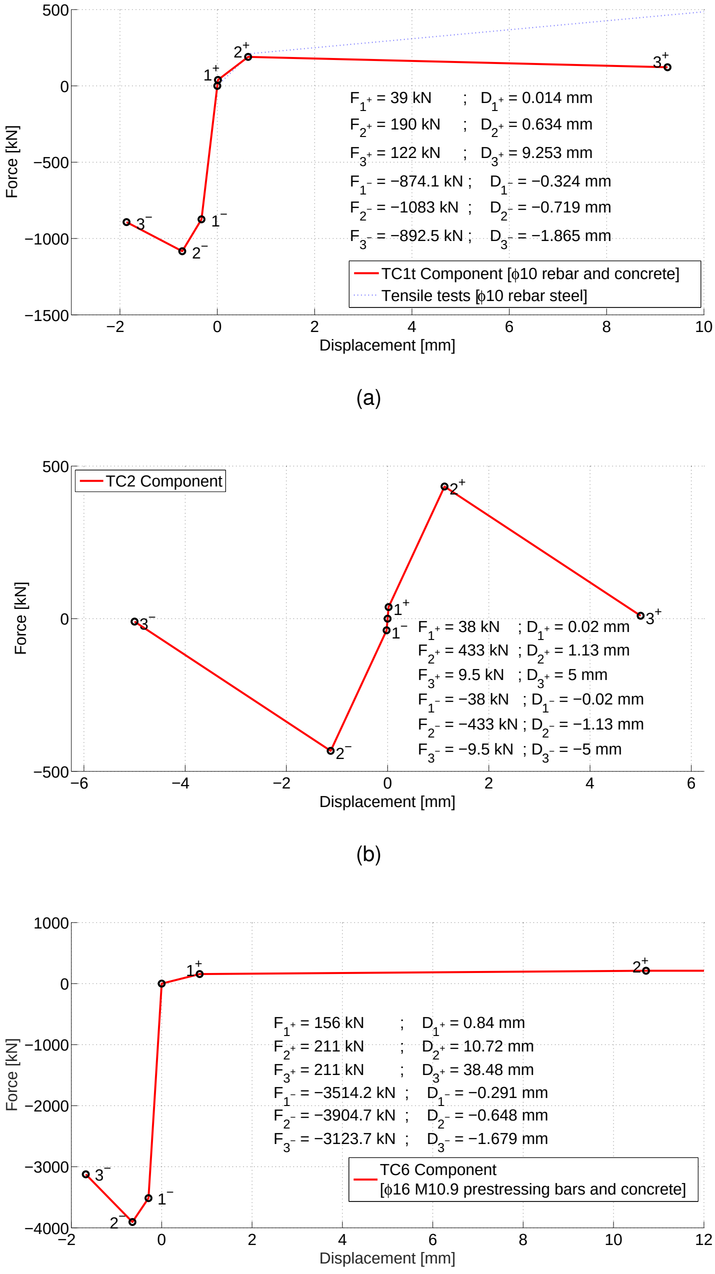

(a)

(b)

(c)

Figure 5.28: Constitutive laws of the main components: a) TC1t; b) TC2; c) TC6.

- **Component TC1t**[$\phi 10 rebars$]: This component reproduces the top layer of rebars and concrete. The tension stiffening effect was implemented following the specifications of CEB-FIP (1993), whilst the force displacement relationship considered for this component was based on the Kent-Scott-Park model depicted in Figure 3.9(a). The hysteretic material for the $TC1t[\phi 10 rebars]$ expressed in terms of force-displacement relationship is depicted in Figure 5.28(a). It has been defined by six points, 3 for the compression side, i.e. $1^-$,$2^-$,$3^-$, and three for tension side, i.e. $1^+$,$2^+$,$3^+$. Moreover, we intended to accurately reproduce tests results at collapse; therefore, additional hypothesis have been made. In detail: *i*) the tensile strength of concrete is halved and equal to $f_t = 0.5 f_{ctm}^{EC2} = 2MPa$;*ii*) the yield strength of $\phi 8$ and $\phi 10$ rebars obtained from tensile tests is reduced by a factor of 0.9. Nonetheless, these values are higher than those required in NTC2008 (2008); *iii*) the ultimate steel strength was reduced to 50 % of the original value. Instead of a hardening branch, a softening was imposed. Thus deterioration processes occurred inside the slab before failure, e.g. slips between concrete and rebars, were taken into account. The relevant relationships for negative and positive regimes, respectively, are listed herein:

$$F_{1-} = 0.9 A_c f_{cm} + n_{s,rebars,spring}(A_{rebar_i} E_{rebar_i} \varepsilon_{1-}) \tag{5.17}$$

$$D_{1-} = l_{spring} \varepsilon_{1-} = l_{spring} \frac{0.9 f_{cm}}{E_{cm}} \tag{5.18}$$

$$F_{2-} = 0.9 A_c f_{cm} + n_{s,rebars,spring}(A_{rebar_i} \sigma_{s,peak,rebar_i}) \tag{5.19}$$

$$D_{2-} = l_{spring} \varepsilon_{2-} = l_{spring} \frac{2 f_{cm}}{E_{cm}} \tag{5.20}$$

$$F_{3-} = 0.8 A_c f_{cm} + n_{s,rebars,spring}(A_{rebar_i} \sigma_{s,u,rebar_i}) \tag{5.21}$$

$$D_{3-} = l_{spring}\varepsilon_{3-} = l_{spring}\varepsilon_{cu} \tag{5.22}$$

with:

$$\sigma_{s,peak,rebar_i} = E_{rebar_i}\varepsilon_{2-} \tag{5.23}$$

$$\begin{aligned}\sigma_{s,u,rebar_i} =& E_{rebar_i}\varepsilon_{s,y,rebar_i} + \frac{f_{s,u,rebar_i} - f_{s,y,rebar_i}}{\varepsilon_{s,u,rebar_i} - \varepsilon_{s,y,rebar_i}} \\ & (\varepsilon_{3-} - \varepsilon_{s,y,rebar_i})\end{aligned} \tag{5.24}$$

$$F_{1+} = N_r = \frac{A_C(1 + \alpha\rho)}{f_t} \tag{5.25}$$

$$D_{1+} = \frac{N_r}{n_{s,rebars,spring}A_{rebar_i}E_{s,rebar_i} + A_C E_{cm}} l_{spring} \tag{5.26}$$

$$F_{2+} = n_{s,rebars,spring}A_{rebar_i}f_{s,y,rebar_i} \tag{5.27}$$

$$D_{2+} = (\varepsilon_{s,y,rebar_i} - \beta_t \Delta\varepsilon_{sr})l_{spring} \tag{5.28}$$

$$F_{3+} = n_{s,rebars,spring}A_{rebar_i}f_{s,u,rebar_i} \tag{5.29}$$

$$\begin{aligned}D_{3+} =& [\varepsilon_{s,y,rebar_i} + \delta(1 - \frac{N_r}{n_{s,rebars,spring}A_{s,rebar_i}f_{s,y,rebar_i}}) \\ & \varepsilon_{s,u,rebar_i} - \varepsilon_{s,y,rebar_i}]l_{spring}\end{aligned} \tag{5.30}$$

where:

$$\alpha = \frac{E_{s,rebar_i}}{E_{cm}} \tag{5.31}$$

$$\rho = \frac{n_{s,rebars,spring} A_{rebar_i}}{A_C} \tag{5.32}$$

$$\begin{aligned}\Delta\varepsilon_{sr} &= \frac{\sigma_{1+}}{E_{s,rebar_i}} - \varepsilon_{1+} \\ &= \frac{N_r}{(n_{s,rebars,spring} A_{rebar_i} E_{s,rebar_i}) E_{s,rebar_i}} \\ &- \frac{N_r}{(n_{s,rebars,spring} A_{rebar_i} E_{s,rebar_i} + A_C E_C m}\end{aligned} \tag{5.33}$$

$$\beta_t = 0.4 \qquad for \quad short \quad term \quad loadings \tag{5.34}$$

- **Component TC1b**[$\phi 8 rebars$]: This component reproduces the bottom layer of rebars and concrete. The equations implemented in the model were the same proposed for the $TC1t[\phi 10 rebars]$ with the adaptation of the rebar diameter.

- **Component TC2:** This component represents the shear resistance of the slab $V_Z$, by means of elements located in the central layer. In order to allow longitudinal forces to be transferred through top and bottom layers only, these springs have been implemented with negligible axial stiffness and a rigid behavior was assigned to the remaining degrees of freedom. In particular, the shear behavior has been implemented following Kelly (2004) and Bentz et al. (2007); as a result, $V_{crack,z}$, $V_{peak,z}$, $V_{res,z}$, $d_{crack,z}$, $d_{peak,z}$, $d_{res,z}$ ,and therefore $F_1$, $F_2$, $F_3$, $D_1$, $D_2$ and $D_3$, illustrated in Figure 5.28(b), have been quantified as follows:

$$V_{crack,z} = \frac{\beta (f_{cm})^{0.5} (h_{slab} d_{z,slab})}{n_{spring}} \tag{5.35}$$

$$d_{crack,z} = \frac{V_{crack,z} n_{spring} l_{spring}}{G_C h_{slab} d_{z,slab}} \tag{5.36}$$

$$V_{peak,z} = V_{crack,z} + 1.25 V_{s,z} \tag{5.37}$$

$$d_{peak,z} = 0.0045 l_{spring} \tag{5.38}$$

$$V_{res,z} = 0.25 V_{crack,z} \tag{5.39}$$

$$d_{res,z} = 0.02 l_{spring} \tag{5.40}$$

with:

$$V_{s,z} = \frac{2A_{stirrup} f_{y,stirrup} 0.9 d_{z,slab}}{s_{stirrup} n_{spring}} \tag{5.41}$$

- **Components TC3u**: This component is one of the characteristic components of the DOMI-II type connection shown in Figure 5.7,i.e. the Nelson studs welded on the girder web protrusion. In detail this component is the one implemented to take into account the shear resistance in the horizontal (X) direction. The relevant springs linked with rigid elements are shown in Figure 5.27(a). In greater detail the *TC3u* component represents the shear resistance of six studs, i.e. three studs on each side of the web panel on the top layer of studs. The maximum force of the component Pr,tot reads:

$$P_{r,tot,TC3t} = 6 \cdot min((\frac{0.8 f_{y,ns} \pi (d_{ns})^2)}{4}; 0.29\alpha (d_{ns})^2 (f_{cm} E_{cm})^{0.5}) \tag{5.42}$$

$$K_{r,tot,TC3t} = 6 \cdot K_{i,ns} \tag{5.43}$$

- **Components TC3l**: This component represents the bottom layer of studs on the DOMI-II type connection, the values of stiffness and strength were evaluated as presented for the *TC3u* component.

- **Components TC4:** This component has been implemented to take into account the shear resistance and stiffness of Nelson studs in the vertical (Y) direction, conversely from the TC3 relevant to the horizontal (X) direction. In detail, each spring of the *TC*4 component represents the shear resistance of twelve studs, i.e. six studs on each side of the web panel. As before, maximum force Pr,tot has been evaluated as follows:

$$P_{r,tot,TC4} = 12 \cdot min((\frac{0.8f_{y,ns}\pi(d_{ns})^2)}{4}; 0.29\alpha(d_{ns})^2\sqrt{f_{cm}E_{cm}} \quad (5.44)$$

$$K_{r,tot,TC4} = 12 \cdot K_{i,ns} \quad (5.45)$$

- **Components TC5:** In this case, a *ZeroLength* element was employed for the web panel. It reproduces both the shear stiffness and strength of the web plate in the Z direction evaluated accordingly with EN1993-1-1 (2005).

$$R_{TC5} = \frac{A_{shear}f_y}{\sqrt{3}} \quad (5.46)$$

$$K_{TC5} = GA_{shear} \quad (5.47)$$

- **Component TC6:** Prestressing bars connecting the head plates on both sides of the CCB and the compression zone, in the hypothesis of uniform compression distribution, of the CCB, have been implemented by a hysteretic material implemented in a *ZeroLength* element. Two elements reproducing half of the total bar length have been inserted for each side of CCB. In this condition, in Figure 5.28(c) is shown the force-displacement relationship for a spring length of $225mm$. As a result, the relevant values can be quantified as follows:

$$F_{1-} = 0.7f_{cm}A_c \quad (5.48)$$

$$D_{1-} = l_{spring}\frac{0.9f_{cm}}{E_{cm}} \quad (5.49)$$

$$F_{2-} = f_{cm}A_c \quad (5.50)$$

$$D_{2-} = l_{spring}\frac{2f_{cm}}{E_{cm}} \tag{5.51}$$

$$F_{3-} = 0.8 f_{cm} A_c \tag{5.52}$$

$$D_{3-} = \varepsilon_{c,u} l_{spring} \tag{5.53}$$

The relevant tension branch has been implemented by using *ad hoc* component test data whilst the prestressing force applied during the test was considered as an external load on the CMM.

### 5.4.3 Validation and calibration of component-based mechanical model

Here the procedure of improvement relative to FE models was used to prove the effectiveness of the CMM of DOMI-II connection.

The numerical outcomes have been compared with the SQ3M test results presented in Subsection 5.3.1. In detail, attention was devoted to the behavior of *ZeroLength* elements reproducing the slab CCB interface, i.e. the $TC1t$ and $TC1b$ component that resulted to be the most significant for the case study. Furthermore, test results demonstrated the high stiffness of specimens and allowed to identify collapse mechanisms characterized by concrete crushing in interface regions. The influence of dead loads and self-weight on the structural response was negligible compared to the applied transversal actions. Furthermore, the other components of the DOMI-II type connection, i.e. $TC2$, $TC3u$, $TC3l$, $TC4$, $TC5$, $TC6$ , were lightly solicited.

As a result, the benchmark functions and the error quantities have been chosen. In greater detail the validation and calibration benchmarks were:

$$B_1^{Val} = [f_{y-B450C\phi 8mm}] \tag{5.54}$$

$$B_2^{Val} = [E_{0-B450C\phi 8mm}] \tag{5.55}$$

$$B_3^{Val} = [f_{u-B450C\phi 8mm}] \tag{5.56}$$

$$B_4^{Val} = [f_{y-B450C\phi 10mm}] \tag{5.57}$$

$$B_5^{Val} = [E_{0-B450C\phi 10mm}] \tag{5.58}$$

$$B_6^{Val} = [f_{u-B450C\phi 10mm}] \tag{5.59}$$

$$B_7^{Val} = [E_{0-S460M-flange}] \tag{5.60}$$

$$B_8^{Val} = [E_{0-S460M-web}] \tag{5.61}$$

$$B_9^{Val} = [E_{0-M10.9\phi 16mm}] \tag{5.62}$$

$$B_{10}^{Val} = [f_{cm}] \tag{5.63}$$

$$B_{11}^{Val} = [E_{cm}] \tag{5.64}$$

$$B_{12}^{Val} = [f_t] \tag{5.65}$$

$$B_{13}^{Val} = [Elongation\ \ of\ \ concrete\ \ slab\ \ right\ \ side] \tag{5.66}$$

$$B_{14}^{Val} = [Elongation\ \ of\ \ concrete\ \ slab\ \ left\ \ side] \tag{5.67}$$

$$B_{1}^{Cal} = [Moment - Curvature\ \ law\ \ on\ \ the\ \ right\ \ side\ \ of\ \ CCB] \tag{5.68}$$

$$B_{2}^{Cal} = [Moment - Curvature\ \ law\ \ on\ \ the\ \ left\ \ side\ \ of\ \ CCB] \tag{5.69}$$

$$B_{3}^{Cal} = [GlobalForce - Displacement\ \ law\ \ ] \tag{5.70}$$

$$B_{4}^{Cal} = [Energy\ \ dissipation\ \ right\ \ side] \tag{5.71}$$

$$B_{5}^{Cal} = [Energy\ \ dissipation\ \ left\ \ side] \tag{5.72}$$

In this case the comparison functions used to evaluate the difference between benchmarks and FE models were the NRMSEs adapted to validation and calibration cases:

$$D_i(M, B_i^{Val}) = NRMSE_i(M, B_i^{Val}) = \frac{\sqrt{\frac{1}{n}\sum_{i=1}^{n}(M - B_i^{Val})^2}}{max(B_i^{Val}) - min(B_i^{Val})} \tag{5.73}$$

$$D_i(M, B_i^{Cal}) = NRMSE_i(M, B_i^{Cal}) = \frac{\sqrt{\frac{1}{n}\sum_{i=1}^{n}(M - B_i^{Cal})^2}}{max(B_i^{Cal}) - min(B_i^{Cal})} \tag{5.74}$$

With regard the validation aspects, among the material parameters, also the elongations predicted by five springs of CMM positioned on the two interfaces and the experimental data provided by the external *Gefran* sensors were compared with $B_{13}^{Val}$ and $B_{14}^{Val}$ to prove that composite slab sections remain plane and agreed with

| **Calibrated CMM** | | | | | |
|---|---|---|---|---|---|
| | $D_1^V$ | $D_2^V$ | $D_3^V$ | $D_4^V$ | $D_5^V$ |
| $w_k^{Val}$ | 1 | 1 | 1 | 1 | 1 |
| SQ3M | 0.1 | 0 | 0.5 | 0.1 | 0 |
| | $D_6^V$ | $D_7^V$ | $D_8^V$ | $D_9^V$ | $D_{10}^V$ |
| $w_k^{Val}$ | 1 | 1 | 1 | 1 | 1 |
| SQ3M | 0.5 | 0 | 0 | 0 | 0 |
| | $D_{11}^V$ | $D_{12}^V$ | $D_{13}^V$ | $D_{14}^V$ | |
| $w_k^{Val}$ | 1 | 0.8 | 1 | 1 | |
| SQ3M | 0 | 0.5 | 0.026 | 0.078 | |
| $D_{Tot}^V = 0.121$ | | | | | |
| | $D_1^C$ | $D_2^C$ | $D_3^C$ | $D_4^C$ | $D_5^C$ |
| $w_k^{Cal}$ | 1 | 1 | 1 | 1 | 1 |
| SQ3M | 0.075 | 0.038 | 0.093 | 0.08 | 0.01 |
| $D_{Tot}^C = 0.059$ | | | | | |

Table 5.12: Results of component-based mechanical model during validation phase

the sensors, as shown in Figures 5.31(a) and 5.30(b).

In greater detail, calibration-wise the curvature adopted in the benchmark functions $B_1^{Cal}$ and $B_2^{Cal}$ was evaluated as follows:

$$\chi = \frac{\mid \varepsilon_{edge}^{+} \mid + \mid \varepsilon_{edge}^{-} \mid}{L_{Gefran}} = \frac{\mid \frac{d_{edge}^{+}}{L_{ref}} \mid + \mid \frac{d_{edge}^{-}}{L_{ref}} \mid}{L_{Gefran}} \tag{5.75}$$

where the reference length $L_{ref}$ was set equal to the instrument initial length of *Gefran* LVDTs, i.e 200$mm$. Moreover, $L_{Gefran}$ defined the distance between *Gefran* sensors located on the external sides of the concrete slab: it was equal to 1225$mm$ as shown in Figure 5.27(b). The curvature $\chi$ was associated to the bending moment at the CCB about the concrete slab strong axis. As a result, in Figure 5.30 the comparisons between experimental and numerical curvatures relevant ot right and left sides of CCB interface.

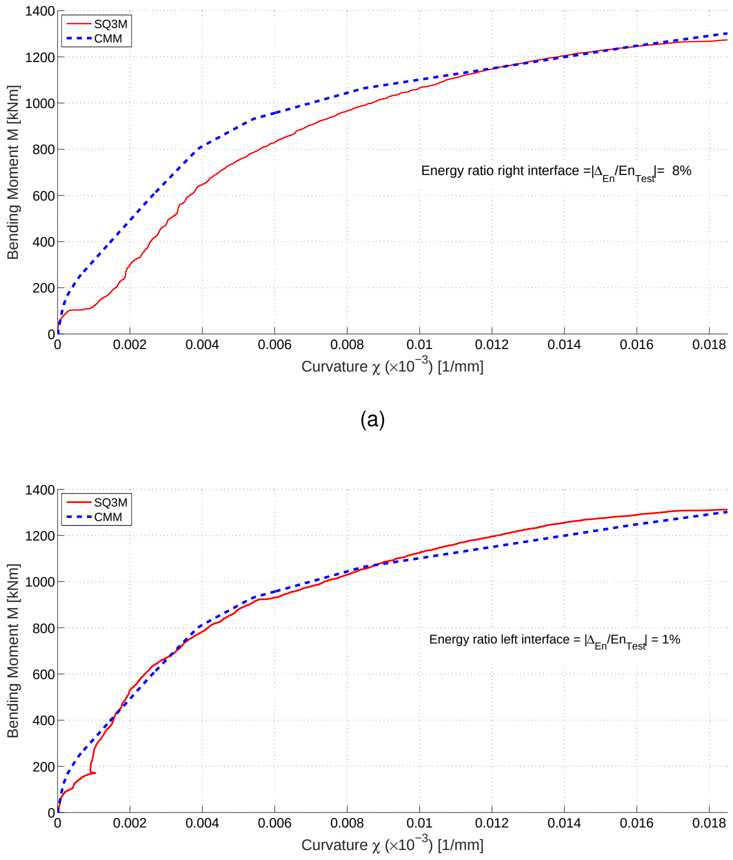

(a)

(b)

Figure 5.29: Outcomes of the validation: a)Moment- curvature of right interface; b) Moment- curvature of left interface.

In addition, both test results and the CMM responses were compared in terms of dissipated energy *E*. With regard to the left side of the CCB the difference in terms of energy shown in Figure 5.29(a) was 1% , while for the right side, it amounted to almost 8%. Through the analysis of both energy dissipation and NRMSEs of $B_1^{Cal}$ and $B_2^{Cal}$, it is possible to conclude that the responses in terms of moment-curvature between experimental data and CMM agree with each other.

For the analysis of global behavior, i.e. $B_3^{Cal}$, a comparison between the force displacement response of the SQ3M and the relevant CMM numerical response as shown in Figure 5.31. In detail, the absolute displacement of the CCB in the

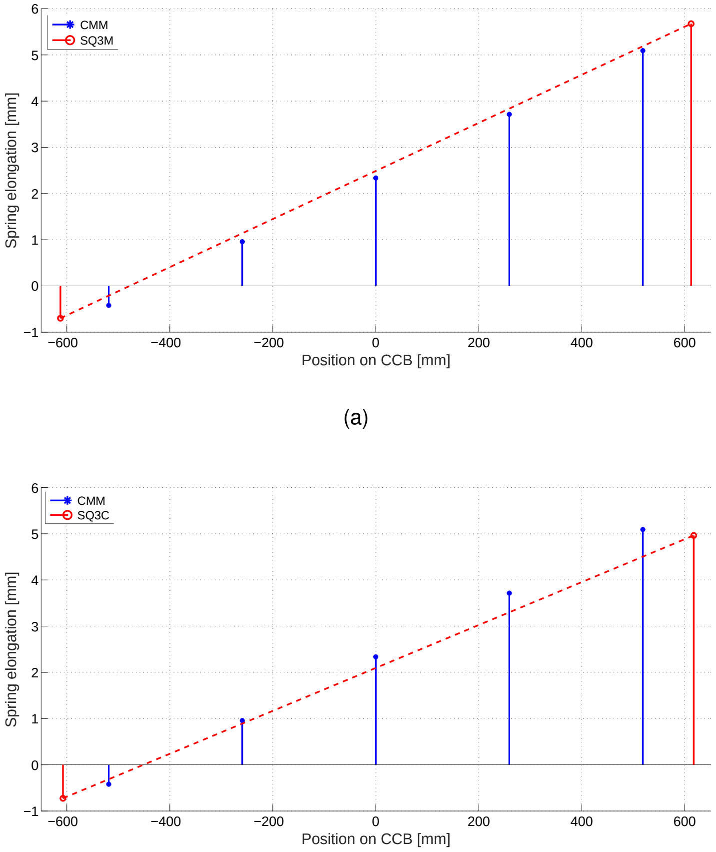

(a)

(b)

Figure 5.30: Outcomes of the validation: a) elongation of springs and Gefran of right side; b) elongation of springs and Gefran of left side.

transversal direction (Z) was measured by an external wire transducer fixed on the front face of the beam. The reaction forces were recorded by load cells at pin hinges, i.e. *Load Cell Pin left* and *right*.

In conclusion, the distinguishing features of the DOMI-II type connection experienced negligible stresses and deformations in agreement with experimental data as show by the validation errors shown in Table 5.12. As a result, they demonstrate that the CMM is capable of reproduce the actual behavior of the DOMI-II connection with an acceptable error. Above all, local deformations were accurately reproduced by means of the springs of the slab CCB interface for both tension and

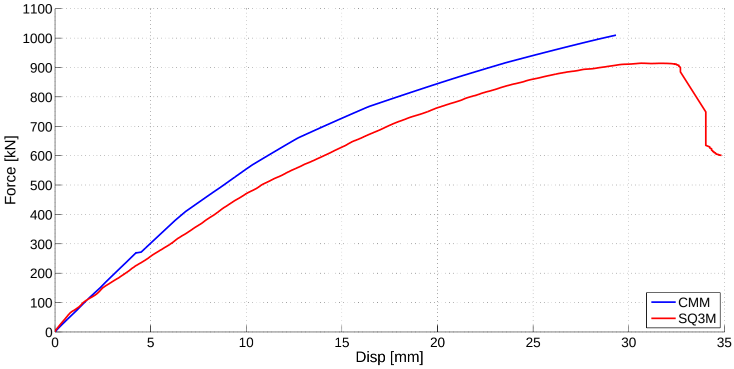

(a)

Figure 5.31: Global comparison in term of force-displacement.

compression regimes. This isolated connection model can be used to reproduce the connection response in the full composite bridge,i.e. CSIII and hence was incorporated in a global FE model as described in Subsection 5.5.1.

## 5.5 Probabilistic seismic demand evaluation of case study III

### 5.5.1 Incorporation of the component-based mechanical model in the full-scale bridge model

In order to quantify the actual damage of the connection during strong seismic events, the isolated CMM was incorporated in the full-scale bridge CMMCSIII. The relevant FE model can be observed in Figure 5.32 where the connections between CCB and steel I-girders, i.e. CMM, were located at different distances from the neutral axis of the whole composite slab. Moreover, since the CMM were validated up to collapse and was endowed with axial spring in the slab, it that can reproduce axial effects either due to axial loading or to bending and can be located in any position of the composite deck depth.

In order to reduce the computational burden, the concrete slab of each CMM has been reproduced with 12 springs, i.e. 4 TC1t, 4 TC1b and 4 TC2. In addition, all the fiber elements reproducing the composite deck were replaced by elastic element. The others components instead were implemented with the procedure reported in Section 5.4.2. As shown in Figure 5.33 the refined model improved by the implementation of the CMM keep the same dynamic properties of the PMCSIII. In fact the modes of vibrations are the same in terms of deformed shape and have a good agreement in terms of periods of vibration. Because of the huge number of springs, the CMMCSIII model became quite complex and not simply manageable, for this reason it was important to do this check to prove the absence of unexpected modes of vibration. The boundary conditions of pier and abutments were the same of PMCSIII, whilst all the material parameters were updated on the base of characterization tests reported in Table 5.8.

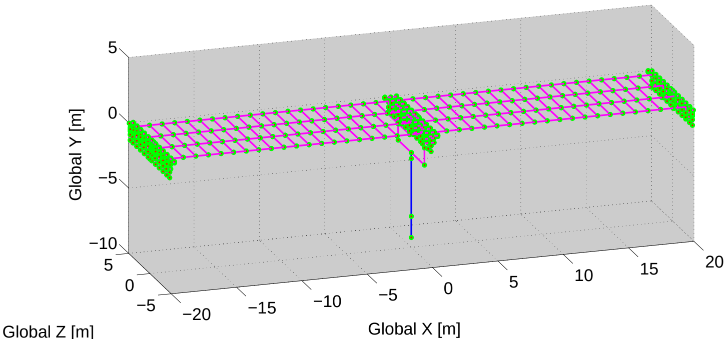

Figure 5.32: Overall Bridge with component-based mechanical model.

| Period T[s] | | |
|---|---|---|
| **SMCSIII** | **PMCSIII** | **CMMCSIII** |
| 0.897 | 0.902 | 0.890 |
| 0.405 | 0.411 | 0.345 |
| 0.262 | 0.256 | 0.216 |
| 0.103 | 0.106 | 0.088 |
| 0.082 | 0.080 | 0.067 |

Table 5.13: Forces and displacements of experimental tests at substructure failure.

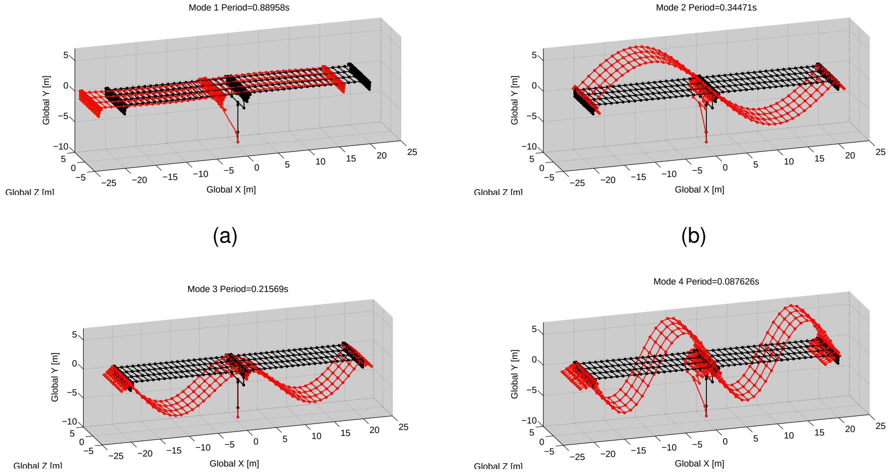

(a) (b)

(c) (d)

Figure 5.33: Mode shapes of CMMCSIII in the non isolated configuration: a) $1^{st}$ *Mode*; b) $2^{nd}$ *Mode*; c) $3^{rd}$ *Mode*; d) $4^{th}$ *Mode*.

### 5.5.2 Input ground motions

The site of Priolo Gargallo (Sicily - Italy), is characterized by a strong seismic action, for this reason has been selected as construction site. As a result, the annual hazard curve of Priolo Gargallo, determined by using a classical Probabilistic Seismic Hazard Analysis Cornell (1968) performed by means of the software MatHazard Giannini (2000), is depicted in Figure 5.34(a). The design of the CSIII for seismic loading was carried out considering a reference life of 50 years; therefore on the basis of statistically independent events, the annual rate of exceeding was factored with the reference life. Then, a set of 15 ground motions has been selected with the assumption that the normalized mean spectrum fit, in a least square sense, the reference Uniform Hazard Spectrum (UHS) with maximum difference in the lower bound equal to the 10 %; the relevant spectra are shown in Figure 5.34(b). The spectrum is called UHS because every spectra acceleration has the equal rate of being exceeded. It is an envelope of separate spectral acceleration values at different periods as shown in Figure 5.35 (Bursi et al. (2015)).

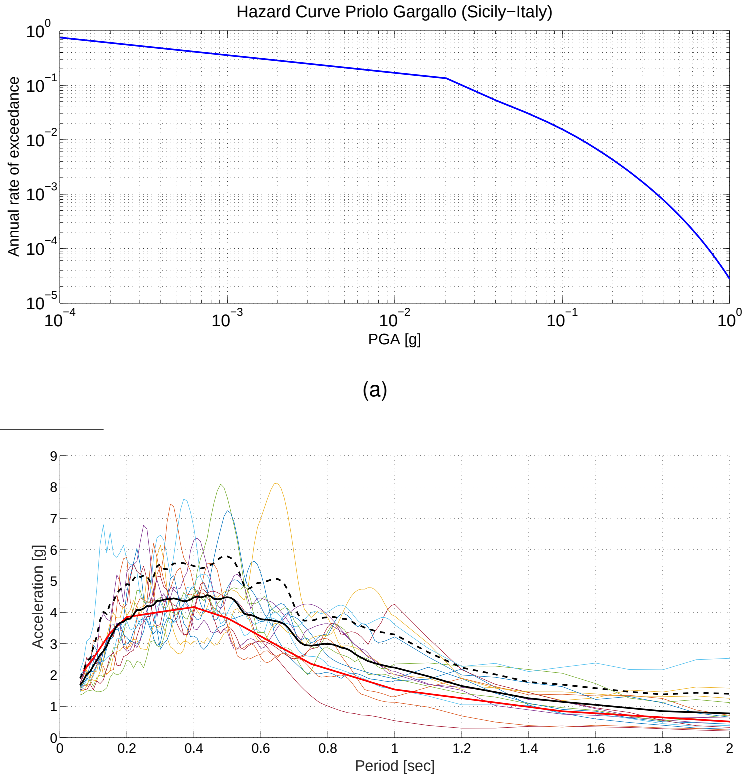

(a)

(b)

Figure 5.34: Inputs of the hazard and structural analyses: a) annual Hazard Curve of Priolo Gargallo (Italy); b) UHS with return period of 475 years

### 5.5.3 Results of probabilistic seismic demand analysis

Since the bridge seismic response depends on the intensity of the ground motion, in order to represent several possible earthquake scenarios, a comprehensive bridge assessment requires several nonlinear dynamic analyses at various levels of intensity measures (ims). For this reasons, Incremental Dynamic Analyses (IDAs) have been performed on the CSIII following the approach suggested by Vamvatsikos and Cornell (2001). The simulations were performed with the simultaneous application of two motion components to the deck axis, longitudinal and transversal, respectively. As a result, the CCB behavior resulted to be quite stiff and strong for lateral loadings; therefore, in order to prove the applicability of CCB

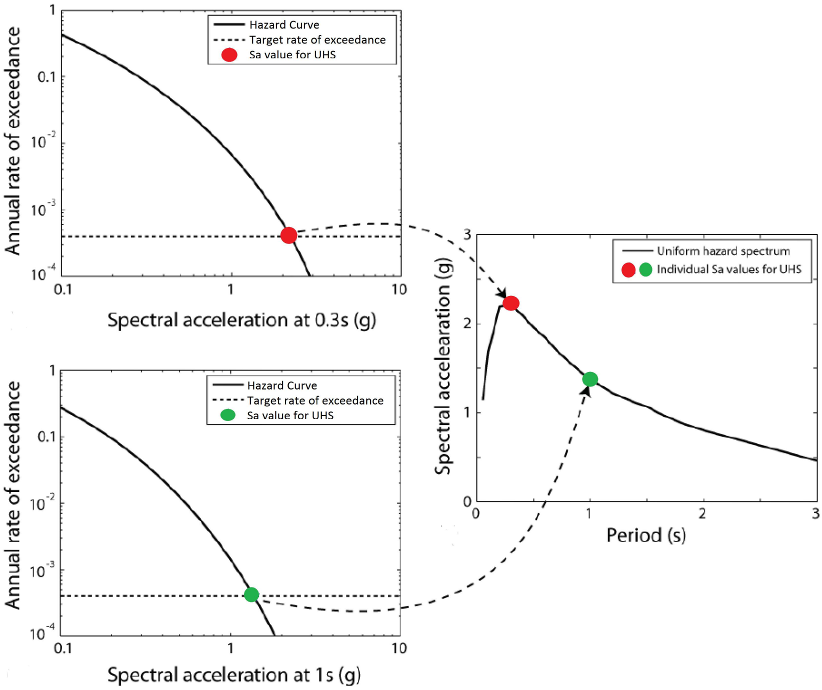

Figure 5.35: Evaluation of uniform hazard spectrum.

in high seismicity prone areas, only the engineering demand parameters (edps) listed in Table 5.14 and relevant to both the pier and concrete slab have been selected. It is possible to underline that *edp*1 is relevant to the longitudinal motion of the bridge whilst *edp*2 and *edp*3 characterize failure for its transversal motion.
The selected im was the PGA, however the selection of ground motions was performed by means of the searching of the best set which fitted the UHS on the range of periods between 0 abd 2s. As a result the effective im was something hybrid that will be identified for simplicity in the thesis as PGA, each simulation was plotted as a function of each edp relevant to the described im. Each Incremental Dynamic Analysis (IDA) covered the range of PGA between $0.1g - 1.9g$obtained through a linear scaling of the selected accelerograms. In addition, the multi-record IDA responses as a function of *edp*1, *edp*2 and *edp*3 are depicted in Figure 5.36.

In a greater detail, these results have been used to evaluate the fragility curves of the CSIII following the method proposed by Baker (2015). Moreover, the method of moments was applied in the context of IDA simulations through the following

| **edp name** | **edp description** | **edp limit state** |
|---|---|---|
| edp1 | Drift of Concrete Pier<br>(Global X direction) | Spalling of concrete<br>2 % |
| edp2 | Deformation of CCB-concrete<br>slab interface bottom side<br>(TC1t CMM component) | Elastic limit strength<br>of concrete $f_t$<br>0.0289 mm |
| edp3 | Deformation of CCB-concrete<br>slab interface bottom side<br>(TC1b CMM component) | Elastic limit strength<br>of concrete $f_t$<br>0.0289 mm |

Table 5.14: Selected edps for pier and concrete slab

equations:

$$\hat{\mu} = \frac{1}{n}\sum_{i=1}^{n} lnSa_i \tag{5.76}$$

$$\hat{\sigma} = \sqrt{\frac{1}{n-1}\sum_{i=1}^{n}(lnSa_i - \hat{\mu})^2} \tag{5.77}$$

Nonetheless, because of the reduced number of accelerograms selected and described in Subsection 5.5.2, the fragility curves provided by the method of moments have been verified with those estimated by the method of MLE. The reliability of the estimated parameters, with both methods, has been checked by means of the Kolmogorov-Smirnov statistical test Benjamin and Cornell (1970). It can be appreciate from Table 5.15 that parameters of both methods were verified with the aforementioned test. The fragility curves for all the edps are shown in Figure 5.36.

It can be observed that curves obtained with the two different procedures are very close and reflect moment values collected in Table 5.15. Moreover, the fragility curve of *edp*1 shown in Figure 5.36(b) exhibits a limited dependence on PGA. Conversely and in agreement with experimental data discussed in Subsection 5.3.1, both *edp*2 and *edp*3 are in practice not affected by seismic loading along the transversal direction. In fact as illustrated in Figure 5.36(d) and 5.36(f), the limit

| Method of moments | | | | | |
|---|---|---|---|---|---|
| **edp** | $\hat{\mu}$[g] | $\hat{\sigma}$[g] | $KS_{\alpha 0.05}$ | **D2** | **Test** |
| **edp1** | -0.387 | 0.589 | 0.34 | 0.1658 | Ok |
| **edp2** | -0.203 | 0.170 | 0.34 | 0.2156 | Ok |
| **edp3** | -0.179 | 0.172 | 0.34 | 0.2133 | Ok |
| Maximum likelihood estimation | | | | | |
| **edp** | $\hat{\mu}$[g] | $\hat{\sigma}$[g] | $KS_{\alpha 0.05}$ | **D2** | **Test** |
| **edp1** | -0.387 | 0.569 | 0.34 | 0.1739 | Ok |
| **edp2** | -0.203 | 0.164 | 0.34 | 0.2181 | Ok |
| **edp3** | -0.179 | 0.166 | 0.34 | 0.2108 | Ok |

Table 5.15: Estimated parameters and statistical tests of edps fragility curves.

state of concrete cracking was exceeded in average for $1.0g$ PGA. Finally, the relevant probabilities $G(edp)$ provided by Equation 2.19 are reported in Table 5.16; their values confirm the trends of the previously defined fragility curves.

| **G(edp) non isolated case** | |
|---|---|
| **edp1** | $2.4 \cdot 10^{-2}$ |
| **edp2** | $3.9 \cdot 10^{-3}$ |
| **edp3** | $3.6 \cdot 10^{-3}$ |
| **G(edp) isolated case** | |
| **edp1** | $9.6 \cdot 10^{-3}$ |

Table 5.16: G(edp) in 50 years of reference life

## 5.6 Conclusions

The seismic assessment of a SCC based on cyclic test was conceived within the SEQBRI Project (Paolacci et al. (2015)), in which three novel structural joints for SCCBHs have been investigated on the base of QSCTs and a fully probabilistic analysis. In order to reach the objective of the project that were: *i*) to investigate

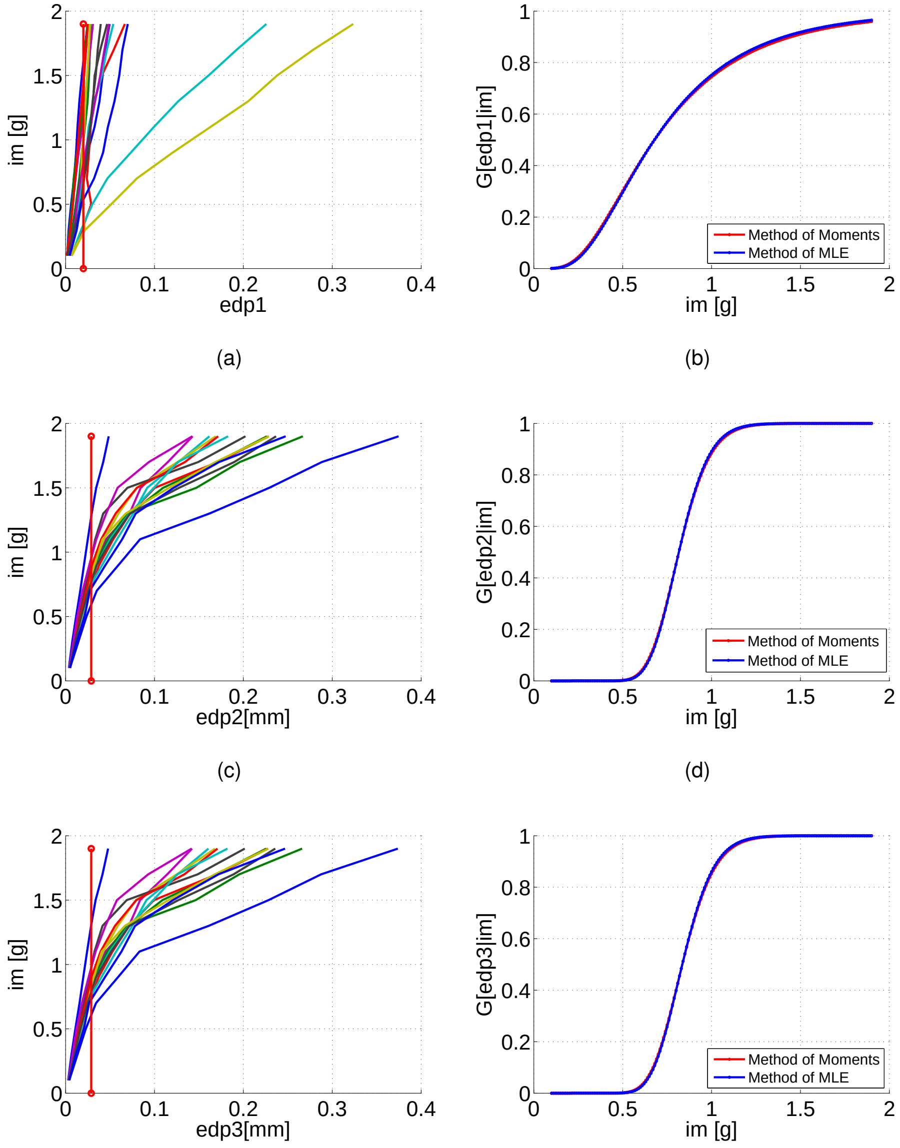

(a) (b)

(c) (d)

(e) (f)

Figure 5.36: IDA results and fragility curves: a-b) edp1; c-d) edp2; e-f) edp3.

the seismic response of a novel connection between the CCB and the steel I-girder beam; *ii*) to apply the fully probabilistic PBEE to a functional composite bridge designed according to Eurocodes; in this chapter have been developed Step I, II, III, IV of APSPAB.

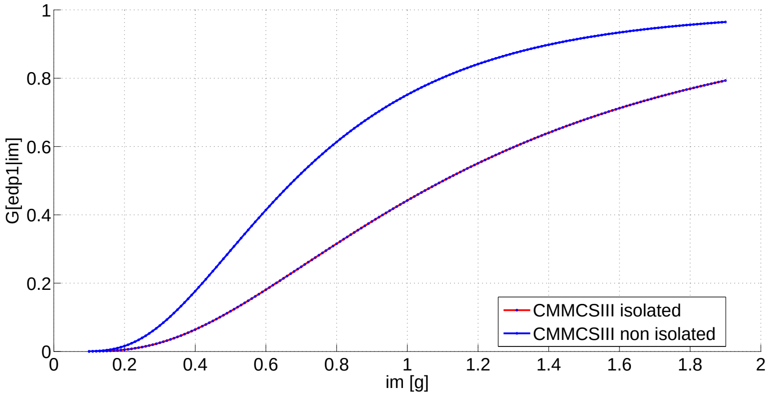

Figure 5.37: Comparison between fragility curves in the isolated and non isolated cases.

Firstly, a PMCSIII has been implemented in the Opensees environment to predict the behavior of the CSIII in both isolated and non isolated configurations, the FE model shown an optimum seismic response of the facility due to the limitated weight of the deck. The simulations were used to set the proper testing protocol, in fact the reduced damage produced by the design earthquake have driven the decision to the choice of the ECCS procedure. Then, seven tests, monotonic and cyclic, have been performed to investigate the transversal response of the novel SCC joints between CCB and steel I-girder.

Experimental tests provided information about the collapse mechanisms for the transversal actions, in detail for this type of joints the collapse was governed by the crushing of concrete at the interface between the CCB and composite sections. The other components, characterizing each joint type (prestressing bars, Nelson studs, etc.) were slightly stresses. The experimental data were considered to create a novel CMM of the bridge connection, able to reproduce the local mechanisms generated during the test. In detail it was implemented by means of the reproduction of the mechanical components acting on the CCB. In greater detail, due to experimental evidences, particular attention was dedicated to the CCB interface components, i.e. concrete slab and rebars, were the damage was located.

Finally, in order to obtain the refined model of the CSIII the CMM of CCB joint have been implemented in the full-scale bridge and compared with the PMCSIII. The refined model of the full-scale CSIII bridge were used to perform the probabilistic seismic demand analysis as a part of the innovative PBEE approach. In greater detail, the structural part of the method was fully developed through structural and hazard analysis. This part of the procedure provided information about the structural seismic response of both non isolated and isolated configurations based on three edps investigeted for earthquake up to 1.9g of PGA.

As a conclusion, with regard the transversal seismic direction the SCCBHs made with CCB showed a good behavior and hence are perfect candidates for the designed in high seismicity prone areas.

## CHAPTER 6

# RELIABILITY ANALYSIS OF A FOOT/ CYLCIC BRIDGE - CASE STUDY IV

### 6.1 Introduction

This Chapter presents a simulation-based probabilistic assessment of a complex cable-stayed footbridge erected in an aggressive environment. The scope, in line with the objective of the European HITUBES project (Bursi et al. (2011)) was to investigate the benefits of CHS structural members for this type of structure. The CSIV is located in Pescara, Italy, next to the Adriatic sea. A FE model of the structure has been validated (Bursi et al. (2014)), and then used to perform a probabilistic analysis. General and localized corrosion models capable of evaluating the reduced load bearing section were adopted; and appropriate probability distributions were assigned to input model parameters to evaluate the response of the facility during the design life. The probabilistic evaluation of the bridge response was conducted in an ANSYS (2007) environment using nonlinear MCSs enhanced by LHS to optimize the number of simulations required.

SLS for stresses was satisfied for the foot/cyclic deck bridge service life for both wind and pedestrian loads. Conversely, for the limit states referred to maximum deck deflection and rotation, the probabilities of failure overpassed limit values suggested in EN1990-2 (2002). As a result, the probabilistic analysis was able to predict the exceeding time of limit states' thresholds for the twin deck curved cable-stayed footbridge with CHS members. Therefore, both repair and a retrofit plan within its design life time was set.

Therefore, in Section 6.2 is presented the CSIV with the complete set of loads and limit states. In Subsection 6.2.3 the FE model conceived and validated in Bursi et al. (2014) used to implement a fictitious FE model by replacing Open Section (OS) members with CHS members. Then, in Section 6.3 is described the reliability analysis, random variables and relevant distributions representative of input actions, SLS and material properties are introduced. Furthermore, two probabilistic-based corrosion models capable of reproducing both uniform and pitting corrosion are presented. Finally, in Section 6.4 conclusion are drawn.

## 6.2 Description of the case study IV

Figure 6.1: View of the Ponte del Mare located in Pescara.

The CSIV is the ”Ponte del Mare” Cable-Stayed Footbridge located in Pescara at the mouth of the Pescara river close to the sea, in the center of Italy. The structure has two curved decks supported by cables linked to a tilted mast. The outer deck is a footbridge, while the inner is for cyclic bridge; their lengths are 173 m and 148 m, respectively and both decks have constant curvature radius, 80 m and 100 m each in order. The two decks are connected to two prestressed concrete ramps to allow the access of the users. The two sections of the twin deck are shown in Figures 6.2(a) and 6.2(b). The mast is made with a steel tubular section

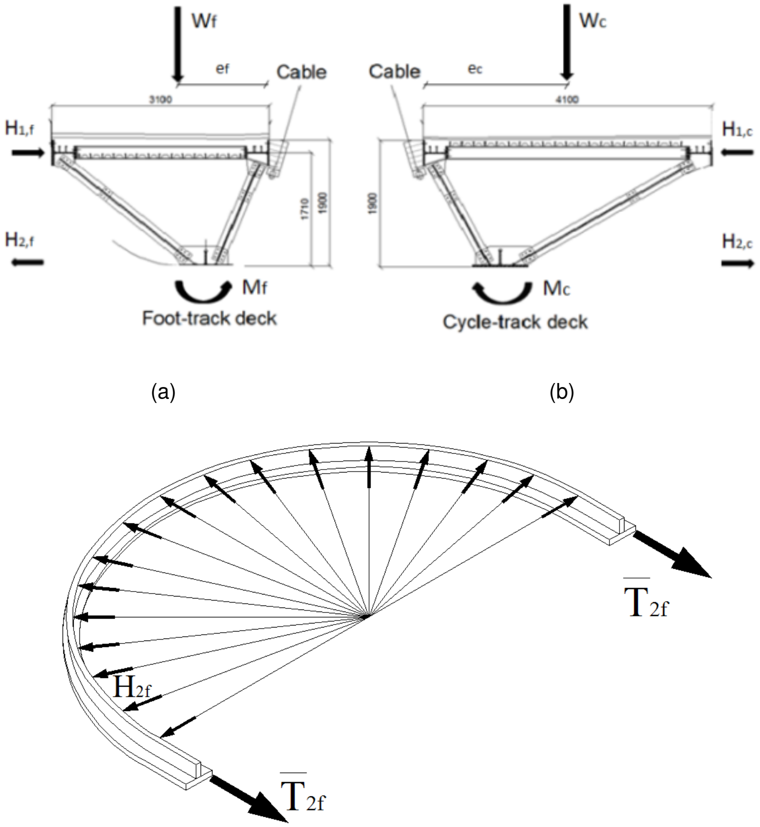

(a) (b)

(c)

Figure 6.2: The Case Study IV (after, Bursi et al. (2014)): a) static scheme of foot-track deck ; b) static scheme of foot-track deck; c) effects of the geometry on foot-track deck.

filled with concrete and rises between the foot and the cycle decks, the inclination is about 11° with respect to the vertical; the mast is anchored to the ground by two cables. Due to the mast location within decks, see Figure 6.2(c), and the relevant eccentricities $e_f$ and $e_c$ of typical vertical loads $W_f$ and $W_c$, rotation moments act on both decks and are equilibrated by horizontal forces $H_{2,f}$ and $H_{2,c}$, respectively. As shown in Figure 6.2(c), the bottom chord of the foot deck constrained at both abutments and subject to horizontal forces $H_{2,f}$, is subjected to a tensile force $T^{-}_{2,f}$ related to the curvature effects. Therefore, both bottom and top chords of decks are subjected to opposite sign axial loads. In detail, the bottom chord of the foot deck is subject to tensile force whilst the one of the cycle deck is subject to compressive force. As shown by Ceravolo et al. (2012), the opposite trend happens for top chords.

In order to satisfy safety requirements to avoid early aeroelastic instability generated by the vibrations induced by wind and pedestrians loads, the CSIV was provided with a dampers based passive control system. The system included 6 devices all of them based on viscous fluid damping and some equipped with spring in series. Three damper types, A, B and C, with different parameter values as listed in Table 6.1, were installed at the locations shown in Figures 6.3(a) and 6.3(b). Dampers of Type B and C are depicted in Figures 6.3(c) and 6.3(d).

| | **Damper A** | **Damper B** | **Damper C** |
|---|---|---|---|
| **Type** | Elastic-viscous | Elastic-viscous | Viscous |
| **Units** | 2 | 2 | 2 |
| **Damping constant** | $128.0 kNs/m$ | $349.0 kNs/m$ | $794.2 kNs/m$ |
| **Spring stiffness** | $127.6(\pm 5\%) kN/m$ | $127.6(\pm 5\%) kN/m$ | - |

Table 6.1: Characteristics of dampers.

The footbridge was monitored from the end of 2009 to the middle of 2011, approximately for one year and a half, with the distributed sensor system reported in Figure 6.4. The monitoring system consisted of 8 accelerometers, 4 resistance thermometers and 2 anemometers. During one of the more extreme events, on 25 December 2009, accelerations were recorded owing to North-South wind excitation from the sea. Accelerations reached 0.4 $\frac{m}{s^2}$ at the foot deck while at the top of the mast the maximum wind speed recorded was 28.0 $\frac{m}{s}$. These monitoring system was the base for the FE model updating and refinement presented in Bursi et al. (2014).

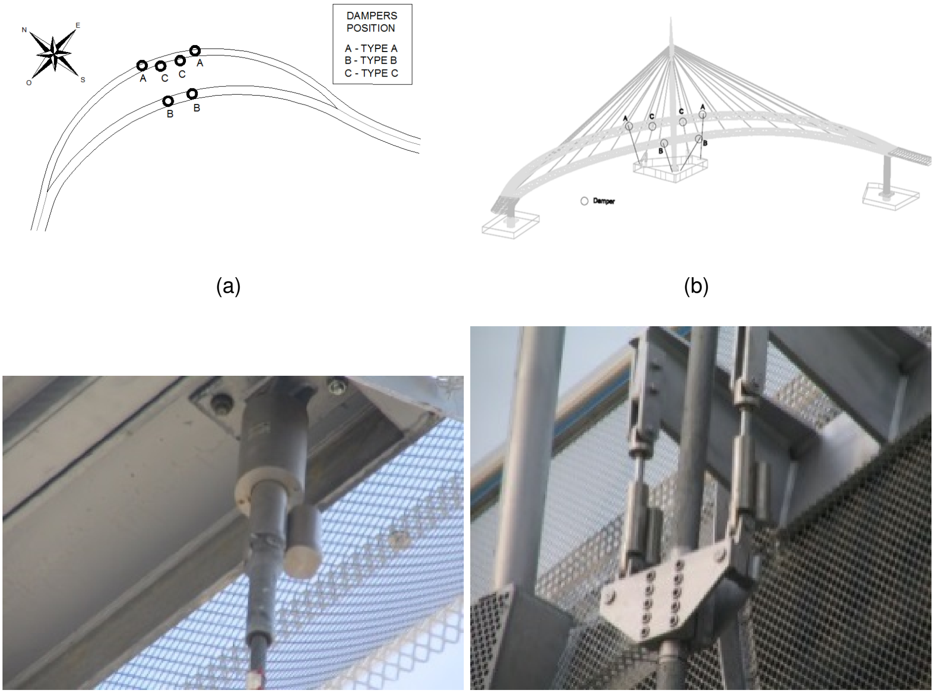

(a) (b)

(c) (d)

Figure 6.3: Details about the position and the type of passive control systems (after, Bursi et al. (2014)): a) 2D view of system position; b) 3D view of system position; c) damper Type B; d) damper Type C.

### 6.2.1 Actions and limit states

The design of the CSIV has been performed by using the following loads:

- **A**: Gravity loads due to deck components such as OS members and concrete slab;
- **B**: Additional dead loads of pavings, hulls, parapets and others finishing elements corresponding to 3 $\frac{kN}{m^2}$;
- **C**: Pedestrian static load of 4 $\frac{kN}{m^2}$;
- **D**: Two-axles load of a service vehicle corresponding to 80 kN and 40 kN spaced at about 3 m with a width of 1.3m;

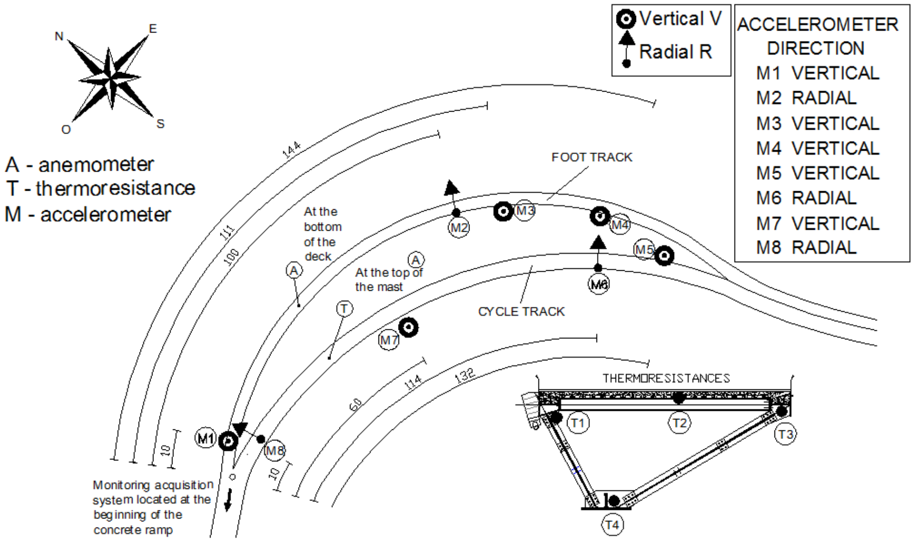

Figure 6.4: Structural health monitoring system (after, Bursi et al. (2014)).

- **E**: Wind load of 2.5 $\frac{kN}{m^2}$ applied transversally to the deck on a surface of 3 m height representing the hulls barrier.

In particular, Loads **A** and **B** came from standard design assumptions, Loads **C** and **D** agreed with values suggested in EN1991-2 (2005), whilst Load **E** followed the prescription of a national standard CNR (2008). Both safety and serviceability threshold can play a significant role in evaluating structural reliability; moreover, the analysis presented considered only SLS. Relevant limit values are reported hereinafter:

- Deck Deflection: $\delta \leq \frac{L}{500}$

- Deck Rotation: $\theta \leq 3.5\%$,

- Safety Margin (SM): $SM = C - D \geq 0$, where: C defines the serviceability limit stress and D defines the stress demand; $\delta$ is the maximum vertical deck deflection; $\theta$ defines the deck rotation as illustrated in Figure 6.5.

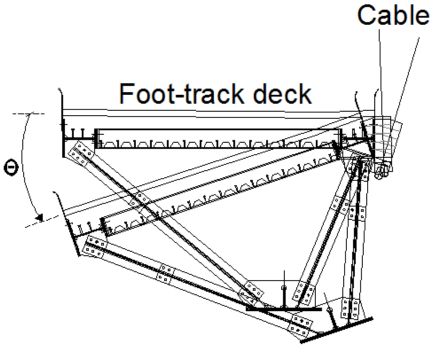

Figure 6.5: Rotation relevant to a rigid motion of the footbridge deck.

### 6.2.2 The FE model of the actual open section-based foot/cyclic bridge

Due to the high geometrical complexity of the CSIV characterized by 3D bending/torsional coupled modes of decks and cable-deck interaction, an RMCSIVOS was immediately implemented (Bursi et al. (2014)). The RMCSIVOS served besides for the analysis of the bridge subjected to high cyclic fatigue loads owing to pedestrians and wind (Bursi et al. (2011)). As a result, in Figure 6.7 is shown the RMCSIVOS, it is composed by 27093 DoFs, and was developed in ANSYS (2007). Beam, shell and solid elements were used to model accurately both the main steel-concrete decks and the access ramps taking into account also geometrical nonlinearities. In greater detail, the two decks trusses and the piers, ramps, mast and rigid connections were modelled using *BEAM*44 elements. To avoid free vibration solutions dominated by cable stays modes, each cable was reproduced with a single geometrically nonlinear *LINK*83*D* truss element Brownjohn and Xia (2000). Moreover, variations in axial stiffness owing to tensile loading were taken into account by means of Dischinger equivalent elastic moduli (Bruno et al. (2008)). The two concrete slabs were modelled by means of *SHELL*63 elements. Each concrete block at the ends was modelled with *SOLID*45 elements. The dampers were modelled with ideal linear viscous *COMBIN*14 elements. The first four frequencies provided by modal analysis are shown in Table 6.2, while for brevity, only two corresponding first and second mode shapes can be observed in Figure 6.7. From Table 6.2, we see how some frequencies are close; while the mode shapes show that the footbridge exhibits complex behavior owing to coupling between bending and torsion, especially for the second mode.

| Mode Frequency | |
|---|---|
| Frequency [Hz] | |
| #1 | 0.681 |
| #2 | 1.003 |
| #3 | 1.087 |
| #4 | 1.144 |

Table 6.2: Numerical frequencies of the predicted modes of RMCSIVOS

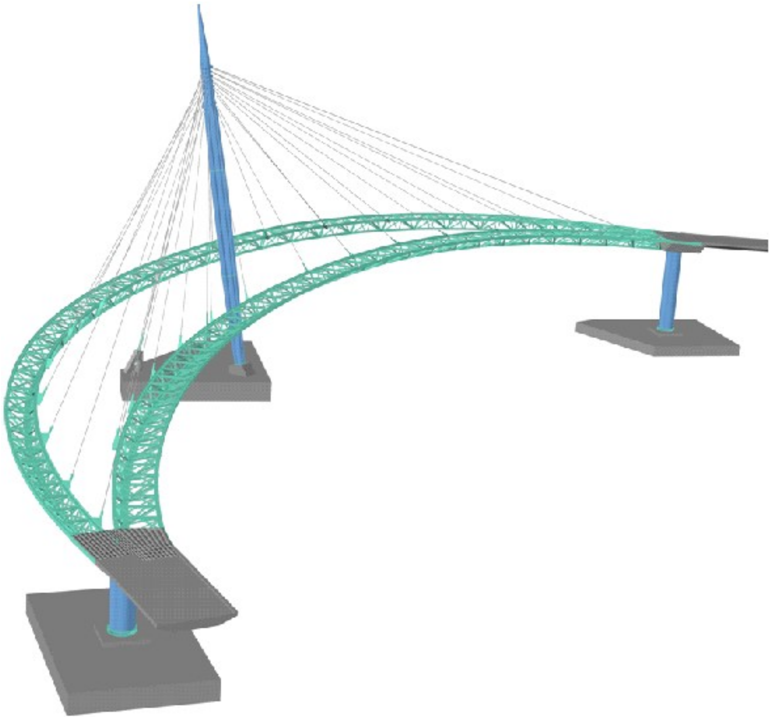

Figure 6.6: 3D view of the RMCSIVOS (after, Bursi et al. (2014)).

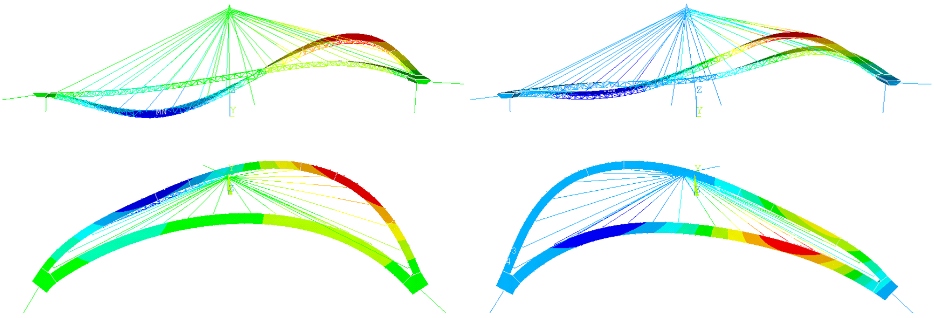

(a) (b)

Figure 6.7: Modal analysis of the RMCSIVOS (after, Bursi et al. (2014)): a) first mode shape; b) second mode shape.

### 6.2.3 Re-design of the case study IV based on circular hollow section elements

An additional refined model RMCSIVCHS was developed on the base of the redesigne of the RMCSIVOS by replacing OS members with CHS in HSS-TS590LH TENARIS (2008) as shown in Figure 6.8. In agreement with EN10027 (2006), this steel is made for hollow sections with a minimum toughness of 27 J at $-50^{\circ}$. This replacement was done in the footbridge FE model sketched in Figure 6.6.

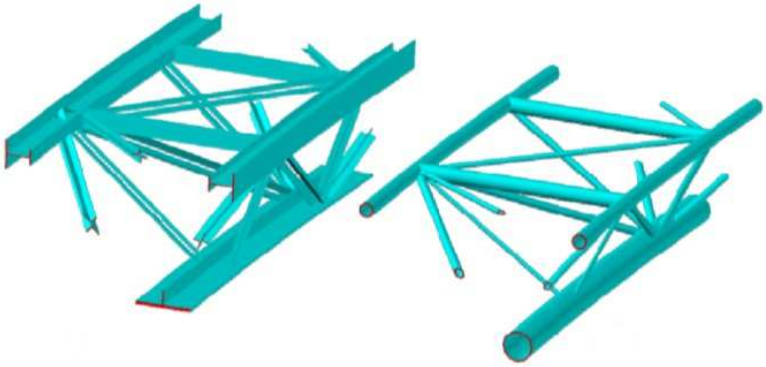

Figure 6.8: Foot track deck with open section members and with CHS members.

The geometry of each deck remained unchanged during the fictitious re-design, whilst all OS members were replaced with CHS members. The replacement was based on the equivalence of the section modulus. The use of steel TS590LH provided the required strength to the members and hence the satisfaction of the design checks for both ULS and SLS. This steel grade allowed use of sections with smaller inertia and area. With reference to TS590LH, note that an average yield and tensile strengths of about 640 MPa and 766 MPa was traced, respectively, with an elongation greater than 19% (Bursi et al. (2011)). From RMCSIVCHS, it has been seen that the possibility of using High Steel Strength (HSS) was limited by the SLS defined in Subsection 6.2.1. In fact, CHS members offered several advantages in terms of:

1. steel savings about 10-11 % in both decks, by replacing OS with CHS members;
2. better deck transparency and possible removal of the hulls shown in Figure 6.9(a);
3. reduction of aerodynamic problems thanks to hull removal, and hence a possible elimination of the dampers discussed;
4. smaller areas to paint with lower cost.

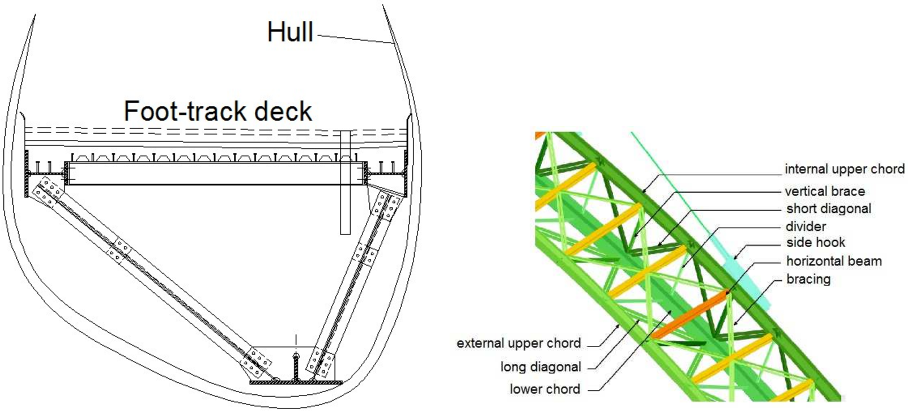

(a) (b)

Figure 6.9: Footbridge deck details: a) section with hulls; b) typical elements of the deck.

A view of the deck, with the set of elements is shown in Figure 6.9(b), while, the relevant dimensions of both OS deck members are depicted in Figure 6.10. Tables 6.3 and 6.4 show typical dimensions of OS whilst Table 6.5 provides a summary of properties of the CHS members that replaced OS members. The CHS members of the fictitious bridge were modelled using BEAM44 elements as the one used for the OS members in the RMCSIVOS.

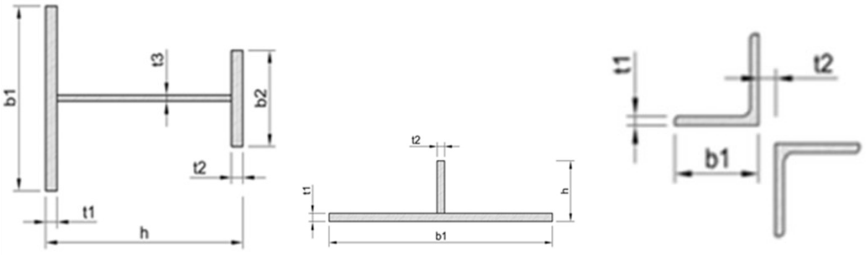

(a) (b) (c)

Figure 6.10: Deck member sections: a) upper chord; b) lower chord; c) diagonals, bracings, vertical braces and dividers.

Successively, the RMCSIVCHS members was used for the probabilistic analysis presented in Section 6.3.

## 6.3 Probabilistic analysis of the bridge

### 6.3.1 Definitions of random variables and distributions

In order to perform probabilistic analyses on the CSIV and to be in agreement with the LHS method (McKay et al. (1979)) the following steps were needed: *i)* to define a domain of random inputs; *ii)* to perform a sampling of relevant inputs randomly in each stripe; *iii)* to perform a deterministic computation based on the inputs; *iv)* to aggregate output results. As a results, PDF of materials, major loads and corrosion input models were set as reported hereinafter.

| **Type** | **Name** | **b1 [mm]** | **t1 [mm]** | **b2 [mm]** | **t2 [mm]** | **h [mm]** | **t3 [mm]** |
|---|---|---|---|---|---|---|---|
| **External upper chord (a)** | C-CSE | 380 | 20 | 200 | 20 | 340 | 25 |
| **Internal upper chord (a)** | C-CSI-20 | 380 | 20 | 200 | 20 | 340 | 25 |
| | C-CSI-25 | 380 | 25 | 200 | 25 | 340 | 25 |
| **Lower chord (b)** | C-TI-20 | 800 | 20 | | 20 | 240 | |
| | C-TI-30 | 800 | 30 | | 20 | 250 | |
| **Vertical brace (c)** | C-M-80x8-18 | 80 | 8 | | 18 | | |
| | C-M-100x12-18 | 100 | 12 | | 18 | | |
| **Diagonal (c)** | C-DC-80x8-18 | 80 | 8 | | 18 | | |
| | C-DC-110x14-18 | 110 | 14 | | 18 | | |
| | C-DL-90x9-18 | 90 | 9 | | 18 | | |
| | C-DL-100x14-18 | 100 | 14 | | 18 | | |
| **Bracing (c)** | CCONTR-80x10-18 | 80 | 10 | | 18 | | |
| **Divider (c)** | C-RL-60x6-18 | 60 | 6 | | 18 | | |
| **Horizontal beam** | HEA 200 | | | | | | |
| | HEB 200 | | | | | | |

Table 6.3: Dimensions of the cycle track deck elements.

| Type | Name | b1 [mm] | t1 [mm] | b2 [mm] | t2 [mm] | h [mm] | t3 [mm] |
|---|---|---|---|---|---|---|---|
| **External upper chord (a)** | P-CSE | 380 | 20 | 200 | 20 | 340 | 25 |
| **Internal upper chord (a)** | P-CSI | 380 | 20 | 200 | 20 | 340 | 25 |
| **Lower chord (b)** | P-TI-25 | 750 | 25 | | 20 | 225 | |
| | P-TI-35 | 750 | 35 | | 20 | 235 | |
| | P-TI-40 | 750 | 40 | | 20 | 240 | |
| **Vertical brace (c)** | P-M-80x8-18 | 80 | 8 | | 18 | | |
| | P-M-100x12-18 | 100 | 12 | | 18 | | |
| **Diagonal (c)** | P-DC-100x10-18 | 100 | 10 | | 18 | | |
| | P-DC-100x14-18 | 100 | 14 | | 18 | | |
| | P-DL-110x14-18 | 110 | 14 | | 18 | | |
| **Bracing (c)** | PCONTR-80x10-18 | 80 | 10 | | 18 | | |
| **Divider (c)** | P-RL-60x6-18 | 60 | 6 | | 18 | | |
| **Horizontal beam** | HEA 200 | | | | | | |
| | HEB 200 | | | | | | |

Table 6.4: Dimensions of the foot track deck elements.

### 6.3.2 Yield strength of steel

The $f_{ys}$ of HSS steel was considered distribute with a Gaussian law. In particular, based on test data of Bursi et al. (2011) it was characterized by $\mu$ = 640 MPa

| **CHS [ODxWT] (mmxmm)** | **OS** |
|---|---|
| 168.3x6 | CCONTR-80x10-18, PCONTR-80x10-18 |
| 168.3x8 | C-DC-110x14-18, C-DC-80x8-18, C-DL-100x14-18, C-DL-90x9-18, C-M-100x12-18, C-M-80x8-18, C-RL-60x6-18, HEA200, P-DC-100x10-18, P-DC-100x14-18, P-DL-110x14-18, P-M-100x12-18, P-M-80x8-18, P-RL-60x6-18 |
| 219.1x16 | C-CSE, C-CSI-20, C-CSI-25, P-CSE, P-CSI, HEB200 |
| 445x25 | C-TI-20, C-TI-30, P-TI-25, P-TI-35, P-TI-40 |

Table 6.5: Correlation between the CHS members and the original OS members.

and $\sigma$ = 16.67 MPa.

### 6.3.3 Pedestrian loading

Pedestrian loading consists of a dense crowd with an intensity of $5\frac{kN}{m^2}$ accordingly with EN1991-2 (2005) and a probability of exceedence of 5%. The annual maximum distribution of pedestrian loading follows an extreme value (Gumbel) Type I distribution with location parameter k=2.25 $\frac{kN}{m^2}$ and scale parameter $\beta$=0.399 $\frac{kN}{m^2}$. Since the likelihood of extreme loading conditions increases over time, the maximum live load is also assumed to increase over time. In detail, in agreement with EN1990-2 (2002) increasing Cumulative Distribution Function (CDF) of *n* years was calculated by using the following relationship:

$$P(x < X)_{nyears} = [P(x < X)_{1year}]^n \tag{6.1}$$

Both the PDF and the CDF relevant to different periods of time are shown in Figures 6.11(a) and 6.11(b), respectively. The set parameters describing all the years are summarized in Table 6.6.

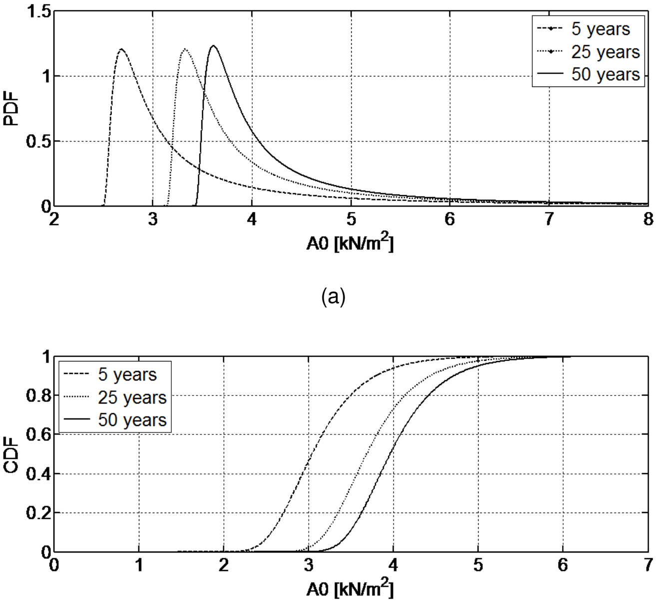

(a)

(b)

Figure 6.11: Distributions for pedestrian loading parametrized as a function of years: a) PDF; b) CDF.

ANSYS (2007) allows for the consideration of few standard Probability Density Functions (PDFs), as a results the MLE was adopted to transform the initial Extreme Values (Gumbel) Type I distribution to an available distribution function. Therefore, a Lognormal distribution with parameters estimated by MLE was considered. The comparison between the parameters is shown in Table 6.6.

### 6.3.4 Wind loads

As anticipated, the likelihood of extreme load conditions increases over time, hence also for wind loading was assumed the increasing over time. For the design of CSIV both sea wind speed and ground wind speed were estimated to be 33.5 $\frac{m}{s}$ and 27 $\frac{m}{s}$ from national standards (CNR (2008)) as the corresponding wind speeds with a return period of 50 years. The following relationships represents the

|  | Extreme value Type I probability functions |  | Lognormal probability functions |  |
|---|---|---|---|---|
| **Year** | k $[kN/m^2]$ | $\beta[kN/m^2]$ | $\mu[kN/m^2]$ | $\sigma[kN/m^2]$ |
| 5 | 2.91 | 0.45 | 3.17 | 0.54 |
| 10 | 3.19 | 0.45 | 3.44 | 0.54 |
| 15 | 3.35 | 0.45 | 3.61 | 0.54 |
| 20 | 3.47 | 0.45 | 3.72 | 0.55 |
| 25 | 3.55 | 0.45 | 3.81 | 0.55 |
| 30 | 3.63 | 0.45 | 3.88 | 0.54 |
| 35 | 3.69 | 0.45 | 3.94 | 0.54 |
| 40 | 3.74 | 0.45 | 4.00 | 0.54 |
| 45 | 3.79 | 0.45 | 4.04 | 0.54 |
| 50 | 3.83 | 0.44 | 4.09 | 0.55 |

Table 6.6: Parameters of the two probability distributions.

CDF proposed by the national standard CNR (2008):

$$v_r = v_b c_r \tag{6.2}$$

$$c_r = \begin{cases} c_r = 0.75 & T_R = 1 \\ c_r = 0.75 + 0.0652 ln(T_R) & 1 T_R < 5 \\ c_r = 0.75\sqrt{1 - 0.2 ln[-ln(1 - \frac{1}{T_R})]} & 5 T_R < 50 \\ c_r = 0.651 - 0.138 ln[-ln(1 - 1/T_R)] & T_R 50 \end{cases} \tag{6.3}$$

where $c_r$ takes into account the return period $T_R$ on the reference wind speed $v_b$ at $T_R = 50$ years. These Cumulative Distribution Functions (CDFs) are plotted in Figures 6.12(a) and 6.12(b) for sea and ground wind, respectively.

The CDFs depicted in Figures 6.12(a) and 6.12(b) were replaced by a Lognormal CDF characterized by parameters estimated with the method of MLE. The obtained parameters are gathered in Table 6.7.

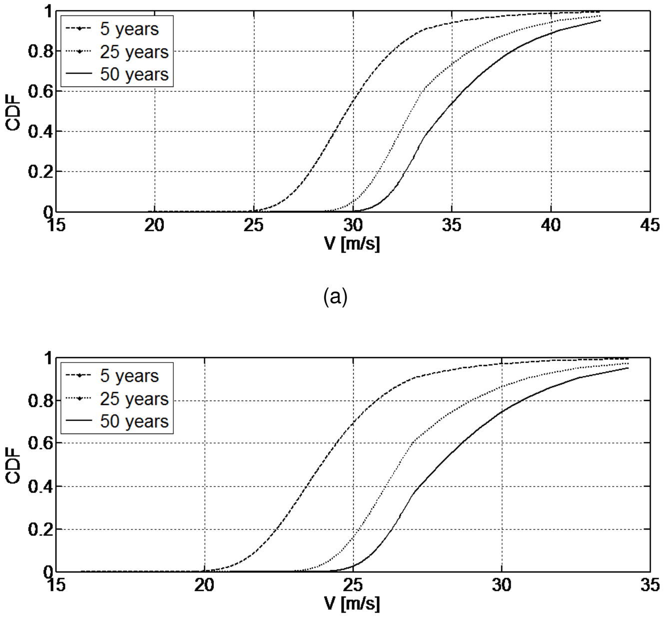

(a)

(b)

Figure 6.12: CDF for wind load: a) sea side; b) ground side.

Both decks of CSIV were subjected to forces, characterized by static, self-excited aerodynamic and turbulent components; as a result, the bridge response owing to by turbulent forces requires the biggest computationally effort. Therefore, with the aim to reduce the computational burden of the LHS, further hypotheses were assumed. In standard wind analyses the extreme structural response is evaluated by means of the following relationship base on dynamic response:

$$R_{max} = \mu_R + k_p \sigma_p \tag{6.4}$$

where $R_{max}$ represents the wind extreme response of the structure, $\mu_R$ defines its mean value due to the static component of wind loading, $k_p$ is a peak factor related to the mean value of the largest response and $\sigma_p$ defines the standard deviation (Dyrbye, C. and Hansen, S. O. (1999)). Equation 6.4 can also be presented in an alternative way,

$$\phi = \frac{R_{max}}{\mu_R} \tag{6.5}$$

where $\phi$ is defined as gust factor. Whilst in literature a few simplified proposal for

|  | Ground wind |  | Sea wind |  |
|---|---|---|---|---|
| **Year** | $\mu[kN/m^2]$ | $\sigma[kN/m^2]$ | $\mu[kN/m^2]$ | $\sigma[kN/m^2]$ |
| 5 | 23.85 | 2.04 | 29.59 | 2.53 |
| 10 | 25.03 | 2.02 | 31.05 | 2.50 |
| 15 | 25.71 | 2.00 | 31.9 | 2.50 |
| 20 | 26.21 | 2.00 | 32.52 | 2.50 |
| 25 | 26.59 | 2.01 | 32.99 | 2.48 |
| 30 | 26.90 | 2.00 | 33.38 | 2.48 |
| 35 | 27.16 | 1.99 | 33.70 | 2.47 |
| 40 | 27.39 | 1.99 | 33.98 | 2.47 |
| 45 | 27.59 | 1.98 | 34.23 | 2.46 |
| 50 | 27.76 | 1.97 | 34.45 | 2.44 |

Table 6.7: Parameters of the Lognormal probability functions vs. time for wind loading.

the definition of $k_p$ and $\sigma_p$ are available, here it was followed a more direct and accurate procedure. In detail, for the specific wind loading and RMCSIVCHS of the bridge to hand, once calculated the static response $\mu_R$ of each deck, it was possible to directly estimate maximum positive/negative responses from buffeting responses. As a result and for each node of interest, gust factors $\psi$ of Equation 6.3.4 were estimated. Figure 6.13 depicts the aerodynamic nodes on both decks, where both gust factors and response maximum/minimum values were estimated. Related maximum $\psi$ values are shown in Figures 6.14 and 6.15 for vertical deck deflections and Figure 6.16 for deck rotations, respectively. With regard to rotations, only maximum values for see wind have been plotted being the ones that will induce greater values on foot track deck. Typical values of $\psi$ are limited to about 10, in agreement with values of literature (Dyrbye, C. and Hansen, S. O. (1999)); also higher values of gust factors appear, e.g. 40 or 50, but in that case their effect was limited, because their amplification was applied to very small mean response values $\mu_R$.

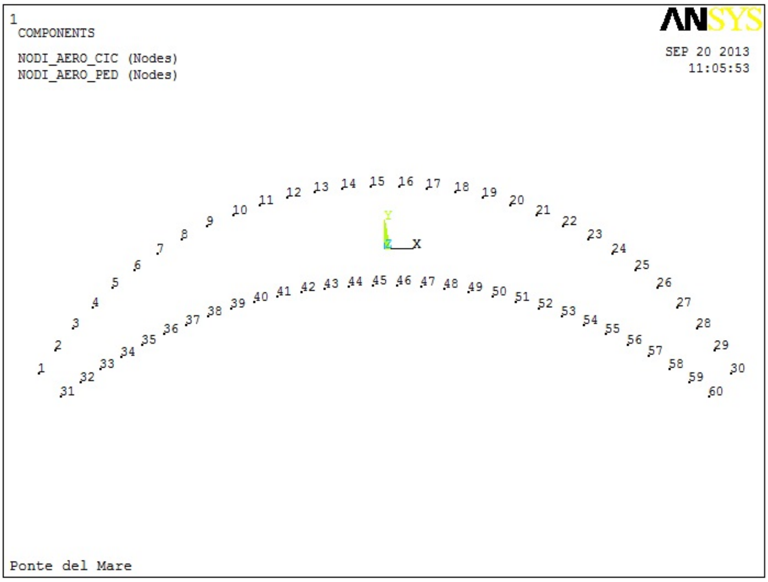

Figure 6.13: Location of aerodynamic nodes on RMCSIVCHS.

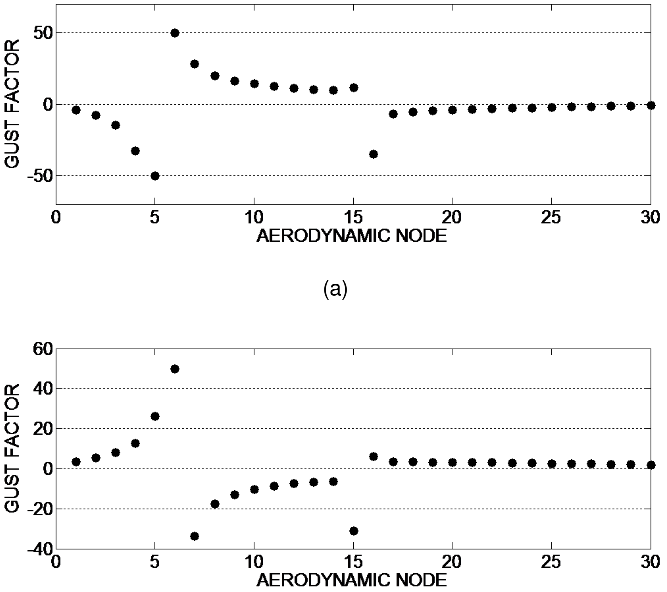

(a)

(b)

Figure 6.14: Foot track deck spatial distribution of gust factor for deflections under: a) ground wind; b) sea wind.

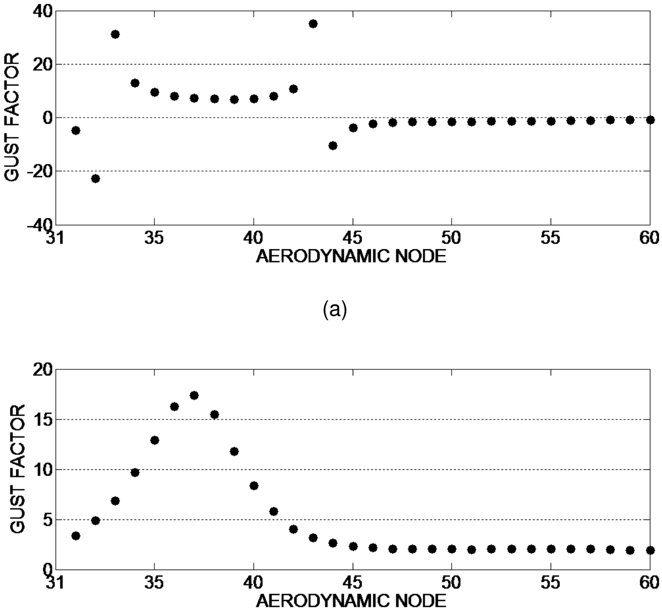

(a)

(b)

Figure 6.15: Cycle track deck spatial distribution of gust factor for deflections under: a) ground wind; b) sea wind.

### 6.3.5 Corrosion deterioration models

In order to prevent corrosion, the structure was treated with specific procedures. In detail, the bridge was painted with a coating system that allows 10-year warranty, subjected to a paint check after 5 years. On this basis and considering the limited literature relevant to corrosion phenomena in structural tubes, two corrosion models were conceived and the implemented in ANSYS environment (ANSYS (2007)). Because the RMCSIVCHS presented in Subsection 6.2.3 was not ready to reproduce welds of complex joints, see for instance Figure 6.8, corrosion phenomena were assumed to happen in connected CHS members.

#### 6.3.5.1 Model #1 - Uniform corrosion

In this case, it was assumed a reduction of cross section area of CHS starting at the outer surface (Marsh and Frangopol (2008)). In particular, at any time t, the

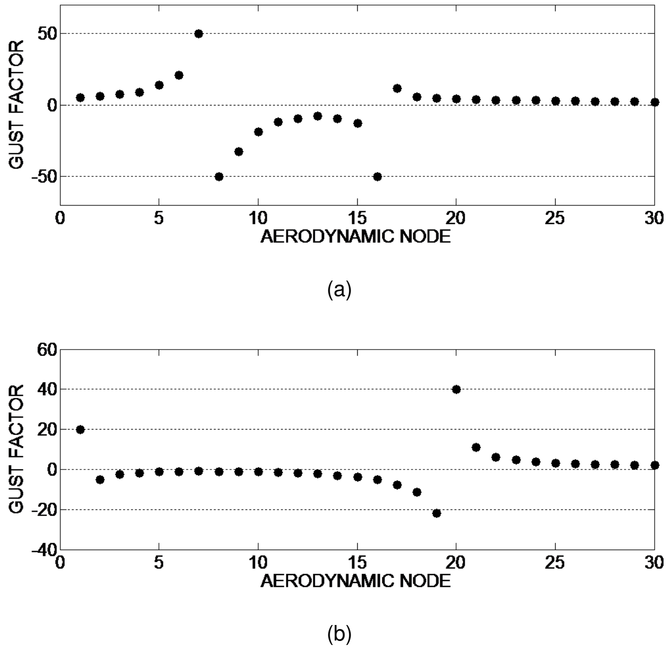

Figure 6.16: Spatial distribution of gust factors for rotations relevant to sea wind for: a) foot track deck; b) cycle track deck.

reduced area A(t) was defined as:

$$A(t) = \frac{\pi}{4}[[D_o - 2r_{corr}(t - T_{corr})]^2 - (D_i)^2] \tag{6.6}$$

where A(t) represents the area of a section at time t in $mm^2$, $T_{corr}$ is the corrosion initiation time in years, and $r_{corr}$ is the corrosion rate in $\frac{mm}{year}$, $D_o$ and $D_i$ are the outer and inner diameters of a CHS, t is the time in years. The experimental values of $r_{corr}$ for both weld metals and base metal steel type TS590LH and S355LH are gathered in Table 6.8 Bursi et al. (2011). The average corrosion rate of TS590LH was slightly lower compared to that of S355LH grade steel in all tested environment conditions.

In agreement with ENISO9223 (2012) and ENISO9226 (2012) and based on experimental tests, the relevant probability functions were evaluated. As a result, $r_{corr}$ was considered to be Lognormally distributed with corresponding $\mu$ = 0.058 $\frac{mm}{year}$ and $\sigma$ = 0.01224 $\frac{mm}{year}$. In addition, the corrosion initiation time $T_{corr}$ was implemented with a Lognormally distributed probability function with a mean value

| **Steel grade** | **Environment type (percentage in weight)** | **Gas bubble** | $r_{corr}[mm/year]$ |
|---|---|---|---|
| TS590LH | 3.5 wt % NaCl | Air bubble | 0.140 |
| TS590LH | 3.5 wt % NaCl | N2 bubble | 0.105 |
| TS590LH | 1 wt % NaCl | N2 bubble | 0.058 |
| S355LH | 3.5 wt % NaCl | Air bubble | 0.168 |
| S355LH | 3.5 wt % NaCl | N2 bubble | 0.114 |
| S355LH | 1 wt % NaCl | N2 bubble | 0.086 |

Table 6.8: Average corrosion rates for base and weld metal of TS590LH and S355LH.

$\mu$ =15 *years* and standard deviation $\sigma$= 1.5 *years*. This hypothesis was set to reflect with the 10-year warranty of the painting system with a check at 5 years. The relevant evolution of $r_{corr}$ is represented in Figure 6.17(a).

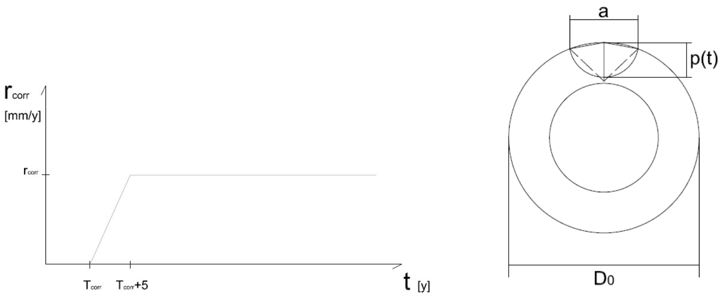

(a)

(b)

Figure 6.17: Corrosion models details: a) evolution of corrosion rate $r_{corr}$; b) pit configuration in a hollow cross section.

#### 6.3.5.2 Model #2 - Localized corrosion

Because the Uniform Corrosion process modelled in Subsection 6.3.5, i.e. Model #1 rarely happens in not immersed deck members, it was decided to consider also a corrosion model including local effects, i.e. pitting, of corrosion. This type of corrosion is one of the most destructive and insidious forms of corrosion that happens in members not directly in contact with marine water. It generally initiates during uniform corrosion and leads to the creation of small holes in member surfaces with only a small percent weight loss of the entire member. Proper 3D FE models of members capable of simulating holes in metal in all the members of RMCSIVCHS, are too heavy for a reasonable time of computation for the whole twin deck bridge. With these considerations, pitting was implemented in RMCSIVCHS members by means of a novel smeared approach, where the following hypotheses were made:

1. the total volume of metal lost by all pits for pitting corrosion in a member is smeared on the surface like an equivalent uniform corrosion process;
2. both localized corrosion -Model #2- and Uniform corrosion -Model #1- entail, in average, the same amount of lost volume;
3. the volume of each single pit is assumed to hold a square base of area $a^2$;
4. the maximum volume of pits $V_{max-pits}$, and the relevant holded area is endowed with bases capable of covering up to half of the total external surface of each member in a chessboard fashion.

It is evident that Hypothesis #1 might underestimate local stress on the members because each FE member is not endowed with single holes; moreover, the lack of holes is practically not relevant at the structural global level for prediction of deflection/rotation values. Hypothesis #2 might appear too safe but considering the situation -deck members next to the sea- and limited pipeline literature (Ahammed and Melchers (1995),Fang et al. (2007),Fang et al. (2009)) it has to be assumed as realistic. On this basis and in agreement with the Stewarts formulation (Stewart (2004)), pitting corrosion, i.e. Model #2 was expressed by means of the following relationships,

$$p(t) = r_{corr} R t \tag{6.7}$$

where: p(t), i.e. the pit or penetration depth, is depicted in Figure 6.17(b); $R = \dfrac{p(t)}{P_{av}}$ i.e. the ratio between p(t) and the average penetration $P_{av}$ computed with uniform corrosion. In particular, R was assumed to be a uniformly distributed random variable with extreme values of 2 and 10, with location parameter 2 and scale parameter 8 in agreement with Stewart (2004).

In order to characterize the pit geometry to be elaborated in ANSYS (2007) and represented in Figure 6.17(b), the following quantities were considered:

$$a = 2p(t)\sqrt{1 - \frac{(p(t)}{D_o})^2} \tag{6.8}$$

$$A_{pit} = \begin{cases} A_1 + A_2, & p(t) \leq \frac{D_o}{2} \\ \frac{\pi D_o^2}{4} - A_1 + A_2, & \frac{D_o}{\sqrt{2}} < p(t) \leq D_o \\ \frac{\pi D_o^2}{4}, & p(t) \geq D_o \end{cases} \tag{6.9}$$

where $A_{pit}$ defines the cross area of a pit, with

$$A_1 = 0.5[\theta_1(\frac{D_o}{2})^2 - a \mid \frac{D_o}{2} - \frac{p(t)}{D_o} \mid]; \tag{6.10}$$

$$A_2 = 0.5[\theta_2 p(t)^2 - a\frac{p(t)^2}{D_o}]; \tag{6.11}$$

$$\theta_1 = 2arcsin(\frac{a}{D_o}); \tag{6.12}$$

$$\theta_2 = 2arcsin(\frac{a}{2p(t)}); \tag{6.13}$$

Once calculated $A_{pit}$ from Equation 6.9, the evaluation of $V_{pit-actual}$ distributed on each member surface is based on the Hypotheses iii) and iv). It reads:

$$V_{pit-actual} = f_X(x \mid \alpha, \beta, x_{min}, x_{max})V_{max-pits}; \tag{6.14}$$

where, $f_X(x \mid \alpha, \beta, x_{min}, x_{max})$ is a limited Beta density function whose limits $x_{min}$ and $x_{max}$ corresponded to 0, for no corrosion, and to 1 for the case corresponding to $V_{max-pits}$, respectively. In greater detail, the beta function reads,

$$f_X(x \mid \alpha, \beta, x_{min}, x_{max}) = \frac{(\frac{x-x_{min}}{x_{max}-x_{min}})^{\alpha-1}(1-(x-x_{min})/(x_{max}-x_{min}))^{\beta-1}}{B(\alpha, 1beta)(x_{max}-x_{min})};$$

$$(6.15)$$

where $\alpha$ and $\beta$ define the parameters of the density function, determined by the solution of the following system of equations,

$$\begin{cases} \mu_{Beta} = \mu = x_{min} + (x_{max} - x_{min})\frac{\alpha}{\alpha+\beta} \\ \sigma_{Beta} = 0.10 = \frac{x_{max}-x_{min}}{\alpha+\beta}\sqrt{\frac{\alpha\beta}{\alpha+\beta+1}} \end{cases} \tag{6.16}$$

with,

$$\mu = \frac{V_{uniform-corr}}{V_{max-pits}}; \tag{6.17}$$

$$Beta(\alpha, \beta) = \int_0^1 x^{\alpha-1}(1-x)^{\beta-1}dx; \tag{6.18}$$

represents the Beta Euler function. This means that the mean value of the beta distribution is the one the provides the amount of corrosion equal to the uniform corrosion volume. In detail, Hypothesis iv) was enforced through Equation 6.17; the above-mentioned Hypothesis i) was implemented by means of a reduced value of $D_o$ applied to each member in a smeared fashion, thus modifying the cross section area of each BEAM44 element. It is evident that a finer dicretization of bridge decks members via BEAM44 elements would reduce the influence of the smeared approach.

### 6.3.6 Numerical simulations setting

In order to accelerate the convergence of the MCS procedure, the analysis of the CSIV was performed using nonlinear simulations based on LHS. In detail, each PDF was subdivided in 50 intervals, sampled each one four time. Nonlinear simulations were performed every 5 years up to 50 years by means of the RMCSIVCHS developed with the ANSYS software described in Subsection 6.2.2 and refined as presented in Subsection 6.2.3. Each MCS, i.e. one for each time period, includes 200 runs in wich the effects caused by dead loads were assumed to be constant. From the literature the aforementioned number of realizations is considered enough to represent lognormal distributions (Yang et al. (2009)).

### 6.3.7 Load cases and limit states

Load cases considered in the reliability analysis were the ones listed in Subsection 6.2.1 coupled with the PDFs for maximum annual values defined in Section 6.3.1. Moreover, since the distributions adopted refereed to maxima values, it is unlike to have maximal simultaneously, for this reason combinations of loads proposed in EN1991-2 (2005) were considered. In particular, the rare combination relevant to SLS was considered,

$$\sum_{j\geq 1} G_{k,j} + P_k + Q_{k,1} + \sum_{i>1} \psi_{0,i} Q_{k,i} \tag{6.19}$$

where both actual loading combination and relevant $\psi_{0,i}$ values can be find in Table 6.9. Then, limit states introduced in Subsection 6.2.1 were considered.

| **Case** | **General Corrosion** | **Pitting Corrosion** | **Ground Wind** | **Sea Wind** | **Pedestrian** |
|---|---|---|---|---|---|
| 1.1 | X | | | | X |
| 1.2 | | X | | | X |
| 2.1 | X | | X | | X (0.4) |
| 2.2 | | X | X | | X (0.4) |
| 3.1 | X | | | X | X (0.4) |
| 3.2 | | X | | X | X (0.4) |
| 4.1 | X | | X (0.3) | | X |
| 4.2 | | X | X (0.3) | | X |
| 5.1 | X | | | X (0.3) | X |
| 5.2 | | X | | X (0.3) | X |

Table 6.9: Load cases for the probabilistic analysis.

### 6.3.8 Time variation of output parameters.

The probability distributions of the output parameters presented in Subsection 6.2.1 is reported herein. Nonetheless, on the basis of the MLE coupled with a

Chi square acceptance test following the procedure proposed by Ayyub, B.M. and McCuen, R.H. (2011), the PDFs selected for each output variable considered are summarized in Table 6.10. Notice that, the Extreme Generalized Value distribution, that represents many of the extreme distributions, i.e. Gumbel, Frechet, and Weibull, allow the Chi square test to be easily passed. As expected and due to both different types of input distributions and to nonlinearities effects, distributions associated with output values did not obey to Gaussian distribution or the like, and therefore, the classical reliability analysis based on the Cornell $\beta$ index (Cornell (1968)) adopted by EN1990-2 (2002) was not feasible. Nonetheless, reference failure probabilities associated to SLS and suggested in EN1990-2 (2002) will be considered in Subsection 6.3.9. The variation of maximum deck deflection, $\delta$ over time for a 50 years time horizon due to Case 5.2 of Table 6.9 is reported in Figures 6.18(a) and 6.18(b) for the foot bridge deck and cycle bridge deck, respectively.

| **Output** | **Distribution** |
|---|---|
| Vertical deck deflection and Rotation | -Log-normal<br>Log-normal<br>Weibull<br>Esponential<br>Beta<br>Generalized Extreme Value |
| Stress | Gaussian<br>Generalized Extreme Value |

Table 6.10: Types of probability density functions selected for the maximum likelihood estimation.

In the same figure, are indicated the mean value, the standard deviation and

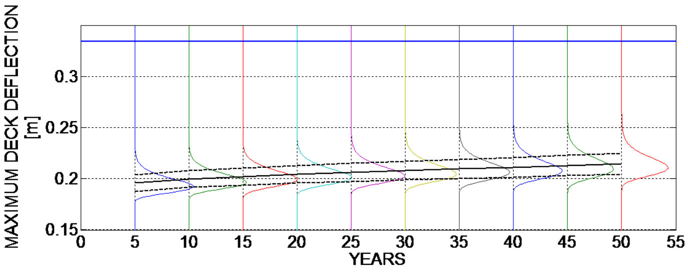

(a)

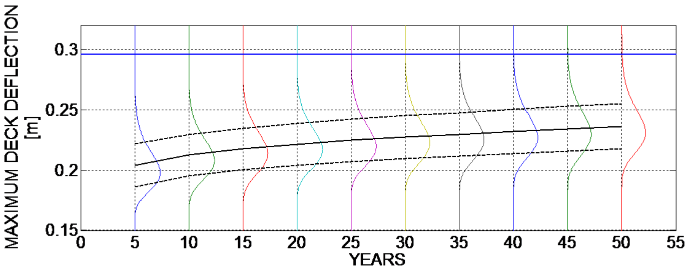

(b)

Figure 6.18: Evolution of maximum deck deflection of Case Study IV corresponding to Case 5.2: a) foot track deck; b) cycle track deck.

the deflection limit of $\frac{L}{500}$ corresponding to the relevant deck. As expected, the mean value increases more than the standard deviation which increasing is very limited. Nonetheless, deflection limits were not exceeded by the mean values at each time step and the foot bridge deck resulted to be more reliable in the life time of the structure. In order to show favourable/unfavourable wind effects on decks, variations of maximum deck deflection, $\delta$ due to Case 2.2 and 3.2, relevant respectively to full ground wind and full sea wind, of Table 6.10 are reported in Figures 6.19 and 6.20, respectively.

Given the bridge configuration Bursi et al. (2014), whilst the ground wind induces favorable effects on decks, especially on the foot bridge deck being the most flexible one, sea wind entails opposite and unfavorable effects on decks, especially on the foot bridge deck, with reductions of deflections, rotations and stresses. Likewise, the distribution of rotation maxima of both decks vs. time is synthesized in Figure 6.21. As before, the mean values remain below the rotation limit value es-

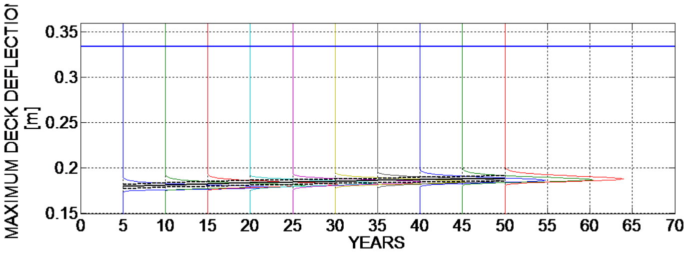

(a)

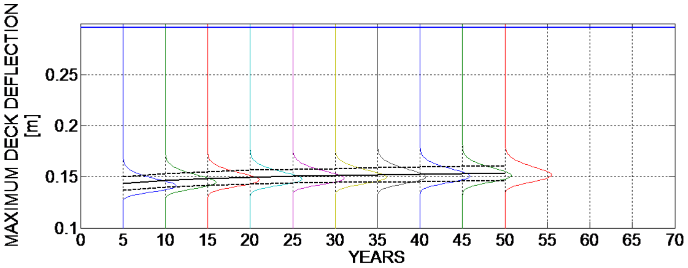

(b)

Figure 6.19: Evolution of maximum deck deflection corresponding to Case 2.2: a) foot track deck; b) cycle track deck.

tablished in Subsection 6.2.1, i.e. 3.5 %, though the increase of standard deviation is more evident for a greater design life.

With regard to SM defined in Subsection 6.2.1, the relevant trend is shown in Figure 6.22 with limit value of 0. It remains relatively constant during the first 15 years due to a time lag in corrosion initiation; for instance for uniform corrosion described in Subsection 6.3.5 it was assumed a mean value $\mu$=15 *years* and standard deviation $\sigma$= 1.5 *years* for the relevant Lognormal distribution. After that time, SM decreases. In any case, this result is affected by the smeared approach of Hypothesis i) of Model #2 that entailed a stress underestimation.

### 6.3.9 Estimation of out-of-service conditions

The availability of distributions provided by the Chi square test and relevant to output quantities defined in Subsection 6.3.8, allowed probability of failure to be computed with respect to limit values assumed in Subsection 6.2.1. Moreover,

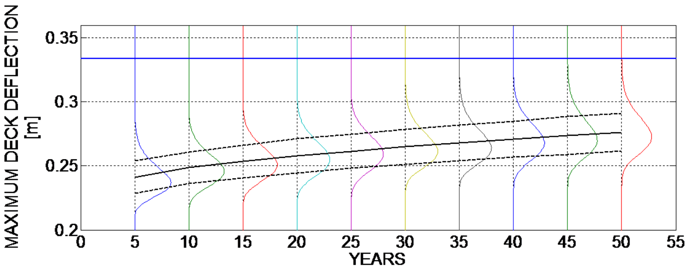

(a)

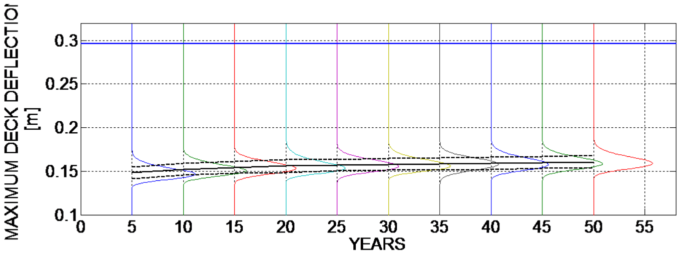

(b)

Figure 6.20: Evolution of maximum deck deflection corresponding to Case 3.2: a) foot track deck; b) cycle track deck.

EN1990-2 (2002) provides probabilities of failure and Cornell $\beta$ index for SLS as reported in Table 6.11. Therefore just for the sake of comparison, it was straightforward to check the exceeding of these limit states by means of failure probability.

| $P_f$ | 0.009 | 0.027 | 0.045 | 0.072 | 0.089 |
|---|---|---|---|---|---|
| $\beta$ | 2.3 | 1.9 | 1.7 | 1.5 | 1.3 |

Table 6.11: Probability of failure and Cornell $\beta$ index for SLS (after EN1990-2 (2002)).

As a consequence, Figures 6.23(a), 6.23(b), 6.24(a), 6.24(b), 6.25(a), 6.25(b), report the comparison between probability of failure associated with output deck maxima for all load cases of Table 6.9 and EN1990-2 (2002) SLS values for deflections, rotations and SM, respectively. One can notice that the bridge exceeds the Eurocode limit states at 40 years with respect to deck rotations. In particular

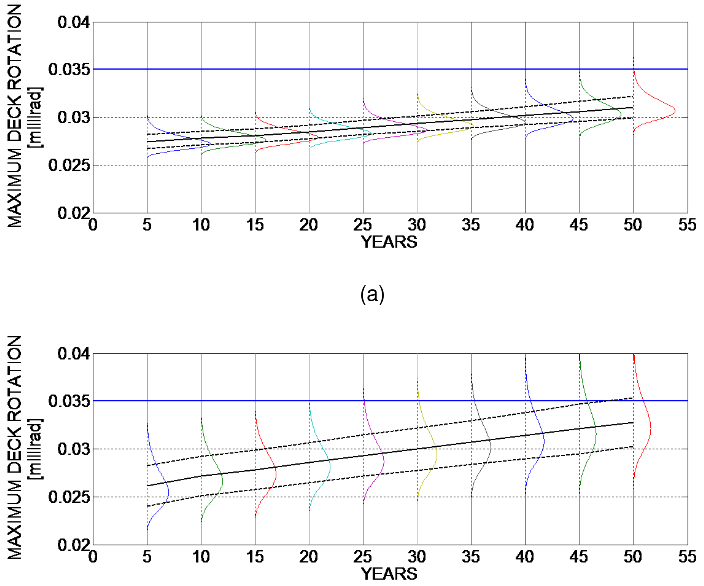

(a)

(b)

Figure 6.21: Evolution of maximum deck rotation corresponding to Case 5.2: a) foot track deck; b) cycle track deck.

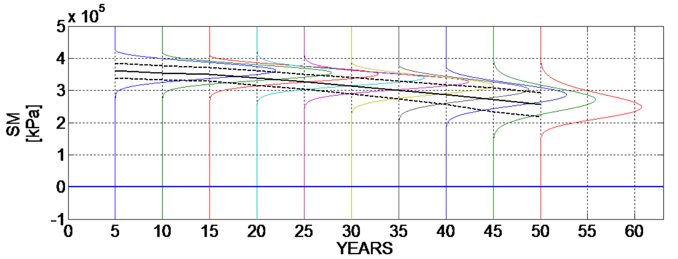

Figure 6.22: Evolution of Safety Margin corresponding to Case 5.2.

on the basis of de-aggregated data, this happens for the cycle track deck and the Load Case 5.2 of Table 6.9 and EN1990-2 (2002), for which effects due to Model #2 of pitting, i.e. localized corrosion, to the full value of sea wind and to reduced values of pedestrian loading were considered. The remaining cases, i.e. the one relevant to foot bridge deck rotation, deflections and stresses were in agreement with the results of the previous Subsection 6.3.8. In addition, effects of corrosion models on failure probabilities presented in Subsection 6.3.5 are shown in Figures

6.23(a), 6.23(b), 6.24(a), 6.24(b), 6.25(a), 6.25(b). A careful reader can notice that these models have equivalent effects on the probability of failure for both deflection and rotations; the difference is more evident for SM, but associated probabilities are really small, because stresses are small due to actual design limitations on deflections/rotations.

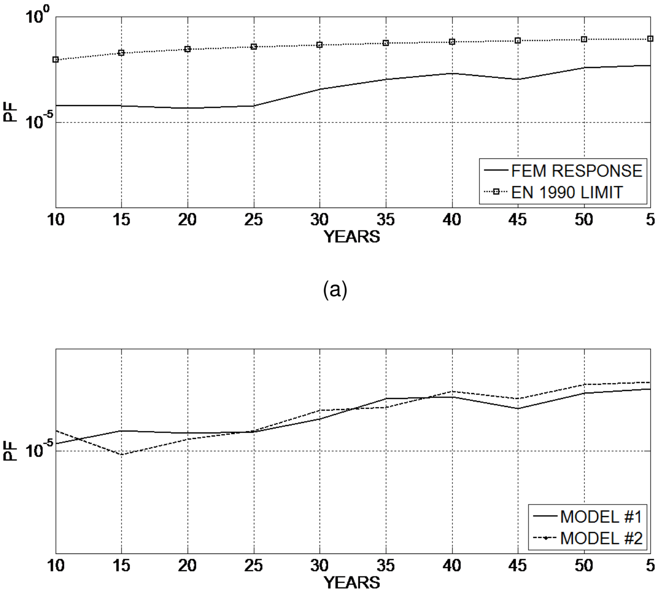

(a)

(b)

Figure 6.23: Time variation of failure probability of footbridge relevant to deck deflection: a) comparison between Model #2 outcomes and Eurocode 0 limits; b) comparison between corrosion models.

## 6.4 Conclusions

In line with the objective of the European project HITUBES, which was to investigate the benefits of CHS structural members for structure erected in an aggressive environment. In this chapter Step IV of SPAB has been carried out within a reliability multi-input analysis. In detail, a cable-stayed footbridge equipped with dynamic viscous dampers and subjected to corrosion and other hazards was analyzed. Owing to some notable advantages of tubular members, trusses made with

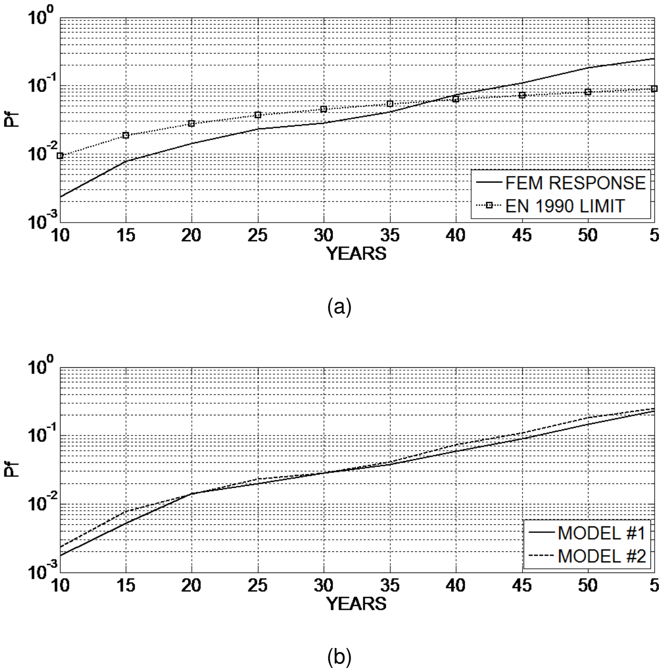

(a)

(b)

Figure 6.24: Time variation of failure probability of footbridge relevant to deck rotation: a) comparison between Model #2 outcomes and Eurocode 0 limits; b) comparison between corrosion models.

OS members of both decks were replaced by CHS members. Hence, in order to estimate section reduction of tubular members under progressive corrosion and other hazards, two corrosion models, the first one relying on uniform corrosion and the second one based on pitting corrosion were proposed. A probabilistic evaluation of the SM and risk of the footbridge for SLS was conducted using nonlinear simulations based on LHS. Limit states were satisfied under wind and pedestrian loadings within the CSIV design life. Nonetheless, with reference to maximum deck rotations, the relevant probability of failure crossed a set limiting value of 3.5 %, corresponding to 40 years. Moreover given the bridge configuration, it was shown that sea wind induces unfavorable effects on bridge decks, whilst ground wind entails opposite and favorable effects with reductions of deflections, rotations and stresses. Therefore, on the basis of decisions taken with wind loading and in order to increase the bridge reliability, the repair and/or a retrofit plan of the foot-

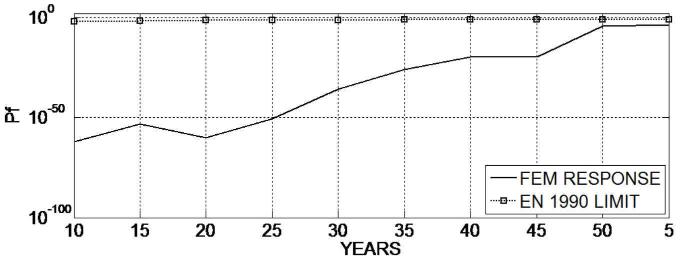

(a)

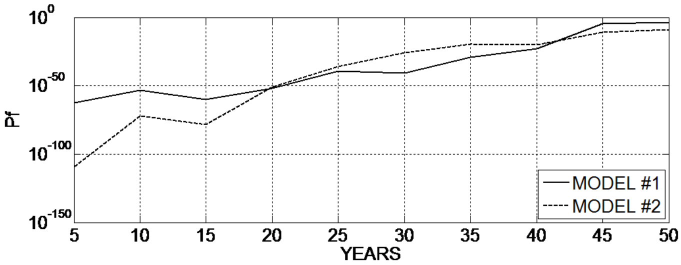

(b)

Figure 6.25: Time variation of failure probability of footbridge relevant to SM: a) comparison between Model #2 outcomes and Eurocode 0 limits; b) comparison between corrosion models.

bridge decks should be activated within 40 years of bridge design life. Finally, in order to better capture the effect of localized corrosion in hotspot areas of welded joints, an efficient FE mesh refinement in joints of deck truss members deserves further study.

## CHAPTER 7

# SUMMARY, CONCLUSIONS AND FUTURE PERSPECTIVES

### 7.1 Summary

As anticipated in Section 1.2 the performed research activity was focused on four main objectives: *i*) application of the APSPAB to different complex case studies; *ii*) employment of advanced testing techniques to investigate the different aspects of structural problems; *iii*) interpretation of experimental data through refined spring based numerical models with the aim to reproduce the actual behavior of the tested specimens and to extend the knowledge obtained; *iv*) application of advanced probabilistic numerical analyses based on refined FE models able to take into account the main uncertainties of the problem under investigation.

The assessment of the seismic performances of an old RC viaduct was conceived within the RETRO project (Paolacci (2014)). Steps I, II, III of APSPAB procedure have been developed In Chapter 3 in order to reach the objectives of the project. In particular they were: *i*) to cover the lack of knowledge in the nonlinear behavior of portal frame piers in presence of plain steel rebars; *ii*) to employ large scale experimental tests for the seismic assessment of existing bridges; *iii*) to study the effectiveness of a seismic isolation systems based on CSBs. A complex experimental setting for HSs was implemented at the ELSA laboratory of the Joint Research Center in Ispra (VA). It included PSs to represent the tested elements, i.e. RC piers and CSBs, and nonlinear S-DoF reduced models to represent the remaining part of the viaduct. Through this setup both transversal seismic response and effectiveness of the CSBs based isolation system were analyzed. Furthermore, several numerical FE models were produced to analyze the experimental outcomes and to quantify the effects of steel plane rebars. Two 2D stick models and a 3D refined model were implemented in the ABAQUS environment (SIMULIA (2011)) to reproduce the Pier #11 including all the nonlinearities showed by the portal frame pier.

The seismic assessment of a twin piers continuous RC bridge by means of HSs testing campaign was developed at EUCENTRE Tress Laboratory located in Pavia (PV) and was presented in Chapter 4. The investigations included the analysis of the transversal seismic response in both the isolated and the non isolated configurations. The BTS of EUCENTRE Laboratory, which has been initially designed to carry out standard qualification tests in force and/or displacement control of isolation devices, was used to substructure a prototype of CSB and to apply the correct boundary conditions in terms of vertical load and horizontal displacement. In greater detail, the seismic assessment of the structure, have been developed by means of steps I, II, III and partially IV of APSPAB procedure. Four aspects have been investigated: *i*) the effectiveness of a prototype of CSB with an innovative rate independent behavior; *ii*) the advantage of a novel partitioned time integration tailored for first order system (Abbiati et al. (2014)); *iii*) the improvements produced by an online model updating based on UKF(Julier et al. (1995)). In grater detail, the prototype of CSB was initially characterized by means of traditional dynamic tests and then implemented in the HSs setup. The experimental setting was composed by PSs of pier and CSB and S-DoF nonlinear reduced models to represent the NSs. To couple these substructures an innovative time integration algorithm was used. The algorithm, thanks to the implementation of state-space variables allowed for the implementation of an online model updating based on the UKF. As a result the NSs parameters were updated step by step on the base of the instantaneous observed PS outcomes, i.e. restoring force and displacement.

The seismic assessment of steel steel concrete composite bridges made with hot rolled beams (SCCBHs) based on cyclic test was conceived within the SEQBRI project (Paolacci et al. (2015)) in which three novel structural joints for SCCBHs have been investigated by means of quasi static cyclic tests and a fully probabilistic analysis. The objective of the project were: *i*) to investigate the seismic response of three novel connections between the CCB and the steel I-girder beams; *ii*) to apply the fully probabilistic PBEE to a functional composite bridge designed according to Eurocodes. In Chapter 5 steps I, II, III, IV of APSPAB have been taken. In greater detail, several FE models were implemented in Opensees environment (Mazzoni et al. (2009)) to predict the behavior of these novel connections. The numerical predictions were used to chose the proper cyclic tests loading protocol. In order to analyze both advantages and disadvantages of these joint connections, the experimental campaign included several tests for each joint type. The outcomes were finally used to develop an innovative CMM model able to reproduce the main nonlinearities observed during the tests. Thanks to this numerical powerful tool the hazard and structural parts of PBEE were widely developed (Cornell and Krawinkler (2000)).

The benefits of CHS structural members for structure erected in an aggressive environment were investigated in Chapter 6. STEP IV of APSPAB has been carried out within a reliability multi-input time dependent analysis (Marsh and Frangopol (2008)). In detail, a twin decks cable-stayed footbridge equipped with dynamic viscous dampers and subjected to corrosion and other hazards was analyzed. Owing to some notable advantages of tubular members, trusses made with OS members of both decks were replaced by CHS members. Hence, in order to estimate section reduction of tubular members under progressive corrosion and other hazards, two corrosion models, the first one relying on uniform corrosion and the second one based on pitting corrosion were proposed. A probabilistic evaluation of the probability of failure of the SLS quantities was conducted using nonlinear MCSs enhanced by LHS (McKay et al. (1979)).

## 7.2 Conclusions

The seismic retrofitting of an old RC viaduct represented by the Rio Torto bridge was performed within the RETRO project. The complex experimental campaign and the huge set of numerical investigations allowed to analyze the effects of steel plane rebars and the effectiveness of a retrofitting system based on CSBs. In greater detail, a set of HSs has been designed and performed at ELSA laboratory to test the Rio Torto Viaduct in both *asbuilt* and isolated configurations. The implementation of the tests required high speed in numerical calculations due to the needs of substructures coupling. It resulted in the definition of nonlinear reduced models representing the NSs, which implicated additional numerical investigations to prove the effectiveness of the reduction. The final NSs setting has been reached passing through identification and optimization tools developed by interfacing different numerical/FE software. In greater detail, a modified Bouc-Wen model (Smyth et al. (1999)) and a Mostaghel model (Mostaghel (1999)) have been used for piers and CSBs NSs, respectively. Furthermore, relevant to the structural degradation, the damage generated during tests has been taken into account by an offline model updating technique. The method allowed for the updating of NSs parameters before starting each HS test. Event though the updating was devoted only to concrete strength ($f_{cm}$) and young's modulus $E_{cm}$ of PMCSI, it was suitable to set S-DoF reduced models and to quantify the damage gathered in the PSs. In fact, the identified values of $f_{cm}$ showed a drop of almost 50% with respect the initial value. In addition, the potential of DS has been exploited to solve the problem of yielding variation generated on CSBs due the slow speed of PDT procedure. In fact, during each HS the friction coefficient ($\mu$) of the CSBs was identified as almost twice the design value, i.e. $\mu_{test}$=7% and $\mu_{des}$=4%. As a result the risk to damage the pier increased. In this case thanks to dynamic substructuring was possible to modify the vertical load on the PSs and maintain the design characters of the isolators. In fact, once modified the yielding point through the variation of vertical load, the nonlinear behavior was reported to the design features by the numerical compensation of the restoring force coming out from the physical CSBs before sending it to the time integration algorithm.

With regard to the local scale numerical analysis, thanks to the huge set of FE-based investigations supported by experimental data, the effects of plane rebars have been quantified. In grater detail, two refined FE models, i.e. 2D and 3D, based on SBM approach have shown the effective drop in stiffness due to the weak connection provided by the piers joints. The validation and calibration of numerical FE models allowed for the identification the joints stiffness. It permitted to quantify the effective degradation produced by plane rebars and compare it with the degradation due to shear effects on the transverse beam. In fact, initially the damage of the pier was driven by nonlinear effects due to joints rotations; later, once the joints lost rotational stiffness additional damage affected in the transverse beam. The experimental campaign has been used to prove the effectiveness of the seismic CSBs-based retrofitting system up to ULS earthquake. In fact, when the isolated configuration has been tested piers remained in the elastic range for both SLS and ULS ground motions.

The seismic assessment of an RC bridge and the evaluation of the seismic benefits provided by an innovative, rate independent, CSB were investigated in the CSII. Among several seismic assessment objectives, the case study was analyzed with the aim to develop some innovative technologies related to HSs, such as online model updating and first order time integration schemes. Therefore, a novel first order partitioned time integration scheme has been used during the HSs. Thanks to the state-space features, the scheme was tailored to first order systems and allowed for the straightforward accommodation of the UKF. As a result, in order to simulate a consistent degradation of the twin numerical pier, the UKF was used as an online dynamic identification tool. The possibility to consider the evolution of damage step by step during the test is a significative improvement which practically deleted the approximations typical in HS supported by offline model updating procedures. Then, a prototype of CSB has been characterized and used during HSs. The expected rate independent behavior for high speed was proven; in fact for load rate close to the typical design values the friction coefficient ($\mu$) assumed the asymptotic value of 8%. As a result, it was the perfect candidate to solve challenging civil engineering problems related to the variation of seismic loads rate. In fact, quite often, the speed of the earthquake loading can varies with detrimental and unexpected damage in the piers. As happened in CSI, the slow rate of the PDT generated an alteration of the friction coefficient of the isolator. In this particolar case, the problem was the opposite; in fact, $\mu_{test}$=6% and $\mu_{des}$=8%. As a result, the risk to damage the pier decreased; nonetheless, in order to have more reliable results the friction coefficient was kept in the design range. Therefore, the restoring force coming out from the CSBs was again modified numerically before being sent to the time integration algorithm.

The seismic assessment of SCCBHs made with novel joints between CCB and Steel-I girders has been investigated during the SEQBRI project (Paolacci et al. (2015)). Firstly, a PMCSIII has been implemented in the Opensees environment to predict the behavior of the CSIII in both isolated and non isolated configurations, the FE model showed an optimum seismic response of the facility due to the limitated weight of the deck. The simulations were used to set the proper testing protocol; in fact the reduced damage produced by the design earthquake has driven the choice to the standard ECCS procedure. As a result, an amount of 15 tests, monotonic and cyclic, have been performed to investigate the transversal (7 tests) and longitudinal (8 tests) responses of the novel SCC joints. The experimental campaign performed at the University of Trento (TN) provided information about the collapse mechanisms generated by transversal seismic actions, in detail for these type of joints the collapse was governed by the crushing of concrete at the interface between the CCB and SCC sections. The other components, characterizing each joint type (prestressing bars, Nelson studs, etc..) were slightly stressed. The experimental data were considered to create a novel CMM of the bridge connection, able to reproduce the local mechanisms generated during the test. In detail, it was implemented by means of the reproduction of the mechanical components acting on the CCB. Furthermore, due to experimental evidences, particular attention was dedicated to the CCB interface components, i.e. concrete slab and rebars, where the most of the damage was located. Finally, in order to obtain the refined model of the CSIII, the CMM has been implemented in the full-scale bridge (CMMCSIII) and compared with the PMCSIII. CMMCSIII was used to perform a probabilistic seismic demand analysis. In greater detail, both hazard and structural parts of the PBEE method were fully developed. These parts of the procedure provided information about the structural seismic response of both non isolated and isolated configurations based on the three edps investigated for earthquake up to 1.9g of PGA. Fragility curves of the relevant edps have been defined; for the design earthquakes they showed that the probability of exceeding the tensile strength limit state of slab edps, i.e. *edp*2 and *edp*3, remains in a safe range. As a result, the static design of the SCC deck resulted to be sufficient to cover also the seismic actions. The pier, conversely, accumulated more damage when subjected to the same earthquakes. In fact, the fragility curve of *edp*1 showed larger probability of exceeding the concrete spalling limit state. As a conclusion and with regard to the transversal seismic action, since the major damage happened in the pier, the novel CCB steel I-girders joints exhibited a favorable behavior and are perfect candidates to be exported in high seismicity prone areas.

The benefits of CHS structural members for structures erected in an aggressive environment were investigated within the CSIV. The reliability time-dependent analysis performed by means of MCSs enhanced by LHS allowed to analyze the effect of aging and variation of loads magnitude during the life of the structure. Limit states were satisfied under wind and pedestrian loadings within the CSIV design life. Nonetheless, with reference to maximum deck rotations, the relevant probability of failure crossed a set limiting value of 3.5%, corresponding to 40 years. Moreover given the bridge configuration, it was shown that sea wind induces unfavorable effects on bridge decks, whilst ground wind entails opposite and favorable effects with reductions of deflections, rotations and stresses. Therefore, on the basis of decisions taken with wind loading and in order to increase the bridge reliability, the repair and/or a retrofit plan of the footbridge decks should be activated within 40 years of bridge design life.

All these case studies have shown that every step is fundamental for a complete seismic performance analysis of bridges. Whenever a step is skipped additional uncertainties are introduced in the analysis which can generate unexpected and probably unsolvable issues.

## 7.3 Future Perspectives

The future perspectives proposed on the base of the research activity outcomes outlined above are reported.

With regard to case study I and in particular to the HSs technique, some aspects were improved in CSII such as the overtaking of the limitation of the updating of NSs. It was solved by the model updating online based on UKF. Nonetheless, the quantification of the approximations produced by the implementation of S-DoF as NSs still remains an open question.
Relevant to the local scale, the main task to be concluded is the final evaluation of the plane rebars effects. In the thesis, in fact, the analysis preformed were capable of identifying the local effects and the results of the 3D model. Currently, the model is capable of reproducing the LVDTs elongations in the SLS regime for both columns joints and transverse beams. Moreover, it allowed for the quantification of the unknown behavior of the columns joints and to identify the range in which it is predominant in comparison to the effects of the transverse beam shear deformation. The analysis can be considered complete, when also the ULS regime will be reproduced; for this reason the 3D model requires additional improvements.

With regard to case study II, the novel time integration algorithm introduced several advantages in the field of HSs: above all the possibility to implement the UKF as an online identification tool. The methodology is a Pandora's box in the field of HSs: in fact it allows to investigate the problem of online model updating with numerous options. In addition, to solve the approximations related to the rate dependency of structural devices such as CSBs the objective of RT simulations still remain a priority. As a result, in order to refine the online model updating and to solve speed limitations, several tests are scheduled at the EUCENTRE TRESS Laboratory in Pavia.

With regard to CSIII, the reliability of the novel joint solutions has been widely proven in both seismic directions during SEQBRI project; for this reason, the main future development is the dissemination of the new technology. Therefore, two perspectives can be proposed: *i*) the extension/validation of the CMM, which is a powerful tool, able to extend the investigations to different cases study also with different connections between the pier and the deck; *ii*) the implementation of an automatic tool such as a software able to apply systematically the PBEE method to SCCBHs and provide in real time information about economic risk for the owner of the structure. Relatively to proposal *i*, the component-based the mechanical model (CMM) is completely adaptable to all the different configurations such as the ones tested at the University of Roma TRE (Rome). For this reason, it can be applied to other full-scale bridges, i.e. longer and/or multiple span bridges which require adequate CCB joints. The proposal *ii* is strictly related to the extension of the CMM, in fact thanks to the completeness/adaptability of the CMM it is possible to develop a refined tool capable to take into account all the nonlinear behaviors inside the CCB connection and hence to quantify the decay propagation.

Finally, with regard CSIV, the reliability analysis performed with the local model of corrosion can be improved. In detail, the novel model introduced to predict the pitting evolution is a potential tool that can be extended and widely used in the reliability analysis of steel structures. In greater detail, it will provide the best results if applied in sufficiently discretized domains which allow for the reproduction of holes and hence the evaluation of local stresses amplification. Along this line, a straightforward improvement the presented simulations will be the refinement of the discretization of the refine model of the bridge made with circular hollow section elements.

# CHAPTER 8

# LIST OF ACRONYMS

**ANSYSGM** ANSYS Guyan Model

**ANSYSSM** ANSYS Simplified Model

**ANSYSSMCSII** ANSYS Simplified Model of CSII

**APSPAB** Advanced Procedure for the Seismic Performance Analysis of Bridges

**BTS** Bearing Testing System

**CCB** Concrete Cross Beam

**CCBs** Concrete Cross Beams

**CDF** Cumulative Distribution Function

**CDFs** Cumulative Distribution Functions

**CHS** Circular Hollow Section

**CMM** Component-Based Mechanical Model

**CMMCSIII** Opensees Model of CSIII enhanced by CMM

**CSB** Concave Sliding Bearing

**CSBs** Concave Sliding Bearings

**CSI** Case Study I

**CSII** Case Study II

**CSIII** Case Study III

**CSIV** Case Study IV

**dm** damage measure

**DoF** Degree-of-Freedom

**DoFs** Degrees-of-Freedom

**DS** Dynamic Substructuring

**dv** decision variable

**edp** engineering demand parameter

**edps** engineering demand parameters

**EKF** Extended Kalman Filter

**FE** Finite Element

**HS** Hybrid Simulation

**HSDS** Hybrid Simulation with Dynamic Substructuring

**HSS** High Steel Strength

**HSs** Hybrid Simulations

**IDA** Incremental Dynamic Analysis

**IDAs** Incremental Dynamic Analyses

**im** intensity measure

**ims** intensity measures

**IPMCSII** Optimized Model of Case study II

**LC** Load Cell

**LHS** Latin Hypercube Sampling

**LRB** Lead Rubber Bearing

**LRBs** Lead Rubber Bearings

**LVDT** Linear Variable Displacement Transducer

**LVDTs** Linear Variable Displacement Transducers

**MCS** Monte Carlo Simulation

**MCSs** Monte Carlo Simulations

**MLE** Maximum Likelihood Estimation

**NLGRM** Nonlinear Global Reduced Model

**NRMSE** Normalized Root Mean Square Error

**NRMSEs** Normalized Root Mean Square Errors

**NS** Numerical Substructure

**NSs** Numerical Substructures

**OS** Open Section

**PBEE** Performance Based Earthquake Engineering

**PDF** Probability Density Function

**PDFs** Probability Density Functions

**PDT** Pseudo Dynamic Test

**PGA** Peak Ground Acceleration

**PMCSI** Predictive Model of Case study I

**PMCSII** Predictive Model of Case study II

**PMCSIII** Predictive Model of Case Study III

**PS** Physical Substructure

**PSs** Physical Substructures

**QSCT** Quasi-Static Cyclic Test

**QSCTs** Quasi-Static Cyclic Tests

**RC** Reinforced Concrete

**RMCSIVCHS** Refined Model of Case Study IV made with Circular Hollow Section Members

**RMCSIVOS** Refined Model of Case Study IV made with Open Section Members

**ROTBJ** Rotation of base joint

**ROTBLJ** Rotation of base left side joint

**ROTBRJ** Rotation of base right side joint

**ROTTLJ** Rotation of top left side joint

**ROTTRJ** Rotation of top right side joint

**RT** Real-time Testing

**SBM** Springs Based Modelling

**SCC** Steel Concrete Composite

**SCCBH** Steel Concrete Composite Bridge made with Hot rolled I-girders

**SCCBHs** Steel Concrete Composite Bridges made with Hot rolled I-girders

**S-DoF** Single Degree of Freedom

**SERIES** Seismic Engineering Research Infrastructures for European Synergies

**SFPBOE** Single Friction Pendulum Bearing Opensees Element

**SISO** Single-Input-Single-Output

**SLS** Serviceability Limit State

**SM** Safety Margin

**SMCSIII** Simplified Model of Case Study III

**SPAB** Seismic Performance Analysis of Bridges

**SPBLJ** Spring of base left side joint

**SPBRJ** Spring of base right side joint

**SPTLJ** Spring of top left side joint

**SPTRJ** Spring of top right side joint

**UHS** Uniform Hazard Spectrum

**UKF** Unscented Kalman Filter

**ULS** Ultimate Limit State

# BIBLIOGRAPHY

Abbiati, G. (2014). *Dynamic Substructuring of Complex Hybrid System Based on Time-Integration, Model Reduction an Model Identification Techniques*. PhD thesis, University of Trento.

Abbiati, G., Bursi, O., Cazzador, E., and P., P. (2014). An improved parallel partitioned time integration scheme based on the generalized- method for hybrid simulation. *Proceedings of the 6th World Conference of Structural Control and Monitoring (6WCSCM), Barcelona, Spain*, 86:101–119.

Ahammed, M. and Melchers, R. E. (1995). Probabilistic analysis of pipelines subjected to pitting corrosion leaks. *Engineering Structures*, 17(2):74–80.

Alessandri, S., Corritore, D., Derisi, R., Di Sarno, L., Mohamad, A., Paolacci, F., and Yenidogan, C. (2013). Numerical simulation of the seismic response of the rio-torto viaduct for psd test campaign. retro project. Technical report.

American Institute of Steel Construction (AISC) (2002). Seismic provisions for structural steel buildings. Technical report, American Institute of Steel Construction (AISC). Chicago, IL.

ANSYS, Copyright SAS IP, I. (2007). *Documentation for ANSYS - Release 11.0*.

Applied Technology Council (ATC) (1992). Guidelines for cyclic seismic testing of compo- nents of steel structures. Technical report, Applied Technology Council (ATC). Redwood City, CA.

Ayyub, B.M. and McCuen, R.H. (2011). *Probability, Statistics and Reliability for Engineers and Scientists.* CRC Press.

Azam, S. E. (2014). *Online damage detection in structural systems*.

Baker, J. W. (2015). Efficient analytical fragility function fitting using dynamic structural analysis. *Earthquake Spectra*, 31(1):579–599.

Benjamin, J. R. and Cornell, C. A. (1970). *Probability, Statistics and Decisions for Civil Engineers*.

Bentz, E. C., Vecchio, F. J., and Collins, M. P. (2007). Simplified modified compression field theory for calculating shear strength of reinforced concrete elements. *ACI Structural Journal*, 103.

Brownjohn, J. M. and Xia, P. Q. (2000). Dynamic assessment of curved cable-stayed bridge by model updating. *Journal of Structural Engineering*, 126(2):252–260.

Brun, M., Batti, A., Combescure, A., and Gravouil, A. (2014). External coupling software based on macro- and micro-time scales for explicit/implicit multi-time-step co-computations in structural dynamics. *Finite Elements in Analysis and Design*, 86:101–119.

Bruno, D., Greco, F., and Lonetti, P. (2008). Dynamic impact analysis of long span cable-stayed bridges under moving loads. *Engineering Structures*, 30(4):1160–1177.

Buckingham, E. (1914). On Physically Similar Systems. Illustrations of the Use of Dimensional Equations. *Physical Review*, 4(4):345–376.

Bursi, O. S., Ceravolo, R., Kumar, A., and Abbiati, G. (2014). Identification, model updating and validation of a steel twin deck curved cable-stayed footbridge. *Computer-Aided Civil and Infrastructure Engineering*, 29:703–722.

Bursi, O. S., Ferrario, F., and Fontanari, V. (2002). Non-linear analysis of the low-cycle fracture behaviour of isolated tee stub connections. *Computers and Structures*, 80:2333–2360.

Bursi, O. S., Kumar, A., and et al. (2011). Design and integrity assessment of high strength tubular structures for extreme loading conditions. final report, hitubes project. European Research Fund for Coal and Steel RFSR-CT-2008-00035, UNITN.

Bursi, O. S., Paolacci, F., Zilli, G., Fishbach, G., Movchan, A., Karamanos, S., Hoffmeister, B., and LeMaoult, A. (2015). Component fragility evaluation, seismic safety assessment an design of petrochemical plants under design-basis and beyond-design-basis accident condition (INDUSE2SAFETY). European Research Fund for Coal and Steel RFS-PR-13056, University of Trento, University of Rome TRE, Centro sviluppo materiali spa, Commisariat a l'energie atomique et aux energie alternatives, University of Aachen, University of Thessaly, University of Liverpool, Valter Tosto spa, FISCHBACH MBH.

Cast3M (2003). Un logiciel de simulation numérique.

CEB-FIP (1993). Ceb-fip model code 90. Technical report, Fip-International.

Ceravolo, R., Tondini, N., Abbiati, G., and Kumar, A. (2012). Dynamic characterization of complex bridge structures with passive control systems. *Structural Control and Health Monitoring*, 19(4):511–534.

CNR (2008). Istruzioni per la valutazione delle azioni e degli effetti del vento sulle costruzioni.(in italian language). Technical report, Consiglio nazionale delle ricerche.

Collins, M. P., Mitchell, D., Adebar, P., and Vecchio, F. J. (1996). A general shear design method. *ACI Structural Journal*, 93(1):36–45.

Cornell, C. A. (1968). Engineering seismic risk analysis. *Bull. Seism. Soc. Am.*, 58.

Cornell, C. A. and Krawinkler, H. (2000). Progress and challenges in seismic performance assessment. *PEER Center News*, 3(2).

DIN-FB 104 (2009). Din-fachbericht 104 - verbundbrcken (composite steel and concrete bridges). Technical report, DIN Deutsches Institut fr Normung e. V.

Dyrbye, C. and Hansen, S. O. (1999). *Wind Loads on Structures.* Jhon Wiley and Sons, New York.

ECCS (1986). Recommended testing procedure for assessing the behaviour of structural elements under cyclic loads. Technical report, European Convention for Structural Steelwork - Technical Committee 1 Structural Safety and Loading.

Eftekhar Azam, S., Ghisi, A., and Mariani, S. (2012). Parallelized sigma-point kalman filtering for structural dynamics. *American Control Conference. Seattle, Washington.*, 92–93:193–205.

EN10027 (2006). Designation system for steel part 1: Steel names. Technical report, Comitee Europeen de Normalisation, Bruxelles.

EN1990-2 (2002). Eurocode 0: Basis of structural design. Technical report, Comitee Europeen de Normalisation, Bruxelles.

EN1991-2 (2005). Eurocode 1, actions on structures. part 2: Traffic loads on bridges. Technical report, Comitee Europeen de Normalisation, Bruxelles.

EN1992-1-1 (2005). Eurocode 2, design of concrete structures. part 1-1: General rules and rules for buildings. Technical report, Comitee Europeen de Normalisation, Bruxelles.

EN1993-1-1 (2005). Eurocode 3, design of steel structures. part 1-1: General rules and rules for buildings. Technical report, Comitee Europeen de Normalisation, Bruxelles.

EN1993-1-8 (2005). Eurocode 3, design of steel structures. part 1-8: Design of joints. Technical report, Comitee Europeen de Normalisation, Bruxelles.

EN1994-1-1 (2006). Eurocode 4, design of composite steel and concrete structures. part 1-1: General rules and rules for buildings. Technical report, Comitee Europeen de Normalisation, Bruxelles.

EN1994-2 (2006). Eurocode 4, design of composite steel and concrete structures. part 2: General rules and rules for bridges. Technical report, Comitee Europeen de Normalisation, Bruxelles.

EN1998-1 (2005). Eurocode 2, design of structures for earthquake resistance. part 1: General rules, seismic actions and rules for buildings. Technical report, Comitee Europeen de Normalisation, Bruxelles.

EN1998-2 (2005). Eurocode 2, design of structures for earthquake resistance. part 2: Bridges. Technical report, Comitee Europeen de Normalisation, Bruxelles.

ENISO9223 (2012). Corrosion of metal and alloys - corrosivity of atmosphere - classification, determination and estimation. Technical report, Comit Europen de Normalisation, Bruxelles.

ENISO9226 (2012). Corrosion of metal and alloys - corrosivity of atmosphere determination of corrosion rate of standard specimens for the evaluation of corrosivity. Technical report, Comit Europen de Normalisation, Bruxelles.

Fang, B., Eadie, R., Chen, W. X., and Elboujdaini, M. (2009). Passivation/immersion method to grow pits in pipeline steel and a study of pit nucleation and growth resulting from the method. *Corrosion Engineering, Science and Technology*, 44:32–42.

Fang, B., Han, E., Wang, J. Q., and Ke, W. (2007). Stress corrosion cracking of x-70 pipeline steels in near neutral ph solution subjected to constant load and cyclic load testing. *Corrosion Engineering, Science and Technology*, 42:123–129.

Federal Emergency Management Agency (FEMA) (2006). Interim protocols for determining seismic performance characteristics of structural and nonstructural components through laboratory testing. Technical report, FEMA 461,Washington, D.C.

Gattesco, N. and Giuriani, E. (1996). Experimental study on shear stud connectors subjected to cyclic loadings. *Journal of Constructional Steel Research*, 38.

Giannini, R. (2000). Mathazard: a program for seismic hazard analysis. *University of Roma Tre*.

Guyan, R. J. (1965). Reduction of stiffness and mass matrices. *AIAA journal*, 3(2):380–380.

Holicky, M., Materna, A., Sedlacek, G., Sanpaolesi, L., Vrouwenvelder, T., Kovse, I., and Galvanessian, H. (2005). *Reliability backgrounds - Handbook2 of EN 1990: Eurocode - Basis of structural design. Leonardo da Vinci Pilot Project CZ/02/B/F/PP-134007*.

Hutchinson, T., Zhang, J., and Eva, C. (2011). Development of a drift protocol for seismic performance evaluation considering a damage index concept. *Earthquake Spectra*, 27(4):1049–1076.

Iervolino, I., Galasso, C., and Cosenza, E. (2009). Rexel: computer aided record selection for code-based seismic structural analysis. *Bulletin of Earthquake Engineering*, 8(7):339–362.

International Organization for Standardization (ISO) (2003). Timber structuresjoints made with mechanical fastenersquasistatic reversed-cyclic test method. Technical report, International Organization for Standardization, Geneva, Switzerland.

Ismail, M., Ikhouane, F., , and Rodellar, J. (2009). The hysteresis bouc-wen model, a survey. *Archives of Computational Methods in Engineering*, 16(2):161–188.

Julier, S. J., Uhlmann, J. K., and Durrant-Whyte, H. F. (1995). A new approach for filtering nonlinear systems. *American Control Conference. Seattle, Washington.*, 194:5242–5272.

Kalman, R. E. (1960). A new approach to linear filtering and prediction problems. *Journal of basic Engineering*, 82:35–45.

Kelly, T. (2004). Nonlinear analysis of reinforced concrete shear wall structures. *Bulletin of the New Zealand Society for Earthquake Engineering*, 37(4).

Kent, D. C. and Park, R. (1971). Flexural members with confined concrete. *Journal of the Structural Division, Proceedings of the American Society of Civil Engineers*, ST7(97):1969–1990.

Krawinkler, H., Parisi, F., Ibarra, L., Ayoub, A., and Medina, R. (2001). Development of a test- ing protocol for wood frame structures. report no. w-02. Technical report.

Kumar, S., Itoh, Y., Saizuka, K., and Usami, T. (1997). Pseudodynamic testing of scaled models. *Journal of Structural Engineering*, 123(4):525–526.

Kunnath, S. K. (2007). *Application of the PEER PBEE Methodology to the I-800 Viaduct. PEER 2006/10-report*.

Lanese, I. (2012). *Development and Implementation of an Integrated Architecture for Real-Time Dynamic Hybrid Testing in the Simulation of Seismic Isolated Structures.* PhD thesis, ME School, IUSS Pavia.

Ljung, L. (1999). *System Identification Theory For the User*.

Lomiento, G., Bonessio, N., and Benzoni, G. (2013). Friction Model for Sliding Bearings under Seismic Excitation. *Journal of Earthquake Engineering*, 17(8):1162–1191.

Mackie, K. E., Wong, J. M., and Stojadinovic, B. (2008). Integrated probabilistic performance-based evaluation of benchmark reinforced concrete bridges. *PEER 2007/09*.

Mariani, S. and Corigliano, A. (2005). Impact induced composite delamination: state and parameter identification via joint and dual extended kalman filters. *Computer Methods in Applied Mechanics and Engineering*, 194(7):5242–5272.

Marsh, P. S. and Frangopol, D. M. (2008). Reinforced concrete bridge deck reliability model incorporating temporal and spatial variation of probabilistic corrosion rate sensor data. *Reliability Engineering and system safety*, 93:394–409.

MATLAB (2012). Matlab release 2012b. Technical report, The MathWorks, Inc., Natick, Massachusetts, United States.

Mazzoni, S., McKenna, F., Scott, M. H., L., G., and Fenves, G. L. (2009). Open system for earthquake engineering simulation user command-language manual. Technical report, Pacific Earthquake Engineering Research Center, University of California, Berkeley.

McKay, M. D., Beckman, R. J., and Conover, W. J. (1979). A comparison of three methods for selecting values of input variables in the analysis of output from a computer code. *Technometrics*, 22:239–245.

Menegotto, M. and Pinto, E. (1973). Method of analysis for cyclically loaded reinforced concrete plane frames including changes in geometry and non-elastic behavior of elements under combined normal force and bending. In *IABSE Symposium*, Lisbon, Portugal.

MIKTI (2008). Pont mixtes acier-beton (MIKTI). National french project, French ministry of transportation.

Mostaghel, N. (1999). Analytical Description of Pinching, Degrading Hysteretic Systems. *Journal of Engineering Mechanics*, 125(2):216–224.

Nowak, A. and Collins, K. (2000). *Reliability of Structures*.

NTC2008 (2008). Decreto ministeriale 14.01.2008. norme tecniche per le costruzioni (in italian). Technical report, Ministero delle Infrastrutture.

Paolacci, F., Bursi, O., Popa, N., Cremona, C., Stathopulos, S., and Hoffmeister, B. (2015). Performance-based earthquake engineering analysis of short-medium span steel-concrete composite bridges (SEQBRI). European Research Fund for Coal and Steel RFSR-CT-2012-00032., University of Rome TRE, University of Trento, Arcelormittal, Cerema, Domi Consulting Engineering, University of Aachen.

Paolacci, F. and Giannini, R. (2012). An experimental and numerical investigation on the cyclic response of a portal frame pier belonging to an old reinforced concrete viaduct. *Earthquake Engineering & Structural Dynamics*, 41(6):1109–1127.

Paolacci, F. e. a. (2014). Assessment of the seismic vulnerability of an old r.c viaduct with frame piers and study of the effectiveness of different isolation systems through pseudodynamic test on a large scale model (RETRO) final report. Sismic Engineering Research Infrastructures For European Synergies (SERIES) Project No.: 227887, University Roma Tre, European Commission (JRC), University of Sannio, University of Naples, University of Trento, Politecnico of Torino, Alga Spa.

Pegon, P. and Magonette, G. (2002). Continuous psd testing with non-linear substructuring: Presentation of a stable parallel inter-field procedure - tr 1.02.167. Technical report, European Laboratory for Structural Assessment (ELSA), Joint Research Centre of Ispra (VA), Italy.

Peloso, S. and Pavese, A. (2009). Frp seismic retrofit for insufficient lap-splice: Large scale testing of rectangular hollow section bridge piers. *COMPDYN 2009 ECCOMAS Thematic Conference on Computational Methods in Structural Dynamics and Earthquake Engineering Rhodes*.

Priestley, M. J. N., Verma, R., and Xiao, Y. (1994). Seismic Shear Strength of Reinforced Concrete Columns. *Journal of Structural Engineering*, 120(8):2310–2329.

Priestley, M.J.N. and Calvi, G.M. and Kowalsky, M.J. (2007). *Displacement-Based Seismic Design of Structures.* IUSS Press, Pavia, Italy.

SIMULIA, Dassault Systemes Simulia Corporation, U. (2011). *Abaqus FEA*.

Smyth, A. W., Masri, S. F., Chassiakos, A. G., and Caughey, T. K. (1999). Online parametric identification of mdof nonlinear hysteretic systems. *Journal of Engineering Mechanics*, 125(2):133–142.

Soong, T. and M., G. (1993). *Random Vibration of Mechanical Systems*.

Stewart, M. G. (2004). Spatial variability of pitting corrosion and its influence on structural fragility and reliability of rc beams in flexure. *Structural Safety*, 26:453–470.

TENARIS (2008). Product specification: high strength steel tubing for structural purposes. Technical report, Tenaris.

Trucano, T., Swiler, L., Igusa, T., Obekampf, W., and Pilch, M. (2006). Calibration, validation, and sensitivity analysis: What's what. *Reliability engineering and System Safety*, 91:1331–1357.

Vamvatsikos, D. and Cornell, C. A. (2001). Pseudodynamic testing of scaled models. *Earthquake Engineering and Structural Dynamics*, 31:291–514.

Vecchio, F. J. and Collins, M. P. (1988). Predicting the response of reinforced concrete beams subjected to shear using modified compression field theory. *ACI Structural Journal*, 85(3):258–268.

Wan, E. and Van der Merwe, R. (2000). The unscented kalman filter for non linear estimation. *Adaptive Systems for Signal Processing, Communications, and Control Symposium 2000. AS-SPCC. The IEEE 2000 Lake Louise, Alta.*, pages 153–158.

Wu, M. and Smyth, A. (2007). Application of the unscented kalman filter for real time nonlinear structural system identification. *Structural Control and Health Monitoring*, 14(7):971–990.

Yang, T. Y., Mohele, J., Stojadinovic, B., and Der Kiuregan, A. (2009). Seismic Performance Evaluation of Facilities: Methodology and Implementation, Journal of Structural Engineering. *Journal of Structural Engineering*, (135):1146–1154.